

# Gravure-printed electronics: Devices, technology development and design

*Gerd Grau*



Electrical Engineering and Computer Sciences  
University of California at Berkeley

Technical Report No. UCB/EECS-2017-17

<http://www2.eecs.berkeley.edu/Pubs/TechRpts/2017/EECS-2017-17.html>

May 1, 2017

Copyright © 2017, by the author(s).  
All rights reserved.

Permission to make digital or hard copies of all or part of this work for personal or classroom use is granted without fee provided that copies are not made or distributed for profit or commercial advantage and that copies bear this notice and the full citation on the first page. To copy otherwise, to republish, to post on servers or to redistribute to lists, requires prior specific permission.

Gravure-printed electronics: Devices, technology development and design

By

Gerd Fritz Milan Nino Grau

A dissertation submitted in partial satisfaction of the

requirements for the degree of

Doctor of Philosophy

in

Engineering – Electrical Engineering and Computer Sciences

in the

Graduate Division

of the

University of California, Berkeley

Committee in charge:

Professor Vivek Subramanian, Chair

Professor Andrew R. Neureuther

Professor Costas P. Grigoropoulos

Spring 2016

Copyright © 2016, by the author(s).

All rights reserved.

Permission to make digital or hard copies of all or part of this work for personal or classroom use is granted without fee provided that copies are not made or distributed for profit or commercial advantage and that copies bear this notice and the full citation on the first page. To copy otherwise, to republish, to post on servers or to redistribute to lists, requires prior specific permission.

## Abstract

Gravure-printed electronics: Devices, technology development and design

by

Gerd Fritz Milan Nino Grau

Doctor of Philosophy in Engineering – Electrical Engineering and Computer Sciences

University of California, Berkeley

Professor Vivek Subramanian, Chair

Printed electronics is a novel microfabrication paradigm that is particularly well suited for fabrication of low-cost, large-area electronics on flexible substrates. Applications include flexible displays, solar cells, RFID tags or sensor networks. Gravure printing is a particularly promising printing technique because it combines high print speed with high resolution patterning. In this thesis, gravure printing for printed electronics is advanced on multiple levels. The gravure process is advanced in terms of tooling and understanding of printing physics as well as its application to substrate preparation and device fabrication.

Gravure printing is applied to transform paper into a viable substrate for printed electronics. Paper is very attractive for printed electronics because it is low-cost, biodegradable, lightweight and ubiquitous. However, printing of high-performance electronic devices onto paper has been limited by the large surface roughness and ink absorption of paper. This is overcome here by gravure printing a local smoothing layer and printed organic thin-film transistors (OTFTs) are demonstrated to exhibit performance on-par with device on plastic substrates.

If highly-scaled features are to be printed by gravure, traditional gravure roll making techniques are limited in terms of pattern definition and surface finish. Here, a novel fabrication process for gravure rolls is demonstrated utilizing silicon microfabrication. Sub-3 $\mu\text{m}$  features are printed at 1m/s. Proximity effects are demonstrated for more complex highly-scaled features. The fluid mechanics of this effect is studied and it is suggested how it can be used to enhance feature quality by employing assist features.

Finally, advancements are made to printed organic thin-film transistors as an important technology driver and demonstrator for printed electronics. First, a novel scanned thermal annealing technique is presented that significantly improves the crystallization of an organic semiconductor and electrical performance. Second, transistors are fully gravure printed at a high print speed of 1m/s. By scaling both lateral and thickness dimensions and optimizing the printing processes, good electrical performance, low-voltage operation and low variability is demonstrated.

## Acknowledgements

I would like to thank a number of people who made this work possible as well as enjoyable. First and foremost I would like to thank my advisor Professor Vivek Subramanian. Throughout my time in graduate school he always pushed me to achieve more and gave me guidance when needed whilst giving me the freedom to pursue what interested me and become an independent researcher. I learned many important lessons from him that will be invaluable in the future – be it in research, mentoring, writing or teaching. I want to thank my dissertation committee members Professor Andy Neureuther and Professor Costas Grigoropoulos and Professor Ana Claudia Arias who was the chair of my qualifying exam committee. I am also very grateful to Professor Hayden Taylor and Professor Randy Schunk who were great collaborators and mentors during my job search. I am indebted to Professor Clark Nguyen who gave me the chance to teach a class over one summer, which was a very important experience on my road to an academic career.

None of this work would have been possible without collaborators both within the Printed Electronics group at Berkeley as well as from other groups. I am especially thankful to those who worked on gravure printing at the same time as me and with whom I shared many insightful discussions, namely Rungrot (Jack) Kitsomboonloha, Hongki Kang, William Scheideler, Artos Cen and Daniel Hariprasad. Sharing a lab with a large number of people over the years working on a variety of projects has given me many interesting perspectives and practical help with my projects as well as many enjoyable moments. For that I am grateful to Steve Volkman, Lakshmi Jagannathan, Michael Tseng, Jaewon Jang, Eungseok Park, Feng Pan, Kyle Braam, Sarah Swisher, Jake Sadie, Rumi Karim, Andre Zeumault, Adrien Pierre, Garret McKerricher, Seungjun Chung, Jeremy Smith, Nishita Deka, Carlos Biaoou and Matt McPhail.

Both the Nanolab and the Cory machine shop staff were always very helpful when I needed to solve a tool problem or build a custom setup. The mailroom in Sutardja Dai was another place with very friendly people who helped me out many times. I also want to thank Charlotte Jones and Gwen Lindsey who were always very helpful when I needed administrative assistance.

Over the years I have received funding from a number of sources that I am grateful for. I would like to highlight the NASCENT NSF ERC whose semiannual meetings in Austin and Albuquerque were always a great way to meet researchers from other universities as well as Merck who not only provided funding but also organic materials that I used for most of my transistor work.

My family – my parents, my sister and her husband – was always there for me during these years giving me support, advice and perspective in many different situations. Lastly, but most importantly, I want to thank my fiancée Angela. She was patient with me when I worked long hours in the lab, when I wanted to endlessly discuss research or career directions (and she gave me good feedback) or when I told a new acquaintance about my research for the 1000<sup>th</sup> time in her presence. Spending my free time with her has made every moment of my life enjoyable. Meeting her has been the best result of my time at Berkeley.

## Table of Contents

Chapter 1: Introduction.....	1
1.1 Printed Electronics .....	1
1.2 Comparison of different printing techniques .....	3
1.3 Fluid mechanics at the microscale .....	5
1.3.1 Viscous forces .....	6
1.3.2 Surface tension forces .....	7
1.4 Overview of gravure printing process .....	12
1.4.1 Cell filling .....	13
1.4.2 Doctor blade wiping.....	15
1.4.3 Ink transfer .....	18
1.4.4 Pattern formation on the substrate .....	20
1.4.5 Overall process optimization .....	21
1.5 Printed organic thin-film transistors (OTFTs) .....	22
1.6 Thesis organization .....	24
Chapter 2: Gravure printing enabled transistors on novel paper substrates .....	26
2.1 Introduction .....	26
2.2 Paper characterization .....	27
2.3 Paper modification .....	31
2.4 Printed devices on smoothed paper .....	39
2.4.1 Dielectric evaluation .....	39
2.4.2 Printed transistors on paper.....	42
2.4.3 Bending tests .....	47
2.5 Conclusions .....	48
Chapter 3: Fabrication of gravure roll for high-resolution printing .....	50
3.1 Introduction .....	50
3.2 Roll fabrication process.....	53
3.3 Printing results.....	57
3.3.1 Plate mounting on magnetic roller .....	57
3.3.2 Printing optimization .....	59

3.3.3	Effect of hard layer on roll scratching .....	63
3.4	Conclusions .....	65
Chapter 4:	Proximity effects in high-resolution gravure printing .....	66
4.1	Introduction .....	66
4.2	Experimental .....	68
4.3	Printed pattern analysis .....	69
4.3.1	Proximity effect .....	69
4.3.2	Automated pattern analysis.....	71
4.3.3	Design rules and assist features .....	73
4.4	Proximity effect fluid mechanics .....	78
4.4.1	Fluid analysis on printing plate.....	78
4.4.2	Ink transfer .....	80
4.4.3	Proximity effect analysis.....	83
4.5	Conclusions .....	99
Chapter 5:	Printed organic thin-film transistors .....	100
5.1	Introduction .....	100
5.2	A novel scanned thermal annealing technique to optimize organic semiconductor crystallization.....	101
5.2.1	Simulation of thermal gradient .....	103
5.2.2	Device fabrication.....	106
5.2.3	Results and discussion .....	107
5.3	Fully gravure printed organic thin-film transistors .....	113
5.3.1	Device fabrication.....	114
5.3.2	Device characterization.....	127
5.4	Conclusions .....	135
Chapter 6:	Conclusions and future work .....	136
6.1	Conclusions .....	136
6.2	Future work .....	137
Chapter 7:	References.....	140
Appendix A:	Bending test strain calculation .....	150

# Chapter 1: Introduction

## 1.1 Printed Electronics

The graphics arts industry has used printing techniques for centuries to print patterns of colored ink onto innumerable products. This has led to the development of very sophisticated printing machines, processes and inks. Patterns can be printed onto very large webs that are several meters wide at high print speeds on the order of 10m/s. This results in very large production throughput and thus low-cost production per unit area of the substrate. The vision of printed electronics is to leverage this expertise to fabricate low-cost, large-area electronics.<sup>1-3</sup> Applications that are fundamentally large-area are particularly promising to take advantage of the low cost per unit area offered by printing. Such applications include displays, solar cells, RFID antennas or sensor networks (see Figure 1-1). Another factor that significantly increases the throughput of printing techniques is their additive nature. Ink is only deposited where it is actually needed. This is very different from traditional microfabrication techniques that are subtractive. Traditionally, blanket layers are deposited by techniques such as chemical vapor deposition (CVD), evaporation, sputtering or thermal oxidation. In order to create functional patterns such as lines or squares, these blanket layers need to be patterned. Typically, photolithography is employed to pattern photoresist that protects the desired pattern whilst unwanted material is etched away. This process involves several steps and tools, some of which require slow vacuum processing, which further degrades process throughput. In contrast, printing is a one-step, additive process, which not only improves throughput but also material utilization.



Figure 1-1. Applications that are fundamentally large-area and thus ideally suited to take advantage of the benefits of printed electronics (a) RFID tag with antenna ([www.wired.com](http://www.wired.com)), (b) Flexible display ([www.display-central.com](http://www.display-central.com)), (c) Electronic skin sensor network ([www.hight3ch.com](http://www.hight3ch.com))

Another key difference between traditional microfabrication and printed electronics is the materials that are used to fabricate devices. Printing requires materials that are solution processable

since printing deposits liquid inks. This means the active material is dissolved or dispersed in a solvent during printing. The solvent is evaporated after printing and the material is converted into its final state. The temperature at which this conversion process occurs constrains the choice of substrate material. If flexible substrates such as low-cost plastic are used, processing temperatures cannot exceed about 200°C and for some plastics need to be even lower.<sup>4</sup> Both of these requirements, solution processability and low thermal budget, make organic materials attractive for printed electronics.<sup>5-7</sup> In particular, dielectrics and semiconductors can be fabricated from polymer and small molecule materials. Such materials can be readily dissolved in a variety of organic solvents and typical processing temperatures are around 100°C. However, conductors fabricated from organic materials tend to exhibit poor conductivity compared with metals.<sup>8</sup> Thus, metal nanoparticles are widely used to print the electrodes for organic devices.<sup>9-11</sup> Organic ligands are attached to metal nanoparticles to solubilize them in solvents and formulate inks. Due to the small size of these nanoparticles (diameter on the order of 10nm), they exhibit a very large surface to volume ratio, which results in a significantly reduced melting temperature. Thus, metal nanoparticles can be sintered at plastic compatible temperatures to form conductive patterns. The combination of metal nanoparticle and organic inks enables the printing of conductors, semiconductors and dielectrics on low-cost plastic substrates to print complete microelectronic devices.

A range of different devices has been fabricated using printing techniques. This includes transistors<sup>12-26,24,27,28</sup>, sensors<sup>29,30</sup>, MEMS devices<sup>31,32</sup>, batteries<sup>33</sup>, solar cells<sup>34</sup>, organic light-emitting diodes (OLEDs)<sup>35</sup>, antennas<sup>36</sup> and passive components<sup>37</sup>. By putting these devices together, fully printed systems can be fabricated. The performance of printed electronics still remains limited by low resolution and low performance materials compared with traditional silicon CMOS processes. It is thus paramount to choose applications that do not require very high performance whilst benefitting from the unique advantages that printed electronics offers. Printing is ideal for large-area, low-cost applications on flexible substrates. Such applications include RFID tags<sup>38</sup>, flexible displays<sup>39</sup> and large-area sensing<sup>40</sup>. Whilst these applications do not require performance on par with traditional silicon microelectronics, the performance of printing processes and printed devices does need to be pushed further to enable real systems. In this dissertation, the performance of gravure printing as well as the performance of printed transistors is pushed towards fully printed systems.

The choice of gravure printing as the focus of this dissertation is discussed in the next section by contrasting different printing techniques that offer different benefits and drawbacks. The physics of gravure printing that underpins large parts of this thesis are described next after a more general section describing fluid mechanics at the microscale. This fluid mechanical understanding is crucial in order to understand the flow of liquid inks during the printing process. The state-of-the-

art in printed transistors, which are the main technology demonstration in this thesis, is discussed in the following section. Finally, an overview of the thesis organization is given.

## 1.2 Comparison of different printing techniques

Many different printing techniques have been proposed for printed electronics.<sup>41,42,3</sup> Each printing technique has its own particular advantages and disadvantages and thus complex systems will likely be fabricated by a combination of different techniques. There are many different categorizations by which printing methods can be classified. The two most immediate dimensions for categorization are throughput and resolution (see Figure 1-2). Traditionally, there has been a trade-off between the two; high-speed printing techniques are often limited to pattern sizes on the order of multiple tens of micrometers.

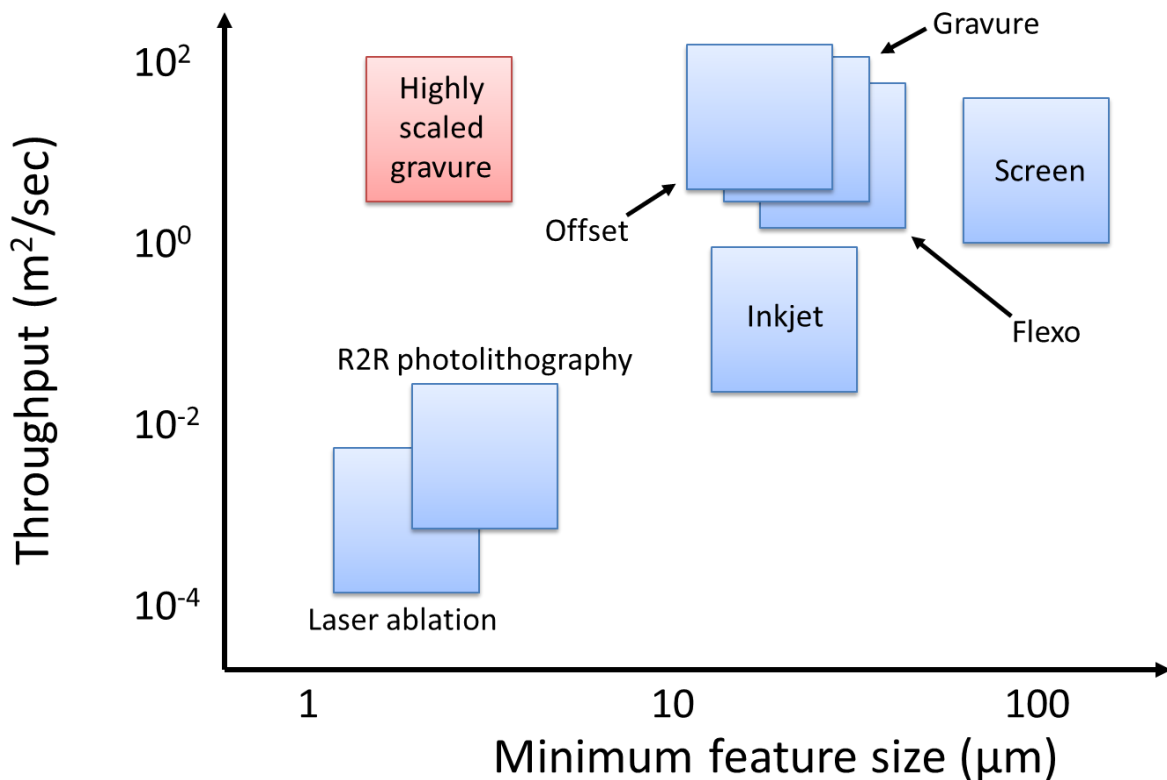


Figure 1-2. Trade-off between printing throughput and resolution for a number of different printing techniques that have been proposed for printed electronics. Recently, it has been shown that gravure can overcome this trade-off and highly-scaled features can be printed whilst maintaining high throughput.

One broad category of printing methods is digital methods such as inkjet printing. Such techniques offer the advantage of being able to easily change patterns on the fly. This is a great advantage in research and prototyping. However, throughput, reliability and resolution are challenges. Inkjet deposits material by jetting droplets from a nozzle that is scanned relative to the substrate. In order to achieve high throughput, a large number of nozzles must be used, which increases the risk of nozzle clogging. Similarly, downscaling of feature size is limited by the nozzle size and drop placement accuracy, especially at high print speeds.<sup>16,43</sup> When downscaling nozzle size, the risk of clogging increases and droplet deviation also worsens. Thus, non-digital printing methods such as screen printing, offset, flexography and gravure are more promising for scaled-up high-throughput manufacturing. These contact printing techniques offer superior pattern fidelity because no jetting from a nozzle is involved. Screen printing is unique in this list because ink is pushed through a mesh onto the substrate. The mesh acts as a support for the stencil that defines the pattern. Screen printing requires high viscosity inks, which makes it ideally suited for the deposition of thick films.<sup>41</sup> The printing of high-resolution features is limited by the mesh. Small feature sizes require a larger mesh count per unit area i.e. smaller openings in the mesh to support the fine features on the mask. This limits the amount of high viscosity ink that can be pushed through the mesh leading to non-uniform features.<sup>44</sup> Thus, the resolution of screen printing is limited to several micrometers; indeed, in commercial use, screen printing typically delivers resolutions worse than tens of micrometers.<sup>45,46</sup> Conversely, offset, flexography and gravure printing all use a roll that is inked, from which patterned ink is transferred to the substrate. They differ in how the pattern is created on the roll. In flexography the pattern consists of raised features that are inked from an anilox roller. The resolution of flexography is limited by the low stiffness of the material from which the patterned roll is fabricated leading to the over compression of fine features during the printing process and reduced pattern fidelity.<sup>47</sup> Offset and gravure are most promising in terms of resolution and print speed. In offset, the pattern and non-pattern areas lie in the same plane on the roll. Patterning is achieved by differences in surface energy. The main drawback is the difficulty in creating inks where the right combination of surface energies, ink surface tension and ink viscosity gives good patterning. In gravure printing, the pattern is made up of recessed cells below the roll surface. These cells are filled with ink and excess ink is removed from the land areas in between the cells using a doctor blade (see Figure 1-3 for an overview of the gravure process). The pattern is typically pixelated into individual square cells. An analogous technique, intaglio printing, makes use of continuous trenches; this is avoided in gravure since the use of such trenches causes the print quality to be much more orientation dependent.<sup>48</sup> Gravure cylinders are typically made from metals such as copper with a chromium coating. This results in excellent dimensional stability, durability and pattern fidelity as well as compatibility with a wide range of solvents. The main challenge with gravure is non-idealities during the doctor blade wiping process. Recently, it has been demonstrated that by understanding the underlying physics in detail, gravure printing can be pushed into a highly-scaled regime with feature sizes well below 10 $\mu$ m whilst still printing at high speeds on the order of 1m/s.<sup>23,49</sup> This makes gravure a very promising technique to deliver high-performance, low-cost printed electronics and it will be the focus of this dissertation.

In order to push the performance of gravure printing, one needs to understand the underlying physical principles of the printing process. Before describing the specifics of the gravure process, it is instructive to consider fluid mechanics at the microscale more generally. The next section describes the forces and phenomena that dictate the behavior of the liquid ink in the gravure process as well as in many other printing processes.

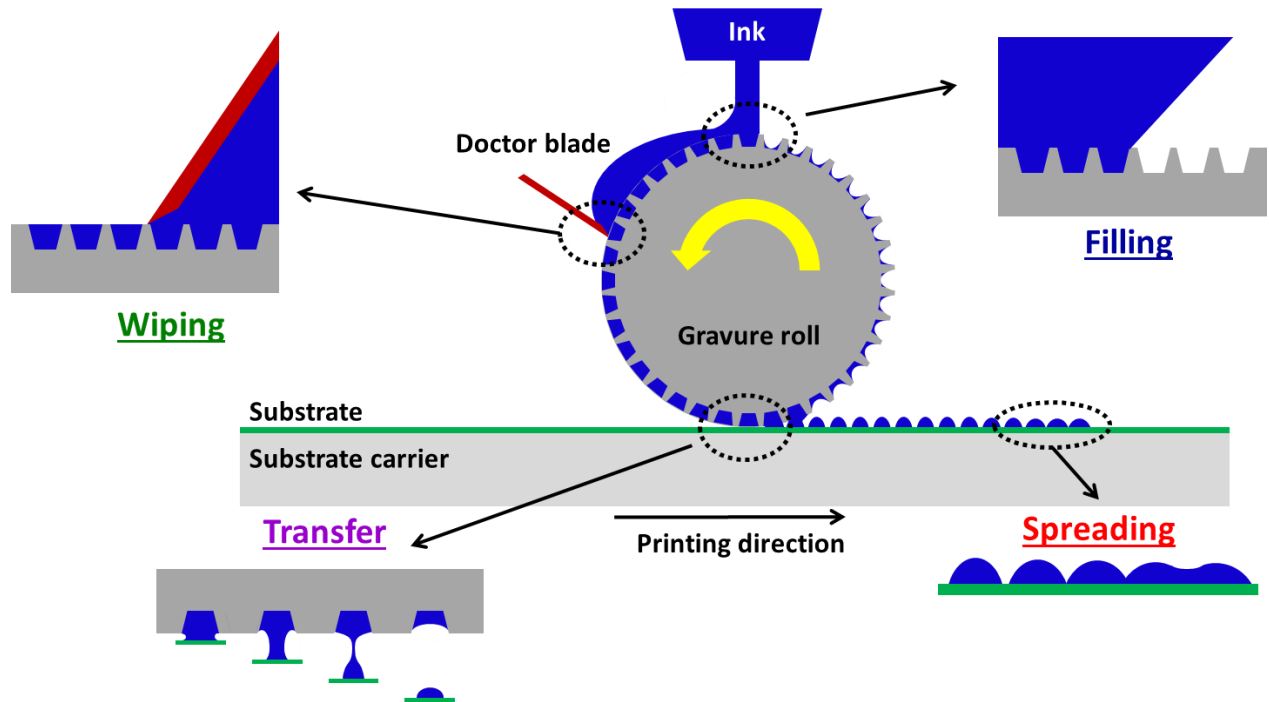


Figure 1-3. Overview of the gravure process and its four sub-processes: cell filling, doctor blade wiping, ink transfer and ink spreading on the substrate. Courtesy of Rungrot Kitsomboonloha.

### 1.3 Fluid mechanics at the microscale

Printing means the deposition of liquid inks. Thus, it is imperative to understand the fluid mechanical processes that occur during the printing process. In this section, the basic fluid mechanics that underpins many aspects of this thesis will be discussed. This discussion will focus on effects that occur at the microscale to enable highly-scaled printing of microelectronics. At the microscale, the two most important forces experienced by fluids are surface tension and viscous forces. Other forces such as gravity and inertial forces scale with the geometrical dimensions of the system. This can be seen from dimensionless numbers that represent the relative magnitudes of these forces:

$$\text{Reynolds number: } Re = \frac{\textit{inertial}}{\textit{viscous}} = \frac{\rho UL}{\mu} \quad \text{Eq. 1-1}$$

$$\text{Bond number: } Bo = \frac{\textit{gravity}}{\textit{surface tension}} = \frac{\Delta\rho g L^2}{\sigma} \quad \text{Eq. 1-2}$$

$$\text{Capillary number: } Ca = \frac{\textit{viscous}}{\textit{surface tension}} = \frac{\mu U}{\sigma} \quad \text{Eq. 1-3}$$

Where  $\rho$  is the fluid density,  $U$  is a characteristic velocity of the problem (for example print speed),  $L$  is a characteristic length scale of the problem (for example channel width),  $\mu$  is the fluid viscosity,  $\Delta\rho$  is the density difference between two fluids that leads to gravitational forces,  $g$  is the gravitational acceleration and  $\sigma$  is the fluid surface tension. As the characteristic length scale  $L$  is scaled down to the microscale, inertial and gravity forces diminish relative to viscous and surface tension forces. There are some situations in printing where inertia does play an important role such as when ejecting low-viscosity droplets from an inkjet nozzle at high speeds.<sup>50</sup> However, in the present work, inertia can be neglected in most situations. Conversely, capillary number ( $Ca$ ), the ratio of viscous to surface tension forces, does not scale with length.  $Ca$  depends on ink (viscosity and surface tension) and printing (characteristic speed such as printing speed in gravure) conditions that can be tuned to optimize printing. Thus, viscosity and surface tension are discussed next.

### 1.3.1 Viscous forces

Viscosity describes the resistance of fluids to flow under an applied load. It is defined as

$$\mu = \frac{\tau}{\frac{\partial u}{\partial y}} = \frac{\tau}{\dot{\gamma}} \quad \text{Eq. 1-4}$$

Where  $\mu$  is viscosity and  $\tau$  is the applied shear stress to drive a velocity ( $u$ ) gradient in the direction perpendicular to the flow direction ( $y$ ). Thus, a shear force needs to be applied to a viscous liquid to maintain a velocity gradient. For example, this is the case when liquid flows past a stationary wall where the fluid velocity is zero due to the non-slip condition. By varying a fluid's viscosity, the amount of flow under an applied force, such as surface tension, can be varied. Typical inks in printed electronics contain multiple components. Active materials such as polymers, small organic molecules or nanoparticles are dissolved or dispersed in a solvent. By varying the concentration of the solute, viscosity can be altered dramatically. Typically, viscosity varies exponentially with solute concentration and can be tuned over several orders of magnitude (see Figure 1-4). This allows the viscosity to be optimized for different printing processes and applications. Gravure printing can print inks with viscosities ranging from around 10cP to several hundred cP. Many inks used for printed electronics are non-Newtonian i.e. viscosity is a function of shear rate. Most commonly, inks are shear thinning i.e. viscosity decreases with increasing shear rate as cohesive forces between polymer chains or nanoparticles become weaker at higher shear rates. This plateaus at sufficiently high shear rates resulting in a constant, low viscosity. Most gravure sub-processes

except for ink spreading on the substrate operate at sufficiently high shear rates such that viscosity can be assumed to be constant with shear rate.<sup>49</sup>

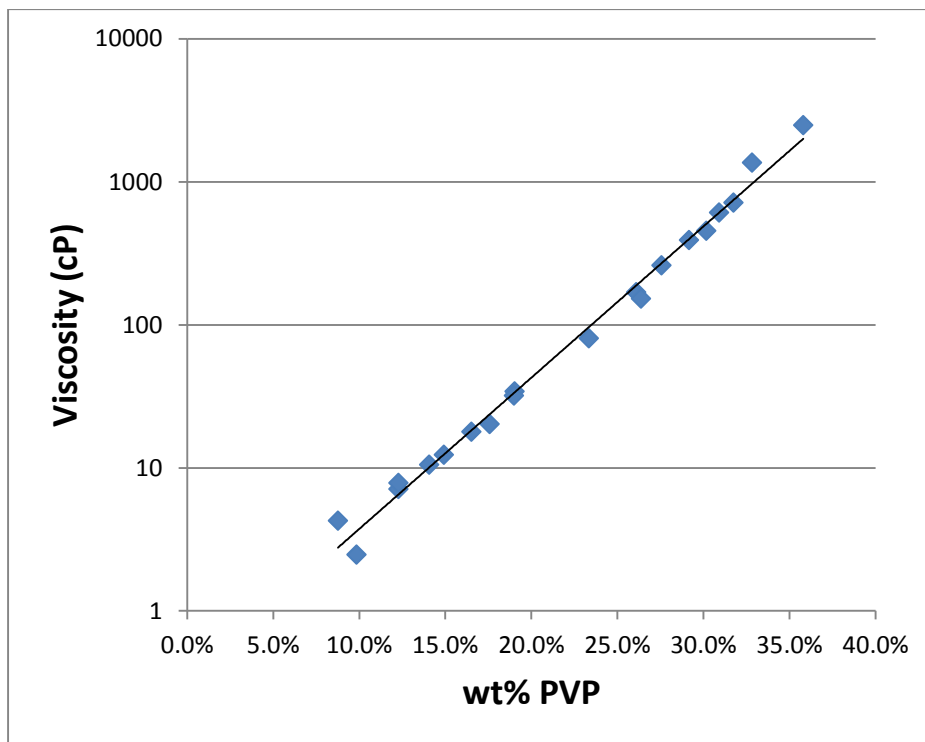


Figure 1-4. Viscosity of poly-4-vinyl phenol (PVP) polymer as a function of concentration in the solvent PGMEA. Viscosity depends exponentially on concentration and can be tuned over several orders of magnitude to optimize printing performance.

### 1.3.2 Surface tension forces

Viscous forces typically inhibit flow whilst the most important driving force for flows at the microscale during gravure printing is surface tension. Surface tension arises due to the fact that fluid molecules at the interface with another material or air do not have a neighboring molecule of the same type on one side. At the fluid-air interface, this is energetically unfavorable for pure liquids. Thus, a surface energy is associated with creating such a fluid-air interface. Fluids will try to minimize their surface energy for example leading to spherically shaped droplets. In order to grow the size of the liquid-air interface, a force needs to be applied that is the spatial derivative of the surface energy. This surface tension always acts tangential to the interface. It is reported per unit length of the side of the interface that the surface tension acts on (see Figure 1-5) and is thus equivalent to the surface energy per unit area. Surface tension creates a flow if there is a resulting force on an interfacial fluid element due to spatial variations in surface tension. Here, the three

main forms of such spatial variations that are encountered during printing are reviewed: curved fluid interfaces that lead to spatial variations in the surface tension force vector, variations in surface tension magnitude and variations due to the presence of multiple disparate interfaces.

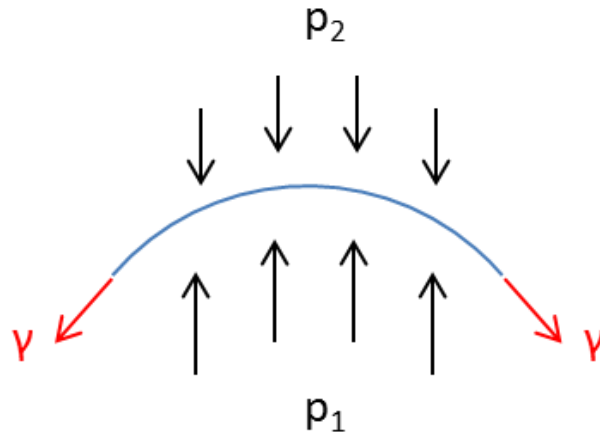


Figure 1-5. Cross-sectional free-body diagram of curved fluid interface (blue). Surface tension  $\gamma$  acts tangential to the fluid interface and is quoted as force per unit length into the page. The curvature of the interface leads to a pressure difference across the interface where  $p_1 > p_2$ .

### 1.3.2.1 Curved interfaces

If the liquid interface is curved, a net force perpendicular to the curved interface is created that generates a pressure difference across the interface. This is described by the Young-Laplace equation:

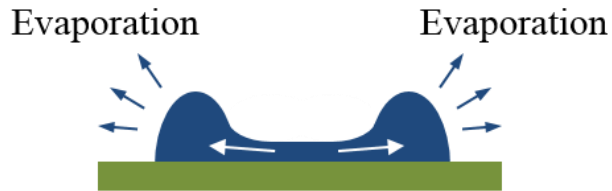
$$\Delta p = -\gamma \nabla \cdot \hat{n} = -\gamma \left( \frac{1}{R_1} + \frac{1}{R_2} \right) \quad \text{Eq. 1-5}$$

Where  $\Delta p$  is the pressure difference across the interface,  $\gamma$  is the surface tension,  $\hat{n}$  is the surface normal and  $R_1$  and  $R_2$  are the principal radii of curvature of the interface. Convex fluid interfaces such as in a spherical droplet result in a positive pressure inside the fluid. The pressure is increased for smaller radii of curvature. If regions of different interfacial curvature are connected, fluid will be driven towards regions with a larger radius of curvature by a pressure driven flow. This will also minimize surface energy. Such flows driven by capillary pressure can be observed at different stages of the gravure process. They dictate for example how printed patterns evolve on the substrate.<sup>51-53</sup>

### 1.3.2.2 Surface tension gradients

The second mechanism by which surface tension induces flow is spatial variations in the magnitude of surface tension, termed Marangoni flow. Surface tension depends on a number of variables. The most immediate variable is the type of fluid. In complex inks such as those encountered in printed electronics with at least two components (solvent and solute), surface tension depends on composition. Especially solutes that act as surfactants by preferentially organizing on the fluid surface can dramatically lower surface tension. Another important variable that determines the magnitude of a fluid's surface tension is temperature. Surface tension decreases with increasing temperature until tending to zero at the boiling point. Thus, spatial variations in solute concentration or temperature can result in surface tension gradients and induce flow. One important situation where gradients in both of these variables can be observed is during ink drying on the substrate after printing. During drying, the liquid solvent evaporates leaving the solute behind. Viscosity increases until it is large enough to prevent any further flow and the final dry shape has been reached. Solvent evaporation requires energy that can locally lower the fluid temperature where the evaporation rate is highest leading to temperature gradients. Concentration gradients can be created due to convective flows during drying. For example, since solvent evaporation is fastest at the edges of patterns, a convective flow is created from the inside of the pattern to its perimeter. Significant amounts of solute material can be deposited at the rim of patterns leading to very non-uniform thickness profiles (see Figure 1-6). This is the so-called coffee ring effect. This problem is more pronounced in inkjet printing but can also be observed when low-viscosity inks are printed by gravure. It can be mitigated by understanding and balancing the temperature and concentration gradient induced Marangoni flows with the outward convective flow.<sup>54-57</sup>

(a)



(b)

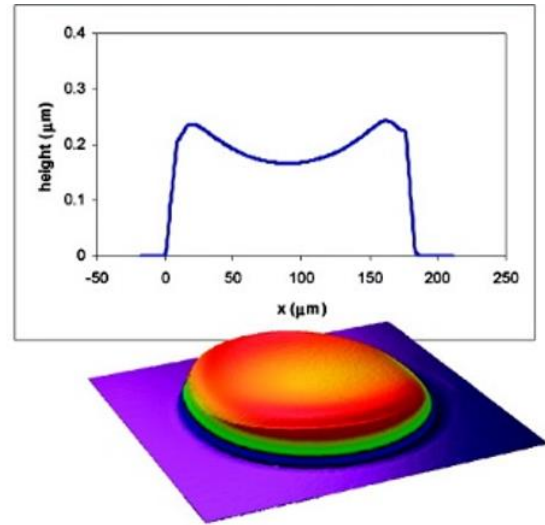


Figure 1-6. (a) The coffee ring effect occurs due to the faster evaporation of solvent at the edges of a feature leading to an outward convective flow. (b) Typical profile and perspective view of droplet exhibiting the coffee ring effect. Reprinted with permission from <sup>57</sup>. Copyright 2008 American Chemical Society.

### 1.3.2.3 Multiple disparate interfaces

The third mechanism by which surface tension induces flow occurs if there is more than one interface and these interfaces have different surface energies. This is very commonly observed when liquid makes contact to a solid such as the substrate or the gravure roll. In this case, there are three interfaces with different surface energies: solid-liquid, liquid-gas and solid-gas (see Figure 1-7).

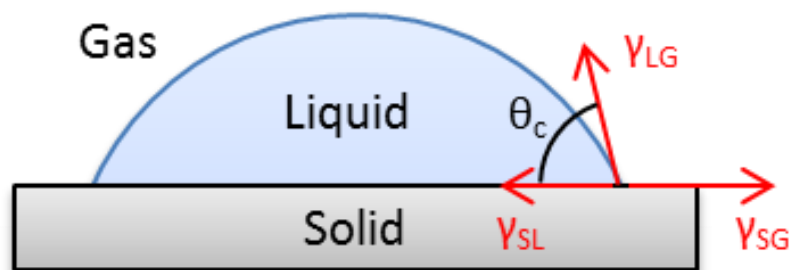


Figure 1-7. The contact angle  $\theta_c$  at the interface between a solid, a liquid and a gas or a second liquid can be calculated using the Young's condition, which can be derived as a horizontal force balance of the three surface tension components. In the absence of contact angle hysteresis, droplets on a surface will assume the shape of a spherical cap.

The contact angle that the liquid-gas interface makes to the solid surface (assumed to be flat here) depends on the balance between these three surface energies as given by the Young's equation:

$$\cos \theta_c = \frac{\gamma_{SG} - \gamma_{SL}}{\gamma_{LG}} \quad \text{Eq. 1-6}$$

Where  $\theta_c$  is the contact angle,  $\gamma$  denotes surface energy and S, G and L denote solid, gas and liquid respectively. If  $\gamma_{SG} - \gamma_{SL} > \gamma_{LG}$ , the contact angle will be zero and the liquid will spread uncontrollably to form a thin film. This situation of total wetting occurs for example in the case of water on clean silicon dioxide. If  $\frac{\gamma_{SG} - \gamma_{SL}}{\gamma_{LG}}$  is between 0 and 1, the liquid partially wets the solid.

The contact angle will lie between 0 and 90 degrees. This is a common situation found in printed electronics for example in the case of many organic solvents on plastic substrates after their surface energy was increased using methods such as oxygen plasma treatment. Such contact angles are often desirable because the ink will spread on the surface to form a uniform film without spreading uncontrollably thereby making effective patterning impossible. If  $\gamma_{SG} - \gamma_{SL} < 0$ , the ink will not wet the solid surface and make a contact angle larger than 90 degrees. For example, many fluorinated polymers such as Teflon have sufficiently low surface energy to be non-wetting. This situation can be desirable to prevent ink from flowing onto certain surfaces such as the doctor blade during gravure printing. However; in the context of substrates to be printed on, non-wetting surfaces are generally undesirable because they tend to cause patterns to break up and ink to ball up to minimize surface energy. In the context of aqueous inks, surfaces with contact angle below 90 degrees are termed hydrophilic and surfaces with contact angle above 90 degrees are termed hydrophobic. This analysis assumes that there is one unique equilibrium contact angle. However, in most real situations this is not the case. Usually, there exists a range of contact angles that are stable. The advancing contact angle marks the upper end of this range. If the contact line reaches this angle, for example because more fluid is added to a droplet on a surface, the contact line will advance i.e. the fluid will spread further on the surface. The receding contact angle marks the lower end of the equilibrium range. If the contact line reaches this angle, for example because fluid is removed from a droplet on a surface, the contact line will recede i.e. the droplet will shrink. This contact angle hysteresis can be caused by microscale roughness or chemical inhomogeneity of the surface. The contact line gets pinned at such variations in equilibrium contact angle as it moves across the surface. Contact angle hysteresis can be exploited to print patterns on a substrate that would be impossible to print if there was only one equilibrium contact angle such as features with sharp corners.<sup>53</sup>

More complex situations with more than three interfaces exist, driving fluid flow. For example, if there are two different solids in contact with a liquid, the liquid will flow towards the surface with the higher surface energy i.e. lower contact angle. This is the case in the gravure process during doctor blade wiping where the ink is in contact with the doctor blade and the roll or during ink transfer from the roll to the substrate where the ink is in contact with the roll and the substrate.

These situations will be described in detail in the next section. In these situations, it is crucial to be able to control the contact angle of an ink on the substrate or other components such as the gravure roll or doctor blade. There are a number of ways in which this can be achieved. One way would be to change the surface energy of the ink. This can be achieved by changing the ink solvent, by changing the solute concentration or type or by adding a surfactant. One challenge with these ink based methods is that they can dramatically alter the properties of the final film and its electrical properties. Additionally, in situations with multiple solid interfaces, it is often advantageous to modify the surface energies of different solids independently. Modifications of the solid surface are thus much more common. Contact angle is typically decreased using UV ozone (UVO) or plasma treatments that remove organic contaminants and activate the surface. The contact angle can be increased by depositing self-assembled monolayers (SAM) on the surface.<sup>58</sup> By choosing the right functional groups, surface energy can be tuned, for example employing fluorinated end groups to achieve contact angles above 90 degrees. Contact angle hysteresis can be reduced by using very smooth substrates that have been cleaned thoroughly to remove any contamination. Conversely, contact angle hysteresis can be increased by intentionally roughening the surface or introducing intentional chemical inhomogeneity.

In summary, the most important forces for microscale printing are viscous and surface tension forces. Their balance is captured by the capillary number. Understanding viscous as well as surface tension effects allows printing to be optimized by the careful tuning of ink as well as printing and surface parameters. The next section describes how this understanding can be applied to gravure printing in particular.

## **1.4 Overview of gravure printing process**

The physics of the gravure printing process underpins many of the findings of this thesis and is thus reviewed here. Many of the processes that affect ink distribution can be understood in terms of the fluid mechanics described in the previous section, namely flows driven by surface tension forces and inhibited by viscous forces. The gravure process can be considered a series of sub-processes (see Figure 1-3).<sup>49</sup> First, ink needs to fill the cells. In continuous production, the roll typically rotates through a large ink reservoir, filling the cells. Afterwards, ideally, the cells are fully filled with ink without any entrapped air. Additional ink will be left on the land areas between cells and there will also be excess ink on top of the cells. This excess ink is removed using a doctor blade. Afterwards, ideally, there is no ink left on the land areas and cells are still fully filled with ink. In reality, there is always a thin lubrication residue film left by the finite gap between the blade and the roll. The blade will also pull ink from the cells and redeposit it behind the cells in the form of characteristic drag-out tails. After wiping, the roll is pressed into contact with the substrate. Ideally, all the ink is removed from the cells and transferred onto the substrate. Finally, the ink

needs to spread on the substrate to fill in the gaps in between individual cells. All of these effects, except for spreading, can initially be analyzed in terms of individual, isolated cells. Initially, they can also be understood as independent processes. An ideality factor can be calculated for each sub-process. The ideality factor describes the volume of ink in the cell or on the substrate respectively after the filling, wiping and transfer processes. The final printed volume fraction is simply the product of these individual ideality factors:

$$\varphi_{print} = \frac{V_{transfer}}{V_{cell}} = \frac{V_{fill}}{V_{cell}} \times \frac{V_{wipe}}{V_{fill}} \times \frac{V_{transfer}}{V_{wipe}} = \varphi_{fill}\varphi_{wipe}\varphi_{transfer} \quad \text{Eq. 1-7}$$

The dominant factor controlling these ideality factors is the capillary number. The different sub-processes in gravure exhibit different dependencies on Ca. Different regimes of capillary number are limited by different sub-processes (see Figure 1-16). Knowledge of these different printing regimes is crucial when optimizing a new printing process in terms of ink design, substrate treatment and print speed.

### 1.4.1 Cell filling

The first process during gravure printing is cell filling. In this process, ink replaces the air initially within each cell, thus filling the cells. Air entrapment is the biggest problem during cell filling. Ideally, the cell is fully filled with ink afterwards. Ink from a large reservoir enters the cell as a large fluid front passes over the cell (see Figure 1-8). As the fluid front approaches the cell, it gets pinned at the edge of the cell. Due to the declining angle of the cell wall, the contact angle is reduced at the edge of the cell. The liquid front will remain pinned until the contact angle becomes larger than the advancing contact angle of the ink on the roll surface. At this point, ink will be driven into the cell by surface tension forces. At the same time, the overall fluid front keeps advancing around the edges of the cell and ultimately over the cell. If the ink has not fully filled the cell when the overall fluid front hits the cell's trailing edge, air will be entrapped inside the cell.<sup>59-62</sup> Thus, the success of cell filling is decided by two competing processes. The overall fluid front moves at the print speed. The velocity of the fluid entering the cell is determined by the balance of surface tension and viscous forces. Lower viscosity and larger surface tension result in faster and more complete filling of the cell. To first order, capillary number determines the filled volume fraction. Large values of Ca mean the overall fluid front moves faster relative to the ink filling the cell. Thus, filling will be incomplete at large values of Ca and the ideality factor will be small.

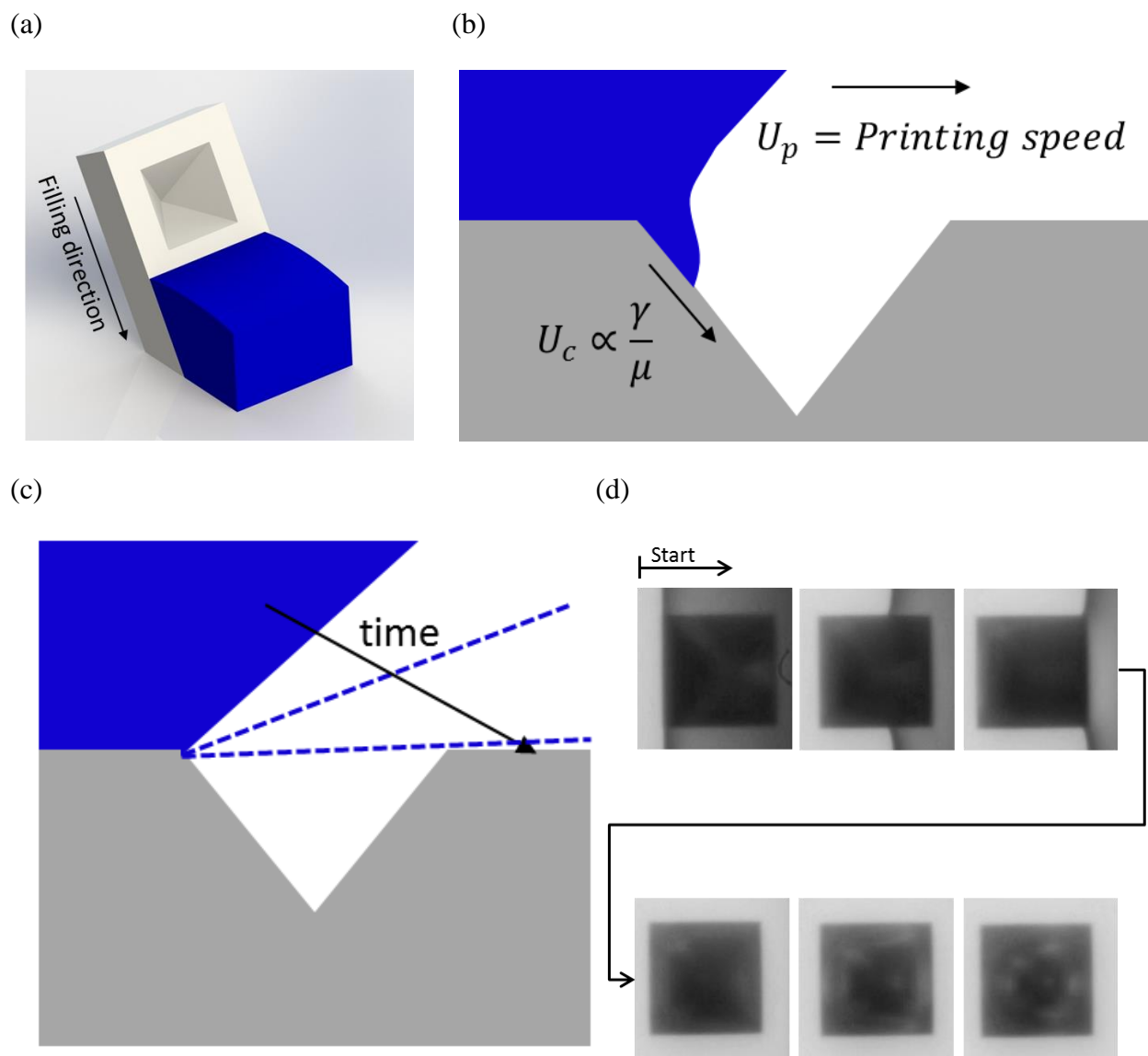


Figure 1-8. Cell filling with ink. (a) The large fluid front from the ink reservoir approaches individual pyramidal cells. Reprinted with permission from <sup>59</sup>. Copyright 2014 American Chemical Society. (b) Side view of ink filling cell. The characteristic speed due to capillary forces ( $\gamma/\mu$ ) competes with the fluid front advancing at the print speed. (c) If the capillary number is too high, air is entrapped in the cell. (d) Optical micrographs experimentally show air entrapment as the fluid front moves from left to right over a cell (top view). Panels (b) to (d) courtesy of Rungrot Kitsomboonloha.

## 1.4.2 Doctor blade wiping

The doctor blade is a component that sets gravure apart from most other printing techniques. It is needed because large amounts of fluid are left on the land areas after the filling process. Ideally, the doctor blade wipes off all excess ink without affecting the ink in the cell. Unfortunately, two major non-idealities occur during doctor blade wiping: homogeneous lubrication residue and ink drag-out from cells.

### 1.4.2.1 Lubrication residue

When the doctor blade passes over the roll surface, it always leaves a thin, uniform residue layer. The fluid moves with the roll as it rotates until the fluid hits the doctor blade. The convergent gap underneath the doctor blade forms a thin channel. In order to achieve a constant flow rate through the channel, a positive pressure is developed underneath the blade. This pressure is balanced by the loading force that is applied to the top of the blade mount (see Figure 1-9). The thickness of the uniform residue layer is controlled by several parameters; however, it can never be avoided completely. Depending on the application, different residue thicknesses can be acceptable. If the residue is very thick, it can lead to electrical shorts between different parts of a circuit when a conducting ink is printed. Electrical shorts can be avoided if the residue is thin enough such that individual nanoparticles from a metal nanoparticle ink do not form a continuous layer after sintering. The particular thickness at which this happens depends on the nanoparticle size, mass loading and sintering conditions. Thin, sensitive layers printed on top of the residue film can be affected by the surface roughness that even discontinuous residue films can produce. It is well known that roughness can lead to dielectric failure<sup>63</sup> as well as crystallization defects in semiconductors<sup>64,65</sup>. Excessive residue can also lead to hazing and degraded transparency of transparent substrates for optical applications. The residue thickness can be reduced by the optimization of ink, printing and doctor blade conditions.<sup>66,67</sup> Both a reduced ink viscosity and a reduced print speed result in lower pressures in the gap underneath the doctor blade and thus thinner films (see Figure 1-10). In the high capillary number regime, printed volume fraction increases due to large amounts of residue. Since this residue is deposited uniformly over the roll surface, the patterning contrast decreases at high values of  $Ca$  and thus the increase in printed volume fraction is undesirable. Thus, printing with low viscosity inks and at low speeds is desirable from a lubrication residue perspective.

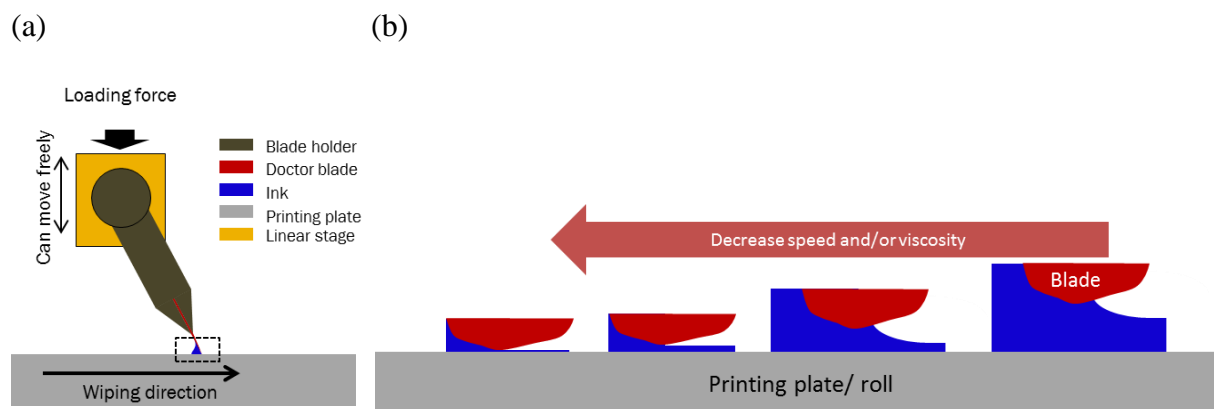


Figure 1-9. Lubrication residue due to doctor blade wiping. (a) Mounting of the doctor blade. The doctor blade can move freely in the vertical direction with an applied vertical load. (b) Lubrication residue is created by ink flowing through the finite gap that always exists underneath the doctor blade. Courtesy of Rungrot Kitsomboonloha.

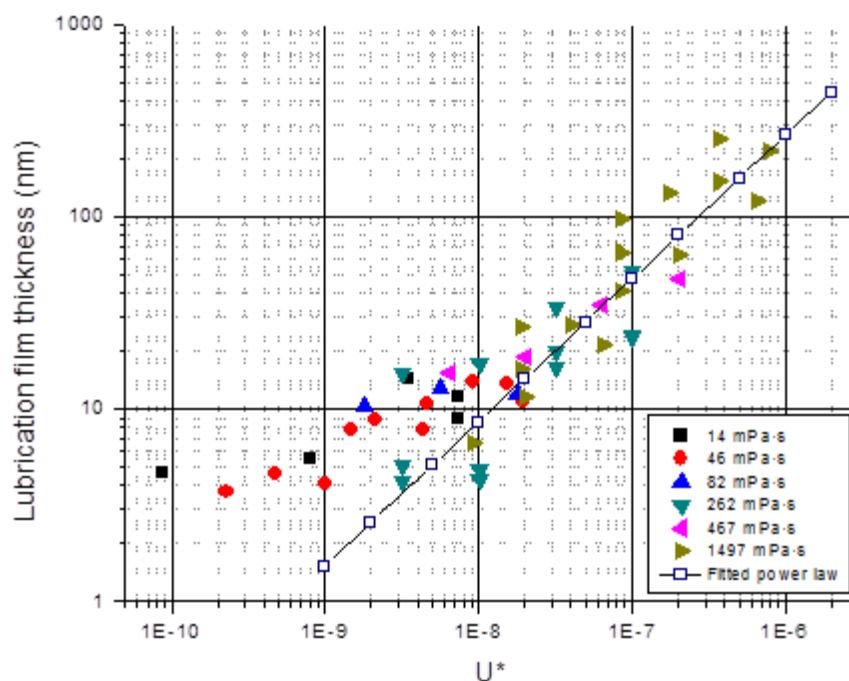


Figure 1-10. Lubrication residue improves for smaller values of print speed and viscosity ( $U^* = \frac{\mu U}{RE'}$ ). Reprinted with permission from <sup>66</sup>. Copyright 2014 American Chemical Society.

### 1.4.2.2 Drag-out

The second major non-ideality during doctor blade wiping is drag-out. Whilst lubrication residue occurs uniformly across the roll surface, drag-out is a result of the interaction between the doctor blade and the cells. The doctor blade pulls out ink from the cells as it passes over them, which has two detrimental consequences: ink is lost from the cells and subsequently redeposited behind the cells. The redeposited ink behind the cells takes the form of characteristic tails, which are generally undesirable because pattern fidelity is deteriorated. The drag-out effect can be explained based on the wettability of the ink on the doctor blade. Kitsomboonloha et al. use experimental results to propose that a 3D capillary effect is responsible for drag-out (see Figure 1-11).<sup>49</sup> As the doctor blade passes over the cell, the ink meniscus underneath the doctor blade will be larger in the cell compared with adjacent land areas. A pressure gradient is created that drives liquid from the cell onto adjacent land areas, both sideways and towards the backside of the doctor blade. The sideways flow is evident from the shape of the drag-out tail whose width extends past the boundaries of the cell (see Figure 1-12). Ceyhan et al. use lubrication theory to analyze the drag-out effect in 2D considering the blade cross-section.<sup>68</sup> It is shown that the ink climbs up the backside of the doctor blade to be pulled out of the cell and to be redeposited as a tail behind the cell. In both cases, the drag-out effect is described by a capillary flow, which is suppressed at higher capillary numbers. At high capillary numbers, there is insufficient time for the ink to be dragged out because the print speed is too high relative to the characteristic velocity of the capillary flow ( $\gamma/\mu$ ). Thus, the printed volume fraction is limited by drag-out at low values of  $Ca$  (see Figure 1-12).

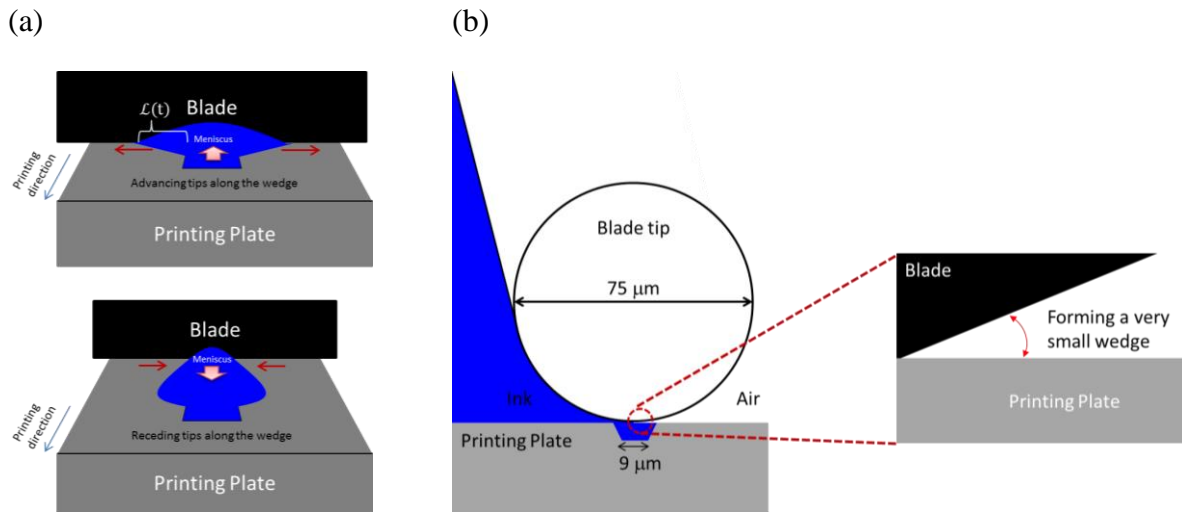


Figure 1-11. The drag-out process. (a) Ink is pulled from the cell as the doctor blade passes over it. Ink wets the blade and flows both sideways under the blade and up the backside of the blade. After the blade has passed over the cell, the dragged-out ink is redeposited on the land area behind the cell. (b) Standard blade tips are significantly larger than the size of highly-scaled cells. They can be modelled as cylinders that create a very shallow angle wedge at the very tip. This small wedge leads to the capillary flow of ink from the cell. Courtesy of Rungrot Kitsomboonloha.

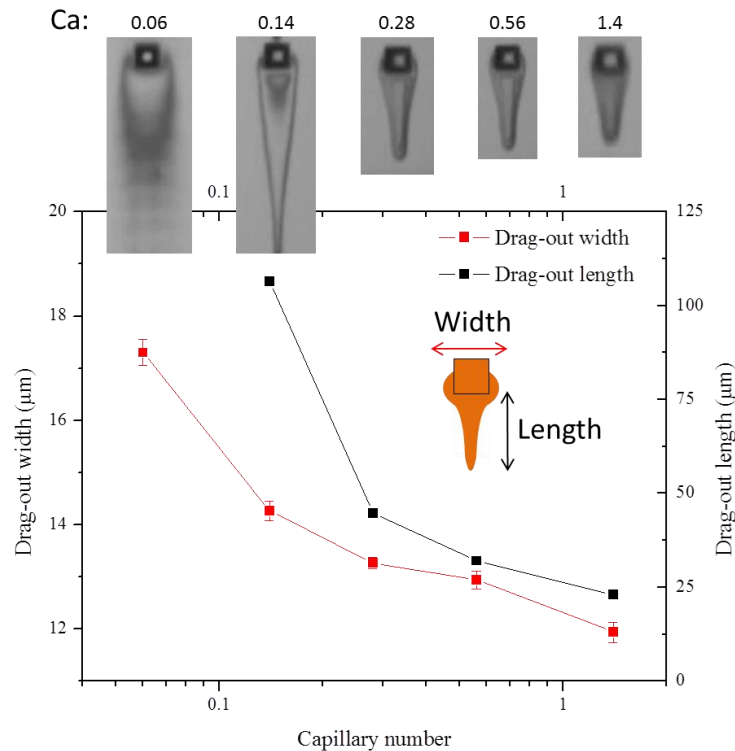


Figure 1-12. Both the width and length of the resulting drag-out tails decrease with increasing capillary number because capillary flow is suppressed in this regime. Reprinted with permission from <sup>49</sup>. Copyright 2012 American Chemical Society.

### 1.4.3 Ink transfer

The final process involving the roll is ink transfer to the substrate. The substrate comes in contact with the ink on the roll. When the two are separated, ideally, all the ink has been removed from the cells and transferred to the substrate. In reality, transfer fractions tend to be much lower than 100%. Ink transfer is the most extensively studied gravure sub-process, both experimentally and theoretically,<sup>69–80</sup> as described in a recent review article by Kumar.<sup>81</sup> During the transfer process, a liquid bridge is created between the roll and the substrate (see Figure 1-13). The breakup of this liquid bridge determines what fraction of ink is left on the roll and what fraction is transferred to the substrate. Initial understanding can be gained by studying the breakup of liquid bridges between two flat plates. If both plates have the same wetting properties, the contact line will slip by the same amount on both plates such that both plates end up with the same amount of fluid after breakup. If the two plates exhibit different receding contact angles, the movement of the contact lines will not be symmetric anymore. The contact line will de-pin faster on the plate with a higher receding contact angle. After break-up, this plate will be left with a smaller fraction of ink.<sup>75</sup> The same considerations apply to the transfer from a cell to a flat substrate.<sup>77</sup> This effect is driven by surface tension forces. At high values of capillary number, viscous forces dominate over surface

tension forces. In this case, the wetting difference between the two plates becomes less important and the liquid will be split more evenly. Thus, the value of capillary number that gives optimum transfer depends on the relative wetting properties of the roll and the substrate (see Figure 1-14).<sup>76</sup>

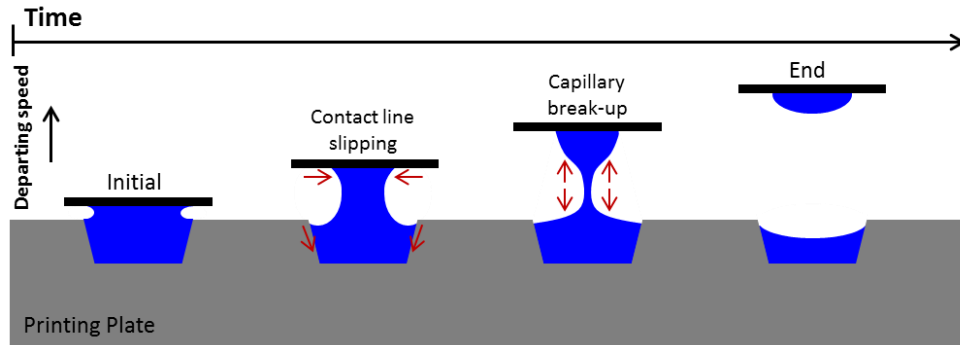


Figure 1-13. During the transfer process, the substrate separates from the roll. A liquid bridge is formed between the substrate and the cells on the roll. The transfer fraction is determined by how fast the contact line slips on the substrate relative to on the roll. Courtesy of Rungrot Kitsomboonloha.

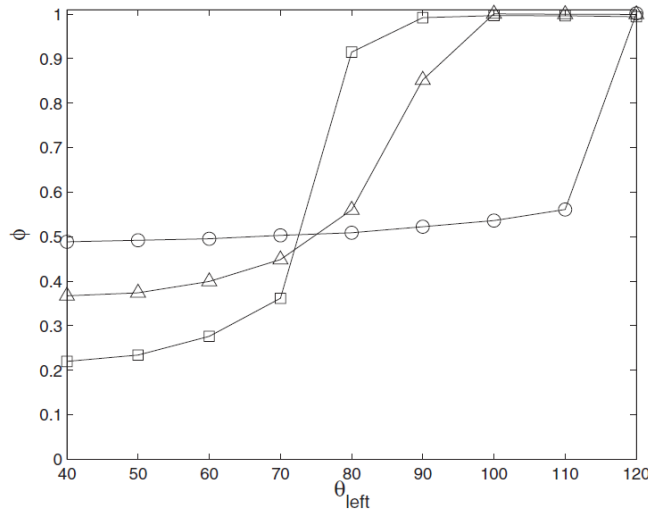


Figure 1-14. Transfer fraction ( $\phi$ ) as a function of the contact angle on the stationary (left) plate for different values of  $Ca = 0.01$  (squares),  $0.1$  (triangles) and  $1$  (circles). The contact line is pinned on the moving (right) plate. Higher values of  $Ca$  reduce the effect of the contact angle due to the suppression of capillary flow. Reprinted from <sup>76</sup> with the permission of AIP Publishing.

### 1.4.4 Pattern formation on the substrate

So far, we have discussed the individual gravure sub-processes that involve cells on the roll, namely filling, wiping and transfer. These processes can mostly be understood in the context of individual cells. However, virtually all realistic electronic applications consist of multiple cells that form a continuous pattern by ink spreading on the substrate. Thus, ink spreading and drying are processes that need to be discussed in the context of pattern formation. The most basic patterns for electronic applications are lines and rectangles, since virtually all electronic patterns including transistor gates and source/drain electrodes, interconnects, capacitors, etc., are constructed out of these basic primitives. Since gravure is a cell based printing method, the desired patterns are pixelated into individual cells (see Figure 1-15). For example, high-resolution lines are typically made up of a string of individual cells. During transfer, the ink is deposited on the substrate in the form of individual droplets. These droplets need to spread to fill in the gaps between individual cells and create a continuous pattern. The final pattern shape depends on both the driving force towards equilibrium, which is surface energy, as well as the timescale available to reach equilibrium. The merging of adjacent droplets is driven by surface energy minimization. Clearly, this depends on both the surface energies of the ink and the substrate. The equilibrium shape can range from de-wetting where individual droplets ball up to complete spreading where pattern definition is lost. Intermediate contact angles are needed to achieve good pattern fidelity. This flow is inhibited by viscous forces. Highly viscous inks (viscosities above a few hundred centipoise) are very challenging to print with gravure because they result in isolated droplets that do not spread sufficiently. This will be observed multiple times in this thesis and will be discussed in the following chapters. The timescale available for droplet spreading is limited by the drying of the solvent. As the solvent dries, viscosity increases and spreading ultimately stops.

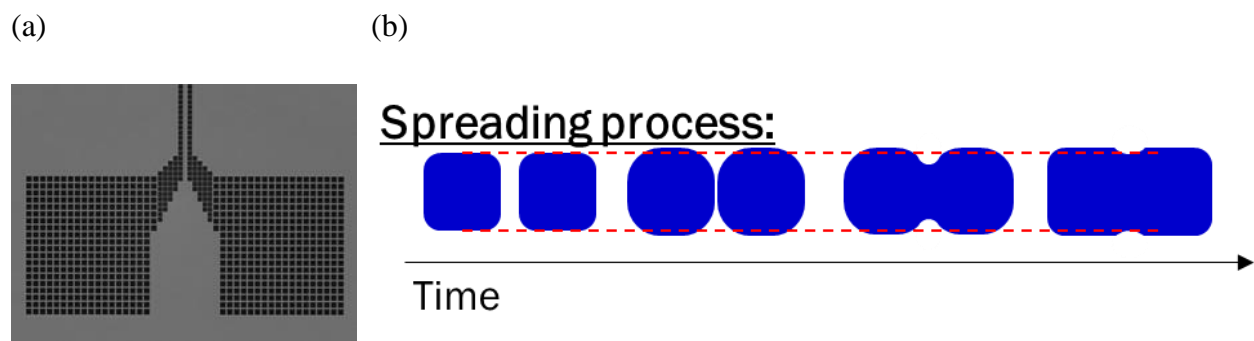


Figure 1-15. (a) Gravure patterns such as these source drain lines with contact pads are subdivided into individual cells. (b) Ink deposited from individual cells needs to spread on the substrate to create continuous patterns. (a) and (b) reprinted with permission from <sup>27</sup>.

### 1.4.5 Overall process optimization

All of these processes, filling, wiping, transfer and spreading, need to be optimized in conjunction to achieve optimum printing performance. The three roll-based processes, namely filling, wiping and transfer, determine the total amount of ink that is printed from each cell. The efficiency of this overall process is measured by the printed ink volume fraction relative to the volume of the cell. When developing a printing process for a new ink or application, the first step is to determine the capillary number that gives optimum printed volume fraction. Knowledge of the general dependence of each sub-process on capillary number facilitates this process (see Figure 1-16 for general trends). By careful consideration of other factors such as the roll, doctor blade and substrate properties, printing performance can be improved further and the regime of optimal capillary number can be shifted to more favorable values. In this dissertation, several ways to do so will be described. A recent review gives a more detailed overview of parameters that affect the gravure process.<sup>82</sup>

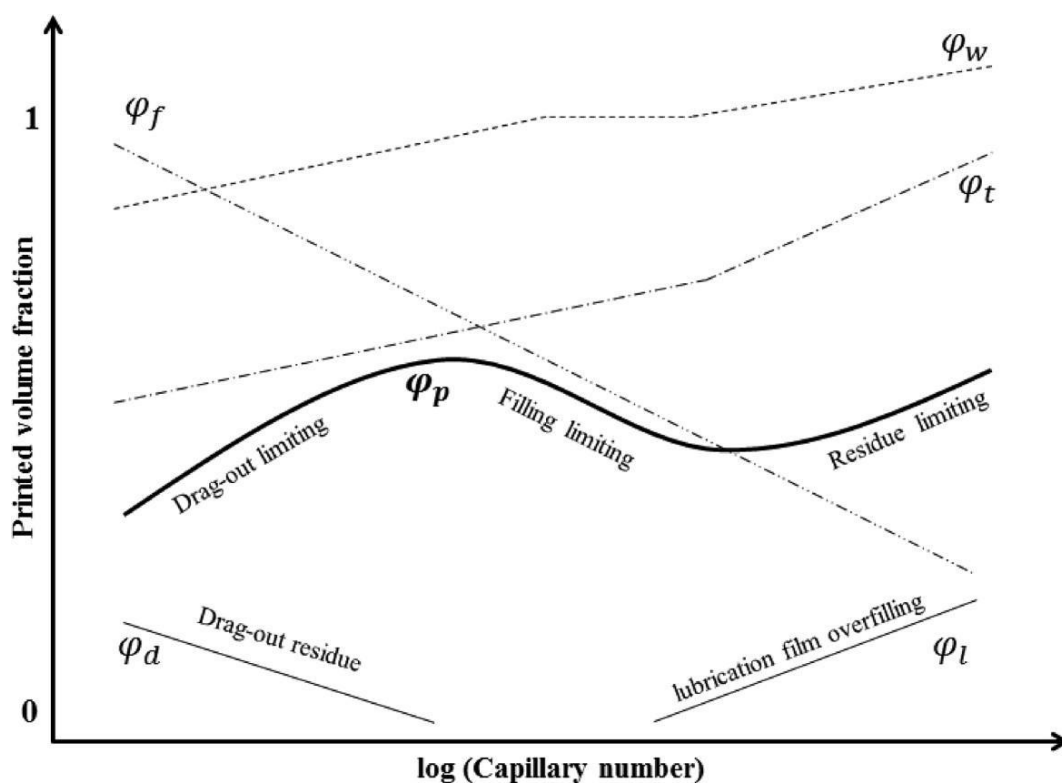


Figure 1-16. Printed volume fraction undergoes different regimes as a function of capillary number. Ideal printing is achieved at the cross-over point between the drag-out and the filling limited regimes. Reprinted with permission from<sup>49</sup>. Copyright 2012 American Chemical Society.

## 1.5 Printed organic thin-film transistors (OTFTs)

So far, the printing of different patterns and layers one at a time has been discussed. In real printed electronics, multiple functional layers need to be combined to create devices. Gravure printing has been used to print a multitude of devices such as OLEDs<sup>35</sup> and organic solar cells<sup>34</sup>. This dissertation will focus on printed transistors. Transistors are technologically very important as most printed systems will include transistors to perform tasks such as digital logic, signal amplification in sensors or pixel selection in displays. Transistors are also a good testbed for a new microfabrication technology because they combine a number of different requirements. High-quality transistors require both the lateral downscaling of feature size as well as the thickness downscaling of highly-uniform layers. Conductors, dielectrics and semiconductors all need to be printed as high-quality materials. Interactions between the different layers are very important both in terms of printing, e.g. solvent compatibility and wetting, and in terms of electronic interfaces, e.g. contact resistance and interfacial trap states. All of these problems need to be solved to create viable fully-printed devices (see device geometry in Figure 1-17).

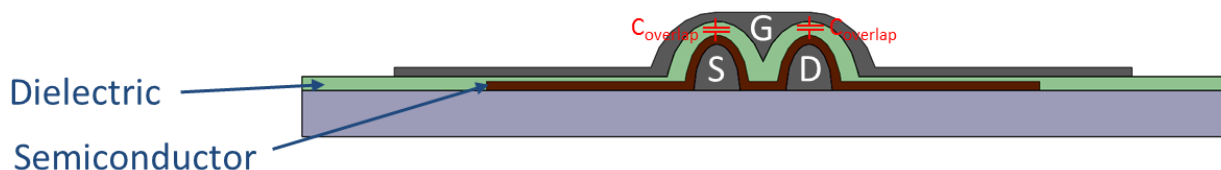


Figure 1-17. Cross-section of fully-overlapped TFT architecture showing all four layers: source (S) and drain (D) electrodes, semiconductor, gate dielectric and gate electrode (G). The interfaces between all layers need to be compatible. The semiconductor and dielectric layer thicknesses need to be scaled i.e. made thin to ensure good electrostatic integrity. The source and drain layer lateral dimensions need to be scaled to ensure good on-state performance both due to a short channel length as well as a small overlap capacitance between the gate and the source and drain electrodes with small linewidth.

There are a number of requirements on transistor performance that determine its viability. In the on-state, transistors are required to drive as much on-current as possible without requiring a large supply voltage. A large drive current is needed to increase the maximum switching frequency for many high-frequency applications. The transition frequency  $f_T$  is defined as the frequency at which the transistor current gain becomes unity and the transistor ceases to work as a voltage controlled switch. Recently, a number of reports have demonstrated printed transistors with  $f_T$  in the range of hundreds of kHz to low MHz.<sup>15,18,83,23,27</sup> However, in these cases, the devices were either not fully printed, especially high-speed printed, and/or were operating at large voltages above 10V, which

increases  $f_T$  as can be seen from the following calculation based on the small-signal equivalent transistor circuit:

$$f_T = \frac{g_m}{2\pi(C_{gs}+C_{gd})} = \frac{\mu(V_{GS}-V_T)}{2\pi L(\frac{2}{3}L+2L_{overlap})} \quad \text{Eq. 1-8}$$

Where  $\mu$  is mobility,  $V_{GS}$  is the applied gate-source voltage,  $V_T$  is the threshold voltage,  $L$  is the channel length and  $L_{overlap}$  is the overlap length between the gate and the source and drain electrodes. Thus,  $f_T$  can be improved by improving mobility and by reducing channel length and overlap capacitance.

Mobility is a material property. It depends on both the semiconductor material as well processing conditions. Organic materials are the most widely explored class of materials for printed transistors.<sup>12–21,25,26,24</sup> Traditionally, the performance of organic semiconductors has been very low. However, recently, novel solution processed organic semiconductor materials have boosted performance considerably achieving mobilities in excess of  $1\text{cm}^2/\text{V-s}$  and in some cases even  $10\text{cm}^2/\text{V-s}$ .<sup>84,85</sup> A novel scanned annealing method is presented in this dissertation that increases mobility by an order of magnitude.<sup>26</sup> However, the main advantage of organic materials is their properties that make them attractive for printing processes on plastic substrates. Organic materials can be readily dissolved in a large range of organic solvents that allow fine control over parameters such as ink viscosity or evaporation rate, which are critical to achieve optimal patterning and layer uniformity. Annealing temperatures are typically very low on the order of  $100^\circ\text{C}$ . This is a major advantage because it enables the use of low-cost, flexible substrates such PET, PEN or paper. Whilst the semiconductor is certainly a key component of any transistor, materials for the other layers also need to be chosen carefully. Organic materials can also be used for the dielectric with the same advantages in terms of printability as organic semiconductors. Organic thin-film transistors (OTFTs) typically utilize metal nanoparticle inks for the source, drain and gate electrodes due to their good conductivity, printability and low processing temperatures that are matched to the thermal limits of the organic materials.<sup>9</sup> Many of the advances in OTFT materials, especially the semiconductor, have been obtained using idealized structures such as silicon substrates, evaporated contacts or spin coated layers. The next step is to employ these high-performance organic materials in devices where every layer is patterned by printing at high speed.

In addition to improvements in material mobility, downscaling of the source, drain and channel dimensions is the second way to improve transistor high-frequency performance. A number of reports have focused on the printing of transistor electrodes with scaled lateral feature dimensions, using a range of different printing methods.<sup>16,18,23,27,25,28</sup> As discussed earlier, gravure printing offers a promising path towards the scalable high-speed printing of downscaled feature dimensions. One major challenge for gravure printed devices is that layer-to-layer registration

accuracy has lagged behind improvements in resolution, which severely limits the downscaling of the overlap length and thus overlap capacitance. A significant overlap capacitance severely limits  $f_T$  as is evident from Eq.1–8. An early solution employed a hybrid approach where a scaled gate electrode was gravure printed and aligned source and drain electrodes were printed using inkjet.<sup>23,83,86</sup> As resolution is scaled further, this technique reaches its limit in terms of accuracy of the inkjet printing especially at high printing speeds. Self-aligned printing is another potential solution to limit overlap capacitance analogous to self-aligned photolithography. Differences in wetting behavior are exploited to guide the ink to a desirable location without the need for top-down alignment. This approach has been applied to create very small gaps between source and drain electrodes.<sup>87–89</sup> However, self-alignment of source and drain electrodes to the gate through the gate dielectric still remains challenging.<sup>17</sup> Gravure printing enables another route towards high-frequency operation by not only scaling the channel length but also the linewidth of electrodes. This limits overlap capacitance even if a fully-overlapped gate is employed that is much larger than the combined channel length and the width of the two electrodes (see Figure 1-17). Thus, requirements for alignment accuracy can be relaxed. Since the conductivity of printed metallic conductors is typically not the limiting factor in printed organic transistor performance, deleterious effects of the series resistance of the narrow source/drain lines are minimal. This has been demonstrated with an inkjet printed gate fully-overlapped with gravure printed source/drain electrodes thus creating a path towards high-frequency transistors based on highly-scaled gravure printed source and drain electrodes.<sup>27</sup> In this dissertation, transistors are demonstrated where the fully-overlapped gate is gravure printed. In addition, the semiconductor and the dielectric are also gravure printed. Thus, all transistor layers are printed at a high speed of 1m/s enabling high-throughput manufacturing. By scaling all layers and optimizing printing processes, high-performance, low-voltage devices are demonstrated with low variability.<sup>28</sup>

## 1.6 Thesis organization

In this thesis, gravure printing is advanced on several levels with the goal to create fully gravure printed devices. First, gravure is used to prepare paper substrates for printed electronics. Then, single-layer printing for highly-scaled device features is discussed in terms of roll tooling as well as pattern formation. Finally, multi-layer printing is demonstrated in fully gravure printed transistors.

In chapter 2, gravure printing is utilized to enable the printing of transistors on a novel substrate: paper. Paper is very attractive for printed electronics because it is low-cost, biodegradable, lightweight and ubiquitous. However, its porosity causes ink absorption and large surface roughness. This is overcome by a gravure printed local smoothing layer. Printed transistors on top of locally smoothed paper substrates are demonstrated that exhibit performance on-par with

previously reported devices on plastic substrates; however, these devices were not fully gravure printed yet.

In chapter 3, a novel fabrication process for gravure rolls is demonstrated to enable gravure printing of highly-scaled devices. By utilizing the strengths of silicon microfabrication, gravure rolls can be fabricated that have superior feature definition as well as superior surface finish compared with traditional gravure roll making techniques, especially for high-resolution features. Modifications of the roll surface properties allow tuning of the printing performance to print high-resolution patterns at high print speeds.

In chapter 4, such highly-scaled gravure printed features are analyzed more closely. More complex patterns than single lines or cells are printed. Proximity effects are demonstrated that occur when lines are printed close to each other. The fluid mechanics of this effect is studied and it is suggested how it can be used to enhance feature quality by employing assist features.

In chapter 5, multi-layer printing for printed organic thin-film transistors (OTFTs) is demonstrated. In the first part of the chapter, a novel scanned thermal annealing technique is presented that significantly improves the crystallization of an organic semiconductor. The separation of grain nucleation and growth leads to increased grain size and significantly improved electrical performance. In the second part of the chapter, transistors are fully gravure printed at a high print speed of 1m/s. By scaling both lateral and thickness dimensions and optimizing the printing processes, good electrical performance, low-voltage operation and low variability is demonstrated.

In chapter 6, the main findings of this thesis are summarized and future research directions are suggested.

## Chapter 2: Gravure printing enabled transistors on novel paper substrates

### 2.1 Introduction

Paper is one of the most ubiquitous materials in everyday life. It has been used for centuries to display printed information in addition to other applications. The reasons are manifold including the low cost of paper itself, the ability for high-throughput, low cost printing on paper, biodegradability, permeability, foldability and many more. There will be countless opportunities if these properties can be integrated with electronic functionalities. One of the most immediate applications is the integration of sensing, communication and display functionalities with paper consumer packaging. This cannot be achieved with traditional microfabrication; however, the advent of printed electronics offers the opportunity to close this gap. So far, the majority of the advances in printed electronics have been made on plastic substrates. Little progress has been made on paper. The largest roadblocks preventing this are the surface roughness and ink absorption due to the porosity of paper.<sup>90</sup> High-resolution printing methods such as inkjet and gravure rely on relatively low viscosity inks, which are absorbed by standard paper. Higher viscosity inks cannot be printed by inkjet. They can be printed by gravure; however, fine lines printed with gravure directly onto paper would still suffer substantially from the large roughness of paper. So far, this has prevented any fully printed devices or systems, compatible with paper packaging flows, from being demonstrated.

One previous approach has been to “hide” the paper under a blanket coating of a smooth material; coating methods such as spin coating<sup>91–93</sup> and parylene evaporation<sup>94–96</sup> have been used to deposit thick smoothing layers. Unfortunately, such approaches are not viable for real packaging applications since all the attractive mechanical properties of paper, such as foldability, breathability etc., are lost when coated with blanket sealing layers. It is also undesirable from a cost perspective since large areas of paper are unnecessarily coated, wasting large quantities of material. Further, other previous work has made use of coated “inkjet paper” substrates<sup>97</sup>, which are too expensive for use in consumer product packaging and don’t have sufficient thermal stability for some higher temperature fabrication processes. There have also been reports of devices fabricated directly on paper. This is mostly done by conventional micro fabrication techniques such as sputtering or vacuum deposition thereby avoiding the problem of ink absorption into paper during printing.<sup>98,99</sup> Whilst this might be viable for some niche applications such as security features on banknotes, it won’t meet the cost requirements of most applications of paper electronics. Direct printing on paper using screen printing has also been attempted, however, with relatively large channel lengths (200 $\mu\text{m}$ ),<sup>100</sup> which highlights the challenges involved in the scaling of printed transistors on rough paper. This can be acceptable for certain applications such as low resolution electrothermochromic displays.<sup>101</sup> However, most electronic applications will require

high-resolution printing of scaled transistors. The shortcomings of the current state-of-the-art in terms of paper-based transistors become especially evident when comparing them to the state-of-the-art in terms of printed transistors on plastic substrates. On plastic substrates, transistors have been demonstrated where multiple if not all layers were fabricated by printing methods. Especially gravure printed transistors have been very successful at scaling down the channel length below  $10\mu\text{m}$  whilst achieving good performance.<sup>24,16,18,23,27,25,28</sup> Overall, therefore, existing paper-based processes and techniques are generally not viable, since they are incompatible with conventional packaging flows, which make use of printing techniques and run in high-speed roll-to-roll processes on low-cost paper stock.

These challenges are overcome by the integrated process flow demonstrated in this chapter.<sup>22</sup> A smoothing underlayer as well as overlying transistors are printed on low-cost paper using gravure printing. Gravure printing is widely used in the graphic arts, and therefore, this work is a natural evolution of consumer product packaging to integrate printed transistors. The smoothing layer is printed locally as defined by the pattern on the gravure roll. This preserves the desirable properties of paper outside of the electronically active areas, which can be a small fraction of the overall size of the paper. Interconnects between multiple smoothed regions with high performance devices could then be fabricated by methods such as screen printing, or indeed, using lower-resolution gravure printing of more viscous (and thus less absorbed) conductor inks, since high-resolution printing would be less of a concern.

In this chapter, first, bare paper is analyzed in terms of its thermal properties, surface topography and ink absorption. Surface roughness and ink absorption are then improved by optimizing the gravure printed smoothing layer and the properties of the smoothed paper are analyzed. Printed capacitors and transistors were fabricated in smoothed regions. Their performance was compared to similar devices previously reported on plastic substrates and devices were tested under bending to demonstrate the viability of the smoothed paper as a substrate for printed electronics.

## **2.2 Paper characterization**

The paper used here is a low-cost smoothed paper from Stora Enso, a large producer of packaging materials. The paper is formed from wood fibers and is coated by Stora Enso with kaolin (clay) as an initial smoothing layer. This paper substrate was analyzed to identify its strengths and weaknesses as a substrate for printed electronics in terms of thermal budget, surface roughness and ink absorption. The results dictate how the paper had to be modified to become a viable substrate for printed electronics.

The thermal budget is a key property of a substrate because it dictates which processes can be performed on it. The thermal budget of the paper substrate was characterized qualitatively in terms of darkening and mechanical degradation (see Figure 2-1) as well as quantitatively by thermogravimetric analysis (TGA) (see Figure 2-2). Qualitatively, first signs of degradation are observed at about 250°C and TGA confirms that no significant degradation occurs below 300°C. This is higher than all low-cost plastics and photo papers, and attests to the viability of the kaolin coating to produce highly stable paper substrates for printed electronics. It is certainly compatible with organic electronics and, in the future, might also allow the use of solution processed inorganic materials with higher temperature requirements.<sup>102</sup>

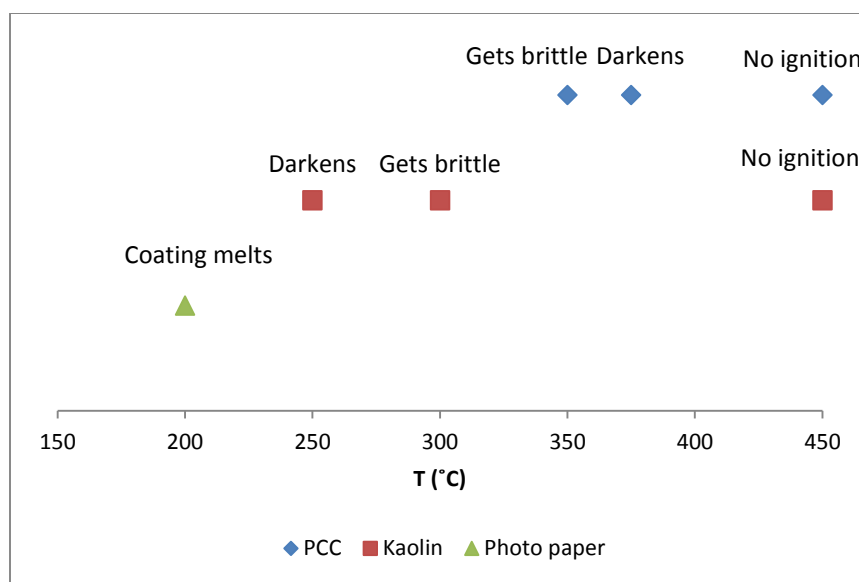


Figure 2-1. Qualitative paper degradation with temperature for three different papers: Precipitated calcium carbonate (PCC) smoothing, Kaolin smoothing and conventional photo paper. Kaolin-smoothed paper was used throughout this work.

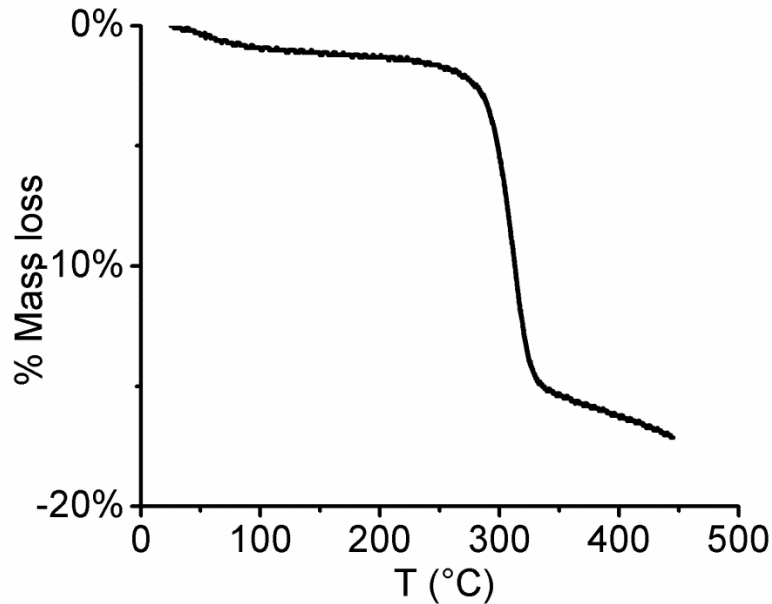


Figure 2-2. TGA of kaolin coated paper confirming qualitative result. No significant degradation can be observed below about 300°C.

Substrate roughness is a key consideration for device performance, affecting parameters such as line edge roughness and the breakdown strength of thin dielectric layers. This is one of the major roadblocks preventing the usage of paper as a substrate for printed electronics because of the fibrous nature of paper. Figure 3 shows an atomic force microscopy (AFM) image of paper as received. It is clear that this micrometer-scale peak-to-peak roughness would be unacceptable for active layer thicknesses on the order of 10s to 100s of nanometers.

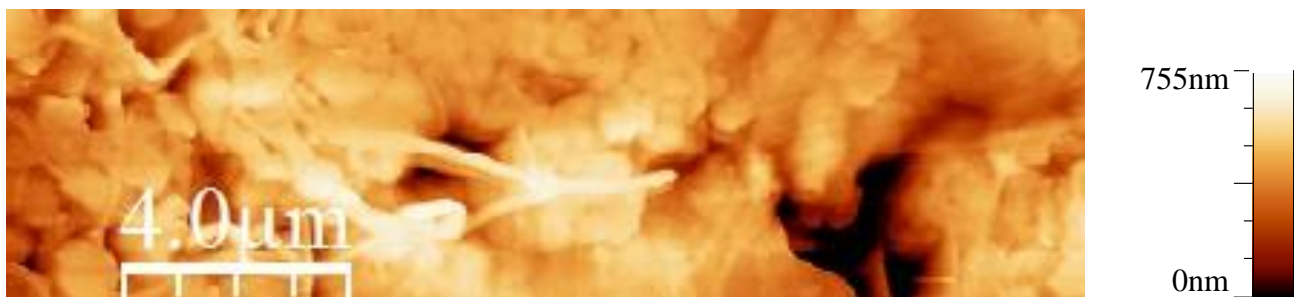


Figure 2-3. AFM topography scan of the paper with initial kaolin smoothing.

Absorption of low viscosity inkjet inks is a major problem for printed electronics on paper. Figure 2-4 shows water being absorbed and permeating through untreated paper within less than 30 seconds. This is due to the pores that invariably exist in between cellulose fibers in paper as well as due to the hydrophilic nature of the cellulose. One can also observe the low contact angle that

the water makes with the paper due to its hydrophilic nature as well as due to uncontrolled lateral fluid spreading. These issues make it very difficult to print well defined features onto bare paper. Figure 2-5 shows inkjet printed silver lines on bare paper. The ink has been absorbed and it has spread laterally leading to irregular features. Silver lines also exhibited poor conductivity after being absorbed by the paper.

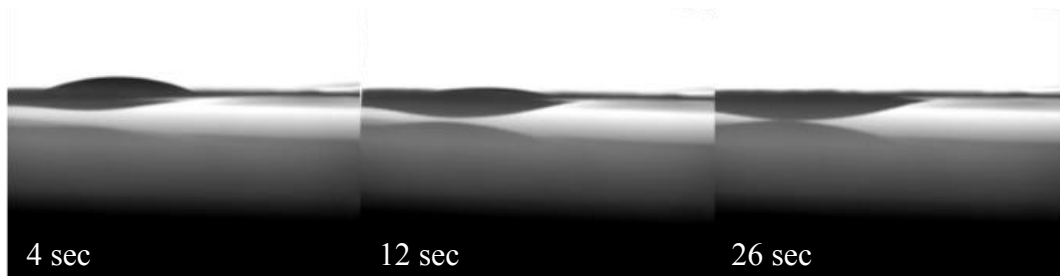


Figure 2-4. Water absorption into bare paper. Within less than 30 seconds the water droplet has completely permeated through the paper.

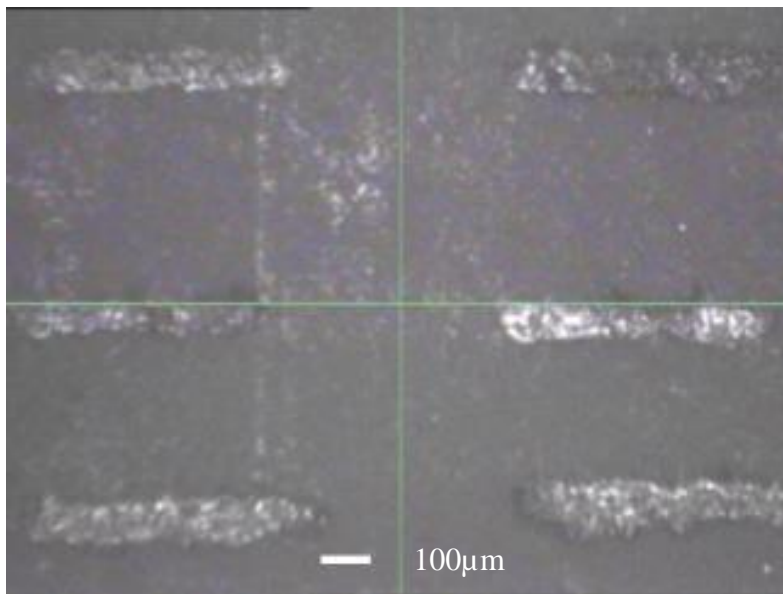


Figure 2-5. Inkjet printed silver lines onto bare kaolin paper. Ink has been absorbed by the paper and shows poor feature definition due to lateral spreading.

## 2.3 Paper modification

Thus, a method is needed to modify the paper. Surface roughness as well as ink absorption and spreading need to be reduced significantly. The modification of paper to prevent fluid flow is well known in the field of paper microfluidics.<sup>103</sup> Barriers to fluid flow are created inside of paper to define channels that fluid can flow through. There are two main techniques to create barriers inside the paper. One technique prevents fluid flow by hydrophobizing the paper. This can be achieved by changing the chemical end groups of the paper fibers from the hydrophilic hydroxyl groups of cellulose to more hydrophobic groups. This was attempted first. However, there are two main drawbacks that make hydrophobized paper unsuitable for printed electronics. Firstly, it does not solve the roughness problem. Secondly, printing on top of hydrophobized paper is challenging because ink will not wet the paper. The second technique used in paper microfluidics is the physical blocking of the paper pores to prevent fluid flow through them. Often, hydrophobic materials are used to block pores. Here, we can employ a similar strategy to modify the paper; however, with a few important differences. Since the goal is to print electronics on top of the modified paper, only the paper pores on the top side need to be blocked rather than all pores throughout the paper thickness. In addition to the blocking of paper pores, the final surface roughness needs to be minimized. The material used to block pores and smooth the surface also needs to have favorable properties. It needs to exhibit good wetting properties. It needs to exhibit sufficient solvent resistance and sufficient thermal stability to withstand subsequent processing.

Poly-4-vinylphenol (PVP) was chosen as the smoothing material. PVP can be readily dissolved in propylene glycol monomethyl ether acetate (PGMEA) for printing. It was cross-linked with poly melamine-co-formaldehyde methylated at 210°C for added stability. The PVP smoothing material was analyzed to find its maximum processing temperature. TGA of cross-linked PVP shows that degradation begins at approximately 210°C (see Figure 2-6). This is sufficient for organic electronics, but could be improved in the future to fully utilize the thermal capabilities of the paper.

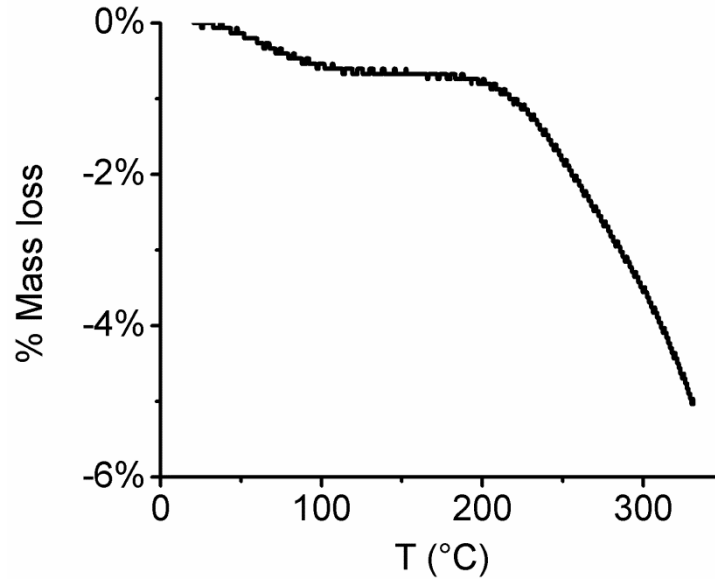


Figure 2-6. TGA of cross-linked PVP confirming sufficient thermal stability to allow organic electronics to be fabricated on top.

The robustness of the PVP to solvent exposure after heat treatment was also tested. A thin layer of PVP was deposited onto glass slides by spin coating and subsequently cross-linked. The PVP was heated to different temperatures for 30 minutes and film thickness was measured. Subsequently, the PVP was exposed to acetone for one minute and the thickness was measured again. Whilst the thickness decreased after heat treatment, exposure to acetone only attacked the PVP after the PVP had been exposed to temperatures above 300°C (see Figure 2-7). This further confirms the viability of the PVP as a substrate for printed electronics.

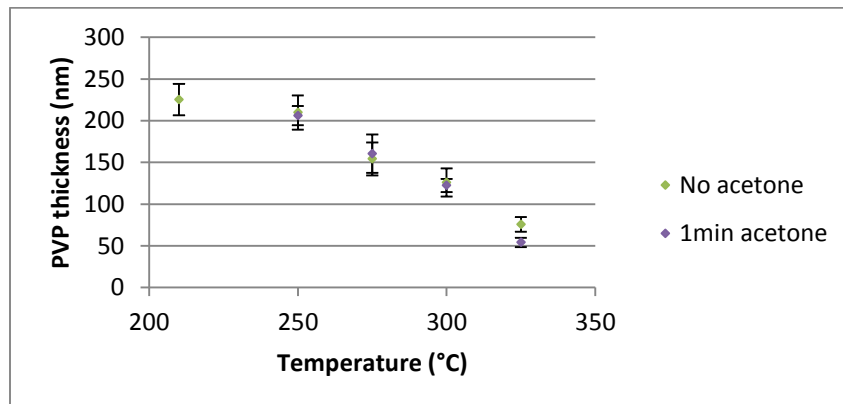


Figure 2-7. PVP degradation after exposure to high temperatures and after subsequent solvent exposure. PVP only loses solvent resistance after exposure to temperatures above 300°C.

PVP was gravure printed to act as a smoothing layer. The use of a printed local smoothing layer allows the creation of smooth regions in the electronically relevant areas, while ensuring that the paper largely retains its intrinsic properties. Figure 2-8 shows the significant improvements that were achieved. The roughness of the original paper and its improvement with the printed smoothing was quantified by the peak-peak roughness extracted from AFM scans ( $30\mu\text{m} \times 7.5\mu\text{m}$ ).

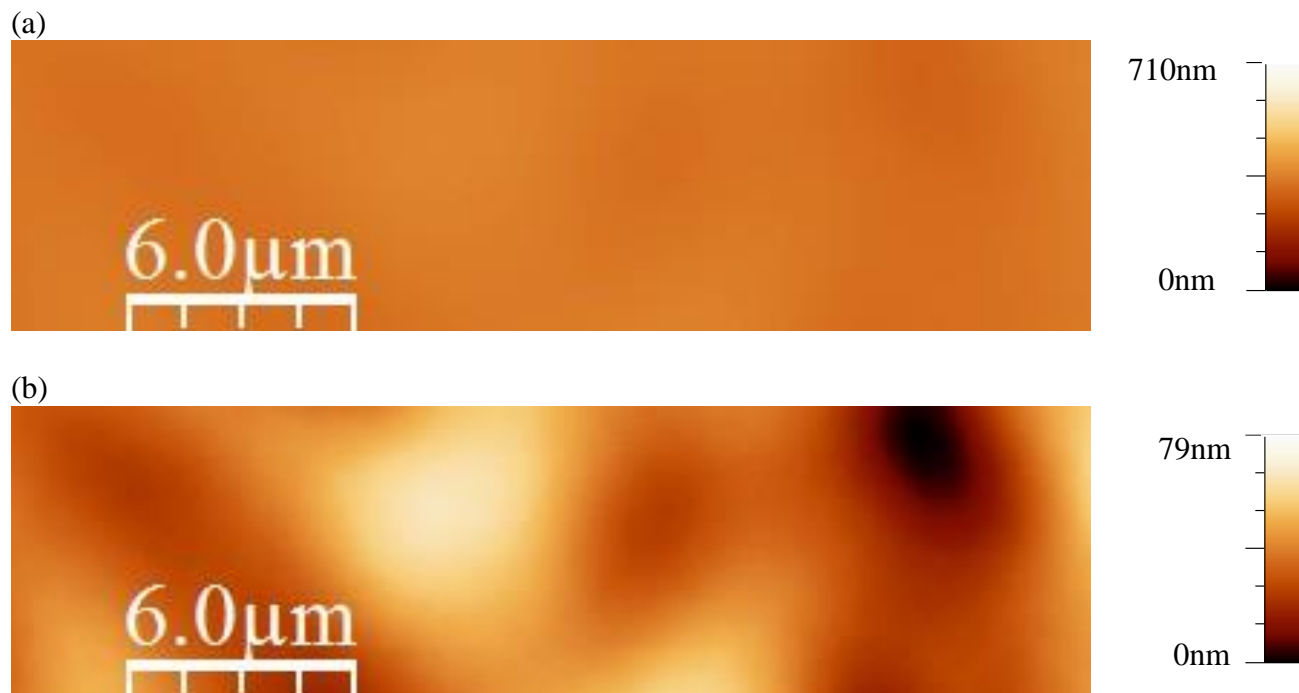


Figure 2-8. AFM topography scans of paper with PVP smoothing. (a) shown on a similar data scale as the bare paper in Figure 2-3 demonstrating significant smoothing. (b) shown on a finer data scale revealing some remaining long wavelength roughness.

The first smoothing layer printing parameter to be studied was ink viscosity, which was varied by changing the polymer concentration dissolved in the solvent. The printing speed was varied at the same time as the ink viscosity to maintain a constant capillary number to keep printing conditions constant. Thus, the spreading and absorption of the ink on the paper substrate could be studied. Two different regimes can be observed (see Figure 2-9). For low viscosities, the ink is simply absorbed by the paper without achieving significant smoothing of the paper. For high viscosities, roughness is increased by printing artifacts. Figure 2-10 shows how these artifacts manifest themselves as holes in the PVP film. Optical measurements with a larger field of view than AFM confirm that the lateral and vertical size of these voids increases with increasing ink viscosity as suspected from AFM. This type of printing artifact is not unique to printing on paper and also occurs on plastic substrates (polyethylene terephthalate (PET), see Figure 2-11). High viscosity ink was printed on PET with different gravure cell spacing to investigate the cause of these voids.

The size of voids increases with increasing cell spacing ultimately leading to isolated drops of size comparable with the cell size (see Figure 2-12). This suggests that voids are not caused by printing instabilities but rather due to insufficient spreading of high viscosity inks during drying. The optimum ink viscosity was found to be approximately 150cP.

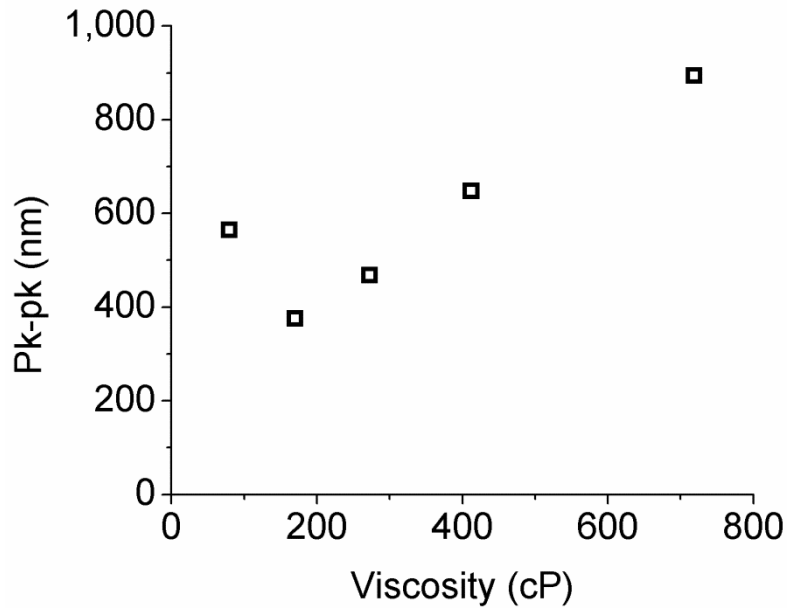


Figure 2-9. Roughness optimization with PVP viscosity showing optimal smoothing at intermediate viscosities (5 layers of PVP).

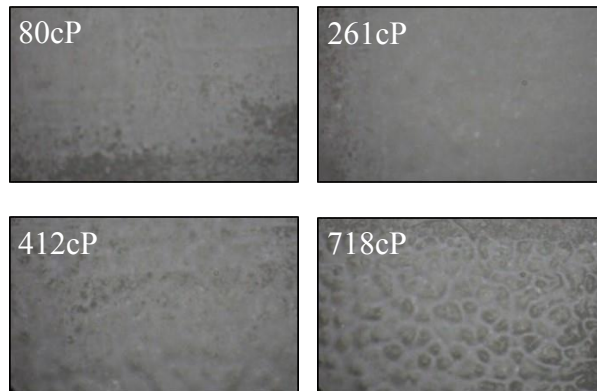


Figure 2-10. Optical micrographs showing absorption of ink for low viscosity ink and increasingly large printing artifacts with increasing ink viscosity (5 layers of PVP).



Figure 2-11. Optical micrograph of printing artifacts on plastic (PET) confirming that printing artifacts are independent of paper substrate (7 layers of PVP, 718cP).

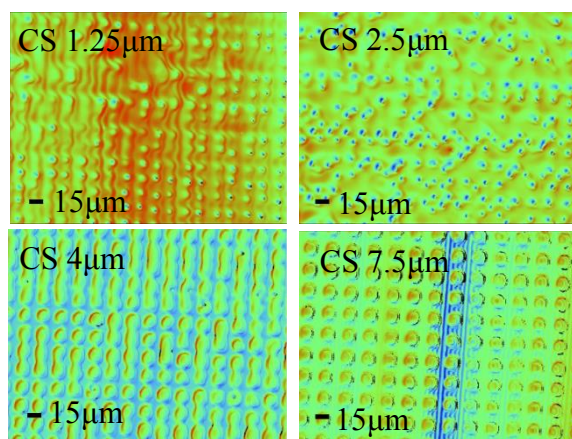


Figure 2-12. Optical profilometry images for different cell spacing (CS) with constant cell size  $15\mu\text{m}$  printed on PET (1 layer of PVP). The increased size of holes in the film with increasing cell spacing, ultimately leading to isolated drops of the same size as the cells, confirms that printing artifacts are due to high viscosity inks (here 2500cP) not being able to flow between cells before drying.

The effect of gravure cell size and the number of PVP layers was investigated using ink with optimized viscosity. Not surprisingly, roughness decreases with increasing cell size and number of layers due to the larger volume of ink deposited per unit area (see Figure 2-13). The decrease with number of layers follows a non-linear trend leading to diminishing returns for large numbers of layers. This can be understood from cross-sectional images (see Figure 2-14). For one and two layers of smoothing, one cannot make out a continuous PVP layer because not all pores in the paper are filled. For three, four and five layers, one can extract a thickness of the PVP layer (see Figure 2-15). This follows a linear trend. For each additional layer, the already printed PVP, which

is not cross-linked yet, is re-dissolved and thus allowed to penetrate the paper further. This explains why the improvements in smoothing diminish once three layers have been printed. The linear trend line can be extrapolated to cross the x-axis in between 2 and 3 layers. This suggests that there will be no continuous PVP layer for fewer than three layers, which is also observed in the cross-sectional images.

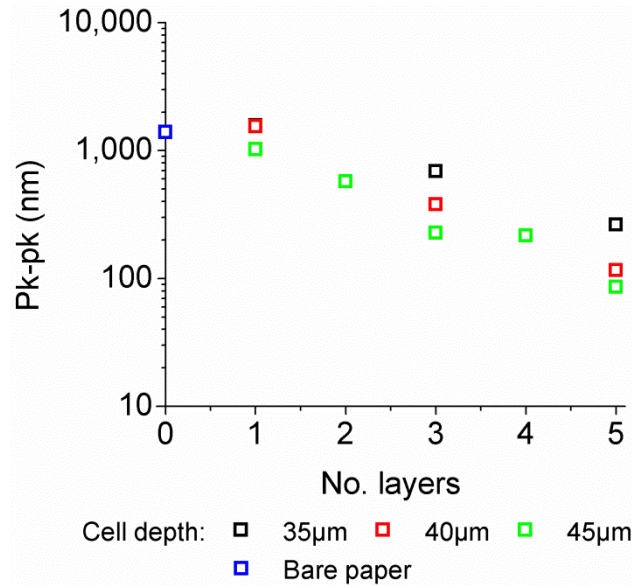


Figure 2-13. Pk-pk roughness with optimized ink viscosity (140cP) showing improved roughness with increasing cell depth and number of layers. The cells here were larger than the cells used to obtain the results in Figure 2-9 further confirming the importance of large cells.

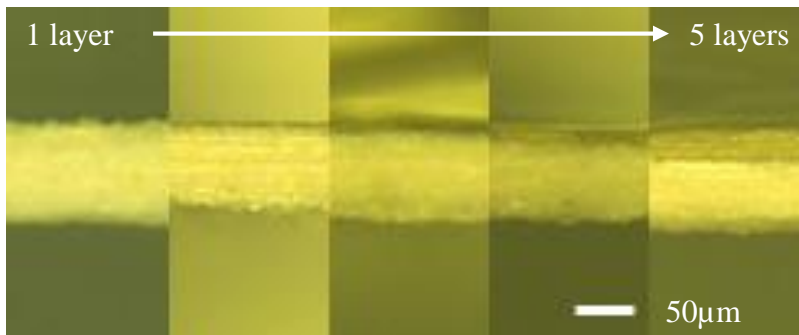


Figure 2-14. Cross-sectional optical micrographs of paper smoothed with an increasing number of PVP layers. A continuous smoothing layer becomes visible for 3 or more layers.

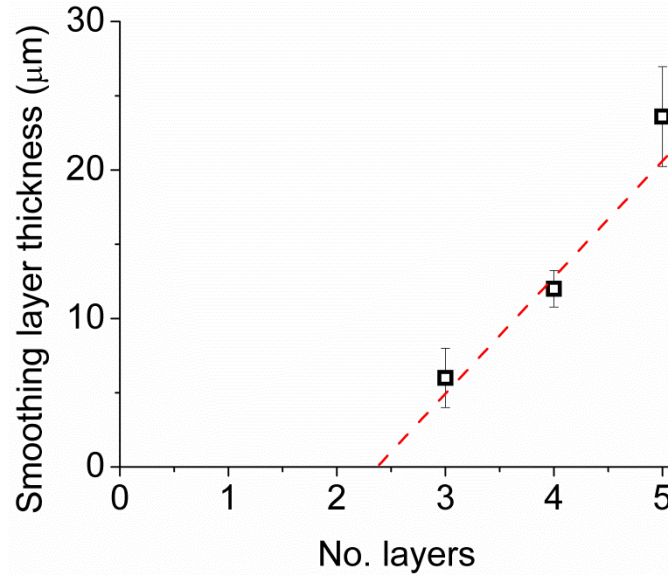
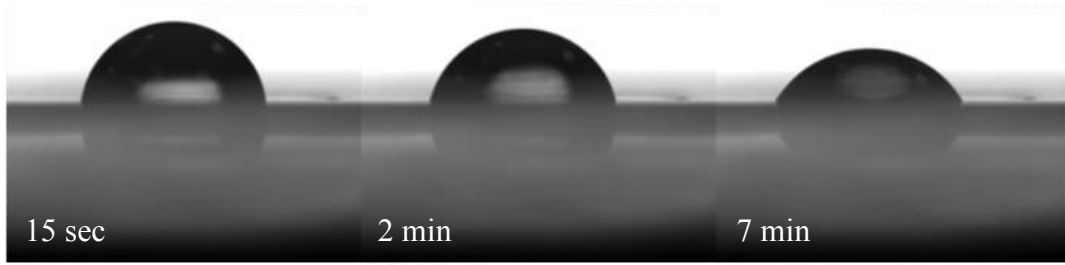


Figure 2-15. The thickness of the smoothing layer increases linearly with number of smoothing layers. Extrapolation of the trend line confirms that no continuous layer is to be expected for fewer than 3 layers.

Therefore, the optimum number of smoothing layers was found to be three and this was used for all further substrate characterization and device printing. Three layers of PVP were printed with the largest cells available here (45μm cell depth), with an ink viscosity of 150cP and with a printing speed of 0.1m/s giving a capillary number of 0.5.

The printed PVP smoothing not only improved surface roughness significantly but also ink absorption. Figure 2-16 shows a water droplet on top of paper treated with PVP. No significant absorption can be observed. The only reduction in drop volume is due to evaporation comparable to a drop on PVP coated plastic. The water contact angle was also improved compared to bare paper. Instead of a very low contact angle that leads to uncontrollable ink spreading, the water contact angle on top of PVP smoothed paper is about 80° (see Figure 2-17). This is similar to the contact angle on PVP that was spun onto PEN, which suggest that printing performance on these substrates will be comparable. Printing high definition features on PVP is routinely done in OTFT fabrication on plastic substrates where PVP is used as a gate dielectric or as a substrate planarization layer.<sup>104</sup> Figure 2-18 shows inkjet printed silver lines on smoothed paper. Problems with absorption and irregular features that were evident on bare paper have been solved (c.f. Figure 2-5). Conversely, the smoothed paper exhibits perfect features only limited by the accuracy of the printer.

Smoothed paper:



PEN with PVP:

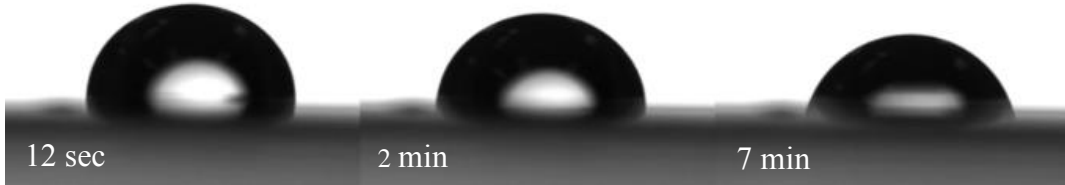


Figure 2-16. Smoothed paper shows no significant water absorption and only exhibits evaporative loss comparable to PEN coated with PVP.

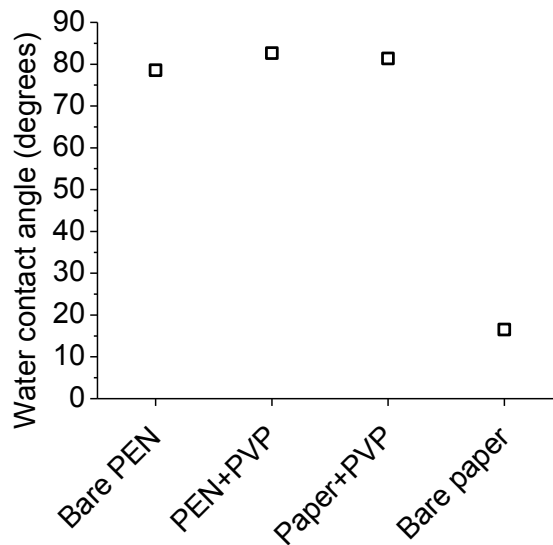


Figure 2-17. Water contact angle is comparable on paper smoothed with PVP, PEN with spun PVP and bare PEN. This suggests good print quality on top of the smoothed paper since fine features are routinely printed on top of PVP. Bare paper exhibits a very low contact angle due to lateral absorption.

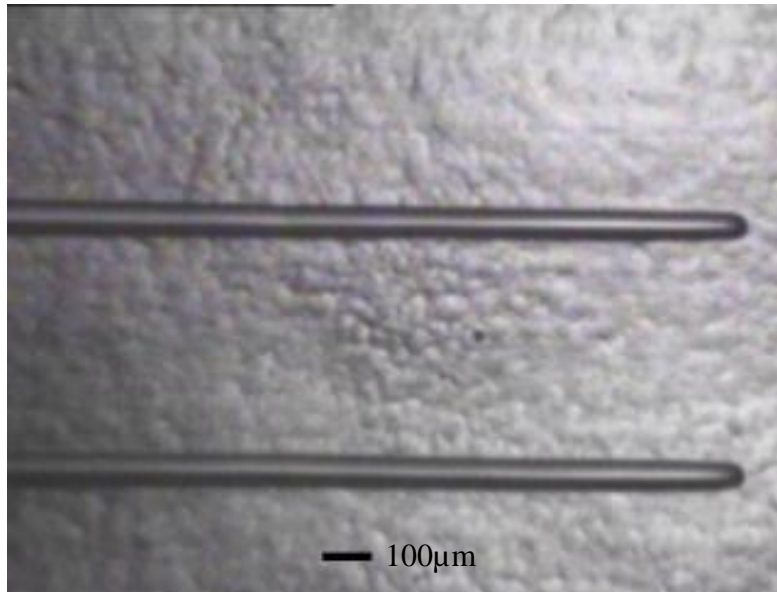


Figure 2-18. Optical micrograph of silver lines printed by inkjet on smoothed paper. Well defined features can be printed on top of smoothed paper.

## 2.4 Printed devices on smoothed paper

### 2.4.1 Dielectric evaluation

Metal-insulator-metal capacitors (MIM) were fabricated on the smoothed paper to verify satisfactory performance of the gate dielectric on this initially rough substrate. The bottom and top electrodes were fabricated by inkjet printing and the PVP gate dielectric was fabricated by gravure printing. Electrodes were printed with a commercial silver nanoparticle ink (CCI-300), which was sintered at 150°C. The gate dielectric was gravure printed with a similar PVP ink as the smoothing layer but with lower viscosities to achieve thin gate dielectric layers. The dielectric thickness was scaled by varying the PVP ink viscosity (see Figure 2-19). Ink viscosity was controlled by the amount of PVP dissolved in PGMEA. Dielectric breakdown was defined as the voltage producing a leakage current density of  $10^{-5}$  A/cm<sup>2</sup> because hard breakdown only occurs at large fields (see Figure 2-20). This current density corresponds to a projected TFT on-off ratio of  $10^4$ .<sup>105</sup> It was found that the breakdown field as defined by leakage does not suffer when the dielectric is scaled, however, device yield does decrease somewhat (see Figure 2-21). MIM capacitors were also fabricated on paper smoothed with more layers of PVP (4 and 5). It was found that this does not alter leakage behavior significantly demonstrating that 3 layers of smoothing are sufficient (see Figure 2-22).

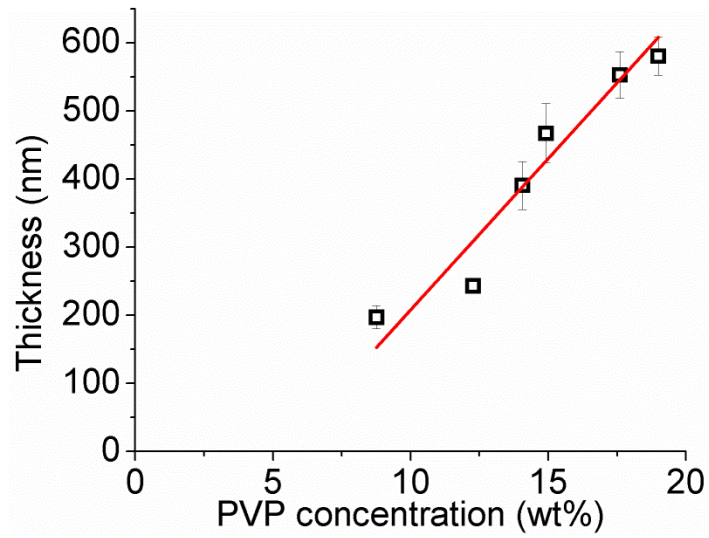


Figure 2-19. Dielectric thickness as measured from MIM capacitance is controlled by the concentration of PVP dissolved in the solvent for gravure printing.

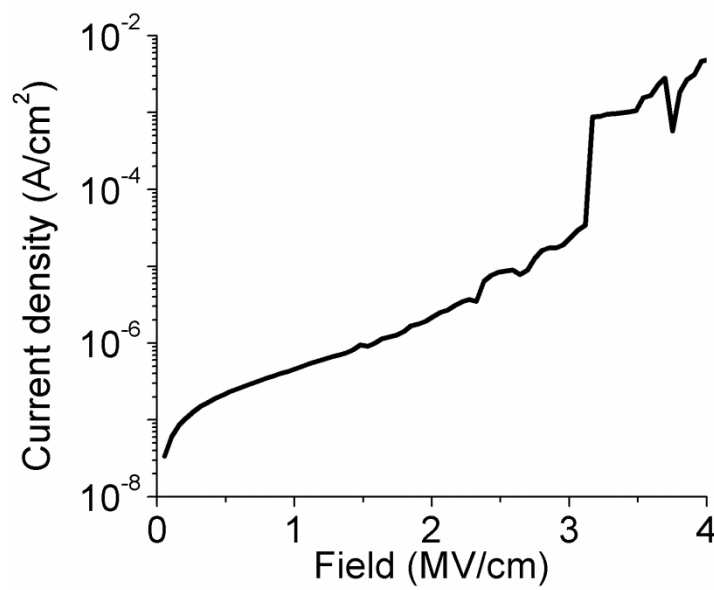


Figure 2-20. Typical leakage J-E-curve for 190nm dielectric.

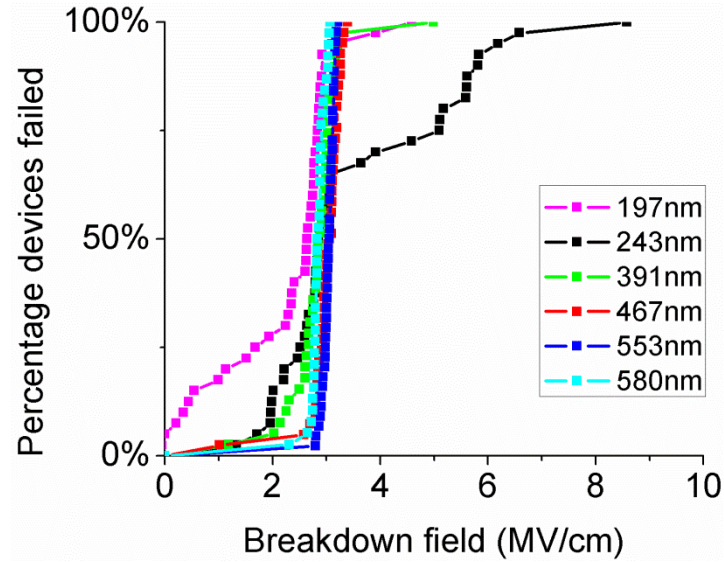


Figure 2-21. Cumulative breakdown plot for MIM capacitors of different dielectric thicknesses exhibiting a consistent breakdown field for different dielectric thicknesses.

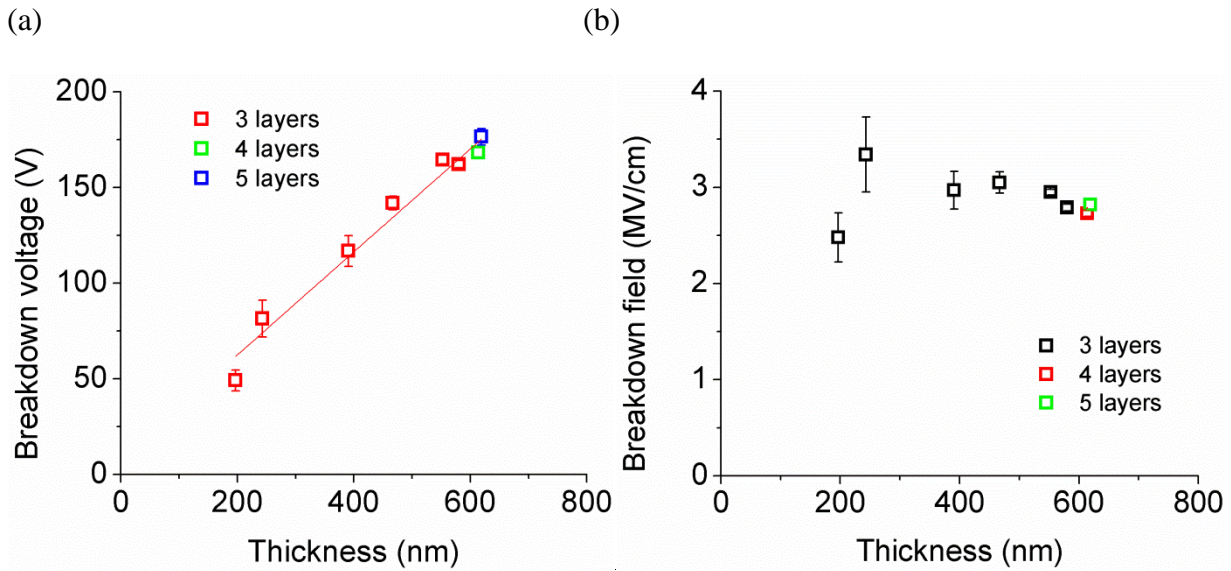


Figure 2-22. Average breakdown (a) voltage and (b) field vs dielectric thickness showing no dependence of breakdown field on dielectric scaling. Data points for 4 and 5 layer smoothing demonstrate that 3 layers of smoothing are sufficient.

## 2.4.2 Printed transistors on paper

Organic TFTs were fabricated with the same process as for the thinnest gate dielectric. Bottom-gate, bottom-contact OTFTs were fabricated using a spun poly(2,5-bis (3-tetradecyl-thiophen-2-yl)thieno[3,2-b]thiophene) (pBTTT) semiconductor layer on top. Spin coating was chosen because it could be performed under an inert nitrogen atmosphere. However, OTFTs with printed pBTTT have been demonstrated in the past<sup>86</sup> making this a fully printable process flow. All transistor measurements were conducted under a nitrogen atmosphere. The TFT fabrication process flow is illustrated in Figure 2-23. Figure 2-24 shows an optical micrograph of printed transistors on locally smoothed pads demonstrating both high quality printed features as well as the truly local nature of smoothed pads.

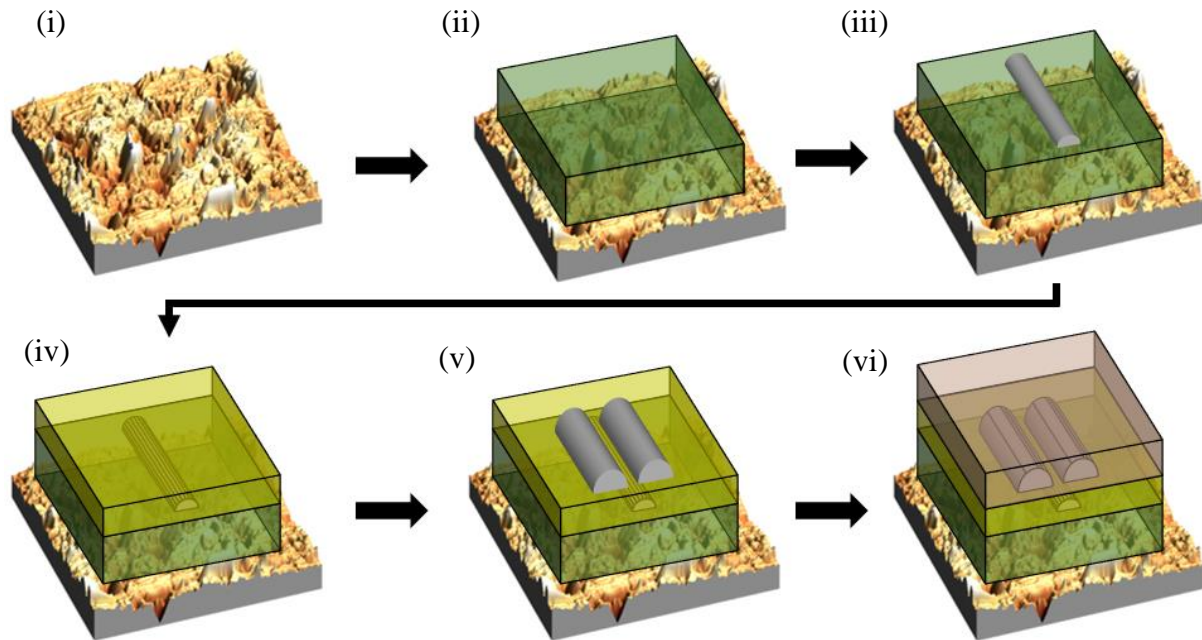


Figure 2-23. Schematic illustration of TFT process flow. The process flow is identical for MIM capacitors except that the last semiconductor deposition step is omitted and the electrodes are fully overlapped. (i) Rough paper with initial Kaolin smoothing. (ii) Gravure print local smoothing poly-4-vinylphenol (PVP), cross-link 210°C 30 minutes. (iii) Inkjet print bottom gate silver (CCI-300), sinter 150°C 30 minutes. (iv) Gravure print PVP gate dielectric, cross-link 210°C 30 minutes. (v) Inkjet print source and drain silver (CCI-300), sinter 150°C 30 minutes. (vi) UVO 10 minutes, Spin coat pBTTT C16, Anneal 160°C 10 minutes, cool slowly.

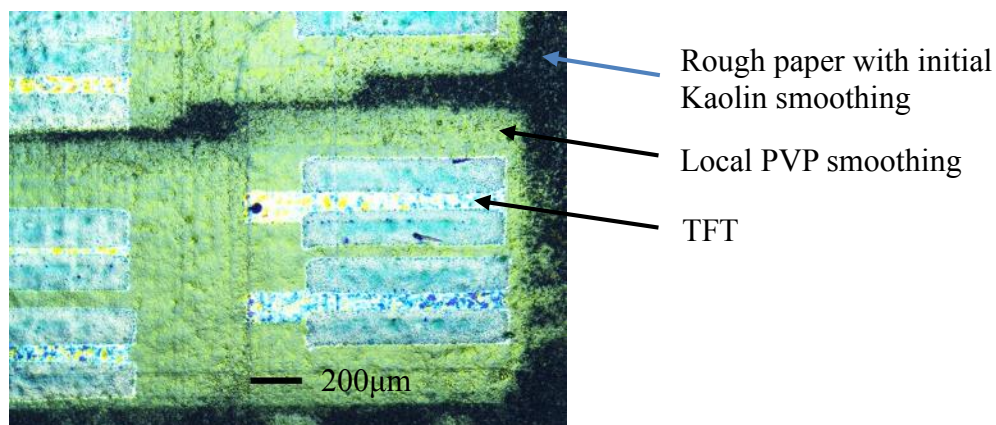
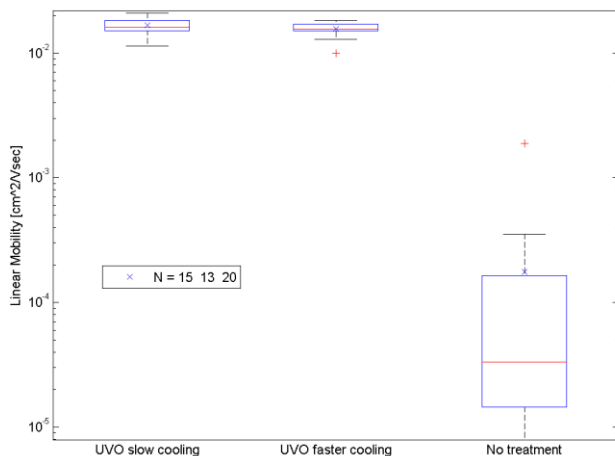


Figure 2-24. Optical micrograph of fully printed transistors on locally printed PVP smoothing (bright pads). The unmodified paper is visible as the dark areas surrounding smoothed pads.

The transistor performance was optimized<sup>106</sup> by exposing the source/ drain and gate dielectric to 10 minutes of UV ozone treatment before semiconductor deposition. When the sample was not treated with UVO before semiconductor deposition, mobility was found to be significantly lower, especially in the linear regime by about three orders of magnitude (see Figure 2-25). One can compare the  $I_dV_d$ -characteristics of two devices with and without UVO treatment (see Figure 2-26). Untreated devices show a clear non-linearity in the non-saturation regime suggesting a significant contact barrier. This explains why the difference is more significant for the linear mobility than the saturation mobility. The removal of the contact barrier might be due to a slight oxidation of the silver electrodes under UVO treatment. The work function of pristine silver at 4.3eV is not well matched to the HOMO level of pBTTT at 5.1eV.<sup>107</sup> Oxidation of the silver can increase its work function by 0.7eV resulting in much improved injection.<sup>108</sup> The UVO treatment might also improve injection by removing organic residue left on the surface after sintering of the printed silver nanoparticles.

(a)



(b)

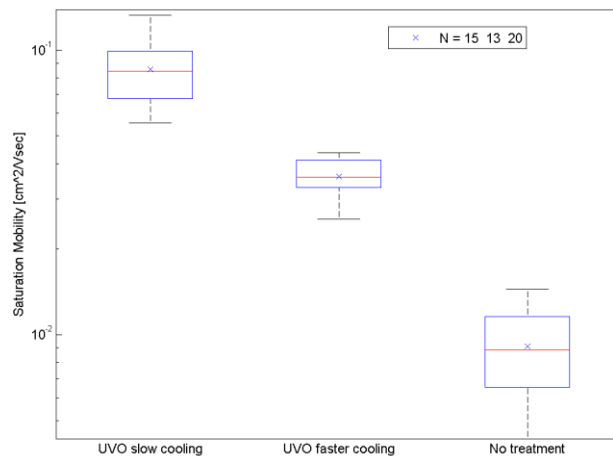
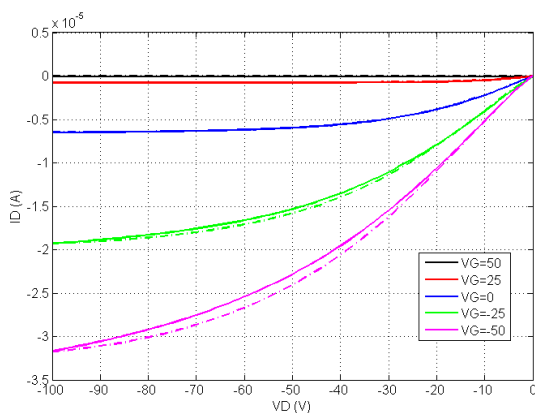


Figure 2-25. Comparison of electrical performance for different processing conditions: (i) slow cooling after pBTTT annealing and prior UVO treatment of electrodes, (ii) fast cooling after pBTTT annealing and UVO treatment and (iii) slow cooling after pBTTT annealing and no UVO treatment.

(a)



(b)

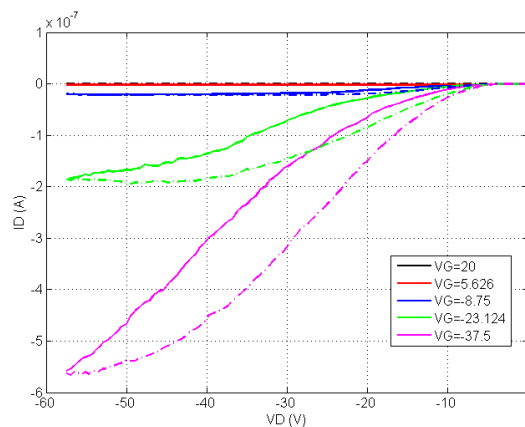


Figure 2-26.  $I_D$ - $V_D$ -characteristics of OTFT a) with and b) without UVO treatment. One can clearly observe the differences in non-linearity in the unsaturated regime indicating a contact barrier without UVO treatment.

The pBTTT was annealed at  $160^\circ\text{C}$  after spin coating. This temperature was chosen to lie above the transition temperature to the liquid-crystalline phase.<sup>107,109</sup> The film crystallizes into its final microstructure upon cooling. Two different cooling rates were explored to improve device

performance (see Figure 2-27). If the cooling rate is too high, the semiconductor is effectively quenched such that there is not enough time to form large crystallites. This can be observed in AFM scans of the semiconductor topography (see Figure 2-28). Consequently, mobility is lower if the cooling rate is too high (see Figure 2-25).

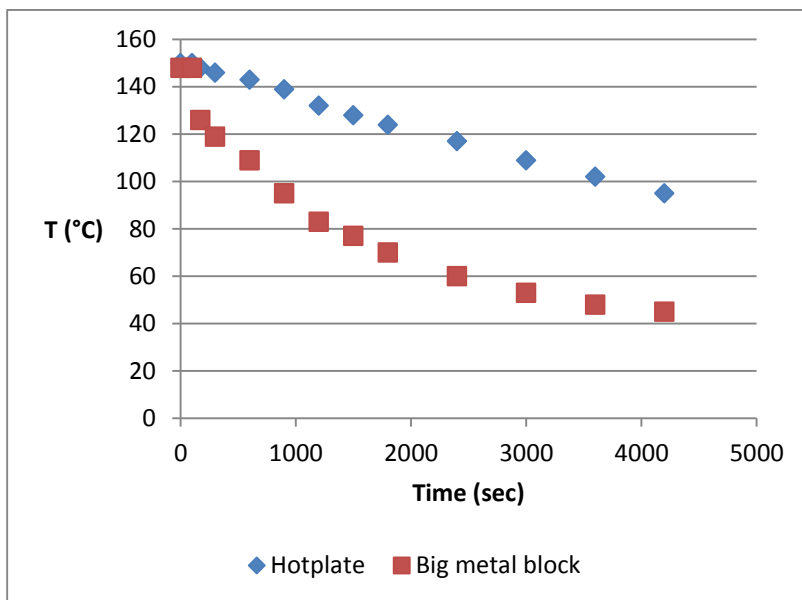


Figure 2-27. Two different cooling rates were used after semiconductor annealing. Slow cooling was achieved by turning off the hotplate and allowing the sample to cool down slowly together with the hotplate, which has a large thermal mass. Faster cooling was achieved by placing the sample on a metal block that was preheated to the same temperature as the hotplate but then placed on an upturned glass beaker.

(a)

(b)

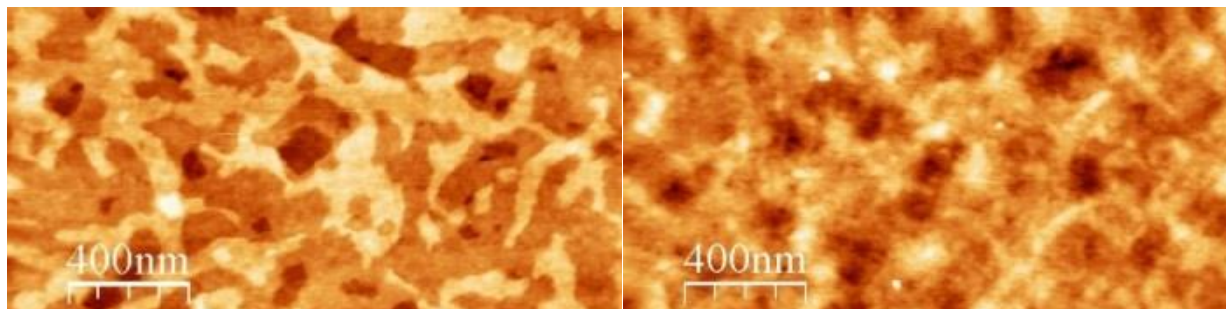


Figure 2-28. AFM images of pBTTT microstructure showing more well defined grains for a) slow cooling than for b) faster cooling

Optimized transistors were thus fabricated with UVO treatment before the pBTTT deposition and slow cooling after pBTTT annealing. Figure 2-29 shows typical  $I_D$ - $V_{GS}$  and  $I_D$ - $V_{DS}$  curves. Transistor parameters were extracted from 15 devices and the mean was compared to values from previous works with the same dielectric and semiconductor materials on plastic substrates.<sup>83,86</sup> It was found that transistors on paper exhibited comparable performance to transistors on plastic, except for showing degraded swing (see Table 2-1). This attests to the quality of the paper smoothing process proposed here.

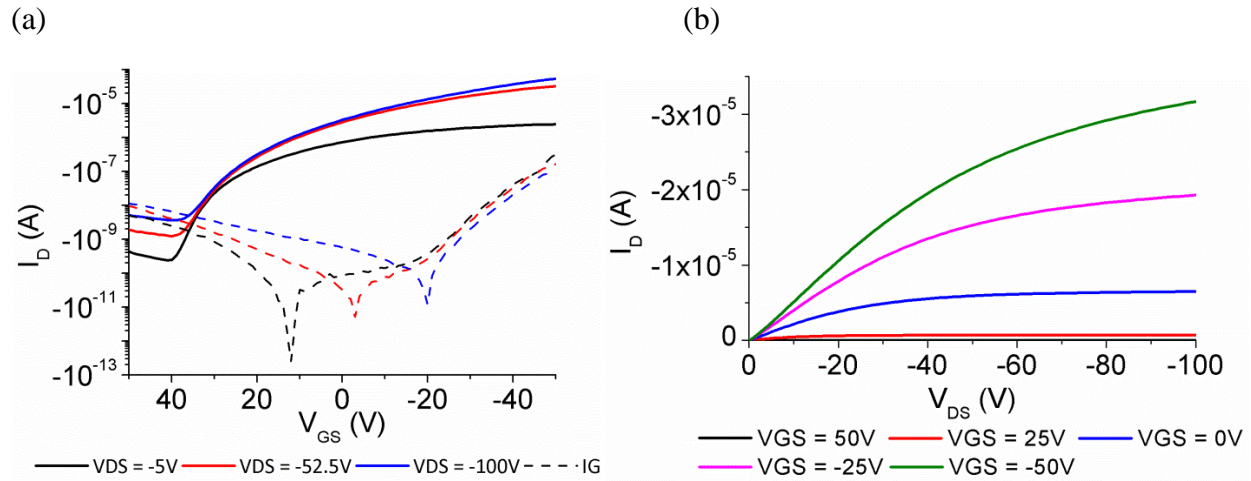


Figure 2-29. (a) Typical  $I_D$ - $V_{GS}$  characteristic of optimized device on paper.  $W/L=800\mu\text{m}/25\mu\text{m}$ . (b) Typical  $I_D$ - $V_{DS}$  characteristic. Same device as in (a).

	<b>This work<sup>22</sup></b>	86	83
Saturation mobility ( $\text{cm}^2/\text{V}\cdot\text{s}$ )	8.6E-2	1.5E-2	7.35E-2
Linear mobility ( $\text{cm}^2/\text{V}\cdot\text{s}$ )	1.7E-2	2.6E-2	3.19E-2
On-off ratio	3.2E+4	3.7E+5	6.96E+2
$V_{th}$ (V)	+0.88	-4	+5
Swing (V/dec)	18.1	9.5	5.48

Table 2-1. Comparison of TFT characteristics with values from previously reported transistors on plastic with the same semiconductor and dielectric materials. Performance on par with devices on plastic confirms viability of the paper smoothing process proposed here.

### 2.4.3 Bending tests

Most applications for printed systems on paper will require flexible and bendable electronics. The mechanical robustness of the devices fabricated here was thus investigated under bending. A series of cylindrical dowels was used to define controlled bending radii. A PEN carrier was used to facilitate handling. This leads to a larger strain in the devices compared to just bending the paper to the same radius. The Young's moduli of both paper and PEN were measured. Treating the sandwich as a composite beam with no uniaxial tension or compression, the strain in the devices and an equivalent bending radius for just bending the paper without a carrier were calculated (see Appendix A for further details).

TFTs on paper were strained in the direction parallel to current flow. No significant device degradation within the measurement error and device-to-device variation could be observed up to a strain of 2.2% (equivalent bending radius 1.59mm). The paper itself tore when bent to the next smaller radius. Figure 2-30 shows the evolution of saturation mobility under bending, which reveals no significant degradation upon bending. Other parameters showed similar behavior. This confirms that this device structure is robust against bending up to the failure point of the paper.

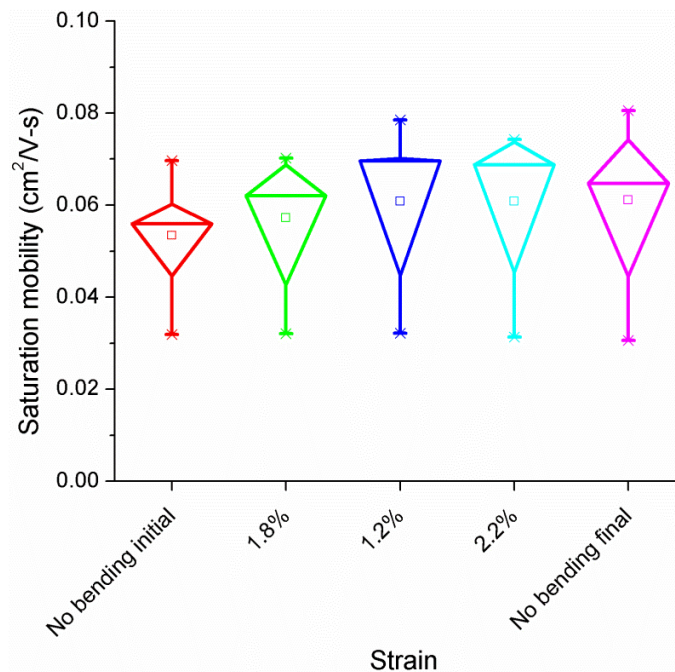


Figure 2-30. Saturation mobility box plots under bending and unbent before and after bending showing no significant degradation under bending. Conditions are plotted in the same order that the experiment was conducted in. Here samples were treated with only 5 minutes of UVO instead of 10 minutes leading to slightly lowered mobility.

Under stress in the direction perpendicular to current flow, the most likely failure mechanism would be cracking of the electrodes. The sheet resistance of the printed silver lines was measured as a function of bending and again no significant degradation could be observed (see Figure 2-31). These results attest to the robustness of printed electronics on paper under bent conditions.

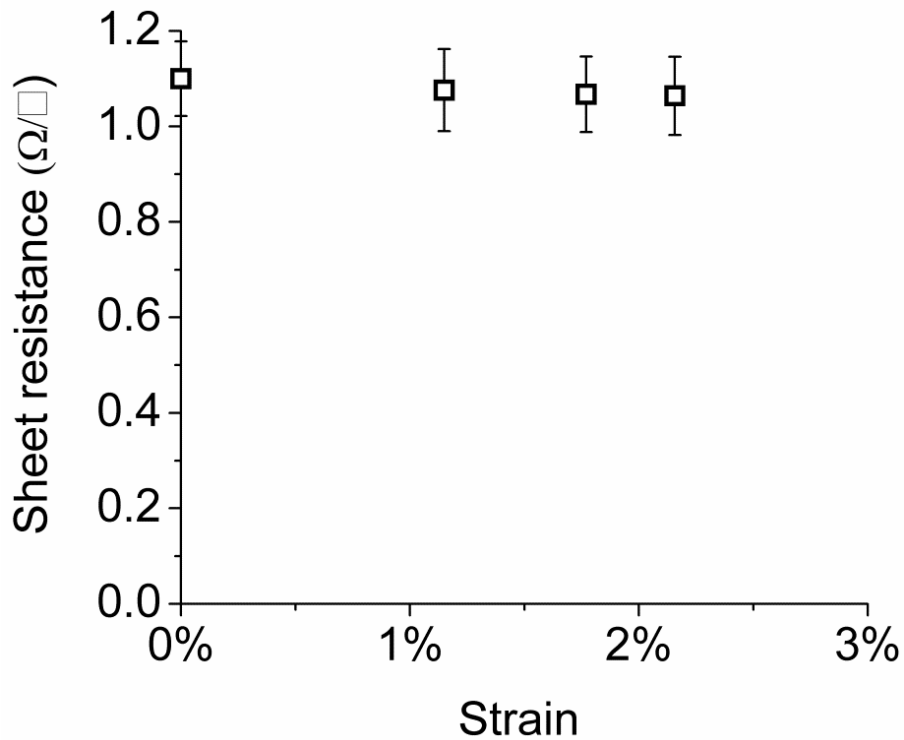


Figure 2-31. Sheet resistance of silver lines under bending confirming robustness to bending.

## 2.5 Conclusions

This chapter demonstrates that roll-to-roll printing can overcome major roadblocks towards printed electronics on paper. A locally printed smoothing underlayer was shown to tremendously improve surface roughness, ink absorption and printability. Printed transistors were fabricated on low-cost paper using this technique, and were shown to exhibit performance comparable to similar transistors on a plastic substrate that had been reported previously. Robustness of devices to bending was also demonstrated. This thus represents an important step towards the realization of smart consumer packaging integrating printed circuits directly onto packaging stock.

The focus of this chapter was the smoothing of paper using gravure printing. Transistors were fabricated with established materials and printing methods to demonstrate the viability of the smoothed paper as a substrate. The following chapters will focus on pushing the performance of the device printing itself, which requires scaling of both lateral and thickness dimensions. The next chapter will thus discuss a new gravure roll fabrication technology that enables the lateral downscaling of feature sizes whilst achieving high printing throughput.

## **Chapter 3: Fabrication of gravure roll for high-resolution printing**

### **3.1 Introduction**

The previous chapter used gravure to print a thick polymer layer to smooth paper as well as to print a thin polymer layer as a gate dielectric. In both cases, the minimum feature size is fairly large. Thus, rolls that had been made with traditional engraving techniques used in the graphics arts could be used. However, if more complex circuits and devices such as transistors are to be fully gravure printed, much smaller feature sizes need to be printed for example as source-drain electrodes. Traditional roll fabrication techniques are not adequate to push resolution very far. These techniques reach their limits below about 10 $\mu$ m cell size.<sup>110,111</sup> The three main engraving techniques currently in use are electromechanical engraving, laser structuring of a resist and direct laser ablation.

Electromechanical engraving uses a stylus to mechanically pattern the roll. The cylinder rotates whilst the stylus moves in and out to cut cells into the roll surface (see Figure 3-1 (a)). The tip of the stylus is diamond shaped resulting in diamond shaped cells. The cell size can be varied by controlling the distance that the stylus moves in by (see Figure 3-1 (b)). Both the cell width and depth are varied simultaneously due to the fixed shape and aspect ratio of the stylus tip.<sup>112</sup> This limits the patterns that can be constructed from such cells. Especially, thin lines of highly-scaled cells are ideally made up of a string of individual cells, which is problematic with cells that are not square and aligned with the line direction. Additionally, as the cell size is scaled down, the cell shape becomes increasingly non-ideal.<sup>23</sup> Cells become rounded due to the finite radius of curvature of the stylus (see Figure 3-1 (c)). Stylus engraving also results in considerable surface roughness. Traditionally, the roll surface is polished after engraving. However, as the cell size is scaled down, this becomes increasingly challenging without removing small cells.

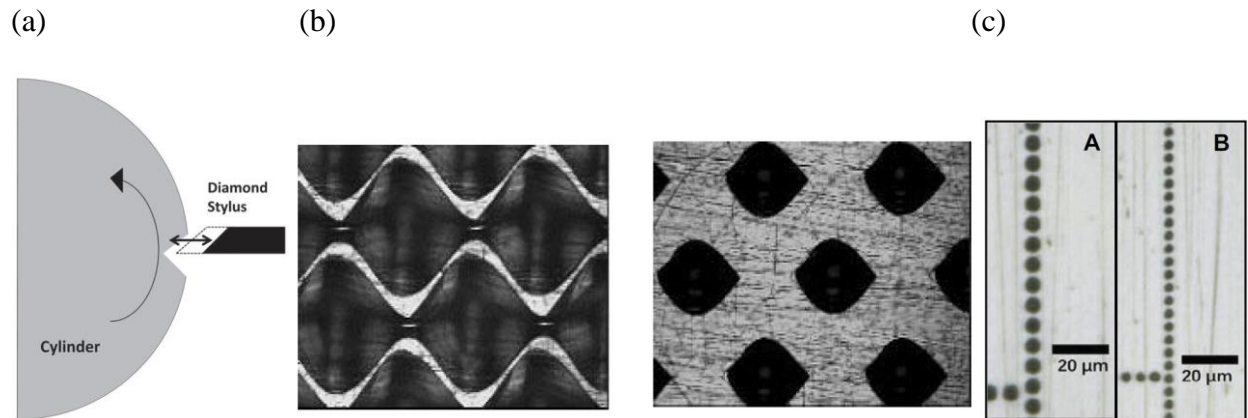


Figure 3-1. (a) Electromechanical engraving operates by cutting material from the rotating roll with a stylus that moves in and out according to the cell pattern. Reprinted with permission from <sup>83</sup>. (b) Cells are diamond shaped. Traditionally the color tone of a cell array is varied by varying the cell size and density. Reprinted with permission from <sup>110</sup>. (c) As cells are scaled down, the cell shape becomes increasing non-ideal and rounded. One can also observe scratches in the roll surface from the engraving process. Reprinted from <sup>23</sup> with permission from Elsevier.

The other two engraving technologies that are commonly used rely on laser patterning. A laser beam is used to either pattern the roll directly by ablation (see Figure 3-2) or to pattern a photoactive resist that is used as a mask during chemical etching of the cells. Both methods are limited by the spot size of the laser beam on the roll surface. Focusing is a challenge on the curved roll surface that is rotating, especially if the concentricity of the cylinder is not ideal. A round laser beam will result in round cells which is again not ideal for highly-scaled lines. Chemical etching of features is further limited by the isotropic nature of the etch resulting in undercutting of the resist thus increasing minimum feature size. Direct ablation of material requires much higher laser powers. Ideally, the metal is directly evaporated without leaving any residue. In reality, it is very difficult to create perfect cell shapes without any burrs. The size of burrs has been reduced to 2-3 $\mu\text{m}$  by using electroplated zinc with organic additives instead of copper that is traditionally used to fabricate rolls.<sup>110</sup> However, this size of burr is still large if cells are scaled below 5 $\mu\text{m}$ .

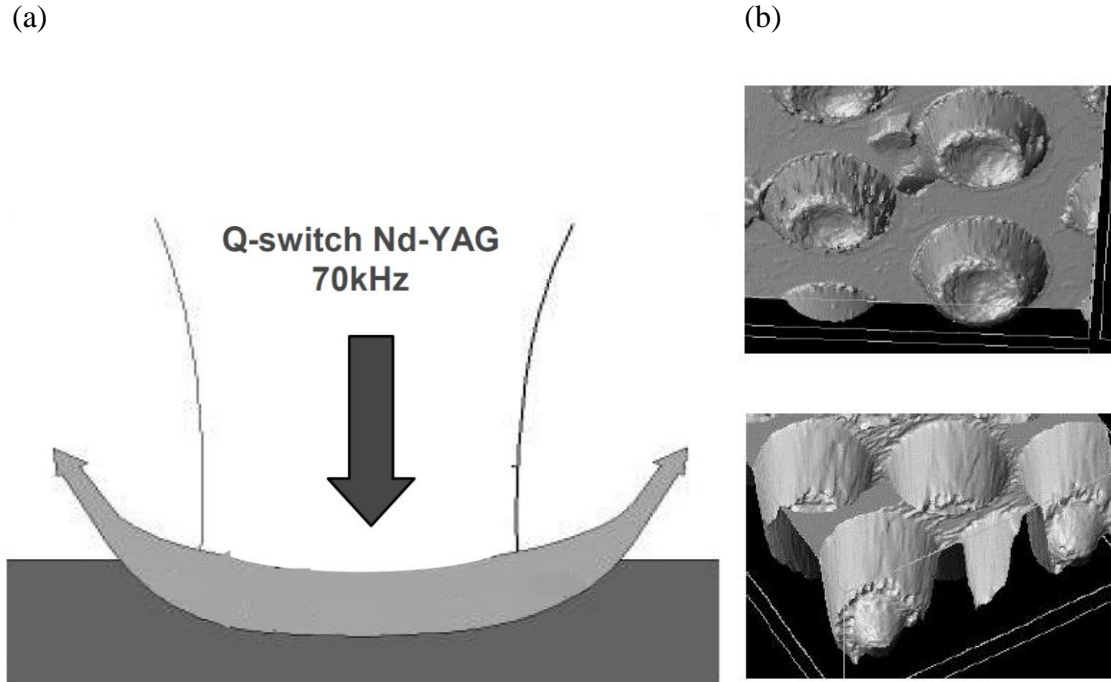


Figure 3-2. (a) Direct laser engraving uses a high-power laser to ablate metal from the roll. (b) 3D profiles showing cell shapes after laser engraving. Both panels reprinted with permission from <sup>110</sup>.

These limitations of traditional engraving techniques mean that a novel method of fabricating gravure rolls is required to successfully push resolution below  $5\mu\text{m}$ . Silicon printing plates offer a route towards this goal. They can be fabricated using traditional microfabrication techniques including photolithography and dry and wet etching. Superior control over cell size, cell shape and surface roughness can be achieved in comparison to traditional roll fabrication techniques. Indeed, some of the best reported results in terms of printing high-resolution features at high print speeds have been obtained using silicon printing plates.<sup>28,49,27,113</sup> However, the main drawback of silicon printing plates is their form factor. For lab-scale experiments, a plastic substrate is wrapped around a rubber cylinder and rolled over such a flat silicon printing plate. However, this is not possible for continuous high-speed printing to achieve low-cost manufacturing with a mass-production roll-to-roll or sheet-fed printer. The superior properties of the silicon printing plate thus need to be transferred to the form factor of a roll. One way to do so is to thin the silicon plate down sufficiently such that it becomes flexible enough to be wrapped around a roller. However, there are concerns whether such a silicon plate would withstand the stresses of printing both in terms of nip pressure and doctor blade pressure without cracking. Indeed, the first demonstration of this method does not use a doctor blade limiting the print speed to  $10\text{mm/sec}$ .<sup>114</sup> This chapter describes a different approach where a flexible metal plate is created that has the same surface topology as the silicon printing plate. This metal plate is wrapped around a cylinder to be used as a roll for gravure

printing. With this novel gravure roll, a printing resolution down to 2 $\mu$ m linewidths can be achieved.<sup>115</sup>

In this chapter, the novel roll fabrication process and its optimization are described first. Printing with such rolls is analyzed next. Mounting of the plate on a magnetic roller is discussed. Two different surface modifications are contrasted and it is shown how they affect printing performance as well as wear during extended print runs.

### **3.2 Roll fabrication process**

The first step in the roll fabrication process is the fabrication of the silicon master. Photolithography is used to define the cell features with a critical dimension of 250nm for the smallest cell gaps. The cells are then etched into the silicon using a silicon dioxide hard mask. Different cell shapes can be obtained by using different etching methods. Square cells are obtained using dry etching. Inverted pyramid shapes that resemble the shape obtained from stylus engraving can be obtained using KOH as the wet etchant for silicon. This limits the orientation of the cells to be aligned with the 110 crystal plane of the silicon wafer; however, this is not a significant limitation for most Manhattan style circuit layouts. The details of this process were published elsewhere.<sup>49</sup>

In order to fabricate the metal printing plate (see Figure 3-3 for an overview of the process), the pattern is first transferred from the silicon master into a polymer through a molding step. After release of the polymer from the silicon mold, the polymer is metallized. First, a chrome gold seed layer is evaporated. Then, a hard surface layer of nickel with boron nitride particles is applied by electroless plating.<sup>116,117</sup> The electroless plating solution was purchased from Caswell Inc. On top of this, the main thickness of the printing plate is built up using electroplating of permalloy (80% nickel, 20% iron).<sup>118</sup> By applying the hard layer on top of the polymer molding before the deposition of the permalloy rather than depositing it on top of the permalloy after release from the molding, it does not distort the highly-scaled features. Before release of the metal stack from the polymer molding, the backside of the metal is polished and the metal is diced into the shape of a rectangular printing plate. The high magnetic permeability of the permalloy allows mounting of the printing plate on a magnetic roll ready for printing (see Figure 3-4). After release, the metal surface with the hard layer is a perfect replica of the silicon master (see Figure 3-5 and Figure 3-6).

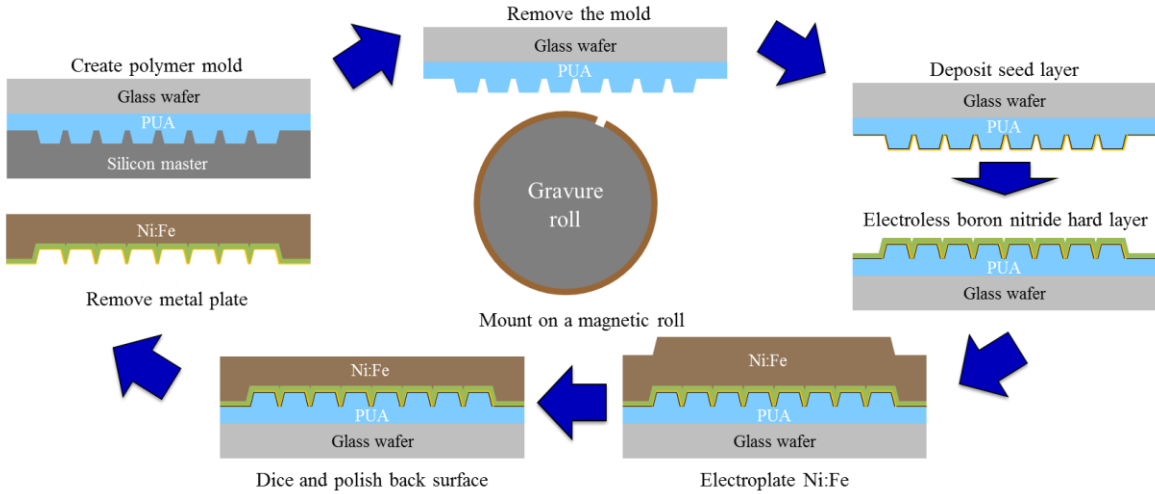


Figure 3-3. Metal plate fabrication process starting from silicon master plate.

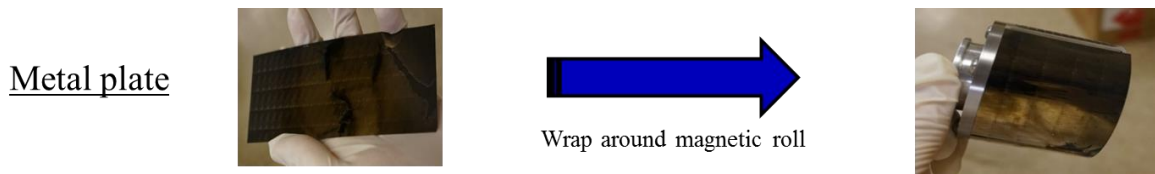


Figure 3-4. Final metal plate after polishing, dicing and lift-off from PUA mold ready to be wrapped around magnetic cylinder for printing.

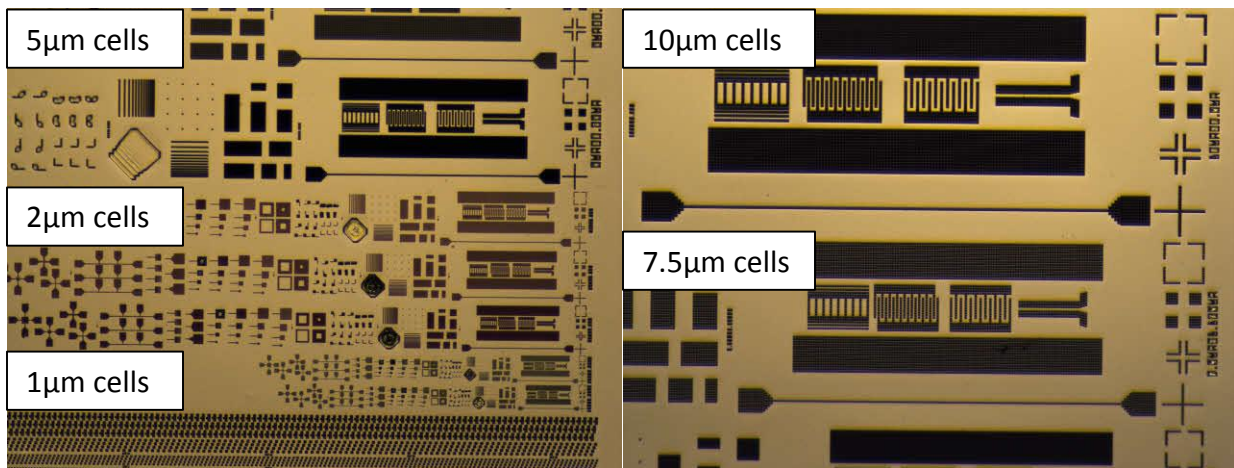


Figure 3-5. Optical micrographs of printing plate surface after release showing good feature replication over large areas.

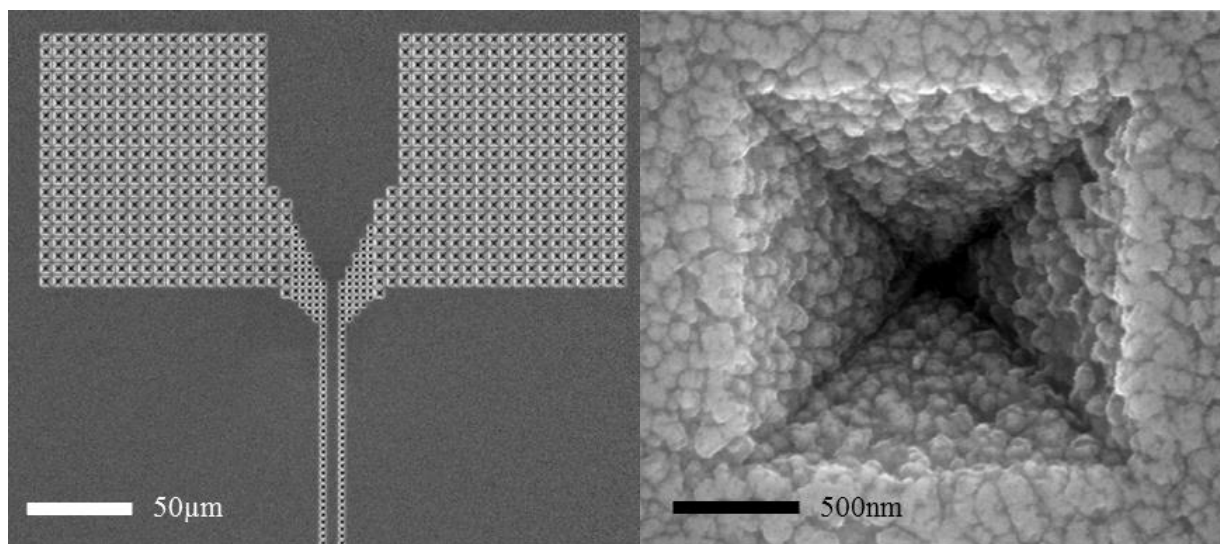


Figure 3-6. SEM images of cell features on metal printing plate at different magnifications. The inverted pyramid shape from KOH etching of the silicon master is clearly visible. One can observe the boron nitride particles making up the hard layer.

The choice of molding polymer is critical for the success of this process. Polyurethane acrylate (PUA, purchased from Minuta Technology Co.) works well both for the molding as well as the metallization steps.<sup>119</sup> Soft materials such as polydimethylsiloxane (PDMS) with a Young's modulus of 1-10MPa can be removed from the silicon master very easily after molding. The PDMS deforms readily as it is peeled away from the silicon master not putting any significant stress on the silicon. However; during metallization, cracks are formed very easily in the metal layer on top of the soft polymer due to internal stresses in the metals (see Figure 3-7). In addition, standard PDMS formulations are high viscosity (3500cP), which makes it more prone for bubble entrapment during the molding. Conversely, epoxy is a material that is hard enough for the metallization process (Young's modulus 1-10GPa). However, this leads to problems during the demolding step. Epoxy being optimized for adhesion needs significant force to be pulled away from the large area of a six inch wafer. This cannot be done by stepwise peeling as for PDMS due to the rigidity of the epoxy. This puts significant stresses on the silicon master as well as the epoxy mold leading to cracking. Similarly, thermal curing can lead to cracking due to thermal stresses (see Figure 3-8) and thus UV curing needs to be employed. PUA combines the benefits of both. Its hardness lies in between PDMS and epoxy at 300-1500MPa. Together with a low surface energy, this enables easy demolding. However, it is sufficiently hard to prevent the formation of cracks during metallization. UV curing prevents the build-up of thermal stresses during curing. A low viscosity formulation (100-150cP) aids in bubble-free molding. Figure 3-9 shows a perfect six inch wafer molding using PUA.

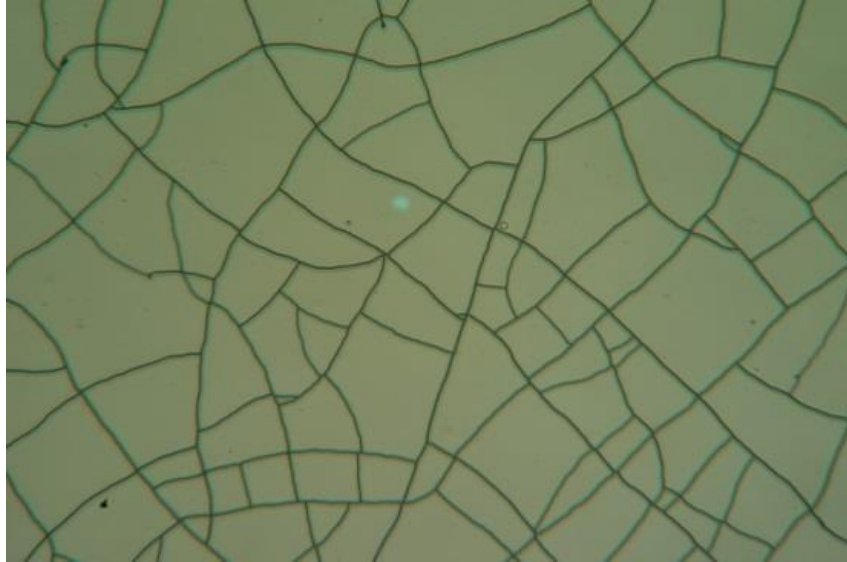


Figure 3-7. Optical micrograph of evaporated chrome-gold on PDMS exhibiting extensive cracking.



Figure 3-8. Epoxy molding on top of six inch glass carrier wafer that has cracked due to thermal stresses during curing.

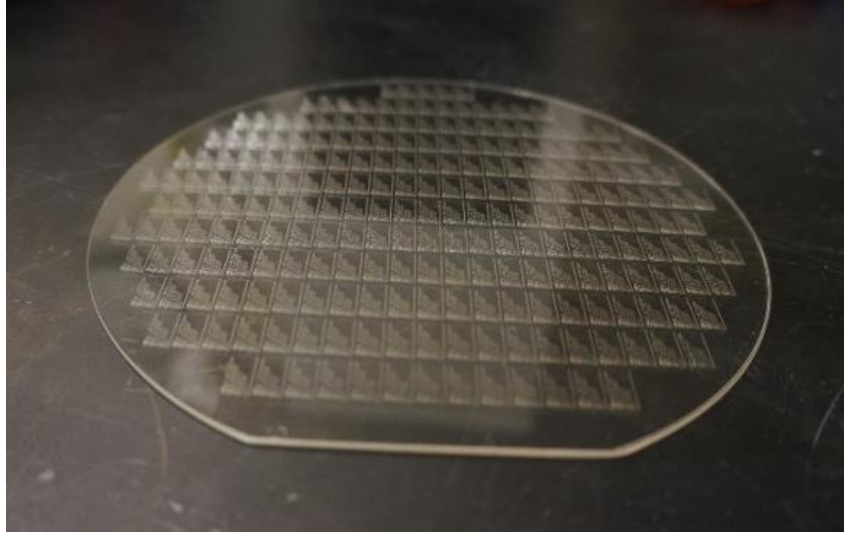


Figure 3-9. Perfect molding of PUA on six inch glass carrier wafer after demolding from the silicon master.

### 3.3 Printing results

#### 3.3.1 Plate mounting on magnetic roller

Finally, after mounting of the metal printing plate on the magnetic cylinder, it can be used for printing. Since the plate is wrapped around the roll cylinder, there will always be a seam as one edge of the plate meets with the other after going around the roll. This can lead to a step that potentially disturbs the doctor blade as well as contact with the substrate during transfer. Here, the worst case scenario is explored. Since the wafer that is used to fabricate the initial master is 150mm in diameter, the metal printing plate is not long enough to completely wrap around the magnetic roller that has a circumference of 200mm. Thus, there is a step at both ends of the plate equivalent to its thickness of 60 $\mu$ m. This step is smoothed by applying kapton tape to the edge. The print quality was recorded as a function of distance from the initial step. Figure 3-10 shows prints of the same repeated pattern at different positions. The initial block exhibits inferior print quality compared to subsequent blocks that all exhibit the same stable print quality. This shows that there is an initial disturbance due to the step at the leading edge of the printing plate; however, this disturbance has diminished by the second block that is located 1cm from the edge. In the future, larger printing plates need to be fabricated to completely cover the magnetic roller and minimize the step at the seam between the leading and trailing edge of the plate. Larger plates can be fabricated by using silicon processes for larger wafers although these processes are limited by the size of silicon wafers available (currently 300mm diameter). Further scale up might be possible by employing tools and processes developed for the display industry that can handle very large glass substrates. Large glass substrates could be used instead of silicon as the material for the master, although processes would have to be adapted for example because pyramid shaped cells could not

be fabricated by KOH etching anymore. The limited resolution of the lithography used for display applications compared with nanometer scale silicon lithography is no concern here because the smallest cells that can efficiently be used for gravure printing are currently larger than  $1\mu\text{m}$  in width.

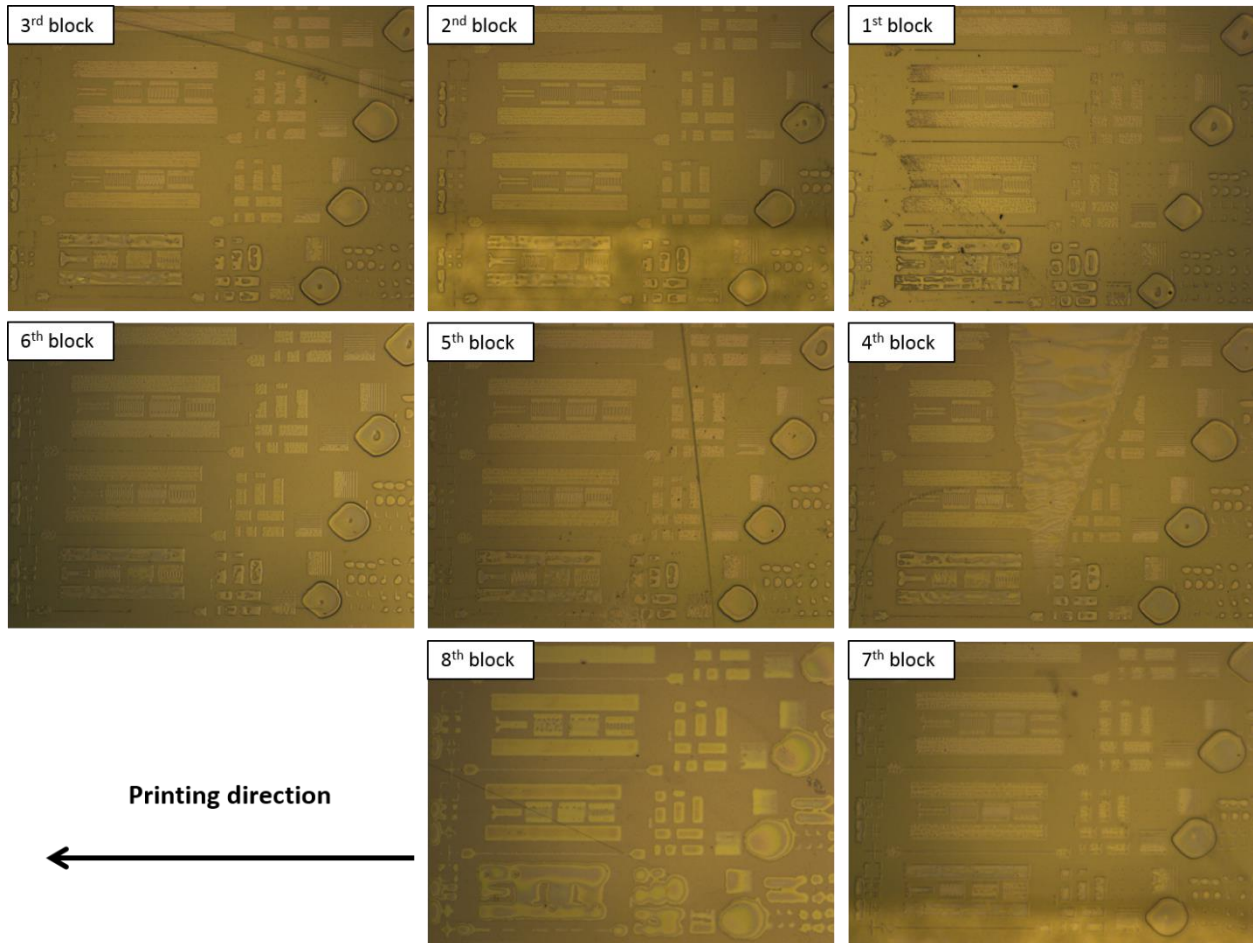


Figure 3-10. Optical micrographs of prints at different positions on the roll along the print direction. The first block of patterns is closest to the leading edge of the plate mounted on the roll and exhibits the poorest print quality. Print quality stabilizes after one block. The distance between blocks is 1cm. The large wedge-like shape in block 4 is due to an air bubble that had been entrapped during the PUA molding causing the doctor blade to momentarily lose contact with the roll surface. Bubbles can be prevented during the molding process by careful degassing.

### 3.3.2 Printing optimization

In order to achieve optimal printing results and fully utilize the high resolution features on the roll, the fluid mechanics of the process needs to be optimized. One needs to consider ink properties, printing speed, doctor blade properties, substrate wetting and roll wetting properties. Optimization of the wetting properties of the roll surface is enabled by the roll fabrication process proposed here. The hard layer on top of the main body of the plate can be modified to engineer the roll's surface properties. Here, two different surfaces are explored: the bare nickel iron printing plate body and a boron nitride hard layer. The capillary number was varied to optimize print quality. The ink used here was again poly-4-vinyl phenol (PVP) dissolved in propylene glycol monomethyl ether acetate (PGMEA) as a model ink.

#### 3.3.2.1 Printing optimization without hard layer

First, consider printing with a roll where no boron nitride hard layer was deposited. By leaving out the hard layer, the top surface of the roll is simply the nickel iron that makes up the body of the plate. One can observe improved print quality for initial increases in printing speed and capillary number from 1.1 to 2.1 due to the suppression of drag-out (see Figure 3-11). As the doctor blade passes over the cells, it picks out ink from the cells. This leads to a reduction in ink volume in the printed feature. At higher values of  $Ca$  there is less time for ink to wick up the doctor blade thus reducing the detrimental effects of drag-out. However, at  $Ca=4.2$ , one can also observe breaks in lines and holes in pads. In this case, the printed ink volume is limited by the cell filling process. The ink requires time to fully fill the cells due to capillary forces. If  $Ca$  is too large, there is not enough time for this process to complete fully and air is entrapped in the cells.<sup>59</sup> Thus optimum printing without the boron nitride hard layer is achieved at an intermediate capillary number of 2.1. The three parameters that determine  $Ca$  are print speed, ink viscosity and ink surface tension. Assuming surface tension is fixed by the chosen solvent and solute,  $Ca$  is proportional to the product of speed and viscosity. For highly-scaled lines, ink viscosity cannot be changed freely due to ink spreading on the substrate after transfer. If ink viscosity is too low, ink will spread too far reducing pattern fidelity. If ink viscosity is too high, ink will not spread sufficiently before drying to fill in gaps between gravure cells leading to line edge roughness and in the worst case disconnected lines. Thus, the ideal ink viscosity is small enough to ensure sufficient spreading but no lower to prevent excessive spreading (see Figure 3-12). This will be studied further in the next chapter. For an ink viscosity of 110cP, an ideal capillary number of 2 and the surface tension of PGMEA of 26.9mN/m, this results in an optimum print speed of 0.5m/s. Ideally, one would want to print at a higher speed to increase fabrication throughput. This can be achieved when the boron nitride hard layer is employed.

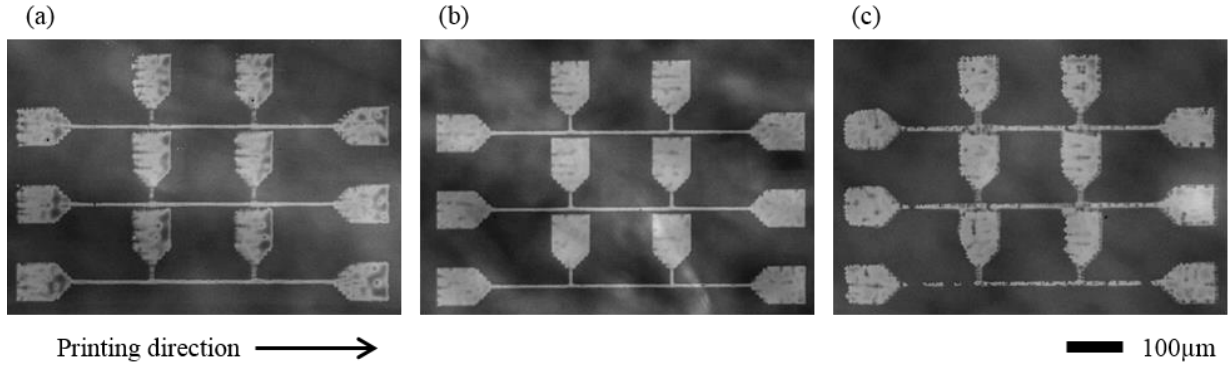


Figure 3-11. Optical micrographs of printed features without hard layer. (a)  $Ca=1.1$ : Some holes in print due to drag-out. (b)  $Ca=2.1$ : Optimal printing at the cross-over point between the filling and drag-out limited regimes. (c)  $Ca=4.2$ : Significant gaps in lines due to insufficient filling of cells.

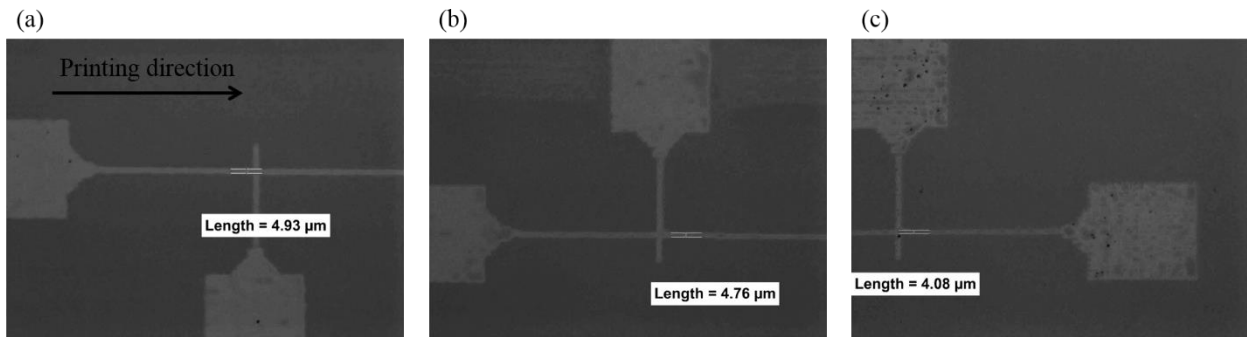


Figure 3-12. Optical micrographs of printed features with different viscosities. (a) 87cP, (b) 113cP, (c) 146cP. The largest viscosity of 146cP leads to some holes in pads and lines due to insufficient ink spreading on the substrate. The intermediate viscosity of 113cP leads to complete features. Further reduction of the viscosity leads to further ink spreading increasing linewidth. Printed with boron nitride hard layer.

### 3.3.2.2 Printing optimization with hard layer

The addition of the boron nitride layer not only increases the hardness of the roll surface but also changes its wetting characteristics and thus printing needs to be optimized differently. One can observe a clear improvement in print quality as  $Ca$  is varied over more than one order of magnitude for a 146cP PVP ink (see Figure 3-13). At  $Ca=0.11$  hardly any ink is printed onto the substrate. This improves substantially when  $Ca$  is increased to 1.1; however, one can still observe holes in printed rectangles as well as breaks in high resolution lines. These defects are removed when printing at  $Ca=5.4$ . The reason for this significant difference in print quality as  $Ca$  is increased is the reduction of drag-out. In the case of severe drag-out at  $Ca=0.11$  one can also observe

characteristic tails of dragged-out ink being re-deposited behind pads. Ca could not be increased further at this viscosity due to equipment limitations in terms of print speed. Large scale roll-to-roll gravure printers can print at higher print speeds that might lead to further improvements in print quality. However, even without being able to probe higher print speeds with the lab-scale printer used here, the hard layer enables printing at higher speeds than the bare nickel-iron printing plate.

This difference can be explained by the different wetting properties of the two surfaces. Boron nitride is used as an extremely slick, low-friction, high lubricity surface coating. This manifests itself in a smaller contact angle hysteresis (Nickel iron:  $\theta_R=25^\circ$ ,  $\theta_A=90^\circ$ . Boron nitride:  $\theta_R=40^\circ$ ,  $\theta_A=80^\circ$ .), which enhances both cell filling and drag-out. Cell filling is enhanced by the lower advancing contact angle, which promotes the advancing of the ink meniscus into the cell during filling. Similarly, ink can be pulled out from the cell more easily due to the larger receding contact angle. Thus, the transition from the drag-out limited regime to the filling limited regime is shifted to higher capillary numbers for the roll with the boron nitride hard layer. For the same viscosity, this translates into higher printing speeds. This is an economic advantage in the manufacturing of printed electronics systems since throughput is increased by higher print speeds. With these optimized printing conditions, the roll with the hard layer can be used to print  $2\mu\text{m}$  lines at a high speed of 1m/s as can be observed in Figure 3-14.

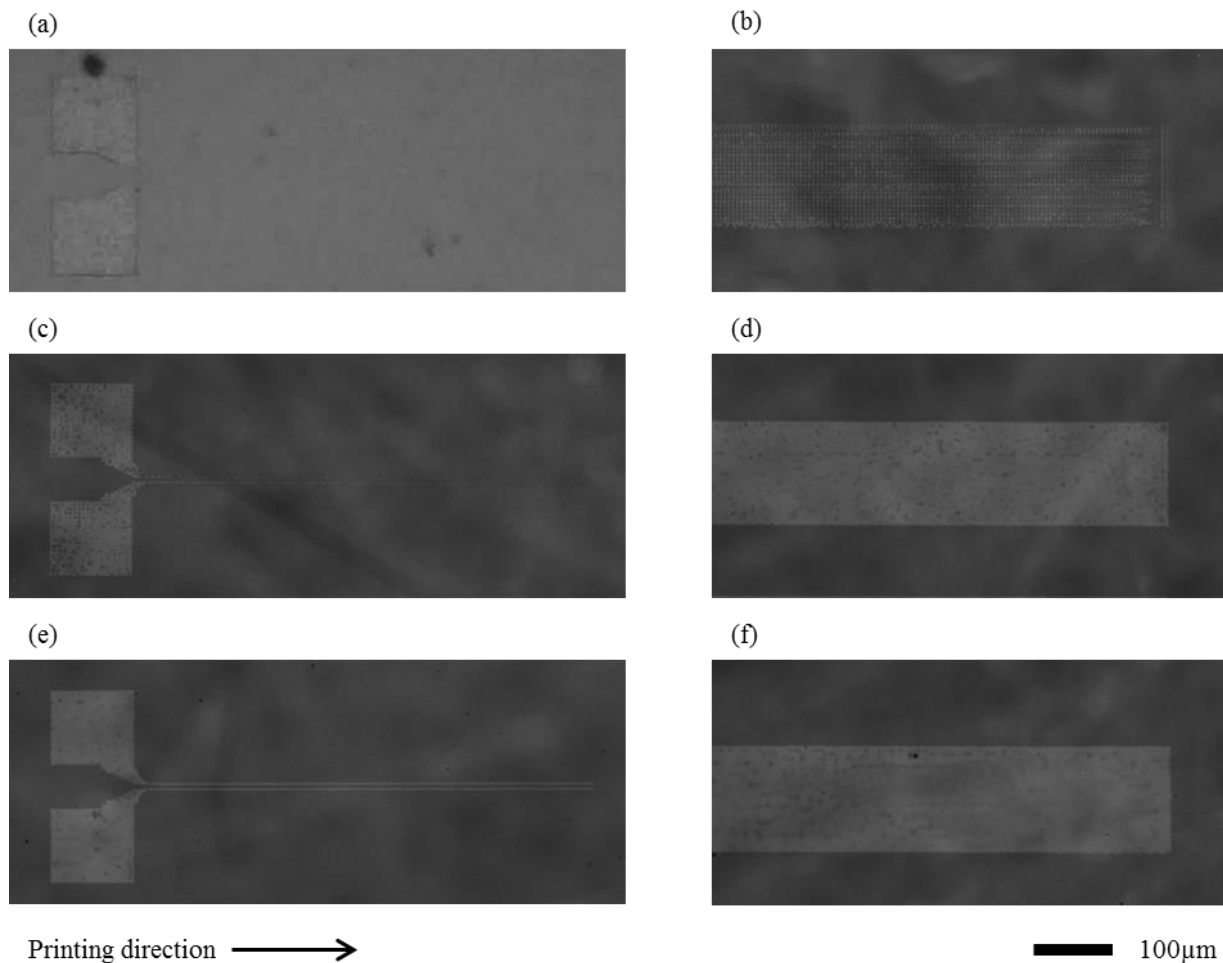


Figure 3-13. Printed features with hard layer. (a) & (b)  $Ca=0.11$ : thin  $2\mu\text{m}$  lines do not print at all and large pads are mostly made up of isolated dots due to drag-out. (c) & (d)  $Ca=1.1$ : thin  $2\mu\text{m}$  lines print partially due to reduced drag-out but lines and pads still have holes. (e) & (f)  $Ca=5.4$ : thin  $2\mu\text{m}$  lines as well as large pads print well due to the suppression of drag-out.

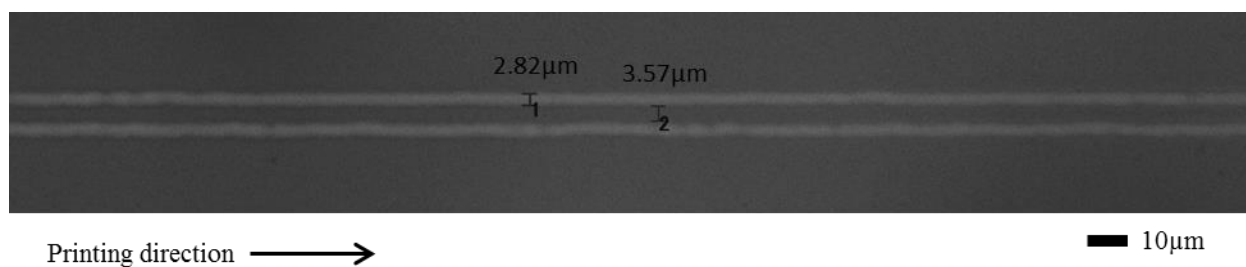


Figure 3-14. Parallel lines printed from  $2\mu\text{m}$  cells resulting in continuous lines with width and spacing of about  $3\mu\text{m}$ .  $Ca=5.4$ , ink viscosity 146cP, print speed 1.0m/s.

### 3.3.3 Effect of hard layer on roll scratching

One benefit of the boron nitride hard layer is the increase in the optimal print speed. The other main effect is the protection of the roll surface from scratching during printing. As the doctor blade, which is made from steel, presses down on the roll, it can produce scratches in the roll (see Figure 3-15). This is especially true when the lubrication film between the doctor blade and the roll is minimized to enhance print quality.<sup>66</sup> This leads to increased roll surface roughness, which can affect print quality detrimentally. The roll surface is still scratched by the blade with the boron nitride hard layer; however, the steady state level of roughness after about 20 prints is reduced by the hard layer (see Figure 3-16). This improved roughness leads to better print quality as evidenced in Figure 3-17. The roll with the boron nitride hard layer still prints continuous lines after 50 prints. Conversely, lines printed with the roll without a hard layer exhibit some discontinuities after 50 prints due to the scratching of the roll surface.

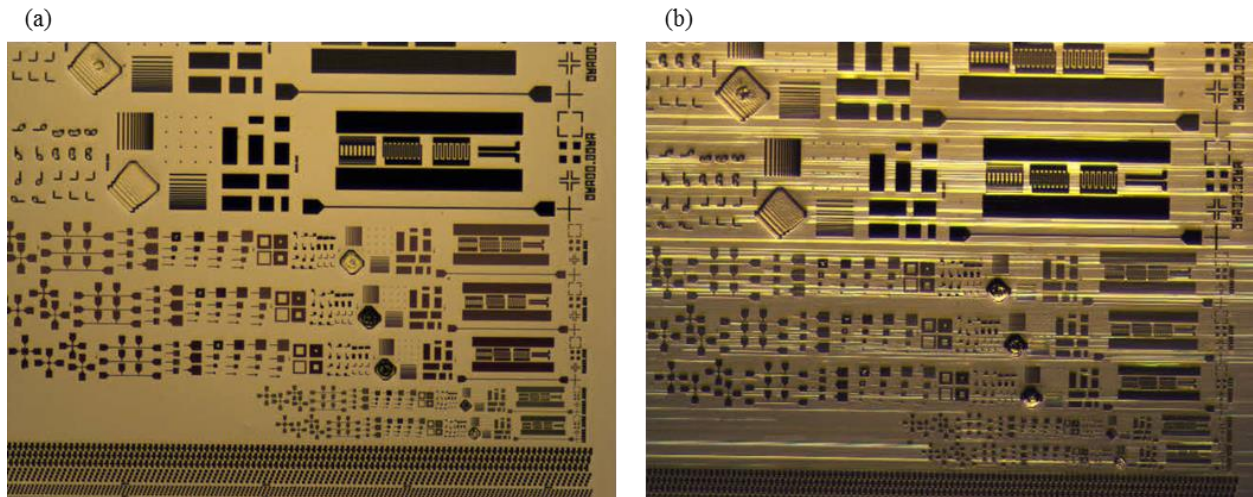


Figure 3-15. Optical micrographs of (a) pristine printing plate before printing and (b) printing plate scratched by doctor blade after two prints.

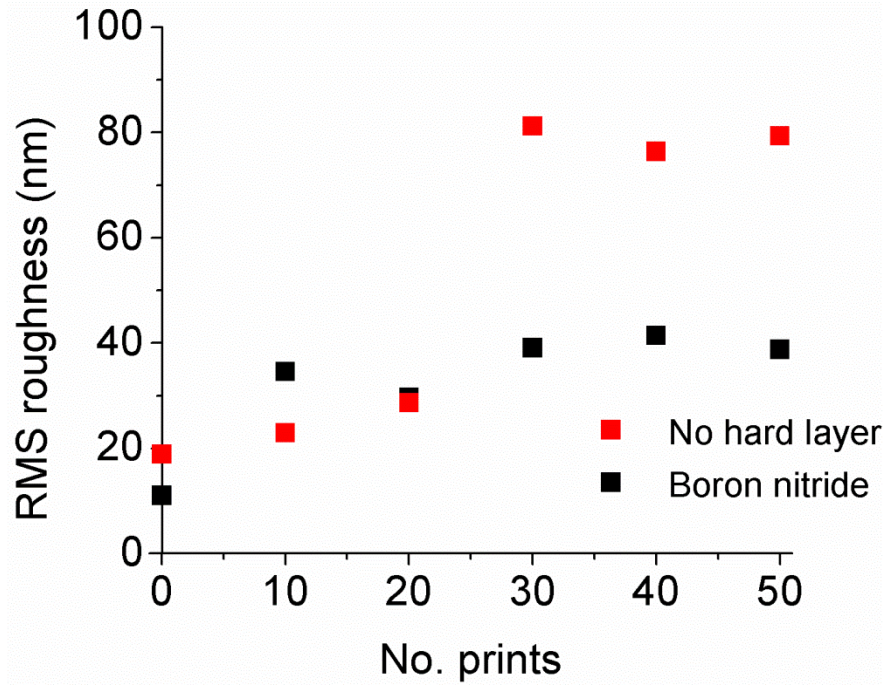


Figure 3-16. Boron nitride hard layer leads to less roll scratching and lower surface roughness after multiple prints.

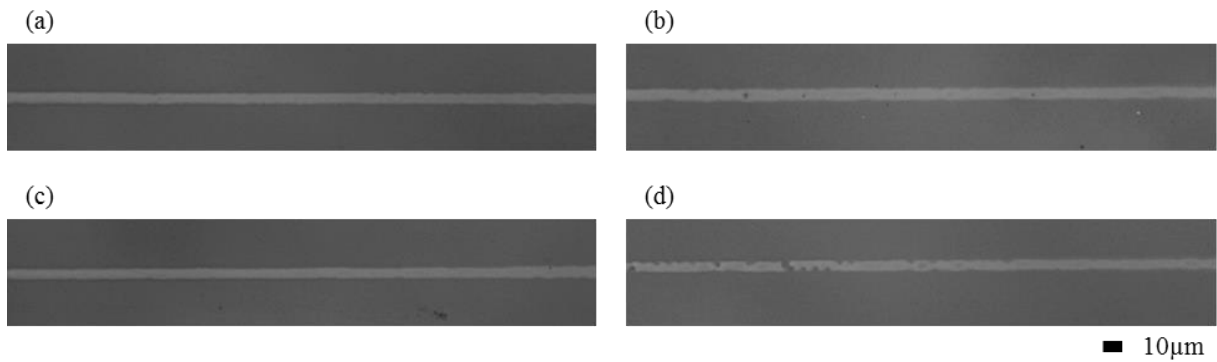


Figure 3-17. Print quality with scratches after multiple prints. (a) With boron nitride hard layer with new roll. (b) Without boron nitride hard layer with new roll. (c) With boron nitride hard layer after 50 prints. (d) Without boron nitride hard layer after 50 prints. With hard layer, print quality does not degrade significantly over 50 prints. Without hard layer, lines show breaks after 50 prints.

### **3.4 Conclusions**

A novel process to fabricate high-resolution gravure rolls is demonstrated in this chapter. With this process, gravure rolls are fabricated by replication of a silicon master. Superior control over feature size, surface roughness, cell placement and cell shape is achieved by using standard microfabrication techniques to fabricate the silicon master. These superior properties are transferred to a metal plate that can be mounted on a roll. Printing of 2 $\mu$ m lines at a high speed of 1m/s is demonstrated with this roll. A hard layer is shown to improve both the maximum printing speed at which high-quality features can be printed as well as surface scratching over the course of 50 prints.

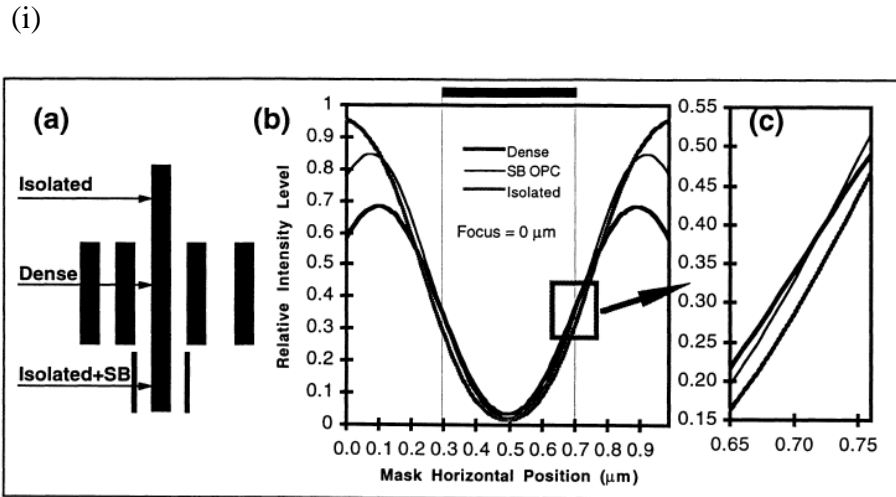
# Chapter 4: Proximity effects in high-resolution gravure printing

## 4.1 Introduction

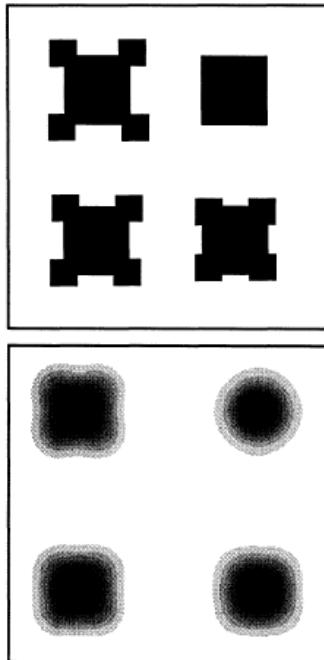
The previous chapter demonstrated how highly-scaled features can be printed at high speeds using gravure. However, these results were obtained for simple lines aligned with the print direction. In real electronic circuits, more complex patterns need to be printed. It is thus imperative to understand complex pattern formation if highly-scaled printed circuits are to become a reality. Effects that arise from bringing patterns into close proximity are especially important. In traditional photolithography, proximity effects have been studied extensively. In this case, the physics of optics needs to be studied to understand pattern formation. The constructive and destructive interference of the light's wave function determines the light intensity that photoresist is exposed to in different locations. For example, denser patterns can lead to increased exposure. Such increased exposure can be desirable to print otherwise unprintable features and it can be added intentionally by adding assist features to the mask that don't print themselves such as the scatter bars enhancing a line in Figure 4-1 (i). This approach can be extended to two-dimensional features as with the serifs in Figure 4-1 (ii). The ultimate goal is to produce tools that take an arbitrary complex pattern and automatically generate a mask pattern that prints the desired pattern (see Figure 4-1 (iii)). This is routinely done in photolithography nowadays.<sup>120-123</sup> In printed electronics, a similar understanding needs to be developed based on the physics of fluid mechanics rather than the physics of optics. Here, proximity effects in highly-scaled gravure printing are studied for the first time.<sup>113</sup>

Here, we show how the printing of multiple features in close proximity can dramatically alter gravure printing performance. Highly-scaled lines that are oriented perpendicular to the print direction are used as a model system. Multiple lines are printed behind each other with varying spacing to isolate the effect of line proximity. Such elements are found in patterns such as closely spaced grids, interdigitated electrodes or indeed any high-resolution circuits of arbitrary shape. Rectangular patterns can also be interpreted as lines that are printed very close to each other and indeed differences in printing between the first row of cells and subsequent cells of a rectangle have been observed previously.<sup>124</sup> The orientation of lines is very important due to the drag-out effect in gravure. Ink that has been dragged-out from a cell is subsequently re-deposited on the land area behind the cell in the shape of a characteristic drag-out tail.<sup>49,68</sup> These tails are aligned with the printing direction. Lines printed perpendicular to the printing direction are thus most susceptible to the drag-out effect and most challenging to print. Here, it is shown experimentally that if subsequent cells are connected by a thin drag-out tail, the transfer of ink from the roll to the substrate is dramatically altered leading to proximity effects. This effect is thus an interaction of

the drag-out and the transfer process and an example of a case where the assumption that the different gravure sub-processes can be analyzed independently breaks down.



(ii)



(iii)

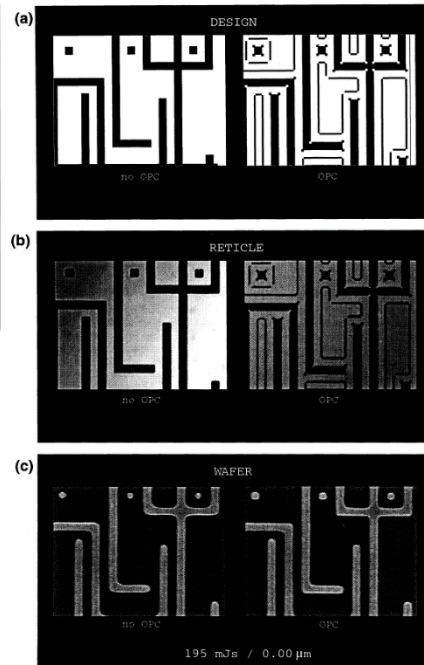


Figure 4-1. Optical proximity correction (OPC). (i) The light intensity in the photoresist depends on the pattern density on the mask and can be modified by adding scattering bars (SB). (ii) Serifs can be used to enhance the pattern quality of 2D patterns. (iii) Ideal mask patterns can be created automatically for complex patterns exploiting optical proximity effects. All reprinted with permission from <sup>123</sup>.

At the beginning of this chapter, after a brief overview of the experimental methods, printed patterns are analyzed on the substrate after ink transfer. The proximity effect is demonstrated and patterns are evaluated using an automated feature quality extraction method. It is shown how the proximity effect can be used to enhance print quality. The fluid mechanics of the transfer process and the proximity effect are studied in detail by measuring ink amounts inside cells before and after transfer. This insight is used to create a simple model to explain the gravure proximity effect based on ink flow during the transfer process.

## 4.2 Experimental

Groups of lines were gravure printed with varying line spacing. Lines were oriented perpendicular to the printing direction to maximize the impact of the drag-out effect. The cell size was varied between 2 and 4 $\mu\text{m}$  and the spacing or gap between cells within lines was varied between 15 and 60% of the cell size. Lines were one cell wide and the ideal printed linewidth is thus identical with the cell size. In reality, ink will always spread somewhat to increase linewidth. Figure 4-2 illustrates the pattern variables studied here.

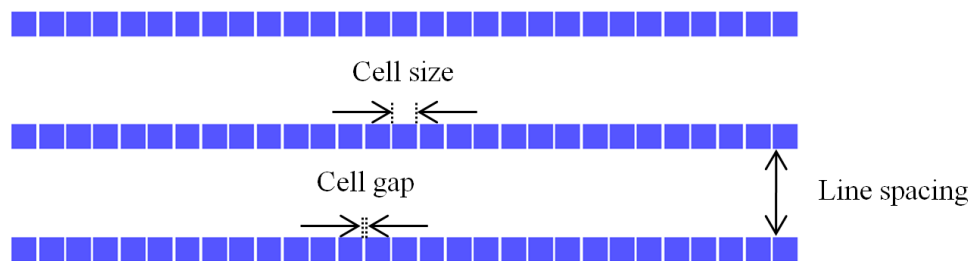


Figure 4-2. Pattern variables studied here: Cell size, cell gap (spacing) and line spacing

Printing results were studied by imaging the final patterns on the plastic substrate. The substrates were planarized polyethylene naphthalate (PEN) substrates (PQA1) provided by DuPont Teijin Films. Substrates were treated with a 30 seconds, 50W air plasma before printing to improve ink transfer. The ink was NPS purchased from Harima Chemicals, a silver nanoparticle ink with 12nm particle size. A silver ink was chosen due to its reflective optical properties when imaged as well as its widespread use in the fabrication of printed electrical circuits. The ink viscosity was tuned by dilution with its solvent AF5. The ink was dried and sintered after printing at 220 $^{\circ}\text{C}$  for 120 minutes. After printing, drying and sintering, the printed patterns were imaged by optical microscopy. The results were analyzed using an automated technique to extract print quality metrics, namely the fraction of lines merged together, the fraction of discontinuous lines, ink

spreading and edge roughness. Spreading was defined as the average distance by which lines extend over their intended edge on either side. Edge roughness was defined as the standard deviation of the line spreading. Spreading and edge roughness were normalized by cell size to compare lines of different cell sizes.

In order to understand the fluid mechanics of the proximity effect, ink was not only imaged after transfer to the plastic substrate but also on the printing plate. Flat silicon printing plates were used as the printing master for inverse direct gravure printing.<sup>49</sup> After filling of the cells with ink and wiping of excess ink with the doctor blade, ink is transferred from the flat master onto the flexible plastic substrate that is wrapped around a rubber roll. These silicon plates are the same plates that were used in the previous chapter to create a polymer molding for the metal printing plate. Thus, results obtained from the flat silicon plates will carry over to roll-based high-throughput printing even though the exact values for example of optimum capillary number will be different. The main advantage of the flat silicon plates is that they facilitate the measurement of ink volumes inside cells during and after the printing process to deconvolute the effect of different gravure sub-processes, namely cell filling, doctor blade wiping, ink transfer and ink spreading on the substrate. The ink volume inside cells was measured after the doctor blade wiping process and after the transfer process. In the former case, the printing process was stopped before transfer to the plastic substrate. In both cases, the ink was dried and sintered. The dried silver inside cells was imaged by scanning electron microscopy (SEM) to achieve the necessary resolution. The ink volume inside cells was calculated from top-down images given the known cell geometry and silver volume fraction in the liquid ink.

## **4.3 Printed pattern analysis**

### **4.3.1 Proximity effect**

Figure 4-3 shows the effect of bringing high-resolution lines into close proximity. One can note that the shape of the lines changes markedly as the distance between lines is changed. If lines are placed too close to each other, they will merge due to the spreading of the ink after transfer onto the plastic substrate. As the spacing between lines is increased, lines become thinner with less ink volume per line. In this case, a line distance of  $6\mu\text{m}$  or two cell widths gives optimal line shapes. With different cell sizes, cell gaps and printing conditions, the optimal line distance will be different. At larger line distances, line edge roughness increases and lines can even become discontinuous. This happens because there is not enough ink in the lines to fill in all the gaps between the cells. This trend holds for all lines except for the first line in each print. In these micrographs the bottom line is always the first one that was filled, wiped and transferred. The first line consistently has less ink than subsequent lines. When line spacing is increased far enough that

lines can be treated as isolated lines, subsequent lines start to exhibit similar behavior to the first line. Lines become isolated when they are not connected by drag-out tails anymore. One can observe faint drag-out tails behind lines, especially when they are sufficiently separated. Lines start to become not connected by drag-out tails at a line distance of  $15\mu\text{m}$  and are fully separated at a line distance of  $21\mu\text{m}$ . One can clearly see that this separation of the lines coincides with an increase in line edge roughness. This suggests that the connection of lines by drag-out tails is responsible for the observed proximity effects. This also explains why the first line behaves consistently differently from subsequent lines since it is the only line that is not connected to another line's drag-out tail at its leading edge. An experiment was also conducted where the printing plate was wiped in the usual way but the printing direction was reversed for the transfer process. The same directionality of the proximity effect was observed as before suggesting it is due to the directionality of the wiping process rather than any directional process during transfer. The tails that connect lines are very thin leading to discontinuous films after transfer to the plastic substrate and nanoparticle sintering (see Figure 4-4); thus, potentially not affecting circuit functionality whilst significantly affecting fluid flow during ink transfer.

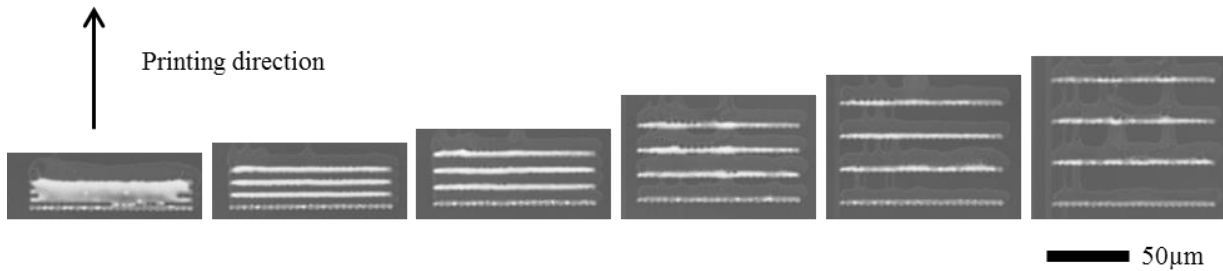


Figure 4-3. Optical micrographs of printed features demonstrating proximity effect. Very closely spaced lines merge together. Lines with medium spacing show optimal printing. Further increases in line spacing lead to lines with large edge roughness. The first line always resembles the shape of isolated lines. The cell size is  $3\mu\text{m}$ , cell gap  $1.8\mu\text{m}$ , printing speed  $0.25\text{m/s}$ , ink viscosity  $68\text{cP}$ . The distance between lines varies from left to right as  $3, 6, 9, 15, 21$  and  $27\mu\text{m}$ .

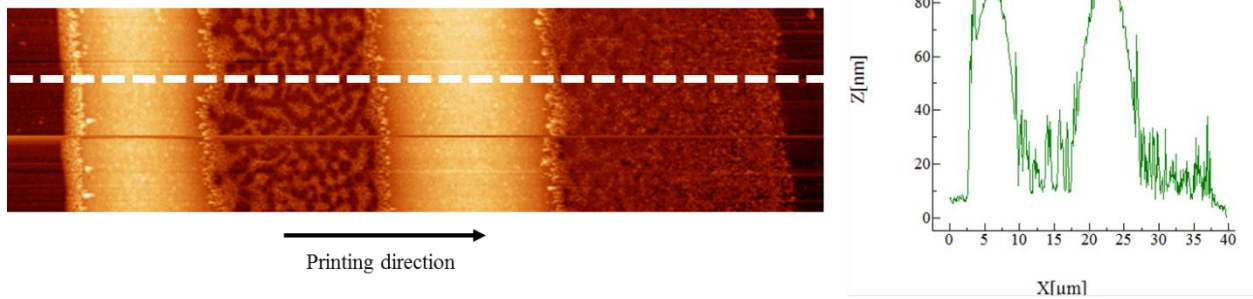


Figure 4-4. AFM scan and profile (along white dashed line) across two closely spaced silver lines on plastic substrate. The drag-out residue in between lines and after trailing line can be observed clearly. The drag-out residue is significantly thinner than the printed lines and is discontinuous especially in between lines.

### 4.3.2 Automated pattern analysis

Patterns were studied in more detail by extracting feature quality from optical micrographs in an automated fashion. A Matlab program was written to automatically compare printed features to the ideal features on the gravure printing plate. This allows the screening of a larger number of printed features and the quantification of feature quality. Image processing methods were employed to overlay images of the printed features with the ideal photolithography mask patterns used to make the printing plate (see Figure 4-5 (a)). First, images are cropped. A thresholding algorithm is then applied to generate binary images signifying areas with ink and without. Images are morphologically opened i.e. first eroded and then dilated. This acts like a spatial low-pass filter removing noise. After this clean-up of the image, it is overlaid with the ideal mask data. The two images are aligned in terms of shift and rotation to give the best overlay. Finally, the thresholded but unfiltered image is substituted back in at this new aligned position to preserve information that had been lost by the filtering step.

The aligned images are used to compare printed features with the ideal mask data. Each feature, such as a line or a set of closely spaced lines, is considered individually to quantify the impact of pattern variables such as cell size, cell gap or line distance. For each of these features, print quality metrics are calculated. Figure 4-5 (b) shows a heat map that visualizes the number of merged features. Brighter colors mean that a printed feature is connected to more of its neighbors. Ideally, each printed feature should be isolated from all its neighbors but this is not always the case due to ink spreading and drag-out. Other metrics studied are the fraction of discontinuous lines, ink spreading and edge roughness.

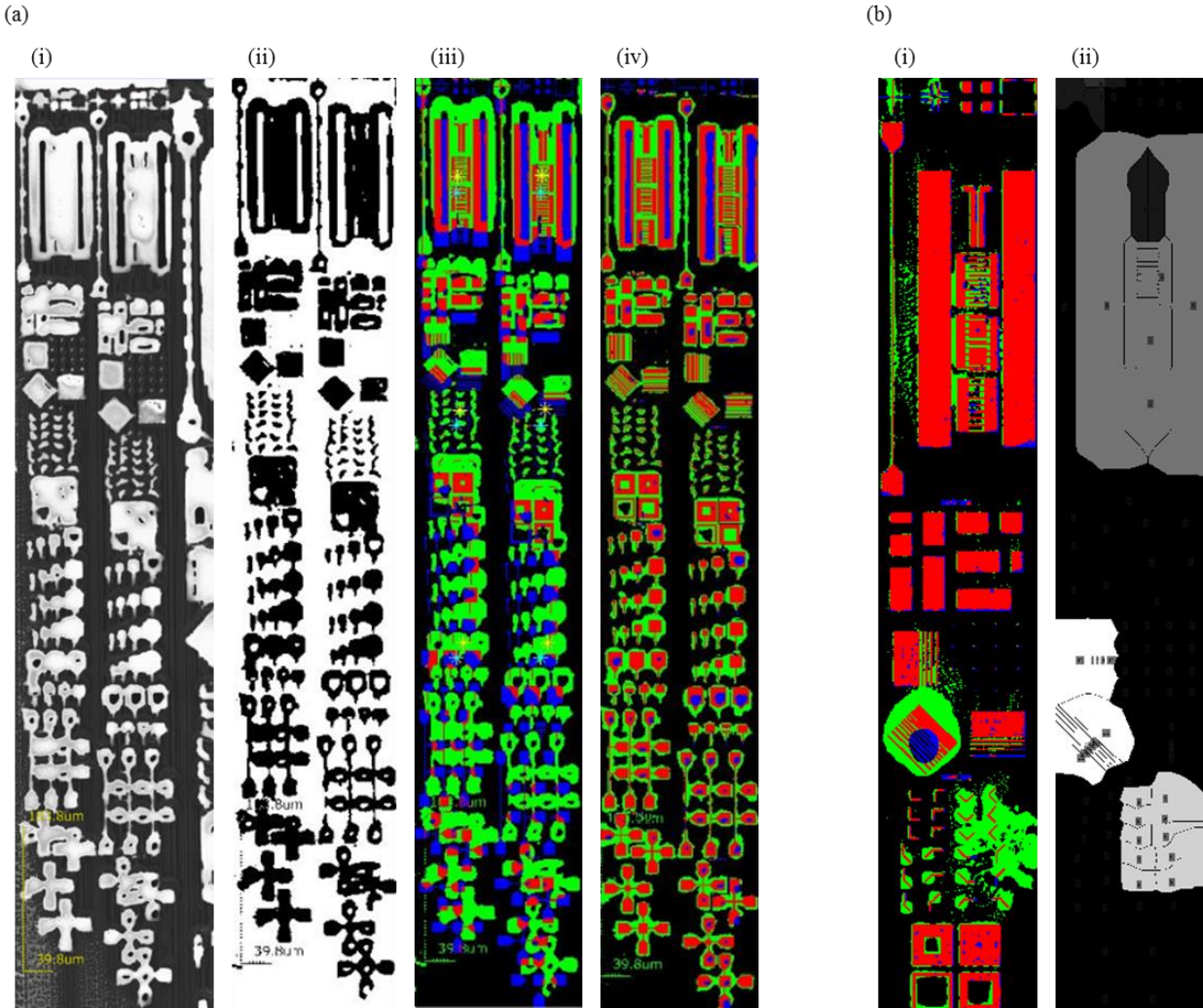


Figure 4-5. Feature extraction and evaluation algorithm (a) Alignment of printed features with ideal mask data. (i) Original image of printed features. (ii) Printed features after cropping, thresholding and filtering. (iii) Mask data (blue) overlaid on top of printed features (green). (iv) Final alignment of printed features and mask data. Overlapping areas are colored red. The original unfiltered but thresholded image was substituted back in to increase accuracy of feature evaluation. (b) Feature quality evaluation. (i) Aligned printed features and mask data (same stage as panel a iv). (ii) Heat map of one feature quality metric: feature merging. The brighter the color, the larger the number of other features a particular feature is connected with due to non-ideal printing.

### 4.3.3 Design rules and assist features

The automated extraction of print quality metrics allows the screening of different parameters, both printing conditions including ink properties as well as pattern variables, to identify design rules for particular situations. Here, closely spaced lines printed perpendicular to the printing direction are taken as an example. First, ink viscosity was varied whilst keeping Ca constant to study the effect of ink spreading on the substrate independently from the other gravure sub-processes and to find the optimum viscosity for these patterns (see Figure 4-6). The lower the ink viscosity, the easier it will be for the ink to spread on the substrate. The lowest viscosity ink studied here at 34cP spreads the most. This limits the minimum feature size that can be achieved, both in terms of line width, as well as minimum line spacing. Lines printed with low viscosity inks are more prone to merge together. In an electrical circuit, this would result in a short circuit, which would be a fatal flaw destroying the functionality of the circuit. A design rule must thus take ink spreading into account and put a lower limit on line spacing to achieve reliably separated lines. This minimum line spacing will be larger for the 34cP ink than for the other inks studied here. Thus the 34cP ink is not optimal. On the other hand, if the viscosity is too high, there is not enough spreading. Gravure relies on ink spreading to fill in the gaps between discrete cells and form continuous lines. If the ink does not spread enough, line edge roughness increases. There will be less ink in the cell gaps in between cells leading to scalloped lines where the wavelength of the scallops corresponds to the placement of cells. In the more extreme case, lines can become discontinuous leading to open circuits. This is another fatal flaw that would render a circuit unusable. The highest viscosity ink studied here at 195cP shows both increased line edge roughness as well as a much larger fraction of discontinuous lines. This is especially true for lines spaced further apart that don't get the benefit of the proximity effect. 68cP was found to be the optimum ink viscosity for the patterns studied here leading to the optimum amount of spreading that minimizes both the merging of adjacent lines and the number of discontinuous lines. This viscosity was used to study the effect of printing speed and cell gap.

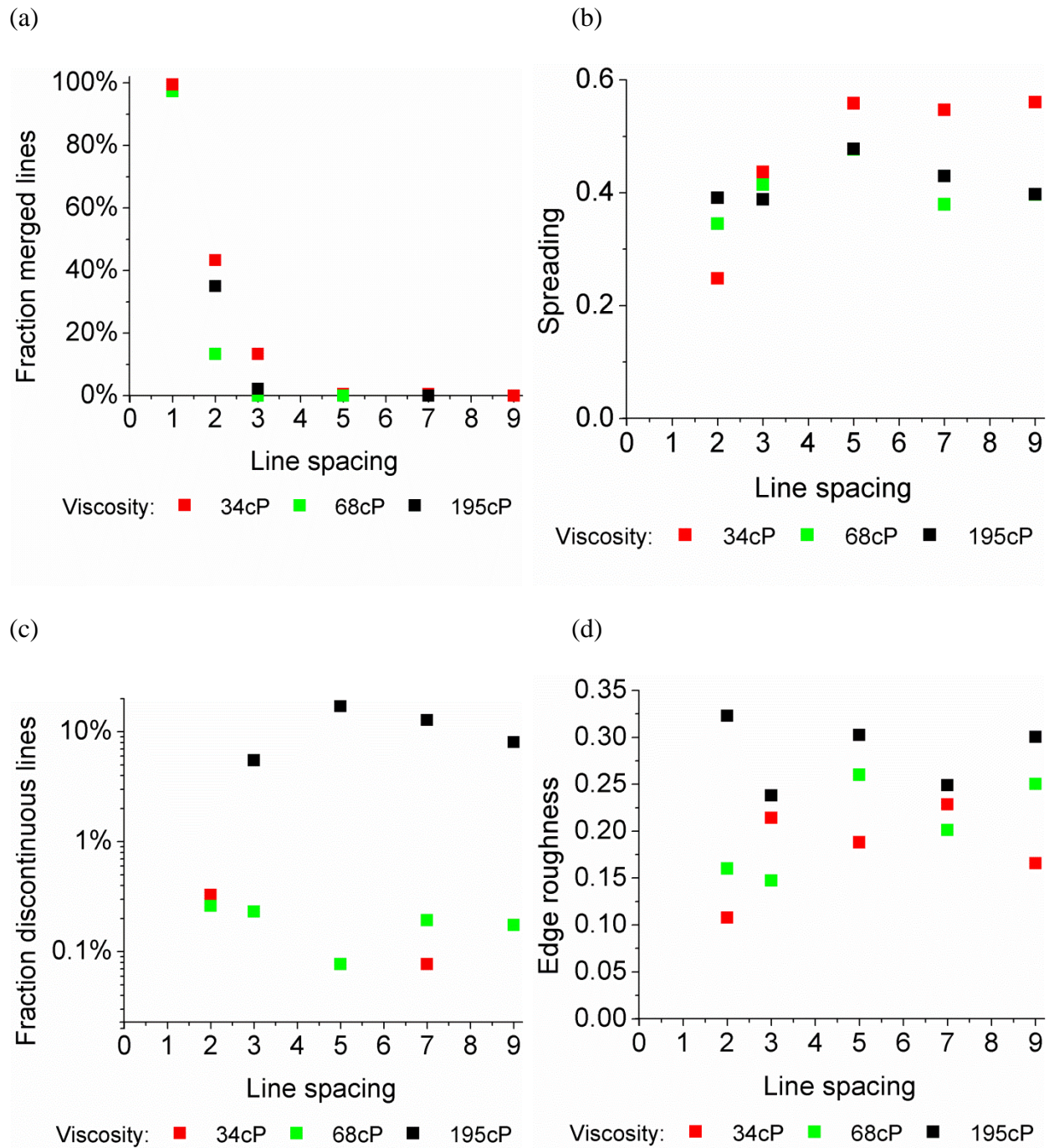


Figure 4-6. Effect of ink viscosity on printed pattern quality. (a) & (b) The lowest viscosity tested here (34cP) exhibits increased line spreading and subsequent merging of closely spaced lines. (c) & (d) The highest viscosity tested here (195cP) exhibits increased edge roughness and increased numbers of discontinuous lines. The optimum viscosity is thus 68cP. Line spacing, edge roughness and spreading were normalized by cell size.

The interaction between printing speed, cell gap, cell size and line spacing is complex. The main competing effects are drag-out, proximity effects and lubrication residue. Drag-out occurs due to ink wicking up the doctor blade. This is driven by surface tension forces and is inhibited by viscous forces. Drag-out therefore becomes more severe at smaller capillary numbers. Drag-out also becomes more severe for smaller cells because a larger fraction of the ink in the cell can be dragged-out by the doctor blade. The relationship between the proximity effect and the capillary number is non-monotonic and will be analyzed in detail in the next section. Lubrication residue becomes more severe at high printing speeds and viscosities. This film is due to ink that passes under the doctor blade. The fluid pressure in this gap between the doctor blade and the printing plate balances the loading force on the doctor blade. This pressure increases with viscosity and speed leading to thicker residue films. In theory, this residue is deposited uniformly across the printing plate; however, in practice residue is concentrated in areas of doctor blade defects due to wear. The impact of this on yield will be discussed further in the next chapter. These different effects control the amount of ink left in the cells after wiping. When trying to print ideal lines, one needs to have the ideal amount of ink per unit length. If the amount of ink per unit length is too large, lines will bulge, become non-uniform and ultimately merge with adjacent lines. If there is not enough ink, lines will become scalloped and ultimately break up. The amount of ink per unit length is not only governed by the amount of ink inside cells but also by the cell spacing within each line. If cells are spaced further apart, there is less ink per unit length and vice versa. Thus it is important to have the optimum amount of ink inside the cells combined with the right cell spacing. These considerations are similar to previous work on inkjet printed lines, although in a higher viscosity regime and with simultaneous printing of all droplets that make up a line.<sup>57</sup>

The goal of understanding these processes is to create design rules that can be used to make choices when designing gravure printed circuits. A principal challenge is that printing conditions such as speed and viscosity apply globally to all patterns printed at the same time. If a circuit contains a diverse set of patterns such as different line widths and separations, these different patterns might require different conditions for optimal printing. The designer has the freedom to change the cell spacing to tune the optimal conditions for a particular pattern and ameliorate conflicts but the scope of this is limited. Consider the case where a design includes a set of closely spaced  $4\mu\text{m}$  lines, such as bus lines packed tightly into a confined area, as well as isolated  $2\mu\text{m}$  lines, such as in a sparse grid. Representative printing results and extracted print quality metrics for these cases can be found in Figure 4-7 and Figure 4-8 respectively. The closely spaced  $4\mu\text{m}$  lines show optimum line edge roughness at low printing speeds, especially  $0.25\text{m/s}$ . At higher printing speeds drag-out becomes less pronounced leading to a larger amount of ink inside the cells. There is also more lubrication residue at higher printing speeds. This leads to excessive and uneven spreading of lines and can even result in lines merging together. Conversely, isolated  $2\mu\text{m}$  lines print best at high printing speeds of  $0.5\text{m/s}$  or  $1\text{m/s}$ . At lower printing speeds drag-out pulls too much ink out of these small cells. This leads to scalloped edges and even discontinuous lines. This is the case even though cell

spacing was already optimized for both cell sizes for the respective conditions. This simple example shows the difficulties when trying to print a diverse set of high-resolution patterns and will only get worse with more complex circuits. Since global printing conditions need to work for all patterns in a print, local patterns need to be adapted to make them compatible. Assist features exploiting proximity effects can be one method to achieve this.

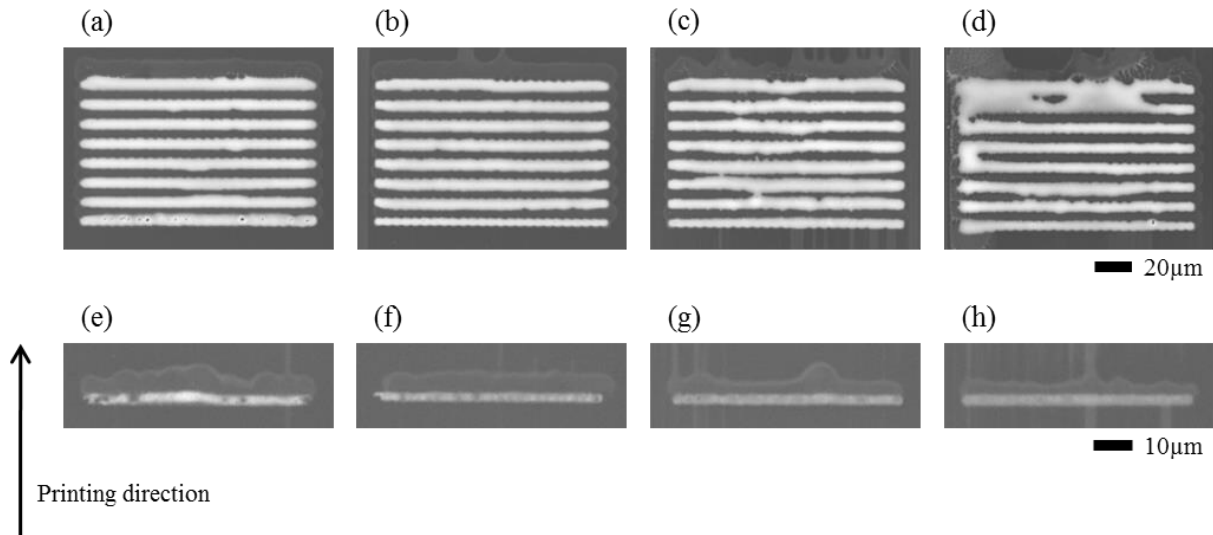


Figure 4-7. Optical micrographs of closely spaced lines with  $4\mu\text{m}$  cell size and  $8\mu\text{m}$  line spacing (first row (a)-(d)) and isolated lines with  $2\mu\text{m}$  cell size (second row (e)-(h)). In both rows, printing speed increases from left to right as  $0.125\text{m/s}$ ,  $0.25\text{m/s}$ ,  $0.5\text{m/s}$  and  $1.0\text{m/s}$ . These two cases exhibit opposite trends of print quality with printing speed. Closely spaced  $4\mu\text{m}$  lines exhibit better line definition with slower speed whereas isolated  $2\mu\text{m}$  lines need to be printed at higher speeds.

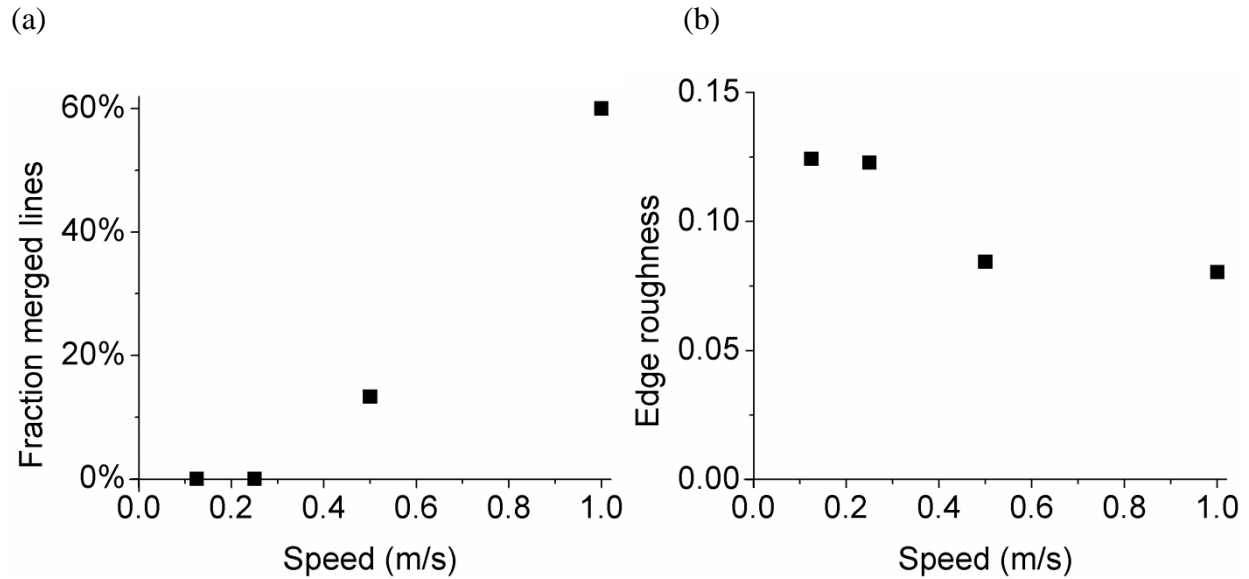


Figure 4-8. (a) Fraction of merged lines increases with increasing printing speed for lines with  $4\mu\text{m}$  cell size that are closely spaced  $8\mu\text{m}$  apart. (b) Edge roughness drops with increasing printing speed for isolated lines with  $2\mu\text{m}$  cell size. Edge roughness was normalized by cell size.

Optical lithography uses assist structures to print high-resolution features. This method exploits optical proximity effects. Sub-resolution features such as scattering bars are placed next to the feature to be printed. For isolated lines, this simulates the situation of densely spaced lines. Even though the assist feature does not print itself, its wave function can constructively interfere with the wave function of the actual feature and assist in its printing. Here, a similar method is proposed for gravure printing to exploit fluidic proximity effects. The real feature is placed behind the assist feature so that it is located inside the assist feature's drag-out tail. This will add ink to the real feature and make it printable. Here, assist features are employed that are of the same size as the real feature to be printed. The print quality of the assist feature is lower because it is not supported by the proximity effect but it will still be printed. In the future, more sophisticated assist features could be explored that don't transfer or only transfer minimally to the final substrate. This concept of fluidic assist features is demonstrated with the example of isolated high-resolution  $2\mu\text{m}$  lines oriented perpendicular to the printing direction. Such lines cannot be printed easily at low printing speeds around  $0.25\text{m/s}$ . Lines tend to break up due to excessive drag-out. With the extra ink from the assist feature, such lines can successfully be printed. The result can be observed in Figure 4-9.

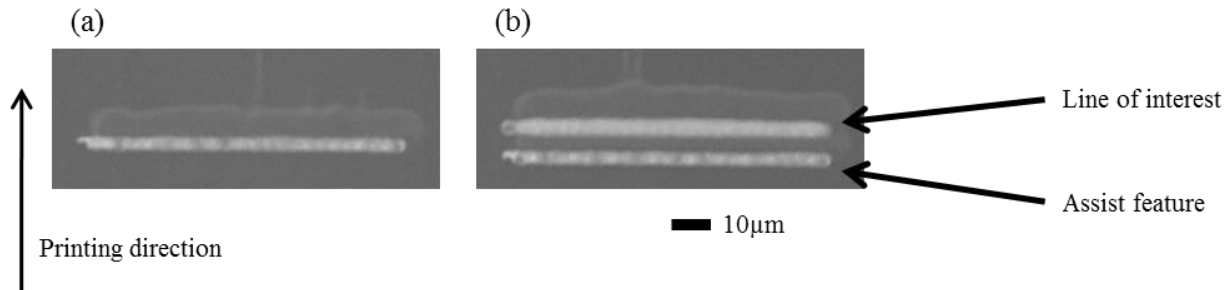


Figure 4-9. Optical micrographs showing improved print quality of line with  $2\mu\text{m}$  cell size printed at  $0.25\text{m/s}$  (b) with assist feature compared with (a) an isolated line. The isolated line shows intermittent holes due to drag-out that can lead to discontinuous lines. The line with a preceding assist feature exhibits no such holes due to the proximity effect. The assist feature behaves similarly to the isolated line.

## 4.4 Proximity effect fluid mechanics

### 4.4.1 Fluid analysis on printing plate

It is clear that the drag-out effect is a key enabler for the proximity effect in highly-scaled gravure. The proximity effect is only observed for lines that are connected to a preceding feature through a thin drag-out tail. However, it is not immediately clear how the drag-out effect creates the proximity effect. In order to understand this, the different sub-processes of the gravure process need to be decoupled. The final printed pattern represents a convolution of all these sub-processes including ink spreading on the substrate after ink transfer. In order to consider sub-processes individually, fluid flow needs to be analyzed on the roll or printing plate. It is very challenging to image such flows directly due to the high speed and small feature size as well as the difficulty of accessing cells during the transfer process where optical access is blocked by the substrate on its holder. However, great insights can be gained from measuring the states in between the different sub-processes. The ink volume left inside cells was measured after the transfer process as well as before transfer after doctor blade wiping. The ink was dried and sintered and cells were imaged using SEM to be able to resolve details within cells of size  $4\mu\text{m}$  and smaller. Figure 4-10 shows cells with ink before and after transfer. The images show good agreement between the fill levels estimated by imaging the cross-section of cells and by imaging cells top-down. Imaging top-down has several experimental advantages. Cross-sectional images require cleaving or dicing of the silicon wafer. This is not only a destructive and slow process if a number of different patterns are to be imaged but it is also difficult to accurately cleave all cells at the same position. Thus, top-down imaging was used to determine the fill level of cells and calculate the ink volume inside.

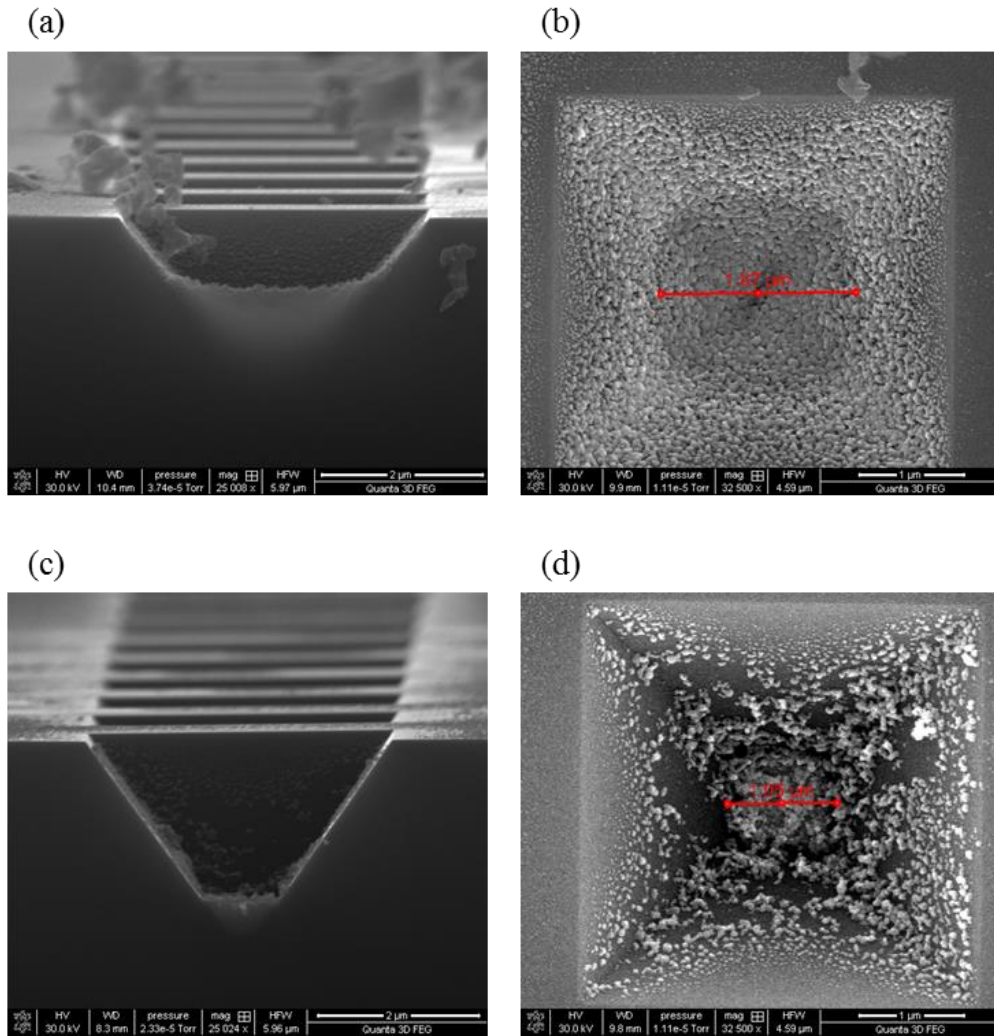


Figure 4-10. (a)+(b) cells before transfer to the substrate, (c)+(d) cells after ink transfer to the substrate with most ink removed by the transfer. In both cases, the cross-sectional views ((a)+(c)) show dense silver inside the pyramidal cell and good agreement with the fill level as estimated from the top-down view ((b)+(d)) thus allowing calculation of the ink volume from top-down images.

Since the ink is imaged after drying and sintering, one needs to back calculate the liquid ink volume from the dry silver volume. This was calibrated for each ink of different viscosity i.e. dilution. Ink was deposited onto a silicon wafer by spin coating and dried and sintered. The initial wet volume was determined by measuring the ink mass after spin coating and the ink density separately. The final dried volume was determined from the film thickness. Thus, the volume percentage of dried silver relative to the liquid ink volume can be calculated.

## 4.4.2 Ink transfer

As a first step, ink transfer from isolated lines without proximity effects was studied. Ink transfer is the most well studied gravure sub-process.<sup>69-81</sup> However, most reports have focused on transfer as an isolated process i.e. transfer of a liquid from a flat surface or a cell onto a flat substrate without taking into consideration how the initial state of the liquid on a roll or printing plate is achieved. In the full gravure process, the starting state for the transfer process is determined by the previous cell filling and doctor blade wiping processes. Since all three processes depend on capillary number, they cannot easily be altered independently. This is demonstrated here by using the ink volumes measured inside cells before and after transfer.

Figure 4-11 shows the transfer fraction as a function of capillary number. The transfer fraction is defined as

$$\varphi_{transfer} = \frac{V_{transfer}}{V_{wiping}} = \frac{V_{wiping} - V_{cell\ transfer}}{V_{wiping}} \quad \text{Eq. 4-1}$$

Where  $V_{wiping}$  is the ink volume left in the cell after doctor blade wiping,  $V_{transfer}$  is the ink volume transferred to the substrate and  $V_{cell\ transfer}$  is the ink volume left in the cell after transfer, which can be measured more easily than  $V_{transfer}$ . At low values of  $Ca$ , transfer is almost perfect with almost all the ink transferring from the cell to the substrate. This can be explained by the different wetting properties of the printing plate and the substrate.<sup>76</sup> The printing plate is a silicon wafer with very small contact angle hysteresis whereas the coating of the PEN plastic substrate has been optimized to increase pinning and contact angle hysteresis. This means the contact line is more prone to recede on the printing plate than on the substrate. If there is enough time for this to happen, all ink is removed from the cell and transfer is perfect. This is the case at low values of capillary number. At higher values of capillary number, there is not enough time for the contact line to move before the liquid bridge between the printing plate and the substrate breaks off. Thus, the transfer fraction should level off around 0.5 for high values of  $Ca$ . This is observed around  $Ca=1$ .

However; at values of  $Ca$  larger than 1, another regime is observed where transfer fraction increases with  $Ca$ . This can be understood in terms of the initial ink volume inside the cell before transfer. Transfer is facilitated by increased initial fill levels.<sup>71</sup> Figure 4-12 shows the fill fraction before transfer as a function of capillary number. Initially, fill fraction increases with  $Ca$  because of decreased drag-out. The dominance of drag-out in this regime can also be seen from the length of the drag-out tails (see Figure 4-13). Especially at very small values of  $Ca$ , drag-out becomes excessive. In this regime, the transfer fraction drops off for very small values of  $Ca$  because there is not enough ink inside the cell to be effectively picked out from the cell. Then, at intermediate values of  $Ca$ , fill fraction decreases slightly because of decreased cell filling. Finally, at high values

of Ca, fill fraction increases again with Ca due to increased lubrication residue.<sup>49</sup> This increase in fill fraction before transfer leads to an increased transfer fraction for large values of Ca.

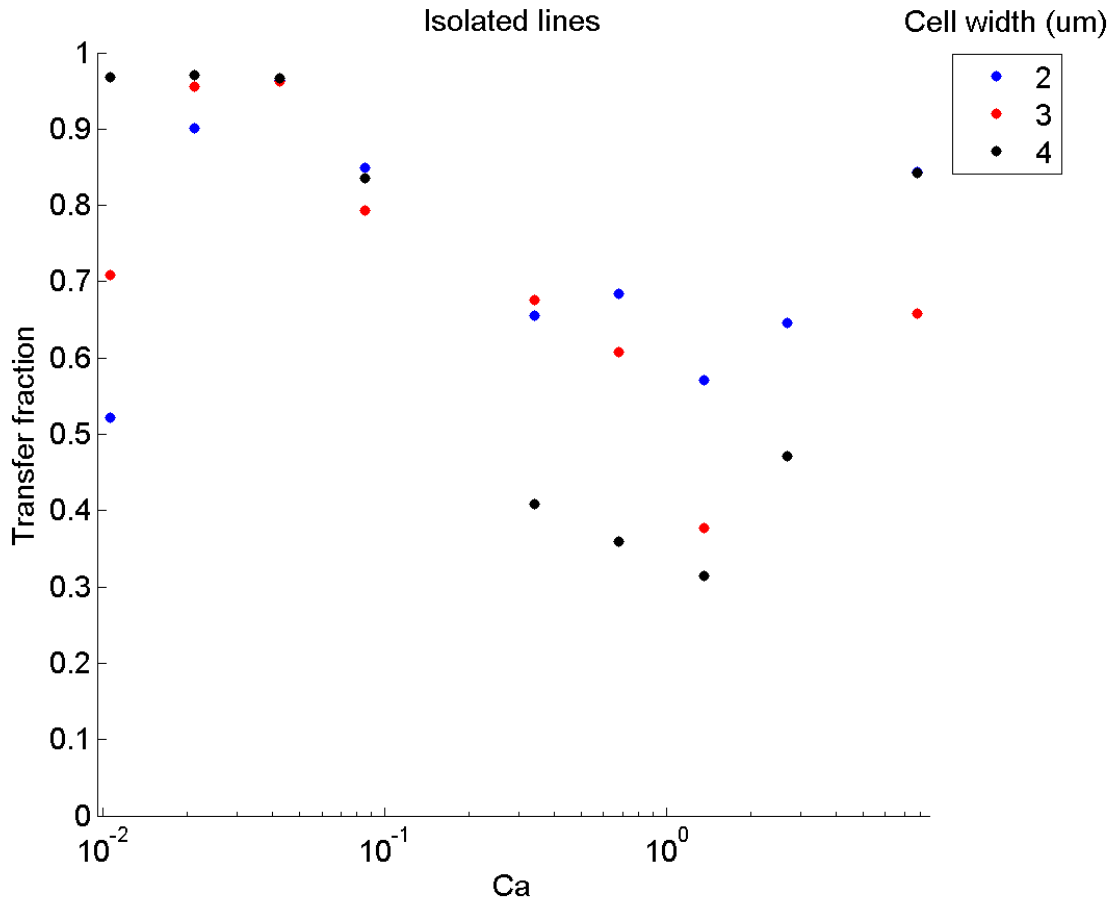


Figure 4-11. Transfer fraction for isolated lines with different cell sizes versus capillary number. At very low values of Ca, transfer fraction drops off. It then stays constant with Ca and almost perfect until it decreases at intermediate values of Ca. Transfer fraction increases again in the high Ca regime.

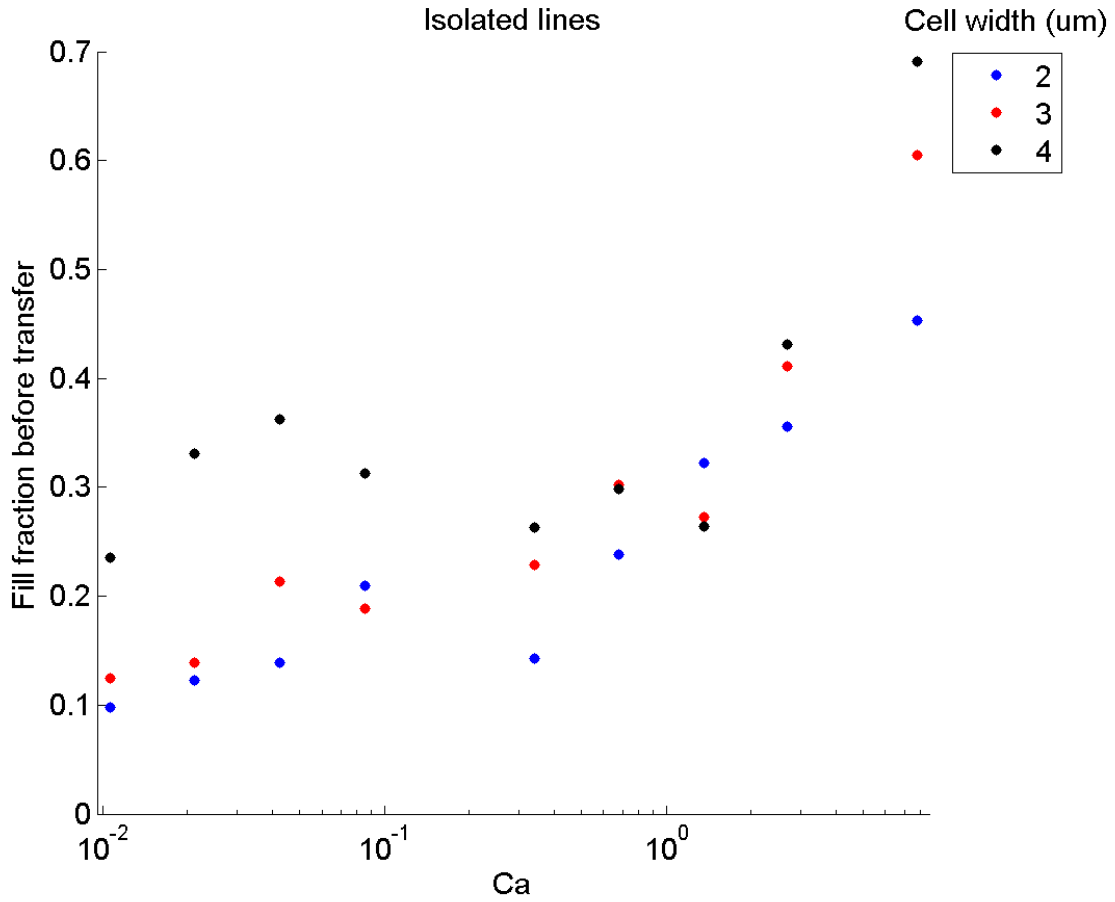


Figure 4-12. Ink volume inside cells before transfer normalized by cell volume. Initially, fill fraction increases with Ca, then it slightly decreases and it finally increases again for large values of Ca.

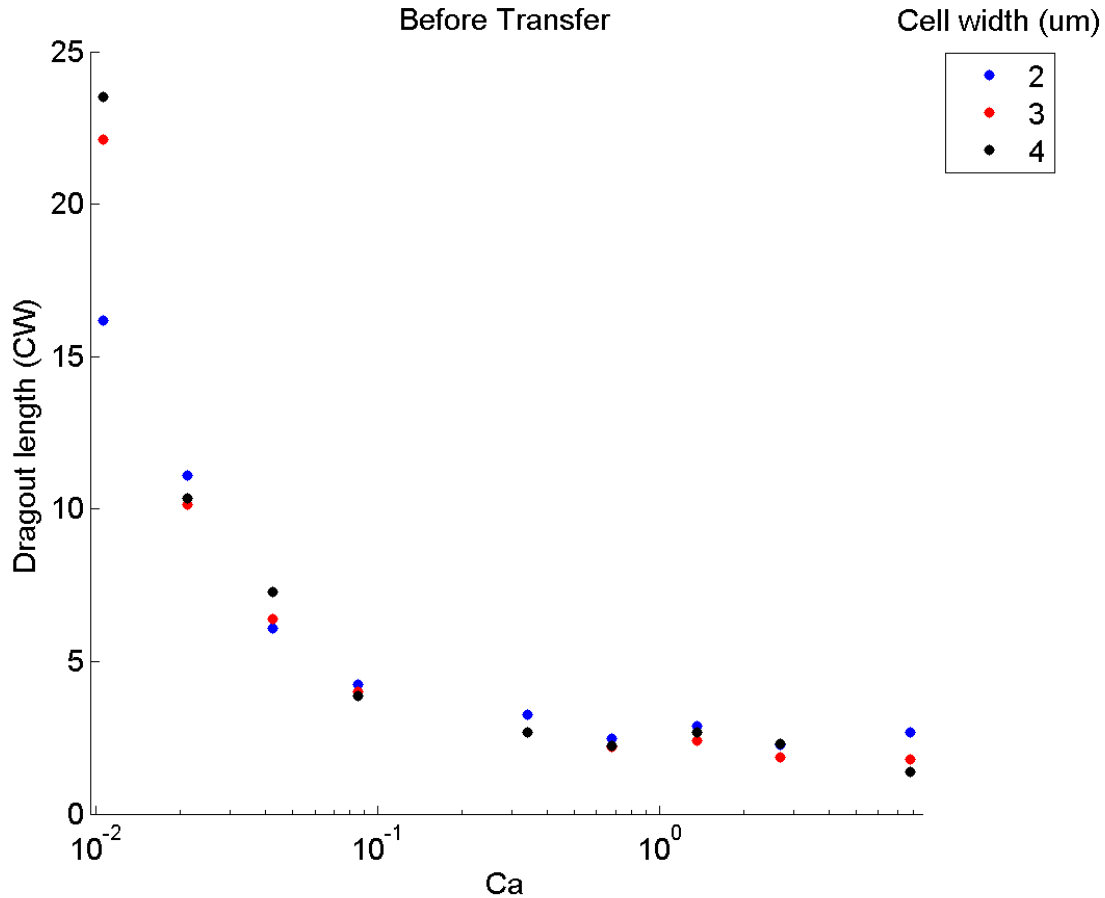


Figure 4-13. Drag-out tail length normalized by cell width. Tail length increases with decreasing Ca due to larger amounts of ink being removed from the cells.

### 4.4.3 Proximity effect analysis

#### 4.4.3.1 Experimental proximity effect

In the previous section, it was shown how the transfer process for isolated lines is affected by the other gravure sub-processes. In this section, proximity effects are analyzed for closely spaced lines and it is shown how this effect is also due to an interaction between the transfer effect and the drag-out effect. Figure 4-14 shows SEM images of lines of different spacing before and after transfer. Lines that are not connected by a drag-out tail do not exhibit any proximity effect as expected from the final printed results on the substrate (cf. Figure 4-3). Lines that are spaced close enough such that the drag-out tail from the first row reaches the second do exhibit a proximity effect. A simple hypothesis could be that ink is dragged-out from the first row and redeposited in the second row thereby adding ink to the second row. If this was true, the proximity effect should be clearly visible before transfer. This is not the case. Ink levels are comparable between the first and the second row. Ink levels in the second row are slightly elevated, especially when lines are

brought very close together (see Figure 4-15). However; after transfer, the difference in ink levels between row 1 and row 2 is far greater. This can be clearly seen in the SEM images as well as from the extracted numbers (see Figure 4-16). Thus, the proximity effect occurs during the transfer process if multiple cells behind each other are connected by a drag-out tail.

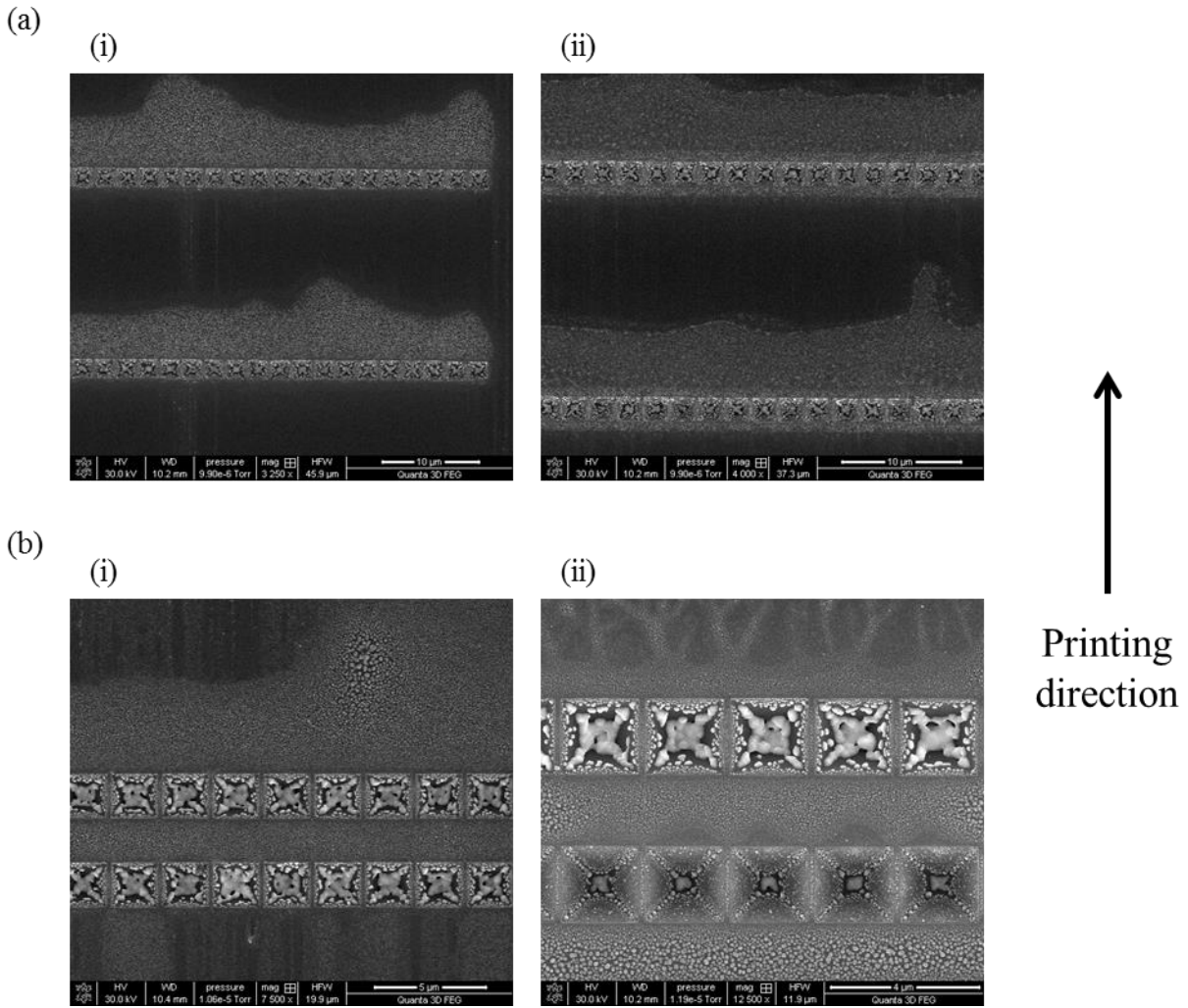


Figure 4-14. SEM images of lines on printing plate with ink (i) before and (ii) after transfer. (a) Lines that are spaced far enough apart such that they are not connected by the drag-out tail of the first row do not exhibit any proximity effect. (b) Lines that are spaced only a short distance apart, which is shorter than the drag-out tail length, exhibit a proximity effect after transfer (b ii). The second row contains much more ink than the first row. Before transfer (b i) both rows have similar ink levels.

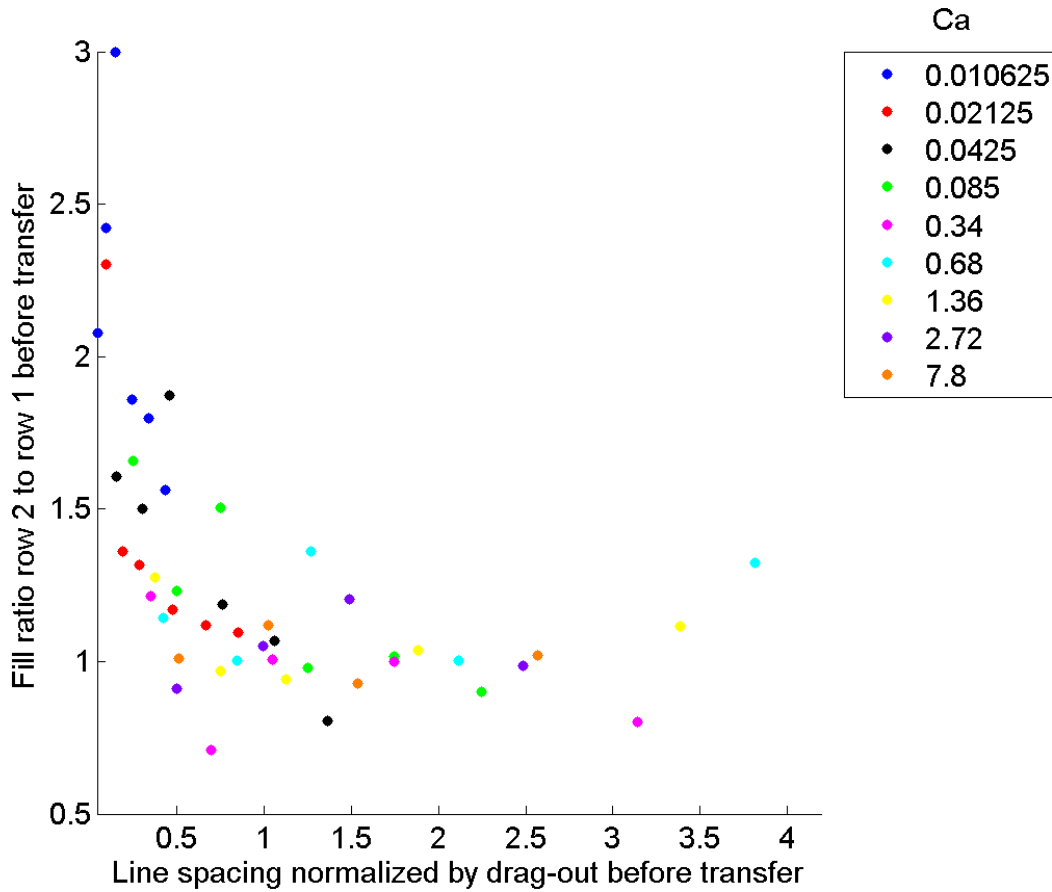


Figure 4-15. Ratio between ink volume in second row and ink volume in first row before transfer i.e. after doctor blade wiping and drag-out. As lines are brought close together, dragged-out ink from the first row is redeposited in the second row. Line spacing is normalized by the length of the drag-out tails before transfer to account for the fact that different capillary numbers exhibit different drag-out lengths.

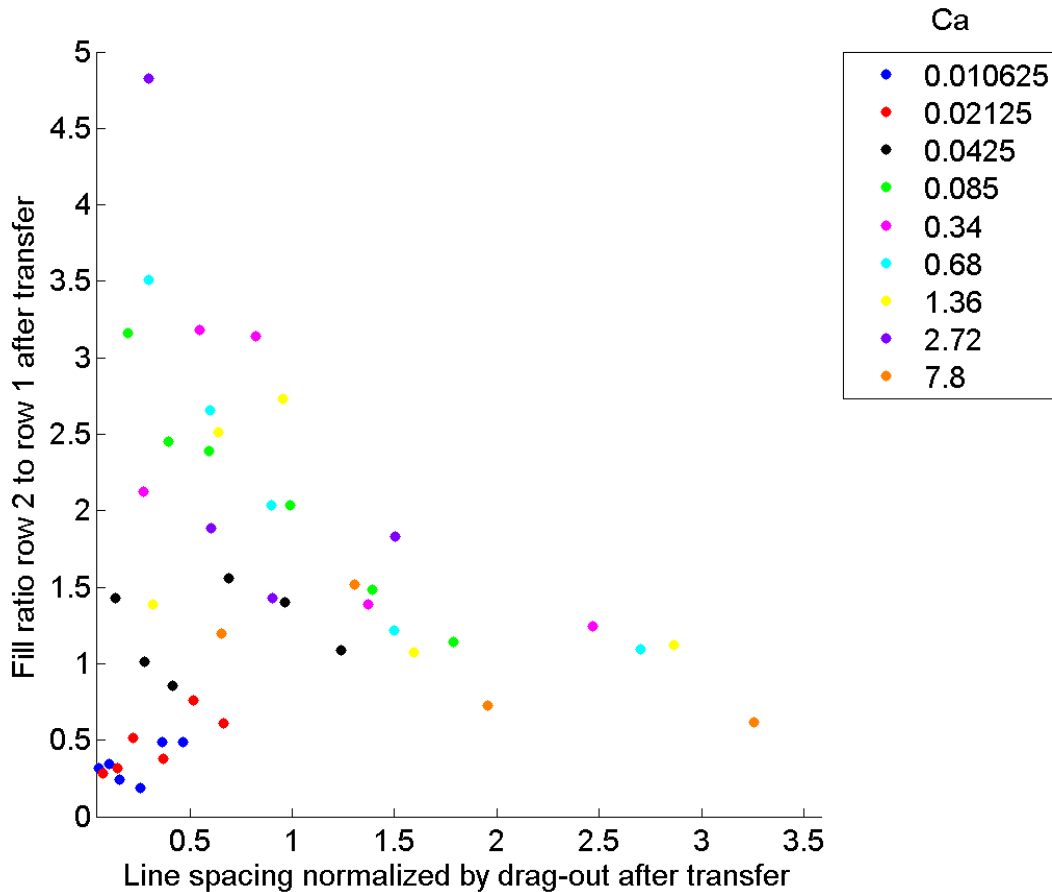


Figure 4-16. Ratio between ink volume in second row and ink volume in first row after transfer. Ink level in second row is significantly higher than first row when line spacing is smaller than the drag-out tail length. This is the case for intermediate values of capillary number. The proximity effect is weaker for high values of  $Ca$  and reversed for very low values of  $Ca$ . Line spacing is normalized by the length of the drag-out tails after transfer, which is slightly larger than tail length before transfer due to ink squeezing during transfer.

One set of potential hypotheses to explain this effect would rely on some form of directionality during the transfer processes, such as that the first row transfers first, that would drive ink from the first row to the second row. If this was the case, reversal of the transfer direction would result in a reversal of the proximity effect. This was tested experimentally by first wiping normally. The printer was stopped after wiping and the direction of motion was reversed for transfer. The results can be observed in Figure 4-17. The bottom row is again the first to be hit by the doctor blade during wiping. But during transfer, the top row now transfers first. This does not alter the outcome of the proximity effect. After transfer, the top row still contains more ink than the bottom row and the usual proximity effect is also observed on the plastic substrate. This means the proximity effect

is not due to any directionality during the transfer process but rather due to the directionality of the wiping process.

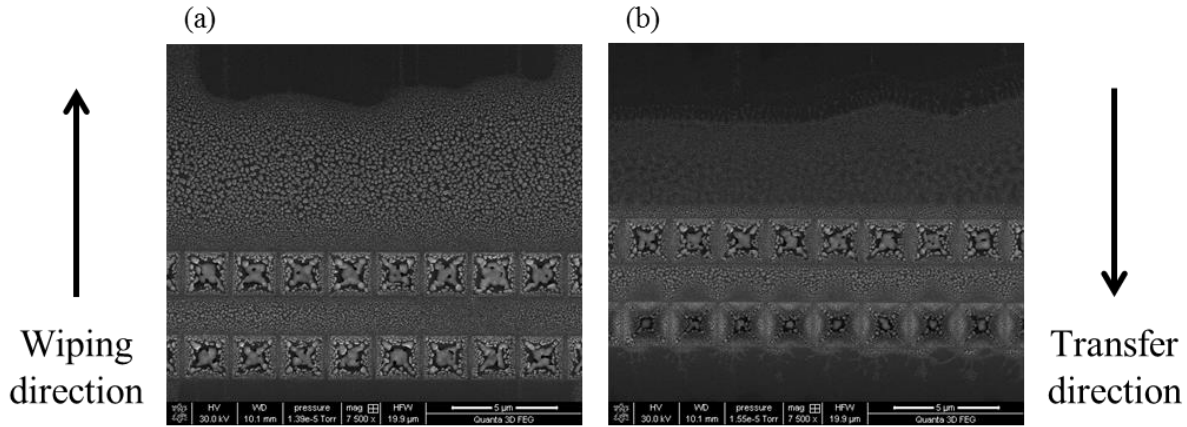


Figure 4-17. Experiment to rule out directionality of transfer as a cause for the proximity effect. (a) Cells after wiping in the familiar way from bottom to top do not show a proximity effect as before. (b) Cells after transfer with reversed direction from top to bottom still show the same directionality of the proximity effect as with the familiar transfer direction.

Further insight can be obtained from considering the proximity effect for different printing conditions. Figure 4-18 shows the relationship of the proximity effect (as measured by the ratio of the ink volume in the second row to the first row after transfer) to capillary number. Two different regimes can be observed. At small capillary numbers, the proximity effect becomes stronger with increasing capillary number. At large capillary numbers, the proximity effect becomes weaker with increasing capillary number. In order to understand this behavior, one needs to consider how the ink flows from the first row to the second.

#### 4.4.3.2 Modelling of proximity effect

As discussed above, features that exhibit the proximity effect have multiple lines connected by a drag-out tail. This means during transfer there is a continuous fluid film between the rows (see Figure 4-19 for an illustration). Without this, each row would have two menisci that empty it, one from its leading and one from its trailing edge. However, in this case, there are no menisci in between the rows because this area is completely filled with liquid. Thus, the first row is only emptied by a meniscus from its leading edge and the second row is emptied by a meniscus from its trailing edge. The difference between the two rows is that in the first row the meniscus starts

right at the cell whereas in the second row it starts at the end of the drag-out tail. In order to understand how this affects fluid flow, a simple 2D model was created.

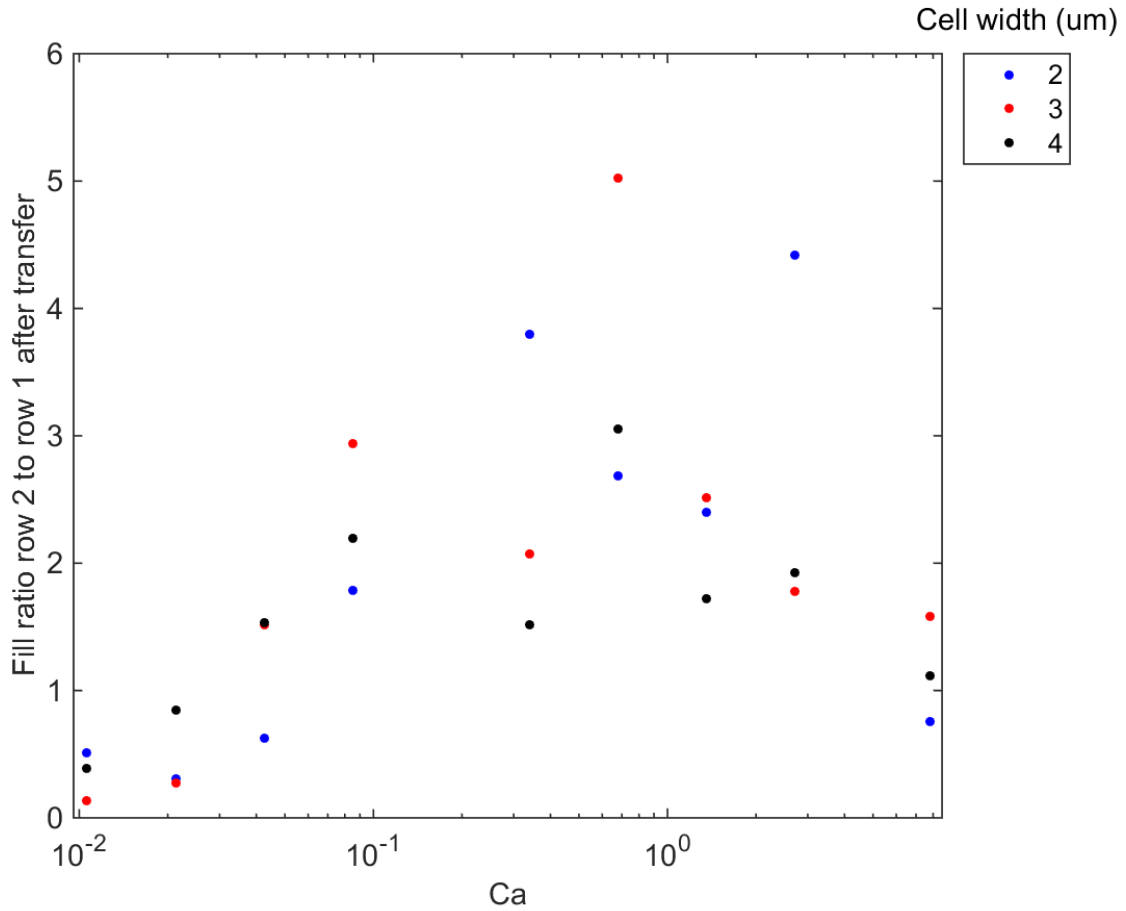


Figure 4-18. The proximity effect (ink volume ratio between row 2 and row 1 after transfer) shows two regimes with capillary number and a maximum at an intermediate value of Ca.

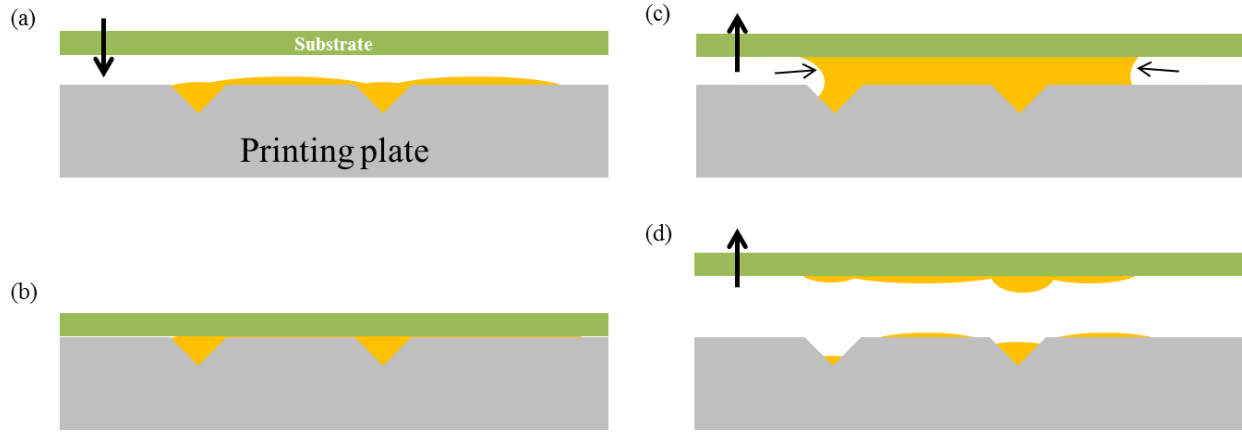


Figure 4-19. Cross-sectional schematic of transfer process with proximity effect. (a) Two rows are connected by drag-out tails. Substrate approaches printing plate. (b) Substrate is in contact with printing plate. (c) Substrate is removed from printing plate and both rows are emptied by menisci that move inwards. (d) After breakup of the liquid bridge, ink transfer is complete and more ink is left in the second row both on the substrate and the printing plate.

The flow in the channel that is formed in between the substrate and the printing plate during transfer is described here as a pressure driven Poiseuille flow. Solving the Navier-Stokes equation by approximating the situation as a thin channel between parallel plates gives the familiar result for flow rate along the channel per unit width into the page  $q_x$  as

$$q_x = -\frac{h^3}{12\mu} \frac{dp}{dx} \quad \text{Eq. 4-2}$$

Where  $h$  is the channel height at a particular position  $x$  along the channel,  $\mu$  is the fluid viscosity and  $p$  is the pressure, which is also a function of  $x$ . Here, flow not only occurs along the channel direction but also due to the substrate moving upwards away from the printing plate. For a small fluid element of width  $\delta x$ , this can be modelled as a vertical flow rate

$$q_z = v_z * \delta x \quad \text{Eq. 4-3}$$

Where  $v_z$  is the vertical velocity of the substrate. Balancing the vertical and horizontal flow components on a fluid element and conserving mass leads to the following differential equations

$$-\frac{dq_x}{dx} = v_z \quad \text{Eq. 4-4}$$

$$\frac{d}{dx} \left( h^3 \frac{dp}{dx} \right) = 12\mu v_z \quad \text{Eq. 4-5}$$

Integrating twice results in the following expression for the pressure  $p$

$$p(x) = 12\mu v_z \int_0^x \frac{x}{h^3} dx + h^3(0) \frac{dp}{dx}(0) \int_0^x \frac{1}{h^3} dx + p(0) \quad \text{Eq. 4-6}$$

The derivative of the pressure at  $x=0$  can be calculated using the pressures at the two menisci as boundary conditions giving

$$\frac{dp}{dx}(0) = \frac{1}{h^3(0) \int_0^L \frac{1}{h^3} dx} \left( p(L) - p(0) - 12\mu v_z \int_0^L \frac{x}{h^3} dx \right) \quad \text{Eq. 4-7}$$

The position of the first row's meniscus is defined as  $x=0$  and the position of the second row's meniscus is defined as  $x=L$ . The two meniscus pressures can be estimated by assuming a circular meniscus cross-section with radius of curvature  $h/2$  giving

$$p(0) = \frac{\gamma}{\frac{h(0)}{2}} \quad \text{Eq. 4-8}$$

And similarly for  $p(L)$ .  $\gamma$  is the ink surface tension. This set of equations allows the calculation of the pressure profile along the channel that is formed between the roll and the substrate.

Figure 4-20 shows the profile of two cells connected by a thin fluid film and with another thin drag-out film after the second cell. The pressure profile for this situation exhibits a parabolic shape in the regions with a thin uniform fluid film as expected (see Figure 4-21). The pressure drop across the cells is negligible compared with the pressure drop across the thin regions. Continuity dictates that the flow rate is a linear function of position due to the constant upward flow caused by the motion of the substrate (see Figure 4-22). However, the flow is not symmetric. There is a larger inward flow at the first cell compared with the end of the drag-out tail (with reversed direction). This is due to the fact that the meniscus at the first cell is immediately adjacent to a cell whereas the second meniscus is adjacent to a long thin region. The thick fluid film in the cell poses less resistance to fluid flow as can be seen from the negligible pressure drop across it. This is the reason for the proximity effect resulting in net fluid flow towards the second row. This imbalance in flow between the first and the second row can be described as the ratio between the two flows and this measure of the proximity effect can be analyzed to understand the experimental results.

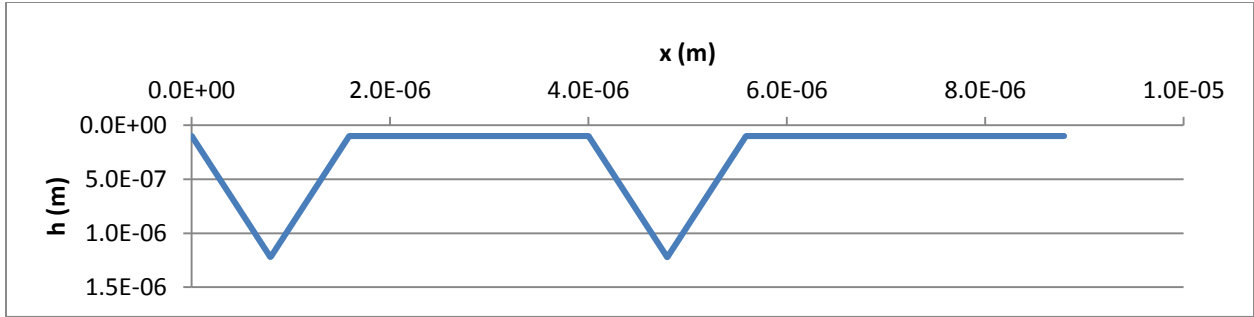


Figure 4-20. Cell profile with two cells connected by a thin fluid film and with a thin drag-out tail behind the second cell.

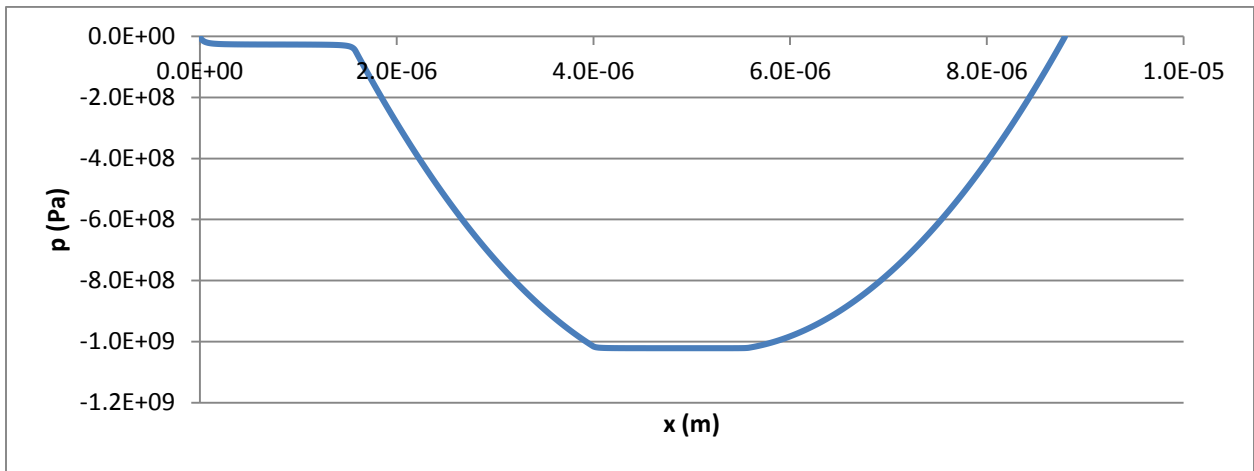


Figure 4-21. Pressure profile for two connected cells with a drag-out tail behind the second cell.

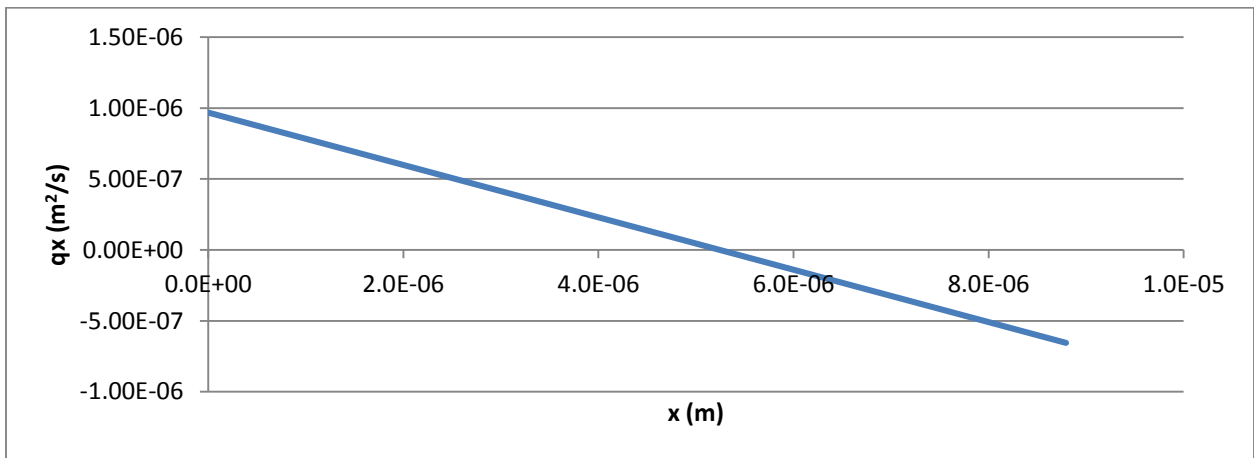


Figure 4-22. Horizontal flow rate exhibiting a linear variation with position due to the upward motion of the substrate.

Experimental results show a strong effect of capillary number on the proximity effect (cf. Figure 4-18). The obvious question is thus how print speed, ink viscosity and ink surface tension affect the flow that is responsible for the proximity effect during transfer. Whilst speed and viscosity certainly affect the flow, they do not affect the imbalance in flow between the two menisci. Both are equally affected by the product of speed and viscosity as can be seen in Eq. 4-6. Surface tension could in principle affect the two menisci differently if they exhibit different radii of curvature. However; for realistic values of surface tension well below 100mN/m, the meniscus pressure due to surface tension is very small compared with the pressure drop across the channel due to the flow. This can be observed in Figure 4-21 where the pressures at either end are negligible. Thus, the capillary number dependence of the proximity effect is not directly due to differences in speed, viscosity or surface tension. However, these variables affect the initial state i.e. the fluid geometry before transfer.

Conceivably, the thickness of the thin fluid regions between the cells and behind the second cell could affect flow. However, its effect on the proximity effect is weak and only becomes apparent as the film thickness becomes larger than 100nm and approaches 1 $\mu$ m (see Figure 4-23). The reason is that for thin films the pressure drop across cells remains negligible irrespective of the exact film thickness. The magnitude of the observed pressure changes but does so equally for both menisci and thus does not affect the proximity effect. For thicker films, the pressure drop across the thin regions drops and becomes comparable to the pressure drop across the cells. Thus, the effect of having a cell close to the first meniscus diminishes. However, such thick drag-out film thicknesses are typically not observed experimentally and so the effect of gap height can be ignored.

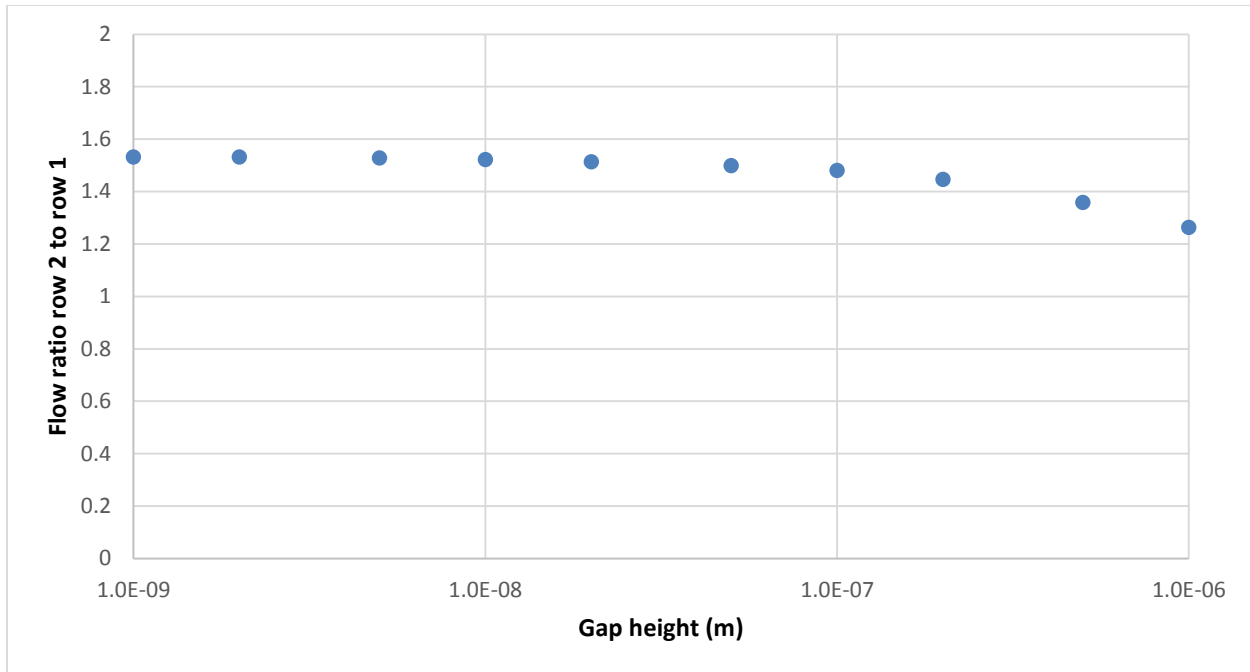


Figure 4-23. The proximity effect does not depend on the gap height between the substrate and the roll in the land areas i.e. in between lines and in the drag-out tail as long as it remains thin compared with the cell size (here  $2\mu\text{m}$  cell width).

The drag-out tail length is another geometrical variable that is determined by the drag-out process and varies with capillary number. Figure 4-24 shows that the strength of the proximity effect does depend on drag-out tail length. The proximity effect is strongest for relatively short drag-out tails of similar length as the cell width. The proximity effect is reduced dramatically for very short tails as this situation approaches the symmetric case without any drag-out tail behind the second row. The proximity effect drops off more slowly for longer tails. In this case, the flow becomes dominated by the long thin fluid region behind the second cell and the effect of the cells diminishes in comparison. In principle, this peak in the strength of the proximity effect with tail length could explain the experimentally observed peak with capillary number. The drop in proximity effect with increasing tail length can contribute to the drop with decreasing capillary number. However, in the present set of experiments even the highest capillary number resulted in drag-out tails whose length was at least 1.5 times the cell width and thus too long to observe a drop in proximity effect due to short tails (cf. Figure 4-13).

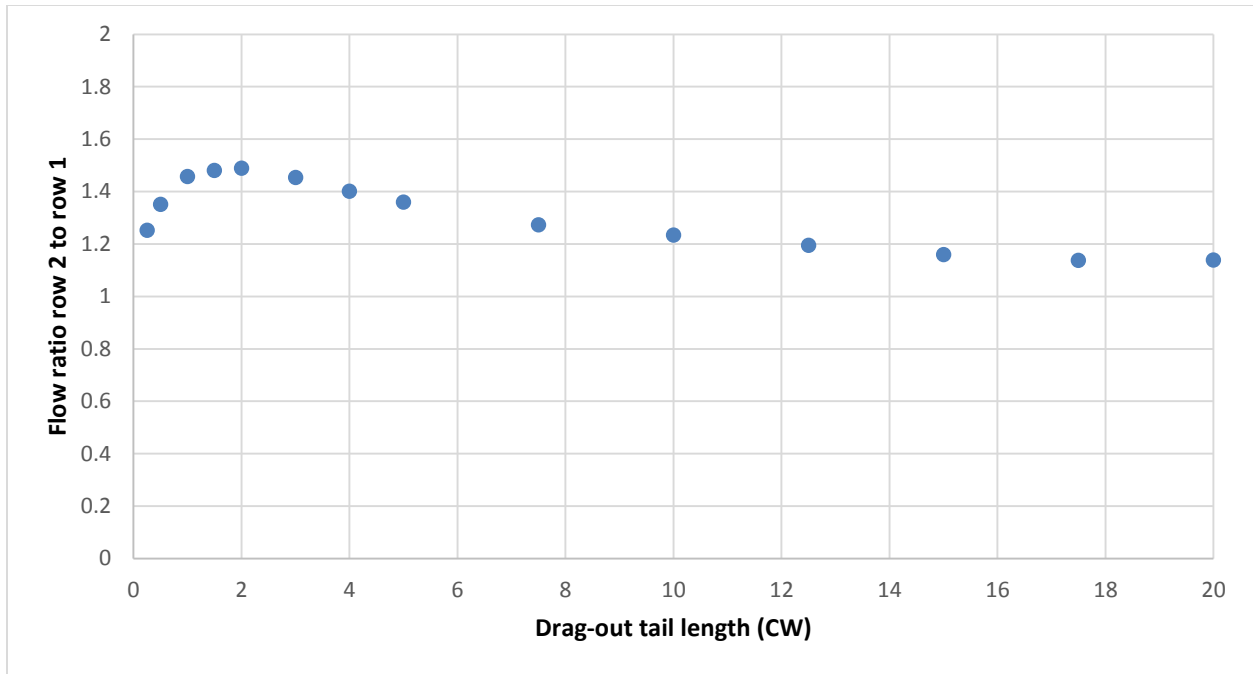


Figure 4-24. The proximity effect shows a peak with drag-out tail length dropping off fast at very small tail lengths and more slowly for tails longer than 1.5 times the cell width. Tail length normalized by cell width.

Capillary number also strongly affects ink volume inside cells before transfer. Assuming that the flexible plastic substrate on a soft rubber backing is deformed enough to conform to the lower ink level inside cells, the channel for fluid flow will be restricted if cells are not fully filled. Both the width of the filled part of the cells as well as the height of the fluid film will be reduced. This reduces the effect that the cells have on the fluid flow and will thus also reduce the proximity effect (see Figure 4-25). This effect is another contributing factor that explains why the proximity effect drops off at low capillary numbers where the initial ink volume inside cells is reduced (cf. Figure 4-12). Again, it cannot explain the experimentally found behavior at large values of  $Ca$ .

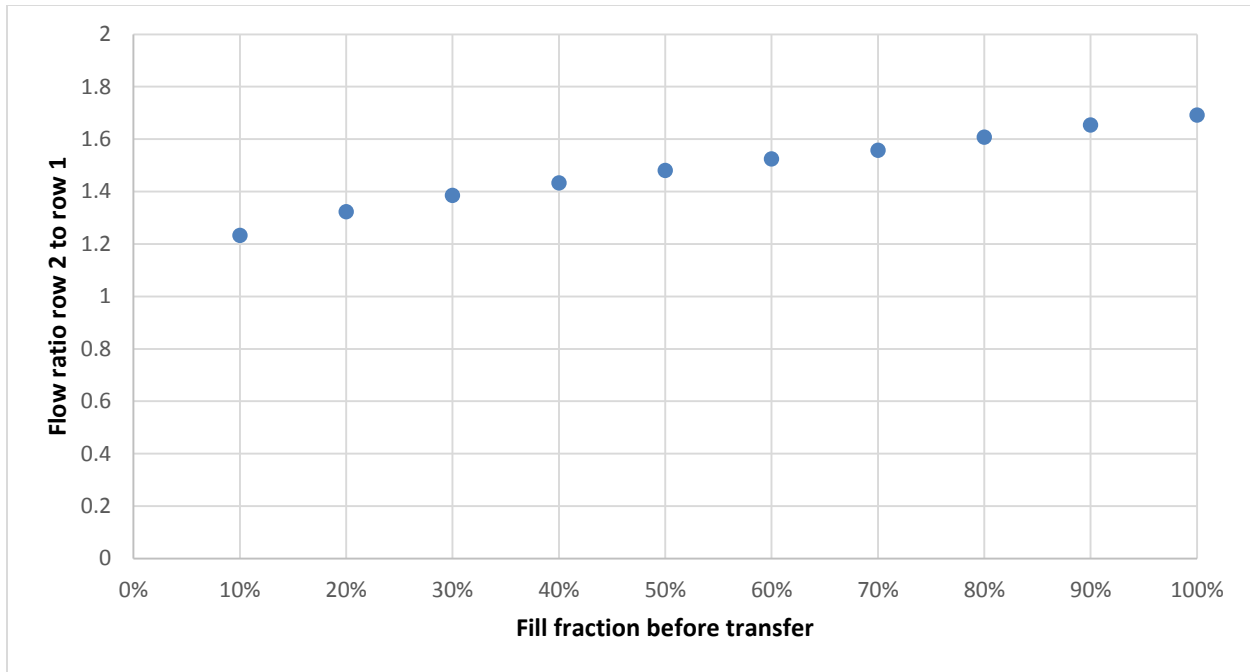


Figure 4-25. The proximity effect increases with ink volume inside cells before transfer. Both cells have equal fill levels here.

In the above figures, one variable was varied at a time to gain understanding of the underlying mechanisms. They were put together by taking the experimentally measured conditions before transfer and putting them into the model. Figure 4-26 shows the expected trend of increasing proximity effect with increasing capillary number. This describes the experimental trend for small capillary numbers. For large capillary numbers, one needs to consider 3D effects that are not captured by this 2D model.

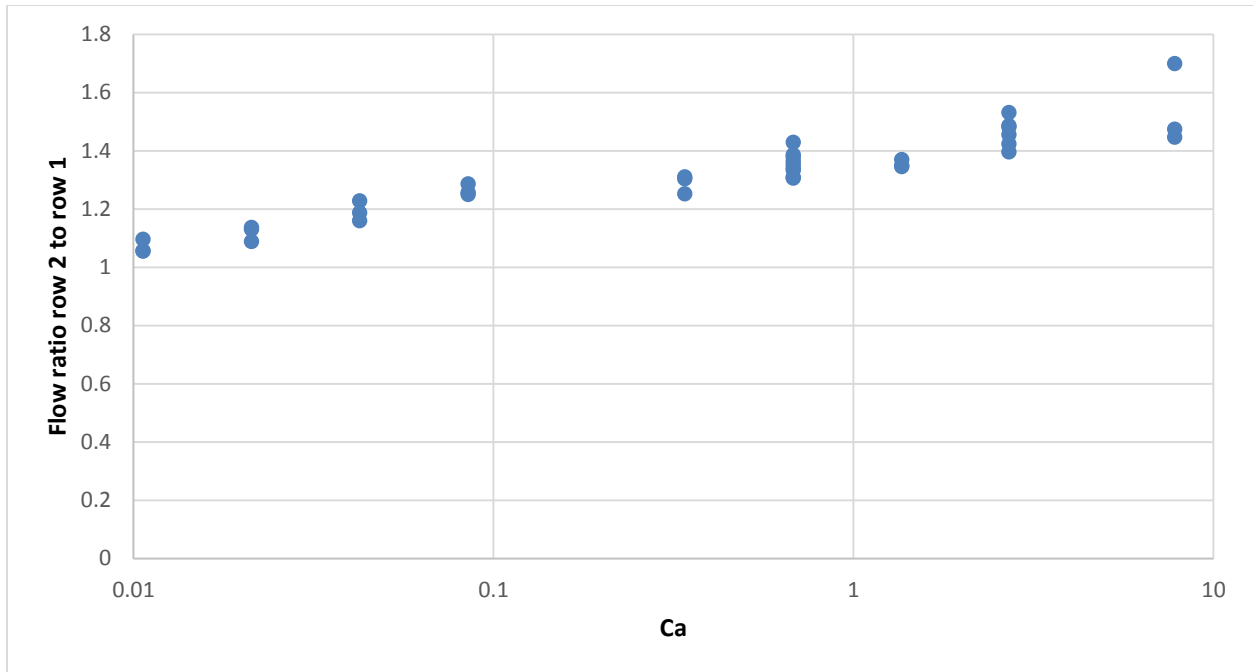


Figure 4-26. Flow model applied to experimental data of ink geometry before transfer. Proximity effect increases with increasing capillary number as found experimentally for small values of Ca but fails to capture the opposite trend for large values of Ca.

There are two main shortcomings of this 2D model. Firstly, it does not describe the experimentally observed behavior at high values of Ca. Secondly, it does not allow the formation of two distinct lines on the substrate since there are only two menisci, one at either end, but none in between lines that are needed to create distinct lines as observed experimentally. In order to explain these two phenomena, one needs to consider 3D effects. A full 3D model is beyond the scope of this work but qualitative understanding can answer the above questions. A top down view of the situation reveals that the leading edge of the first row and the trailing edge of the drag-out tail are not the only locations where an air-ink meniscus exists. As the substrate is being separated from the roll, air will also enter from the sides in between lines and through the gaps in between cells (see Figure 4-27). These menisci will enter the area in between the lines thus cutting off the flow that causes the proximity effect and creating a separation between lines that leads to distinct lines on the substrate.

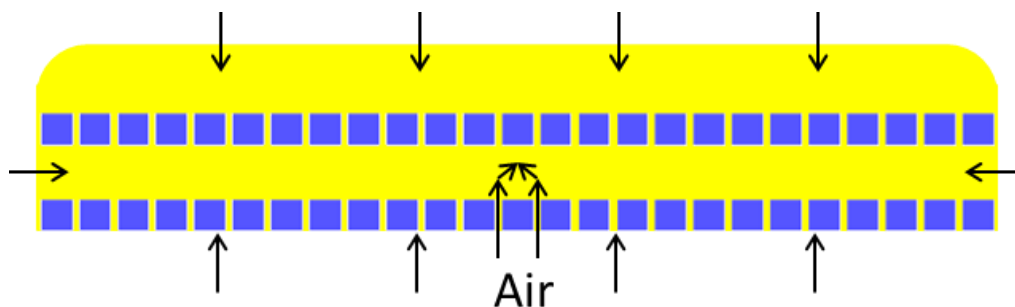


Figure 4-27. Top down view of ink transfer. Air enters the fluid (yellow) that is sandwiched between the roll and the substrate not only through cells (blue) and the drag-out tail but also from the sides in between rows and through the gaps in between cells.

In order to do so, these menisci need to move faster than the meniscus that empties the cells in the first row. This can occur because of the Saffman-Taylor instability leading to viscous fingering.<sup>125,126</sup> The Saffman-Taylor instability occurs at interfaces where a low viscosity fluid (here: air) penetrates a thin, confined film of a high viscosity fluid (here: ink). Any small disturbances in the interface grow due to the difference in pressure gradient in the ink between the tip and the base of air fingers penetrating the ink. The larger pressure gradient at the tip of the fingers accelerates the growth of fingers ultimately leading to a small number of long air fingers penetrating the ink. This phenomenon has been observed in gravure printing as well as other roll based transfer processes.<sup>127-130</sup> The growth of these fingers is greatly enhanced for thinner fluid films. This allows the meniscus to grow faster in the regions with a thin fluid film outside of the cells, to overtake the menisci inside cells and to cut them off in between rows. If this hypothesis is to be true, one would expect the size of the gaps between cells as well as position relative to the end of the lines to be important factors. Positions closer to the end of the lines will experience air coming in from the sides first and thus the proximity effect flow will be cut off sooner. Similarly, wider cell gaps will result in enhanced influx of air that cuts off the proximity effect sooner. Both effects are observed experimentally. Both wider cell gaps and a position closer to the end of the lines result in a diminished proximity effect (see Figure 4-28 and Figure 4-29). The Saffman-Taylor instability also explains the observed effect of capillary number for large values of  $Ca$ . Large values of  $Ca$  lead to thinner air fingers penetrating the viscous ink and thus faster advancement of the meniscus due to continuity.<sup>126</sup> Figure 4-30 shows how more ink is removed from the area in between lines as capillary number increases. Thus, the proximity effect flow is cut off faster for larger values of  $Ca$  giving the observed experimental trend.

In conclusion, the proximity effect can be explained by the difference in resistance to flow at the leading and the trailing edge of the pattern. The cells close to the meniscus at the leading edge exhibit a smaller resistance to flow than the thin drag-out tail at the trailing edge. At small capillary

numbers, the proximity effect is limited by long drag-out tails dominating the flow and by reduced ink amounts inside cells not exhibiting low resistance to flow. At large capillary numbers, the proximity effect is limited by viscous fingering through the cell gaps that cuts off the proximity effect flow in between lines.

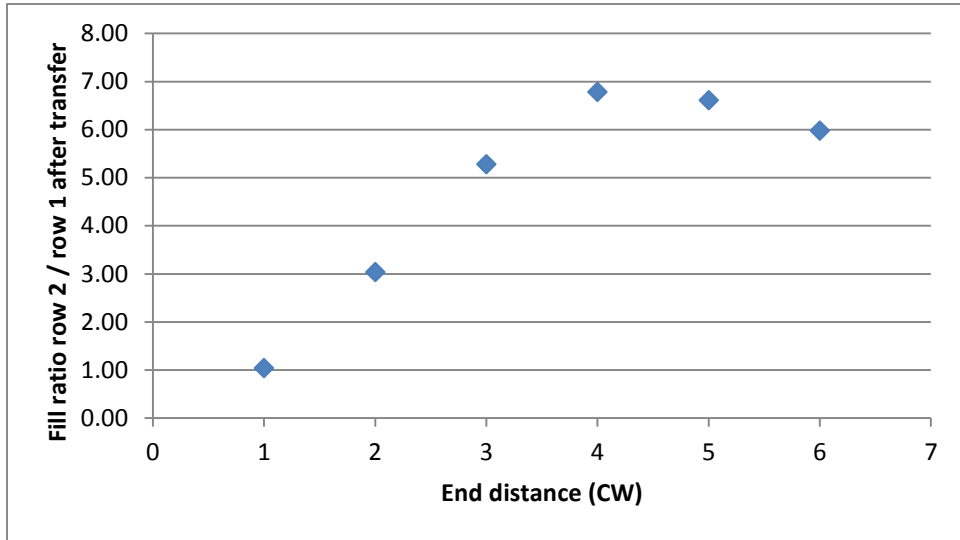


Figure 4-28. The proximity effect diminishes close to the end of the lines because this flow is cut off by air entering from the sides. Distance from end normalized by cell width.

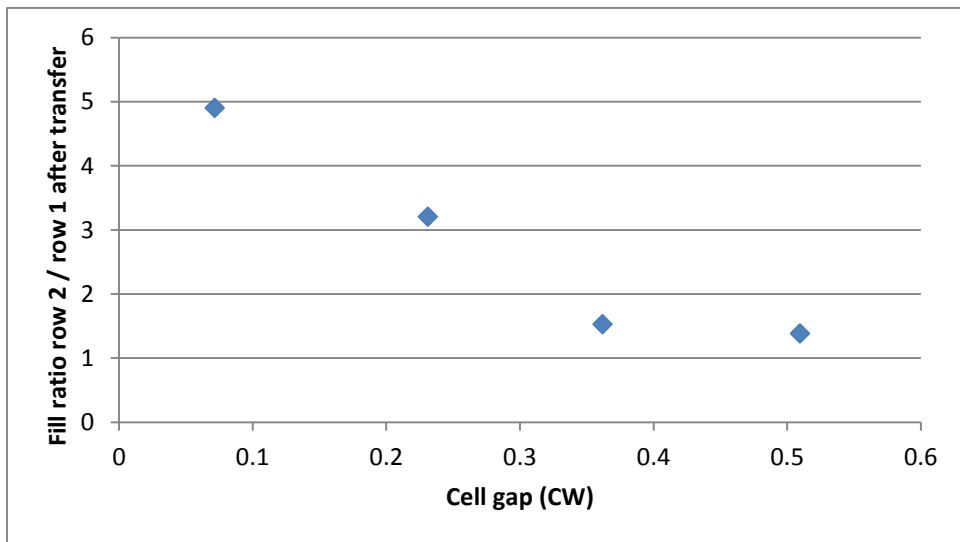


Figure 4-29. The proximity effect diminishes for large gaps between cells because air can easily enter region between lines cutting off proximity effect flow. Cell gap normalized by cell width.

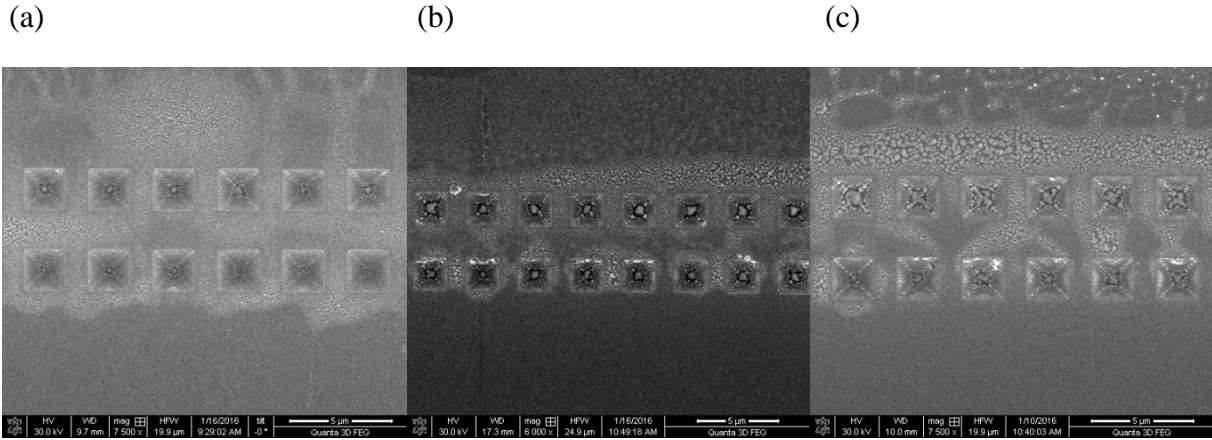


Figure 4-30. More ink is removed from the central area in between lines as capillary number increases due to the increased effect of the Saffman-Taylor instability (a)  $Ca=0.085$ , (b)  $Ca=0.34$ , (c)  $Ca=0.68$ .

## 4.5 Conclusions

Proximity effects in high-resolution gravure printing were studied here for the first time. Proximity effects in gravure printing are due to the drag-out effect that creates tails of ink behind features. Lines oriented perpendicular to the printing direction were studied to demonstrate the implications of these proximity effects. Lines perpendicular to the print direction are significantly more challenging to print than lines aligned with the print direction. Patterns were analyzed automatically to determine optimal printing conditions for such challenging features. It was demonstrated that proximity effects can be exploited by using assist features to print features that otherwise could not be printed reliably. It was shown that proximity effects are due to an interaction between the drag-out and the transfer process. The flow during transfer that is responsible for the proximity effect was analyzed in detail and modelled with a simple 2D model. To fully understand the flow, 3D effects need to be taken into account as well.

This chapter as well as the previous chapter have focused on printing single layers of highly-scaled features both from a tooling and a pattern generation perspective. Such highly-scaled features can form the basis for many different functional systems and devices. One important example is printed transistors that greatly benefit from highly-scaled source and drain electrode widths and channel lengths. Thus, the next chapter will focus on integrating such highly-scaled gravure printed features into a multi-layer transistor structure that is fully printed at a high print speed.

## Chapter 5: Printed organic thin-film transistors

### 5.1 Introduction

Many printed electronic systems require printed organic thin-film transistors (OTFTs) for tasks such as signal amplification, pixel selection in an active matrix or simple logic. In order to fully enable such applications, printed transistors need to fulfill a number of requirements. These OTFTs need to deliver relatively high performance; performance can be improved by exploiting innovations in both materials and printing resolution. Furthermore, the supply voltage will likely be limited. In many such systems, power will be supplied by a printed battery or a printed solar cell, placing constraints on available voltage. Additionally, in order to fully benefit from the promise of high-throughput, low-cost fabrication, all transistor layers need to be printed at high printing speeds. Finally, device-to-device variation needs to be small to realize any realistic circuit.

In the past, many reports have demonstrated tremendous progress in one or more of these areas. Many reports have shown that novel organic semiconductor materials can boost performance.<sup>131-133</sup> In addition, innovation in processing methods can further improve performance. Directional crystallization techniques have been shown to significantly enhance the performance of inorganic semiconductors. Amorphous silicon can be crystallized into polysilicon by selective laser heating.<sup>134-138</sup> The crystallization mechanism involves melting and crystallization on solidification. By scanning the laser heat source, very large grains can be grown. This mechanism cannot be applied directly to solution processed semiconductors where the crystallization mechanism relies on the solvent being driven out of the film. This cannot be done repeatedly unlike melting and solidification of silicon, although there have been some reports for thick organic semiconductor films.<sup>139,140</sup> Multiple techniques have been reported to achieve directional crystallization of solution processed organic semiconductors. However, many of these techniques such as off-center spin coating<sup>85</sup> and crystallization on a tilted substrate<sup>141</sup> are incompatible with roll-to-roll fabrication and have not been shown to work well in realistic flexible substrates. Others, such as solution shearing<sup>142,143</sup> and zone casting<sup>144-149</sup> have shown great promise to leverage directional crystallization for improved electrical performance. However, most reports on solution sheared or zone cast films operate at very low speeds on the order of tens of micrometers per second. Here, a method is demonstrated that operates at 1mm/second, which still requires further improvement, but is orders of magnitude faster than previous reports. A stationary thermal gradient has been used before to enhance the performance of solution processed TIPS-pentacene transistors.<sup>150</sup> This work demonstrates the benefit of thermal gradients for the crystallization of solution processed organic semiconductors; however, does not allow sufficient control due to inherent temperature variations across the sample. Here, a thermal gradient is scanned relative to a plastic substrate thus inducing directional crystallization of an organic semiconductor. Since the

scanning process inherently exploits the relative motion of the substrate, it is very compatible with roll-to-roll processing.<sup>26</sup>

In addition to the work described above to improve the semiconductor, it has also been shown that thin gate dielectrics can be used to reduce the operating voltage significantly.<sup>151–153</sup> However, much of this work was performed with idealized systems that are not compatible with high volume printing, for example using silicon substrates, evaporated contacts or spin coating. In addition, crystallized semiconductors typically exhibit variability due to the random placement of grain boundaries. There has been work to improve uniformity and produce fully solution-processed<sup>19</sup> or printed devices.<sup>154</sup> However, these works did not employ high-speed printing techniques that can run at speeds on the order of meters per second and the feature size was limited to tens of micrometers. Recently, transistors have been fabricated with highly-scaled feature sizes below 5 $\mu\text{m}$  that have been printed using reverse offset<sup>25</sup> and gravure printing<sup>23</sup>; however, some of the layers were still fabricated with lower speed techniques. In the second part of this chapter, printed OTFTs are demonstrated where every layer is printed by gravure with a high print speed of 1m/s including highly-scaled source and drain lines with feature sizes on the order of 5 $\mu\text{m}$ . By scaling the gate dielectric, the operating voltage is reduced to less than 5V. An amorphous polymer semiconductor is used to reduce variability in comparison with polycrystalline small-molecule semiconductors. Thus, for the first time, highly-scaled state-of-the-art high performance organic transistors are realized delivering good performance, low-voltage operation, all realized using a fabrication process based on high-speed gravure printing of all layers.<sup>28</sup>

In the first part of this chapter, transistor performance is significantly improved by scanning a heater relative to the plastic substrate during the crystallization of an organic semiconductor. Since this method depends on the reliable translation of a thermal gradient, the heat distribution inside the substrate is modelled. Then, the impact of the method on grain size and device performance is demonstrated experimentally. The crystallization is understood in terms of different scanning directions and device geometries. In the second part of this chapter, fully high-speed gravure printed transistors are demonstrated. The fabrication process of every layer is analyzed in detail. Devices are characterized in terms of DC and AC performance and in terms of device stability.

## **5.2 A novel scanned thermal annealing technique to optimize organic semiconductor crystallization**

Here, a novel technique is demonstrated, which utilizes a scanned thermal gradient to induce the directional crystallization of a solution processed organic semiconductor. A plastic substrate is translated relative to a heated metal bar that is in contact with the bottom side of the plastic

substrate (see Figure 5-1 for an illustration of the technique). The top side contains devices with the solution deposited semiconductor. A thermal gradient is induced within the plastic substrate at the edge of the heated bar. This leads to a gradient in solvent evaporation rate and thus a gradient in the crystallization driving force. This gradient is scanned across the substrate as the heated bar is translated. The effect of this technique on crystallization is illustrated in Figure 5-2. To understand this, it behooves us to first summarize the kinetics of crystallization. Crystallization is typically described by two phenomena, nucleation and grain growth. Nucleation describes the process by which initial crystallites are formed, while grain growth describes the process by which these crystallites enlarge. Typically, the activation energy for nucleation exceeds that of grain growth; as a consequence, once grains nucleate, they typically grow to fill the available space between nuclei. As a consequence, grain size is typically limited by the density of initial nuclei. Uniform heating as conventionally used leads to the uniform nucleation of grains, which will then grow essentially isotropically. The final grain size is thus determined by the initial nucleation density. By using a scanned heating source, a gradient in crystallization driving force can be introduced using this novel technique, enhancing grain growth in preferred orientations relatively to nucleation. After some initial nucleation, grains can grow freely without impinging on further grains since no grains have nucleated ahead of the gradient yet. This will lead to significantly enlarged grains that are elongated and aligned with the scanning direction.

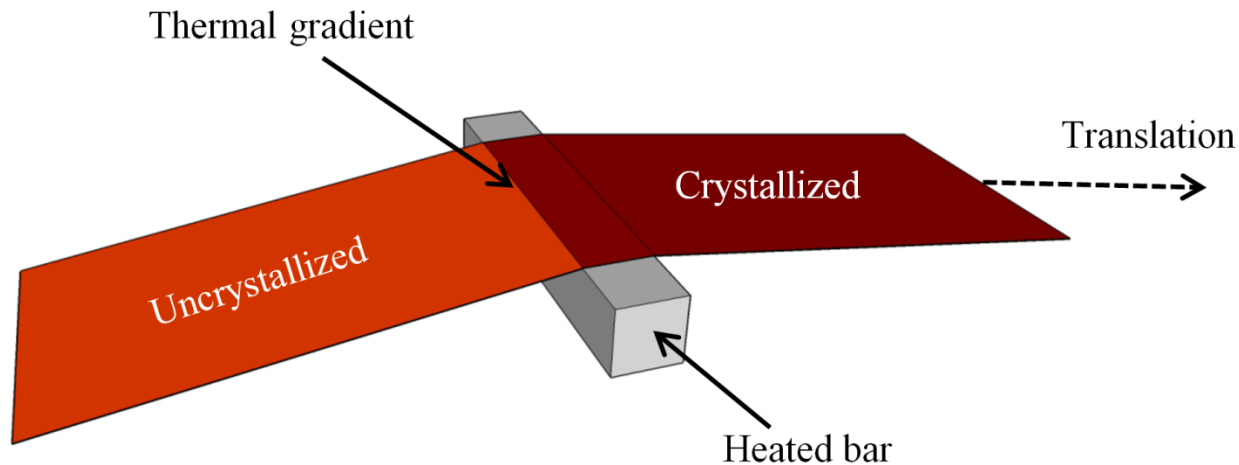


Figure 5-1. Scanned thermal annealing method. A plastic substrate is brought in contact with a heated metal bar and translated to the right relative to the bar. OTFTs with the organic semiconductor are located on top of the plastic substrate. A thermal gradient and thus solvent evaporation gradient exists inside the plastic substrate at the leading edge of the heated bar. Crystallization occurs at the location of the gradient. The semiconductor material to the left of the thermal gradient has not crystallized yet whereas material to the right of it has already crystallized.

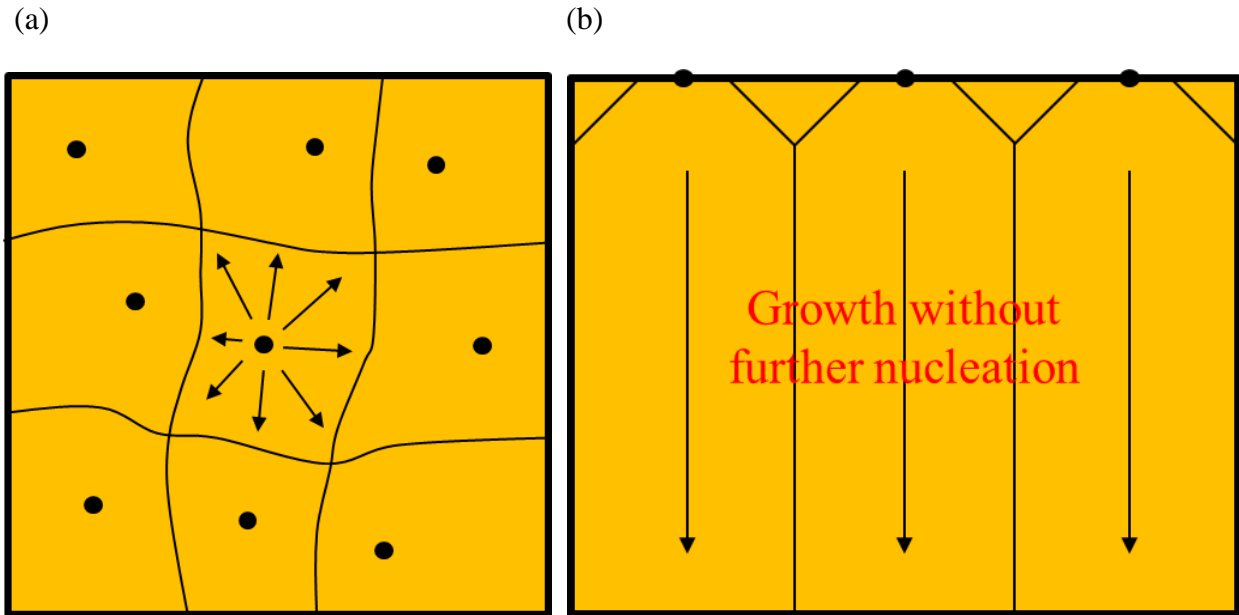


Figure 5-2. Illustration of the crystallization mechanism for (a) uniform and (b) scanned annealing. Uniform heating leads to uniform nucleation and grain growth. Scanned thermal annealing leads to a separation of nucleation and growth and thus significantly enlarged, elongated grains.

### 5.2.1 Simulation of thermal gradient

The key to achieving a reliable, sharp thermal gradient is the correct choice of substrate. The substrate needs to fulfill three criteria. Firstly, since heat is conducted through the thickness of the substrate, a thin substrate is desirable. This guarantees fast heat conduction to the top surface. Secondly, heat must not spread too quickly laterally along the substrate. Otherwise, the thermal gradient is rapidly washed out and the temperature profile approaches the condition of uniform heating. Therefore, the thermal conductivity of the substrate must be limited. Thirdly, heat is coupled into the substrate through a mechanical contact with the heated bar. This is enhanced through a conformal contact, which requires the substrate to be flexible. All three requirements suggest that plastic is an ideal substrate for this application. This was verified by numerical simulations solving the heat diffusion equation using COMSOL Multiphysics:

$$\rho c_p \frac{\partial T}{\partial t} - \nabla(k\nabla T) = 0 \quad \text{Eq. 5-1}$$

The substrate material parameters that determine the result of this equation are  $\rho$  the material's density,  $c_p$  the material's specific heat capacity and  $k$  the material's thermal conductivity. The numerical values of these parameters as used in our simulations are listed in Table 5-1. The heat

diffusion equation was solved to determine temperature  $T$  as a function of time  $t$  and position. The boundary conditions for the bottom surface of the substrate simulate the moving heated bar. A constant hot temperature is assumed for the heated region. The unheated region is assumed to be thermally isolated. The boundary between the two regions is moved with time. This boundary condition corresponds to a moving step function in external temperature. In reality, the moving bar corresponds to a moving pulse, however, since the width of the bar is much larger than the width of the thermal gradient in the plastic substrate (1cm vs. about 500 $\mu$ m), this is an accurate boundary condition to simulate the thermal gradient at the leading edge of the real bar. The boundary conditions for the other surfaces on the side and top of the plastic substrate are set to be natural convection. Figure 5-3 shows a typical simulation result at one time point for PEN (polyethylene naphthalate), a common plastic substrate for printed electronics. This result shows that a sharp thermal gradient develops throughout the PEN film. In order to compare the evolution of this thermal gradient with time and compare PEN with silicon, the thermal profile along the top surface of the substrate was recorded for different points in time. These multiple temperature profiles for different times were plotted on the same axes (see Figure 5-4). The thermal gradient on top of PEN is sharp and steady and only shifted in position as time progresses despite of the fact that the heater is dynamically translated. Conversely, silicon does not exhibit a steady thermal gradient. The gradient very quickly diminishes as heat spreads uncontrollably fast laterally through the substrate. This shows that plastic substrates exhibit beneficial thermal properties for directional crystallization utilizing a scanned thermal gradient, which is very beneficial for flexible electronics.

	<b>Silicon</b>	<b>PEN</b>
$\rho$ (kg/m <sup>3</sup> )	2329	1380
$c_p$ (J/kg*K)	700	1000
$k$ (W/m*K)	130	0.2

Table 5-1. Material parameters used for simulation of thermal gradient

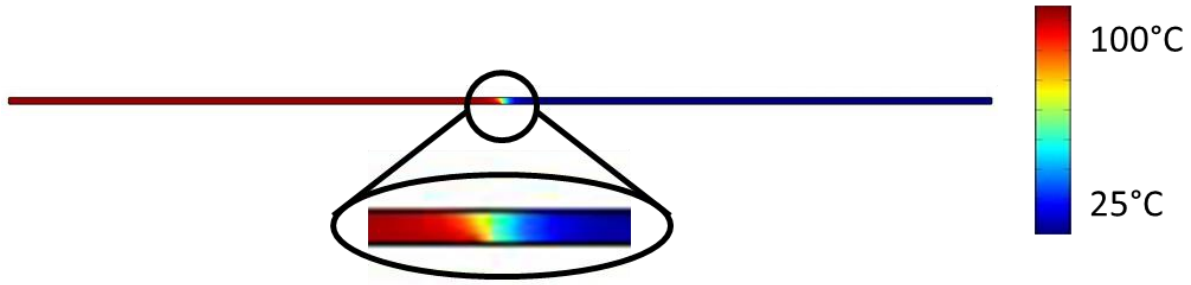


Figure 5-3. Simulated temperature distribution within PEN substrate (side view with translating heater on the bottom left). This shows a clear separation between the hot zone on the left, heated by the metal bar, and the insulated cold zone on the right. The boundary between the two zones is translated to simulate the moving heater. This result is a snapshot in time as the thermal gradient is translated along the length of the PEN substrate.

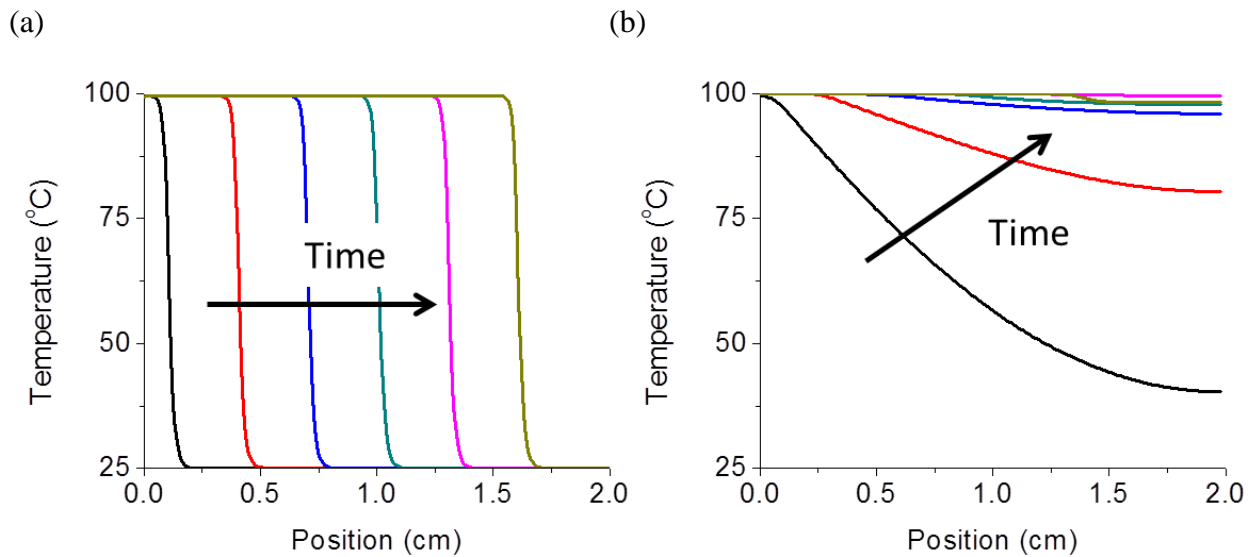


Figure 5-4. Temperature distribution along the top surface of the (a) PEN and (b) silicon substrates. Each curve corresponds to a different point in time as the heater is translated. PEN shows a sharp thermal gradient that stays constant and only shifts in position as the heater is translated from left to right. The thermal gradient in silicon very quickly diminishes as heat spreads rapidly laterally.

## 5.2.2 Device fabrication

Bottom-gate bottom-contact transistors were fabricated to study the crystallization mechanism and electrical performance characteristics of the scanned thermal annealing technique demonstrated here (see Figure 5-5 for device structure). Planarized PEN substrates were laser cut to a size of 9cm by 4cm of which an area of 4cm by 4cm was used for device fabrication. Silver gate electrodes were inkjet-printed using CCI-300, a silver nanoparticle ink purchased from Cabot Corporation, followed by sintering at 150°C for 30 minutes. The polymer gate dielectric lisicon® D207 was deposited by spin coating at 3000RPM. The ink as received was diluted 1:1 by volume with 2-Heptanone before spin coating. This resulted in an average film thickness of 330nm. The spun layer was UV cross-linked for 10 minutes ( $\lambda=365\text{nm}$ ,  $3\text{J}/\text{cm}^2$ ). After a short UV ozone treatment for 2 minutes, the source and drain electrodes were deposited by inkjet printing. The same CCI-300 ink and sintering conditions were used as for the gate electrode. Before depositing the semiconductor, a two-step surface treatment was applied.<sup>23</sup> The source and drain electrodes and the channel region were exposed to a forming gas RF plasma for 30 seconds at 40W. Within 5 minutes after the plasma cleaning step, lisicon® M001 was applied by drop casting. After spin drying, the samples were rinsed with isopropyl alcohol and spin dried again. A state of the art commercial organic semiconductor lisicon® S1200, which has been shown to hold great promise for printed organic devices and circuits, was employed.<sup>19-21</sup> Similar acene based organic semiconductors have been studied extensively by John Anthony and co-workers.<sup>131,155,132</sup> The semiconductor was applied by spin coating. A high spin speed of 9000 RPM was chosen to realize thin semiconductor layers, minimizing short channel effects. The semiconductor was crystallized by uniform and by scanned annealing. Both were performed at the same temperature 100°C. Uniform annealing was done on a standard hotplate for 1 minute. A custom built set-up was used for scanned annealing (see Figure 5-1 for an illustration). The PEN substrate with devices on top was pushed onto a heated aluminum bar. The bar was heated by a fire rod inserted into the bar and the temperature was controlled by a thermocouple attached to the bar close to the area used for annealing. The bar was then scanned at a speed of 1mm/s relative to the substrate. Both uniformly annealed devices and devices with scanned annealing were subjected to a 5 minute post-anneal at 100°C on a hotplate to reduce the defect density and improve performance. Transistor characteristics were measured using an Agilent 4156C semiconductor parameter analyzer in a nitrogen atmosphere. All fabrication steps were performed in air.

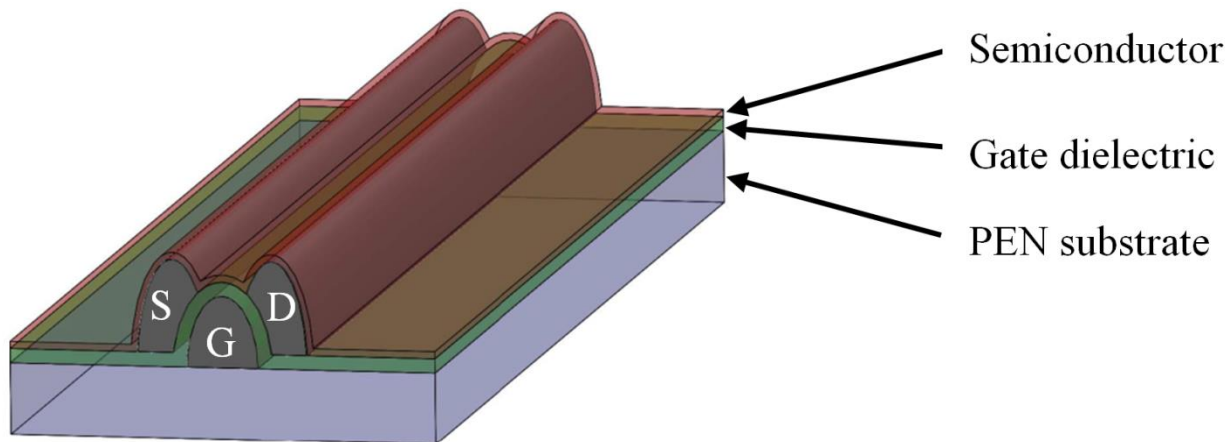


Figure 5-5. Device structure of printed OTFTs.

## 5.2.3 Results and discussion

### 5.2.3.1 Device performance

Devices fabricated using scanned thermal annealing exhibit significantly improved electrical performance when compared with devices fabricated using uniform annealing. Representative transfer characteristics for short channel devices can be observed in Figure 5-6. Median transistor parameters are summarized in Table 5-2. The greatest improvements can be observed for short channel devices where the thermal gradient is scanned in parallel with the electrodes. Mobility is increased by an order of magnitude from around  $0.1\text{cm}^2/\text{V}\cdot\text{s}$  to over  $1\text{cm}^2/\text{V}\cdot\text{s}$ . Off-state characteristics are also improved in terms of subthreshold swing and turn-on voltage. On-off ratio is good in all cases. This significant improvement is due to a greatly enhanced grain size. One can clearly observe the difference between uniformly annealed samples, which exhibit randomly oriented grains, and samples annealed by the scanned thermal gradient, which exhibit elongated grains of much larger size (see Figure 5-7). Grains are aligned with the scanning direction providing evidence of a successful separation of nucleation and growth during crystallization. This is not only observed in areas away from devices but also in the channel region of transistors (see Figure 5-8). This observation is especially clear for long channel devices.

In order to understand the crystallization mechanism better and to optimize performance, devices with different channel lengths and scanning directions were fabricated. Two different scanning directions were investigated: in parallel and perpendicular to the gate and source/drain electrodes (see Figure 5-8 for illustration). A Welch's t-test was performed on the experimentally obtained saturation mobility distributions to identify statistically significant differences between conditions. Statistically significant differences were found between uniformly annealed devices and devices with scanned annealing in both directions. Significant differences were also found between the

two different scanning directions for long channel devices. Short and long channel devices were also found to exhibit significantly different performance in the cases of both uniform annealing and scanning parallel to the electrodes. However, for short channel devices, no statistically significant differences were found between the scanning directions. For scanning perpendicular to the electrodes, no statistically significant differences were found between short and long channel devices either. These effects can be explained by considering both crystallization effects and the effect of contact resistance.

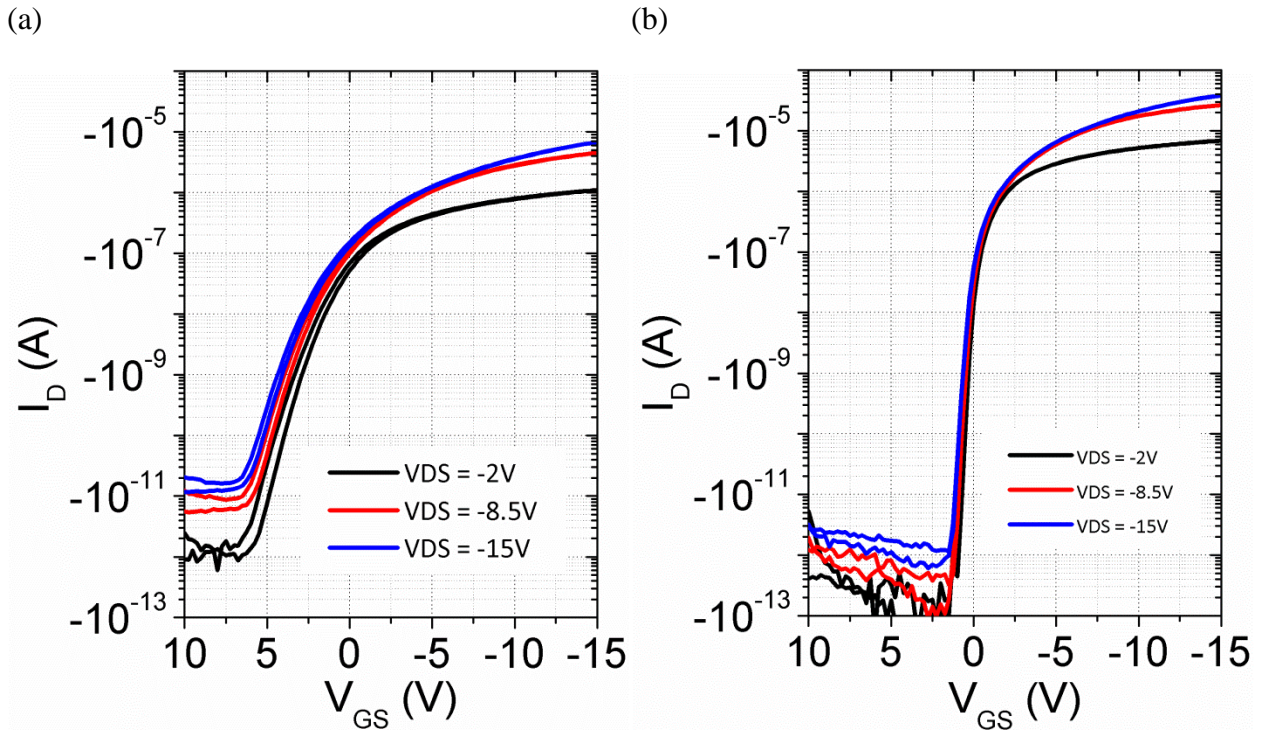


Figure 5-6. Representative transfer characteristics of short channel devices ( $25\mu\text{m}$  channel length and  $830\mu\text{m}$  channel width) crystallized by (a) uniform heating and (b) scanned thermal annealing (scanning direction in parallel with electrodes). The switching performance is significantly improved by scanned annealing both in the on- and off-state.

L [μm]	Anneal	Linear mobility [cm <sup>2</sup> /V-s]	Saturation mobility [cm <sup>2</sup> /V-s]	On-off ratio	Subthreshol d swing [V/dec]	V <sub>on</sub> [V]
30	Uniform	0.086	0.099	1.0*10 <sup>5</sup>	1.27	7.50
30	Scanned perpendicular	0.90	1.08	2.4*10 <sup>7</sup>	0.49	6.63
30	Scanned parallel	0.98	1.27	2.9*10 <sup>6</sup>	0.46	5.25
220	Uniform	0.26	0.32	1.8*10 <sup>4</sup>	1.77	7.00
220	Scanned perpendicular	0.91	1.09	2.0*10 <sup>4</sup>	0.55	0.50
220	Scanned parallel	1.34	1.52	1.1*10 <sup>6</sup>	0.52	2.00

Table 5-2. Median values of transistor characteristics for different channel lengths and annealing methods.

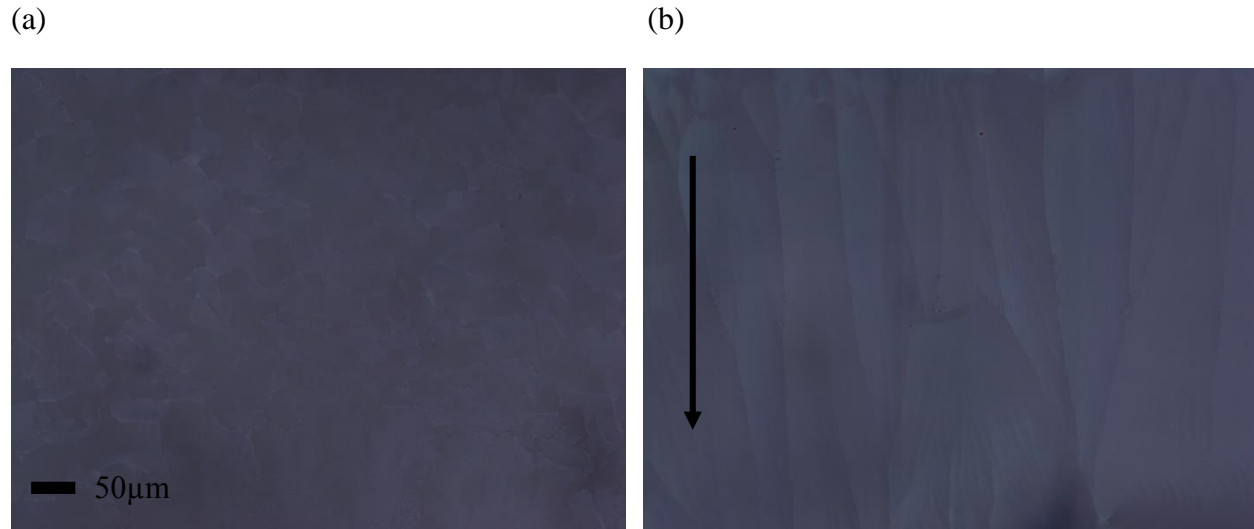


Figure 5-7. Polarized optical microscope images showing crystallization away from transistors. (a) Uniform annealing. Randomly oriented small grains. (b) Scanned thermal annealing. Arrow indicates scanning direction. Grains are clearly enlarged and aligned with the scanning direction as expected for the successful separation of nucleation and growth.

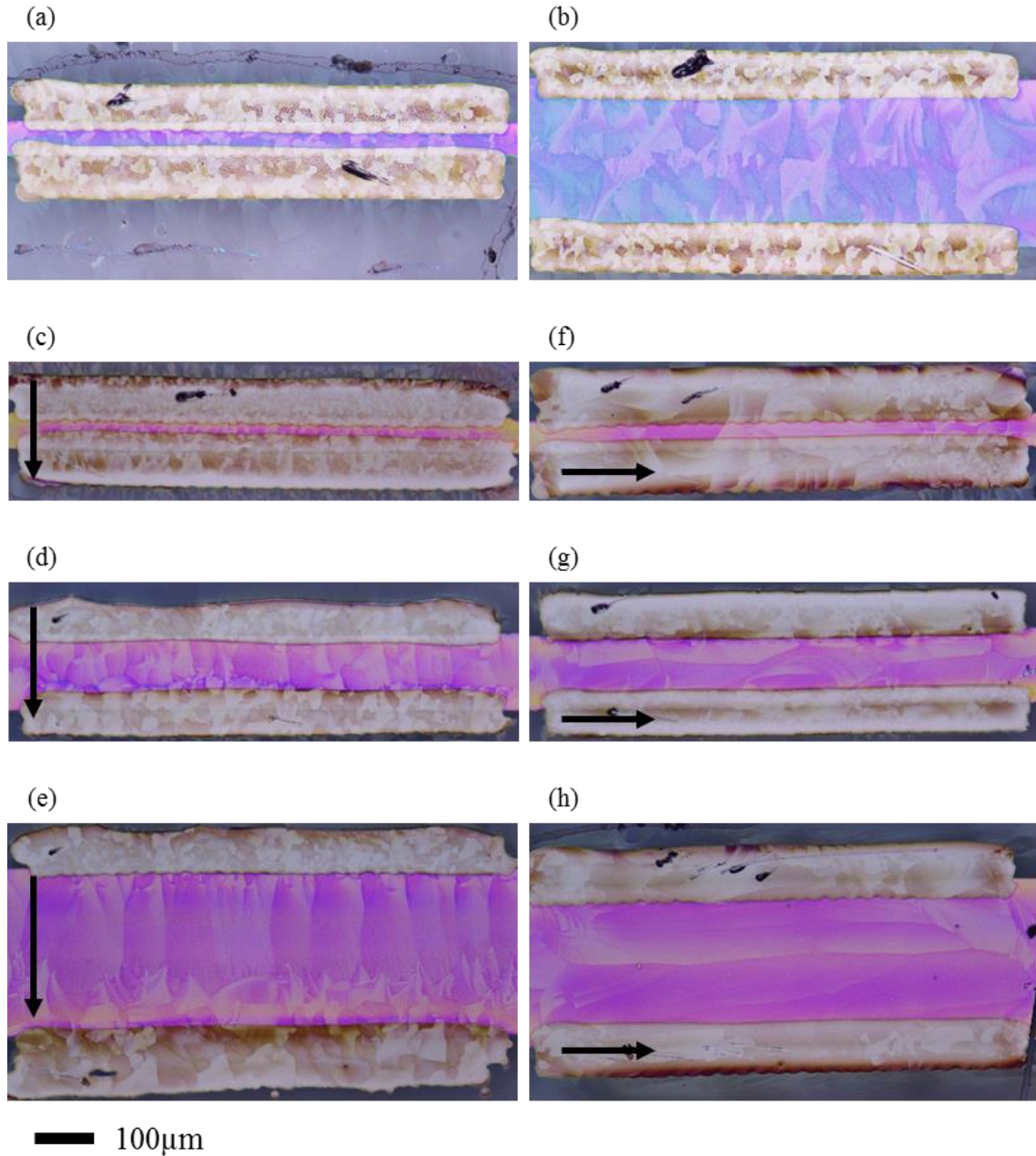


Figure 5-8. Polarized optical micrographs of grain structure for different annealing conditions. Black arrow indicates scanning directions. (a)&(b) Uniform annealing. Grains are randomly oriented and small. (c)-(e) Scanned thermal annealing perpendicular to electrodes. Grains are elongated and aligned with the scanning direction. Small secondary grains impinge on large primary grains close to the second electrode. This is most prevalent for long channel devices. (f)-(h) Scanned thermal annealing in parallel with electrodes. Grains are again aligned with the scanning direction and have the largest size of all the tested conditions. No impingement on secondary grains is observed.

### 5.2.3.2 Effect of channel length

Both uniformly annealed devices and devices with scanned annealing parallel to the electrodes exhibit increased performance for longer channels compared with shorter channel devices annealed under the same conditions. One reason is the preferred nucleation of the semiconductor on the electrodes. This leads to smaller grains on and close to the electrodes. This disruption of the crystallization will impact short channel devices more severely because the region close to the electrodes makes up a larger portion of the channel. Secondly, short channel devices are limited by contact resistance due to a contact barrier. This has been minimized with a surface treatment, however, has not been eliminated completely. In the case of short channel devices, the mean saturation mobility is about 30% higher than the mean linear mobility due to the larger effect of contact resistance in the linear regime. For long channel devices, this difference is reduced to about 10% as one would expect due to the larger influence of channel resistance compared with contact resistance. Both effects combined lead to the limited performance of short channel devices.

### 5.2.3.3 Effect of scanning direction

Devices fabricated using scanning perpendicular to the electrodes generally exhibit lower performance than devices fabricated by scanning parallel to the electrodes. The worst case devices and the variability of performance tend to be worse for devices fabricated using scanning perpendicular to the electrodes (see Figure 5-9 for boxplot of saturation mobility). The difference in mean saturation mobility between scanning directions is more pronounced and only statistically significant for long channel devices. Long channel devices fabricated by perpendicular scanning are limited in performance despite the smaller effect of contact resistance compared with shorter channel devices. Therefore no significant effect of channel length can be observed for perpendicular scanning. To understand this effect, we may consider the details of the crystallization mechanism. This is schematically illustrated in Figure 5-10. For perpendicular scanning, the thermal gradient will initially approach one of the source/ drain electrodes (the upper electrode in Figure 5-8). Nucleation will occur on this electrode and then grains will grow into the channel without further nucleation, leading to elongated grains. As the thermal gradient approaches the second (bottom) electrode, further nucleation will occur on this electrode. These secondary grains can grow back into the channel impinging on the elongated primary grains growing from the primary (top) electrode. This creates significant disorder and smaller grains close to the second electrode, which will limit device performance, and can be observed clearly for the long channel devices in Figure 5-8 (d) and (e) and is illustrated in Figure 5-10. This mechanism does not exist for devices fabricated using scanning parallel to the electrodes. In these devices, grains grow from both electrodes simultaneously and only impinge once at the center of the channel (see both Figure 5-10 and Figure 5-8 (h)). This explains the improved performance of devices where the thermal gradient is scanned in parallel with the electrodes. Further, in the case of devices fabricated using scanning perpendicular to the electrodes, short channel devices are less

limited by primary grains impinging on secondary grains since both primary and secondary grains can bridge shorter channels more easily as the size of the secondary grains is comparable to the channel length. This effect is offset by the effect of contact resistance. Considering these effects together, both the crystallization and contact resistance effects then result in no net difference in performance between short and long channel devices when the thermal gradient is scanned perpendicular to the electrodes. However, even with this slightly lessened improvement in devices fabricated by scanning perpendicular to the electrodes, the scanning technique clearly gives significant improvement in performance across all device geometries relative to uniform annealing. Indeed, scanning perpendicular to the channel results in devices with more uniform device characteristics across all channel lengths, which is beneficial for the design of realistic circuits. The significant performance improvement across the board under these conditions is very attractive, as a result.

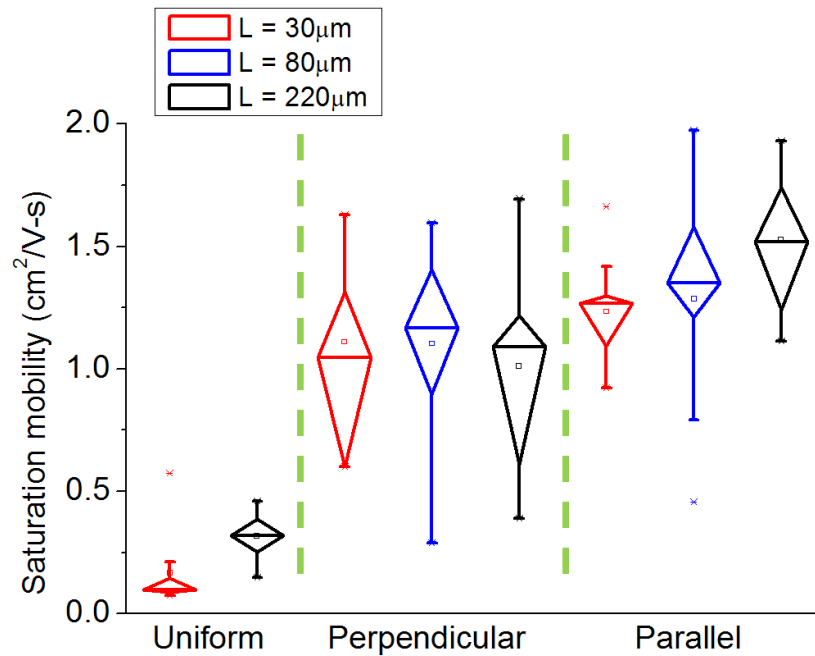


Figure 5-9. Boxplot comparing performance statistics of different annealing conditions (uniform annealing, scanning perpendicular and scanning parallel to electrodes) and channel lengths.

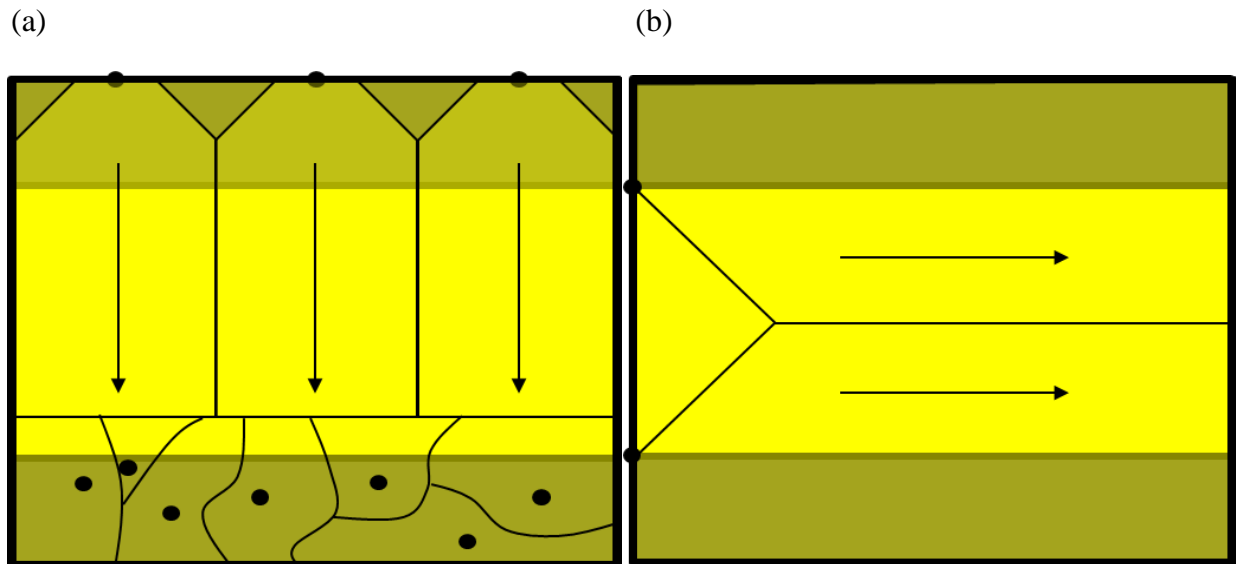


Figure 5-10. Illustration of scanned thermal annealing crystallization mechanism including the source and drain electrodes for scanning (a) perpendicular to and (b) in parallel with the electrodes. Preferred nucleation on the electrodes disrupts the crystallization. For scanning perpendicular to the electrodes, this leads to small secondary grains close to the bottom electrode, which limits performance compared with parallel scanning where elongated grains do not impinge on secondary grains since grains grow in parallel with electrodes rather than towards one.

### 5.3 Fully gravure printed organic thin-film transistors

In the previous section, the performance of an organic semiconductor was significantly improved by using a novel crystallization technique. However, device fabrication still relied on spin coating, which is not roll-to-roll compatible, and inkjet printing, which is not as high-speed as gravure printing. In this section, this is overcome by fully gravure printing devices to achieve high-throughput fabrication. In order to fully gravure print transistors and achieve good performance, every layer needs to be studied carefully. Each layer has its own specific challenges when implemented by gravure. All layers were printed at the maximum print speed achievable on the laboratory scale printer used for this work: 1m/s. Top-gate bottom-contact OTFTs were fabricated. The source and drain electrodes require excellent pattern fidelity in order to achieve high-resolution printing for high-frequency device operation. Highly-scaled  $5\mu\text{m}$  features are printed whilst simultaneously achieving high printing yield. The dielectric is the most important layer to reduce operation voltage. By reducing the dielectric thickness, the gate field and thus gate control is increased. A leveling step is employed to improve thickness uniformity for thin dielectric films. Printing of the semiconductor is challenging because it requires printing-based patterning of a thin uniform layer. The effect of ink viscosity on this printing is explored and optimized. Finally, the gate electrode and device structure are optimized to facilitate gravure-printed device formation.

For gravure printing, alignment accuracy currently lags behind feature size, which means alignment of the gate electrode to the source and drain electrodes is very challenging. Alignment accuracy is reduced both by tool limitations, which will be addressed in future generation tools, as well as by more fundamental issues with flexible substrates such as stretching or dimensional changes during heating steps. Addressing these challenges in the future would be an important step forward for the gravure printing of multi-layer devices. In the meantime, a fully overlapped gate structure is employed with a large gate electrode. Due to the large size of the gate relative to the channel and source-drain dimensions, the structure becomes misalignment tolerant.<sup>27</sup> Thus, gate pattern size is not very critical. The main challenge with the gate is to choose an ink that sufficiently wets the dielectric and whose solvent does not interact with the dielectric. See Figure 5-11 for the device structure and the fabrication process.

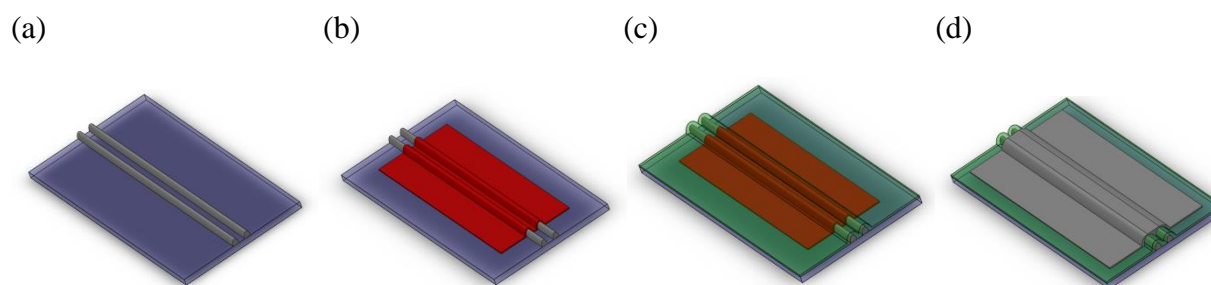


Figure 5-11. Overview of fabrication process and device structure. (a) Highly-scaled silver electrodes are gravure printed on cleaned PEN plastic substrates. (b) After a self-assembled monolayer treatment, the polymer semiconductor is patterned using gravure printing. (c) The dielectric is blanket printed using gravure. (d) The silver gate electrode is patterned by gravure printing. All printing steps are performed at 1m/s in air.

### 5.3.1 Device fabrication

#### 5.3.1.1 Source and drain printing

Downscaling of the source and drain electrodes and their spacing is crucial to achieve high-performance TFT operation. In order to achieve good AC performance, the fully overlapped gate architecture requires not only a highly-scaled channel length but also highly-scaled electrodes to minimize overlap capacitance. Electrodes are printed whose width is on the same order as the channel length. The previous chapters showed how high-resolution features can be printed at high print speeds using gravure. Again, electrodes were printed onto planarized polyethylene naphthalate (PEN) substrates provided by DuPont Teijin Films after a 30 seconds, 50W air plasma treatment. The ink for the source and drain electrodes was again the silver nanoparticle ink (NPS) purchased from Harima Chemicals Group and its viscosity was adjusted by dilution with its solvent

AF5. Inverse direct gravure printing with silicon printing plates was used. The silicon printing plate exhibits a small contact angle hysteresis and thus behaves more like the metal printing plate with the boron-nitride hard layer than the nickel-iron printing plate without the hard layer as discussed in chapter 3. A large capillary number of 3.4 and an ink viscosity of 86cP were chosen. These values give good printing performance and ink spreading on the substrate as discussed in the previous chapters whilst enabling printing at 1m/s. The cell width was varied from 3 to 7.5 $\mu\text{m}$  whilst the cell gap was kept constant at 0.1 times the cell width. The printed line width is linearly related to line width on the printing plate. Ink spreading on the plastic substrate slightly increases the printed line width. Similarly, the printed channel length is reduced by ink spreading from the adjacent lines (see Figure 5-12).

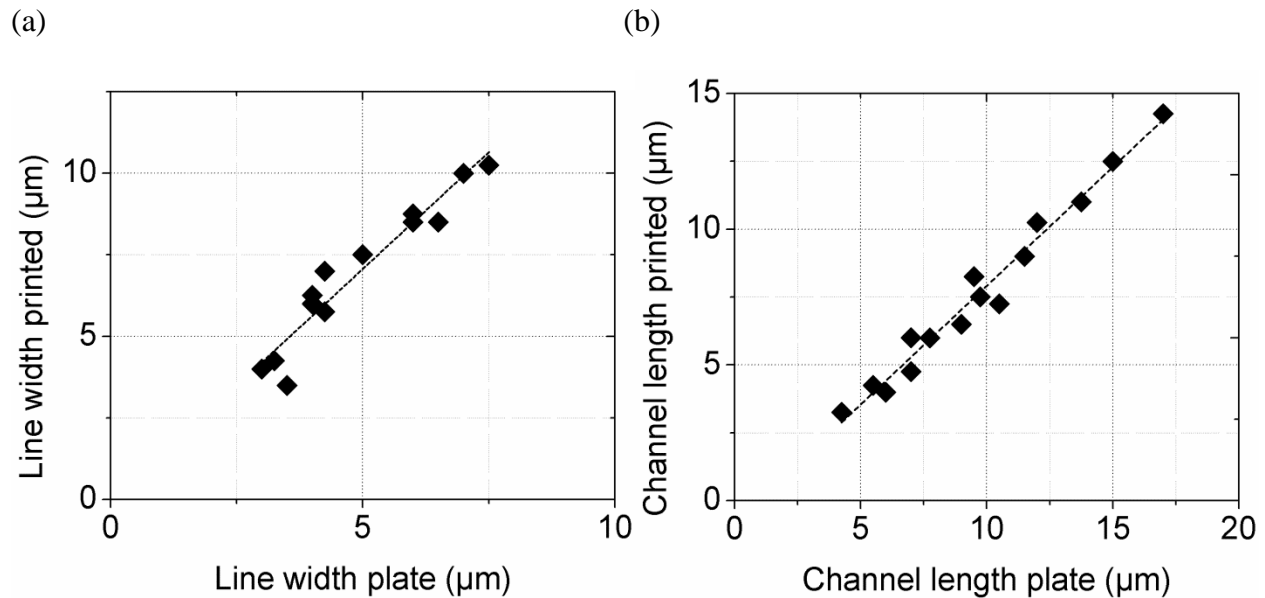


Figure 5-12. (a) Printed linewidth is linearly related to line width (=cell width) on the printing plate. (b) Printed channel length is linearly related to channel length on the printing plate. Printed line width is slightly enlarged and channel length is reduced by ink spreading on the substrate.

At such highly-scaled channel lengths below 5 $\mu\text{m}$ , the limiting factor on yield is the merging together of closely spaced source and drain electrodes. Figure 5-13 shows the relation between channel length and printing yield. Perfect yield can be achieved down to about 10 $\mu\text{m}$  channel length and yield is close to 100% down to 5 $\mu\text{m}$  channel length. Shorter channel lengths can still be printed but yield drops off very quickly. A major factor to achieve this excellent yield is the doctor blade due to its two non-idealities: lubrication residue and drag-out. Here, lines are printed parallel to the printing direction, which minimizes the effect of the drag-out tails; however, ink can still somewhat spread sideways on the blade as it gets dragged out of the cells, which can lead to

the merging of adjacent lines. Ideally, both wiping non-idealities occur uniformly across the print. However, doctor blades typically have local defects whose density gets worse during printing due to doctor blade wear. In the worst case, these defects can cause the printing of large streaks that run throughout the print. Even without such catastrophic streaks, doctor blade defects and wear affect yield dramatically for highly-scaled features. Figure 5-14 shows how yield changes throughout a print for different doctor blade tip thicknesses (see Figure 5-15 for cross-sectional micrographs of different blade tips). Doctor blades were used as supplied by Max Daetwyler Corporation. A thin 60 $\mu\text{m}$  tip shows dramatic degradation in yield as the print progresses because it is very susceptible to wear (see Figure 5-16 for optical micrographs of pattern degradation). A 75 $\mu\text{m}$  tip is far more robust. Yield even increases slightly after the beginning of the print, possibly because initial defects are polished away. However, increasing the tip thickness too much leads to decreased print quality and yield as evidenced by the 95 $\mu\text{m}$  tip. Larger tips develop a smaller pressure at the tip leading to increased lubrication residue and allow more time for drag-out to occur. A 75 $\mu\text{m}$  tip was thus used to fabricate devices.

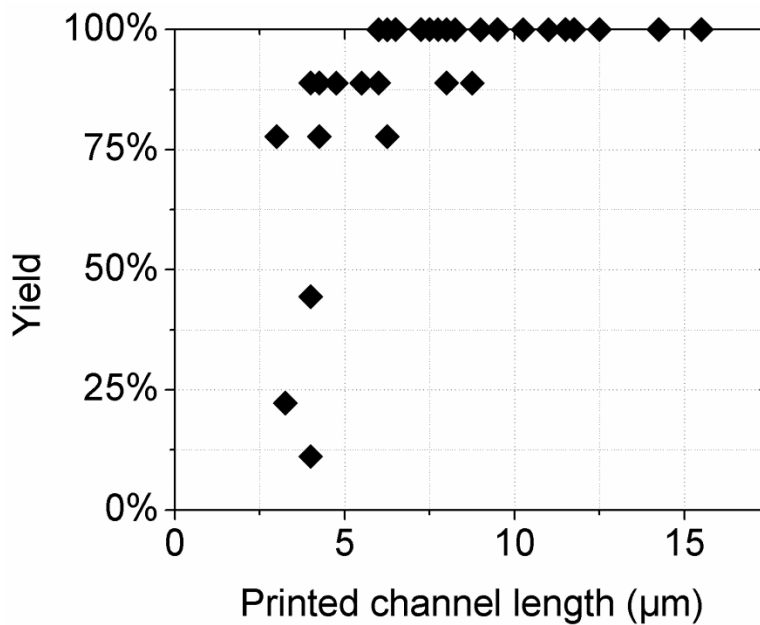


Figure 5-13. Printing yield of source-drain patterns is close to 100% for channel lengths above 5 $\mu\text{m}$ . Below 5 $\mu\text{m}$ , the number of merged lines increases significantly.

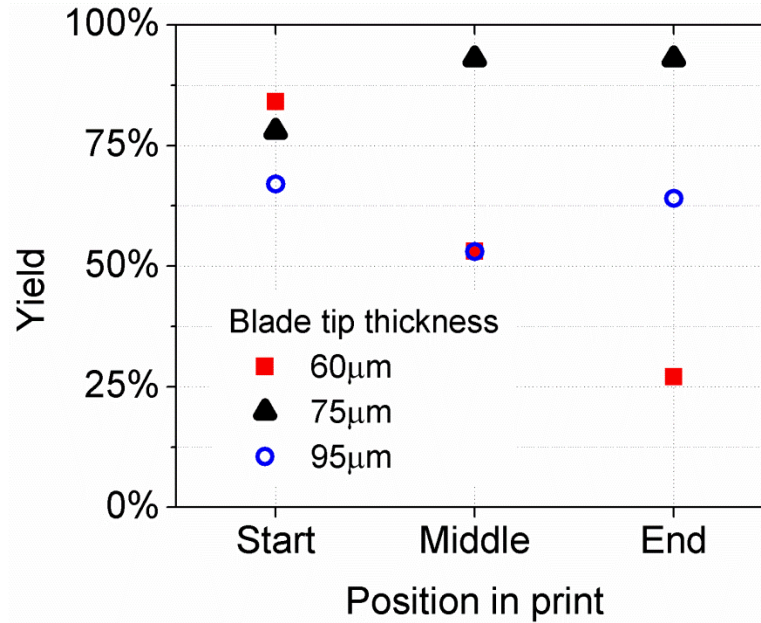


Figure 5-14. Yield depends significantly on the thickness of the doctor blade tip. 60µm blades show significant degradation during prints due to wear. 95µm blades show decreased yield due to insufficient pressure. 75µm blades exhibit good yield with reduced wear.

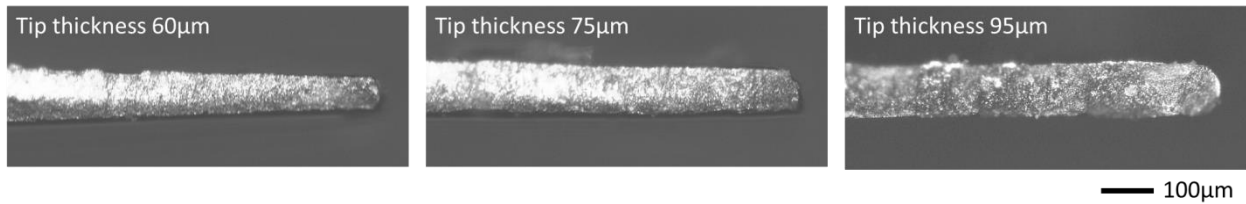


Figure 5-15. Cross-sectional micrographs showing the tip of the doctor blade for three different blade tip thicknesses, which is measured at the very tip of the blade.

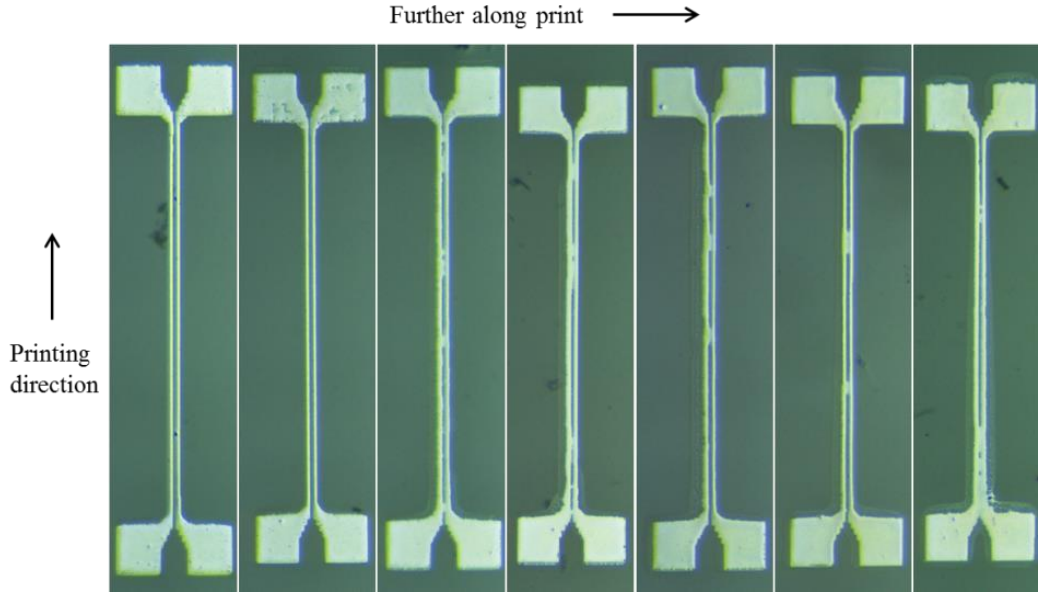


Figure 5-16. Source and drain electrodes printed with 60 $\mu$ m blade tip. From left to right, patterns degrade along the print run due to blade wear.

After printing, the silver ink was sintered at 220°C for 2 hours with a slow ramp rate of 3°C/min to improve electrode adhesion to the substrate.<sup>27</sup> Since gravure is a contact printing technique, features need to be robust in multilayer devices. Otherwise, the printing of subsequent layers can destroy underlying layers (see Figure 5-17). It was found that a particular problem for adhesion of the source and drain electrodes is the surface treatment before the semiconductor printing. A two-step surface treatment was applied to improve contact resistance.<sup>23</sup> First, the source and drain electrodes were exposed to a mild 10W RF plasma in air for 30 seconds. Then, a self-assembled monolayer (SAM) is applied to increase the work function of the electrodes and improve current injection. Lisicon® M001 was applied by drop casting. After drying, the samples were rinsed with isopropyl alcohol, dried again and dried at 100°C for 1 minute. This surface treatment process could easily be implemented with a simple roll-to-roll compatible technique such as blade coating and was thus not implemented with gravure. This SAM layer adversely affected adhesion of the electrodes, presumably by depositing in between the electrodes and the substrate. It was found that this was particularly problematic on days when humidity was high during SAM deposition resulting in almost zero yield during subsequent printing. Thus, there exists an interaction between the SAM and moisture. This can be prevented by drying the sample at 100°C for five minutes after the plasma treatment right before the SAM deposition and 100% yield can be achieved.

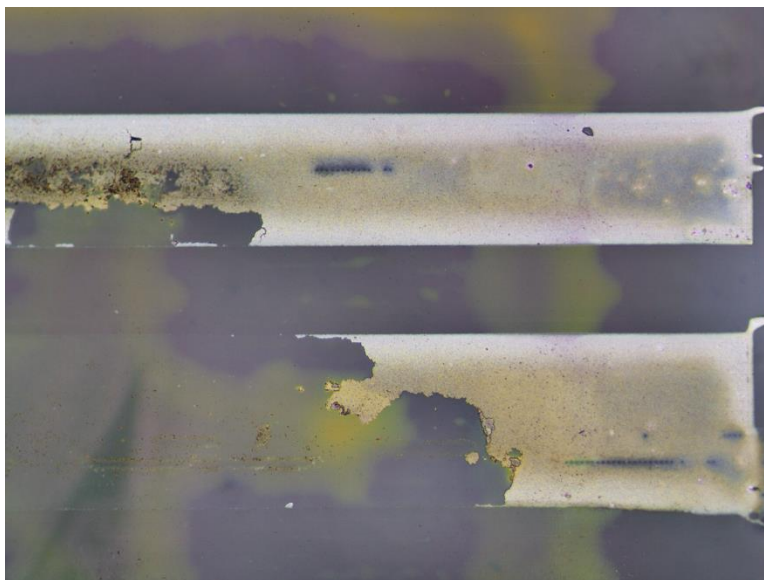


Figure 5-17. Silver rectangles on PEN after SAM treatment without drying and subsequent semiconductor printing. One can clearly observe regions of the rectangles that have been destroyed during the semiconductor printing.

### 5.3.1.2 Semiconductor printing

The semiconductor material is crucial in determining the performance of a transistor. Here, lisicon® SP400 is employed. This material as well as the surface treatment and the dielectric were provided by EMD Performance Materials Corp. (an affiliate of Merck KGaA, Darmstadt, Germany). This p-type semiconductor is a high-performance amorphous polymer. The amorphous nature of the material reduces processing complexity and variability because there is no need for a crystallization step, and device to device uniformity is improved due to the elimination of grain boundary-induced variation as a performance-determining parameter. In addition, patterning and control over the rheology is significantly improved by the fact that lisicon® SP400 is a polymer rather than a small molecule. Patterning of the semiconductor layer is, in practice, imperative to realize functional organic semiconductor-based circuits. When the semiconductor is patterned, leakage paths are removed that would otherwise lead to excessive device off-current and cross-talk between neighboring devices. The pattern dimensions for the semiconductor are much larger than for the source and drain electrodes, typically on the order of tens to hundreds of micrometers. Thus, they can be printed using conventional direct gravure with a metal roll fabricated by electromechanical engraving. The roll was purchased from RotaDyne. However, patterning of the semiconductor is more challenging because low viscosity inks are used to achieve thin films. The use of thin films is desirable to obtain good device electrostatic integrity, resulting in improved off-state behavior. Lowering the polymer concentration in the ink decreases both dry film thickness and ink viscosity. The ink was diluted with its two co-solvents mesitylene and 1-methyl naphthalene. Figure 5-18 shows how the pattern fidelity changes with different ink viscosities. As

the viscosity is reduced, pattern fidelity becomes worse due to increased ink spreading on the substrate. Down to 24cP, individual device patterns are still distinct. At 9cP, the ink spreads so much that no distinct features can be made out anymore. At 9cP, the thickness of the printed film also becomes too thin to be measured accurately on a flexible plastic substrate. The other ink viscosities show the expected trend of decreased thickness with decreased ink viscosity (see Figure 5-19). Higher viscosity patterns also exhibit reduced levels of coffee ring i.e. the accumulation of material at the edges of features where the solvent dries faster than in the center. Thus, from a patterning perspective, higher viscosity semiconductor inks are desirable. However, a thin semiconductor layer is required for optimal device performance. Mobility drops as the semiconductor ink viscosity is increased past 24cP (see Figure 5-20). At 9cP, the semiconductor film is too thin to carry any substantial current. At higher viscosities, contact resistance limits device operation (see Figure 5-21). Contact resistance was extracted using the transmission line method. Since the device structure is top-gate bottom-contact, holes need to be conducted from the electrodes through the thickness of the semiconductor to the channel. This leads to increased contact resistance for thicker semiconductor films. Thus, a 24cP ink was used for device fabrication.

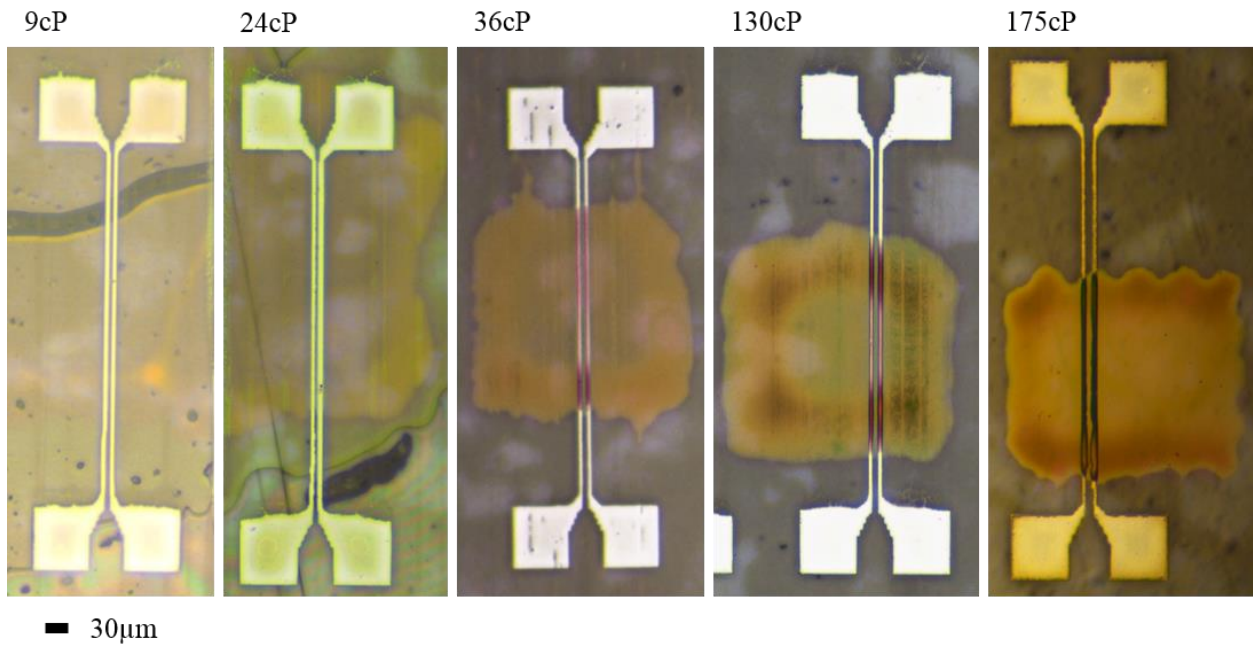


Figure 5-18. Semiconductor pattern definition for different ink viscosities. Optical micrographs show printed semiconductor patterns on top of printed source and drain lines. Lateral pattern definition improves with increased viscosity. 9cP spreads uncontrollably. 24cP and above exhibits defined patterns.

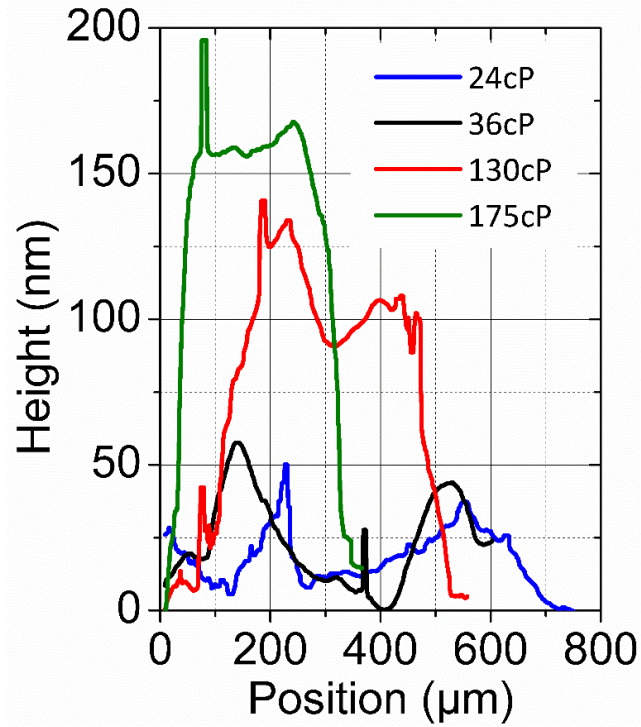


Figure 5-19. Surface profiles of printed semiconductor pads printed with different viscosities. Pattern thickness increases and relative coffee ring height decreases with increasing viscosity.

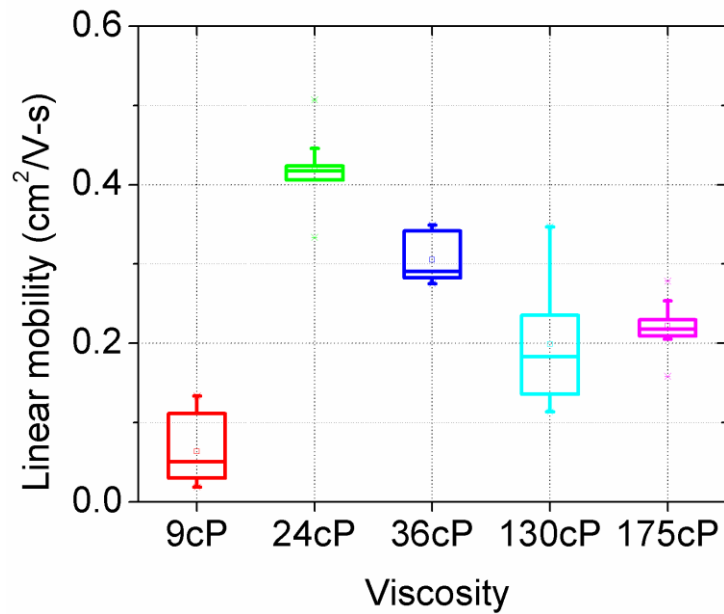


Figure 5-20. Effect of semiconductor viscosity on electrical performance. Linear mobility increases with decreasing viscosity until the semiconductor film becomes too thin to conduct significant current.

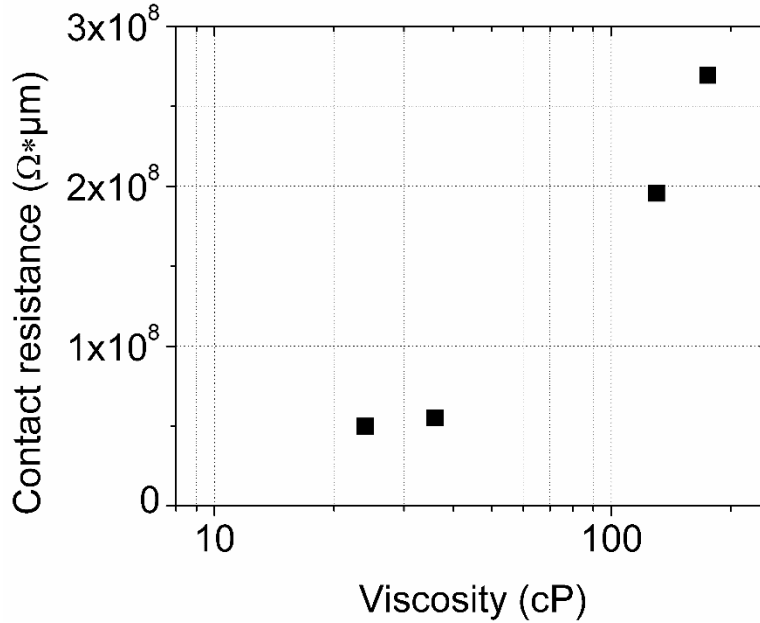


Figure 5-21. Thinner semiconductor films printed with lower viscosity inks lead to improved contact resistance in a top-gate bottom-contact device structure where current is conducted through the semiconductor thickness.

### 5.3.1.3 Dielectric scaling

The gate dielectric is crucial in ensuring good electrostatic control over the channel. Here, lisicon® D320 is used, a polymer dielectric provided by EMD Performance Materials Corp., which has been designed to match with the semiconductor lisicon® SP400. The semiconductor-dielectric interface is optimized to ensure a low trap concentration, enabling the realization of devices with high mobility and low subthreshold swing. In addition, the semiconductor is compatible with the dielectric solvent (decane). It is also important for the dielectric to have a high enough surface energy such that the subsequent gate ink does not dewet, which is a problem for fluorinated gate dielectrics. The dielectric was blanket printed using a roll purchased from IGT Testing Systems (402.101, 45μm cell depth). In order to achieve low-voltage operation, the gate dielectric needs to be scaled down in thickness to increase the gate field and improve gate control over the channel. Here, a number of different dielectric thicknesses were studied. Thickness was varied by dilution of the dielectric ink. As the dielectric thickness is scaled, off-state performance improves significantly (see Figure 5-22). For a 120nm thick dielectric, the magnitude of the threshold voltage decreases to approximately -1V and swing drops below 500mV/decade. In order to achieve such thickness scaling, a very uniform dielectric needs to be printed. Gravure printing often leads to non-uniform films due to fluid instabilities as well as the discrete nature of the gravure cells that requires ink to spread in between cells.<sup>130</sup> Here, a leveling step in a solvent atmosphere is employed before drying at 100°C for 5 minutes to improve the uniformity of the dielectric thickness and dielectric yield significantly (see Figure 5-23). However, dielectric yield still needs to be improved

further (see Figure 5-24). Further improvements might be possible by modifying the gate ink to improve solvent compatibility, which will be discussed in the next section, and by improving the cleanliness of the processing environment. Improvements in the surface roughness of the underlying source and drain electrodes (currently RMS roughness 15.3nm) might also increase dielectric yield (see Figure 5-25). In any case, the current process enables the fabrication of functioning devices with a 120nm thick gravure printed dielectric. Figure 5-26 shows representative device characteristics for such devices. All device measurements reported in this chapter were performed in a nitrogen atmosphere. The operation voltage is below 5V, which is very low for organic transistors, especially when fully printed. On-off ratios exceeding  $10^5$  are achieved at these low voltages.

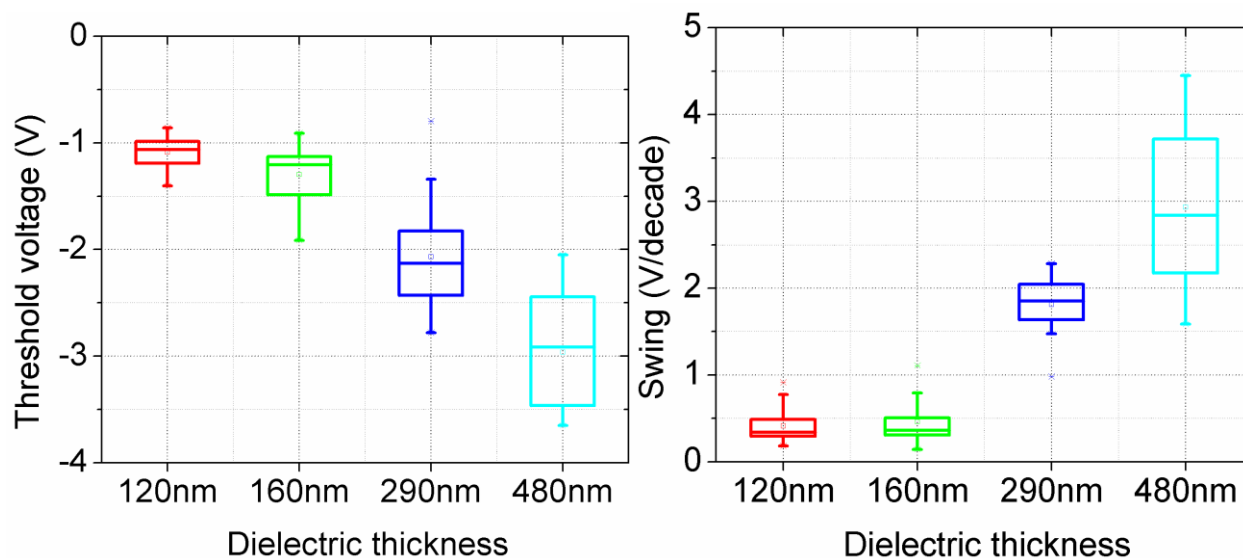


Figure 5-22. Off-state performance improves significantly with thinner gate dielectrics due to better gate control.

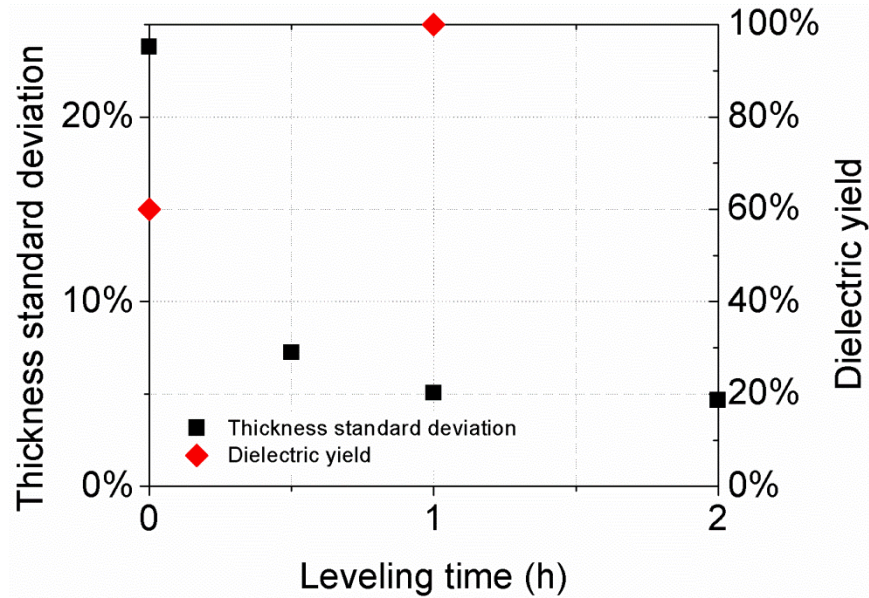


Figure 5-23. Dielectric thickness uniformity and yield are improved significantly by allowing the film to level in a solvent atmosphere before drying, to remove any non-uniformities after gravure printing. Data for 300nm thick film.

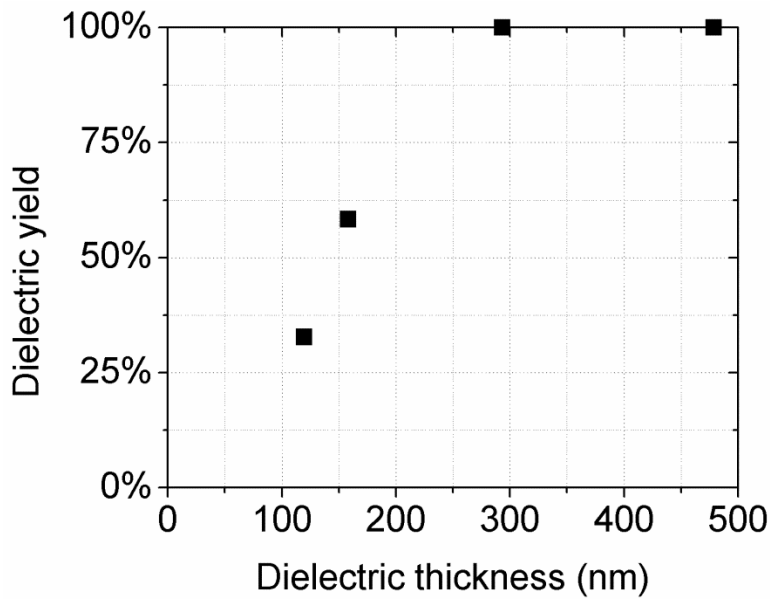


Figure 5-24. The dielectric yield of the gravure printed dielectric is perfect down to a thickness of 300nm. Below this thickness, further improvements in yield are required.

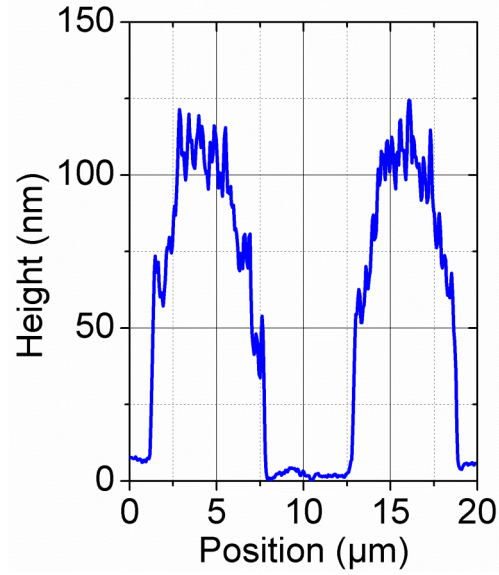


Figure 5-25. Height profile of source and drain lines. The average RMS surface roughness is 15.3nm. Improvements in source and drain surface roughness might improve dielectric yield.

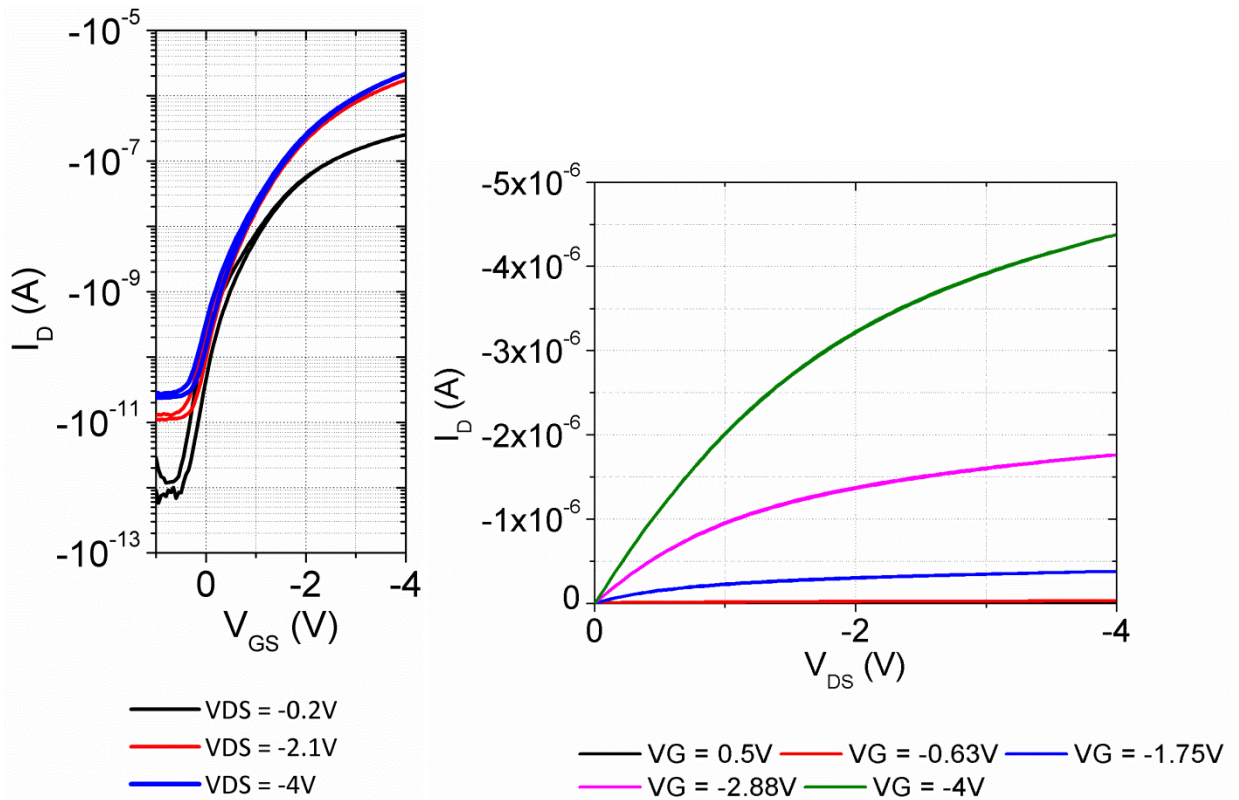


Figure 5-26. Representative transfer and output characteristics exhibiting low-voltage operation with excellent off-state performance.

### 5.3.1.4 Gate electrode printing

The requirements for the gate electrode itself are not very stringent in a fully overlapped structure both in terms of pattern definition and conductivity. The main challenge for the gate is the interaction with the underlying dielectric. The surface energy of the dielectric is high enough, especially after a short plasma treatment (25W 10 seconds air plasma), that wetting of the gate ink is no problem. A much bigger problem is solvent compatibility. Two commercial silver inks were tested: Silverjet DGP 40LT-15C from Advanced Nano Products (ANP) and PFI-722 from Novacentrix. The Novacentrix ink uses water as its main solvent. This does not significantly attack the dielectric and high yield is possible. However, the ink contains an adhesive that is very difficult to remove from the gravure roll once it has dried. Thus, cleaning of the roll was a significant challenge and had to be performed using nitric acid. This attacked the roll and was not sustainable. In a continuous printing system, this might not be a problem if the ink is never allowed to dry on the roll. The ANP ink uses tri(ethylene glycol) monoethyl ether (TGME) as its main solvent. This ink can be cleaned off the roll easily using toluene. However, the TGME attacks the dielectric. Dielectric yield is significantly reduced and holes can be observed on top of the gate electrode that reach through the dielectric. The difference between these solvents can be understood in terms of the solubility of the gate dielectric, which is dissolved in decane. The Hansen solubility parameters describe solubility in terms of three orthogonal energy components: dispersion (nonpolar forces), polarity (dipole forces) and hydrogen bonding.<sup>156-158</sup> By calculating the distance of a solvent from decane in this three-dimensional coordinate system, one can determine how likely it is that a solvent will also dissolve the gate dielectric. Table 5-3 shows that unsurprisingly water exhibits strong hydrogen bonding whereas decane does not exhibit any. Conversely, TGME is much closer to decane thus explaining the partial solubility of the gate dielectric in TGME.

	<b>Dispersion</b>	<b>Polarity</b>	<b>Hydrogen bonding</b>	<b>Distance from decane</b>
Decane	16	0	0	0
Water	15.5	16	42.3	45.2
TGME	16.2	7.2	12.5	14.4

Table 5-3. Hansen solubility parameters from <sup>159</sup> and the Cartesian distance of water and TGME from decane.

One way to solve this would be to test further inks and solvents. Another way is demonstrated here. As a baseline process, the ANP ink was sintered at 100°C for 30 minutes without any ramp directly placing the sample on a heated hotplate. This leads to many holes in the dielectric (see Figure 5-27 (a)). At the beginning of the sintering process, the gate ink is still liquid containing a large amount of solvent. The high temperature increases solubility of the dielectric in the TGME leading to a large number of holes. This can be prevented by drying the gate at a lower temperature.

Drying at 30°C for 15 minutes under vacuum results in a significant reduction in hole density (see Figure 5-27 (b)). The vacuum aids with the removal of the solvent and enables lines to be conductive even at such low temperatures. Further heating of the gate at 100°C after drying improves conductivity but does not result in the creation of holes in the dielectric further confirming that the holes are due to solvent interaction. The vacuum step can be replaced by sintering in air using a very slow ramp of 2°C per minute to ramp up to 100°C. With this process, perfect yield can be achieved down to a dielectric thickness of 300nm (see Figure 5-24). Further improvements are needed for thinner dielectrics.



Figure 5-27. ANP gate on top of D320 gate dielectric after sintering. (a) Sintering at 100°C for 30 minutes without ramp resulting in large number of holes in dielectric (black dots). (b) Sintering at 30°C for 15 minutes in vacuum significantly improves the hole density. (c) Further heating at 100°C for 10 minutes after initial drying at 30°C does not result in the creation of holes.

## 5.3.2 Device characterization

### 5.3.2.1 Comparison with small molecule semiconductor

One reason for choosing a polymer semiconductor is its better printability compared with small molecule semiconductors. This facilitates the printing of patterned semiconductor pads. In addition, the polymer used here is amorphous, which allows for achievement of very good device-to-device uniformity. In contrast, the performance of small molecule polycrystalline organic semiconductors depends very strongly on the grain size and the location of grain boundaries. Due to the random nature of the crystallization process, devices with small molecule semiconductors tend to be more variable than devices with amorphous semiconductors. Furthermore, polycrystalline semiconductors have larger surface roughness due to grain boundaries that can be problematic for the yield of the dielectric deposited on top. Here, we compare our amorphous polymer TFTs with devices fabricated using a state-of-the-art polycrystalline small molecule semiconductor (Lisicon® S1200) supplied by EMD Performance Materials Corp. These small molecule devices were fabricated with a very similar process except the small molecule semiconductor was polycrystalline and not patterned, the dielectric was 200nm thick and the gate was patterned by inkjet printing.<sup>27</sup> Figure 5-28 shows the difference in electrical performance

between the polymer and the small molecule devices. The improved uniformity of the polymer devices both in the on- and the off-state is clearly visible. Small molecule devices typically exhibit better on-state performance due to their crystallinity. This can be observed in the saturation mobility. Linear mobility is similar for the polymer and the small molecule devices because of the excellent contact resistance achieved here. Off-state performance is improved significantly by using the polymer semiconductor because of the thinner dielectric and the patterning of the semiconductor. This allows the polymer devices to be operated at significantly lower voltages.

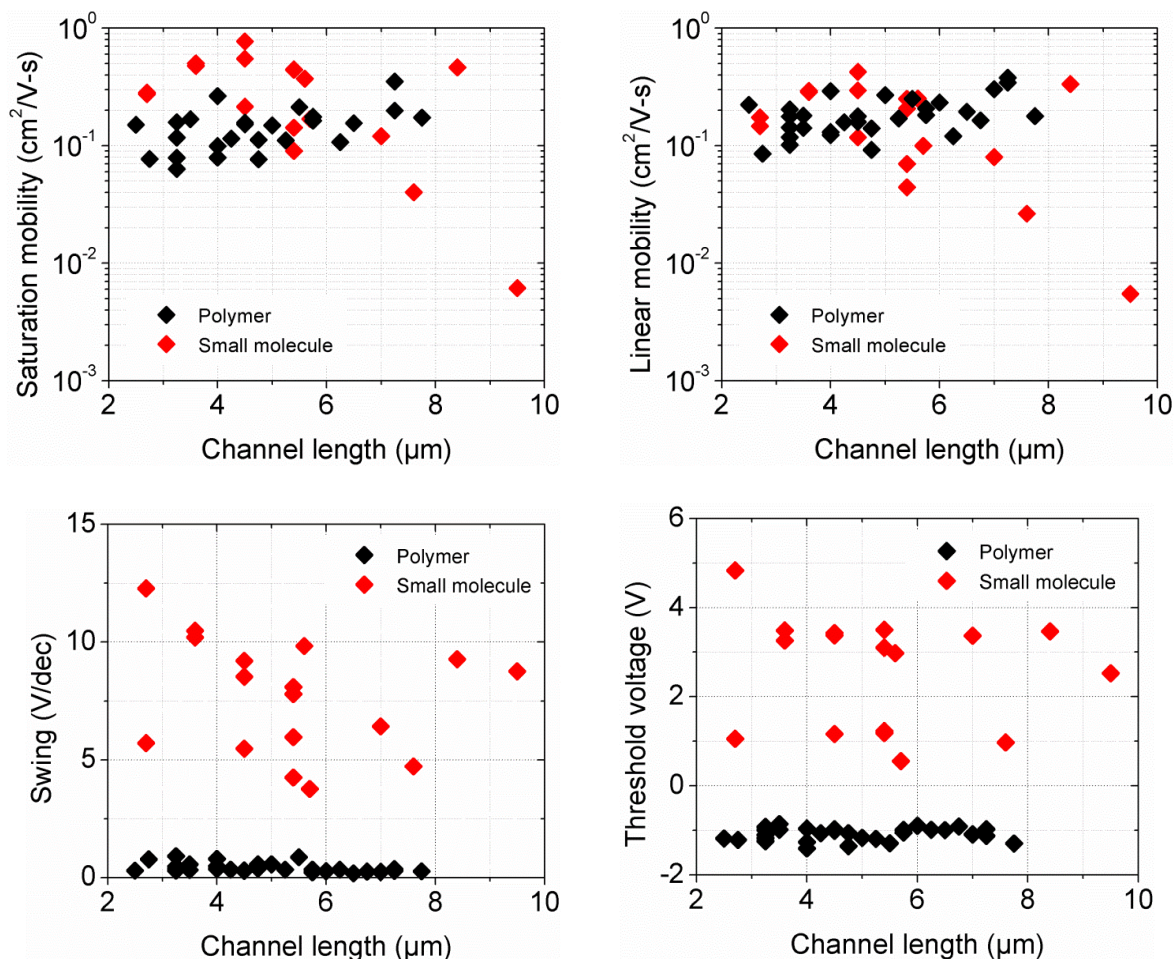


Figure 5-28. Comparison of amorphous polymer and polycrystalline small molecule semiconductor devices. Polymer devices exhibit better uniformity. Small molecule devices exhibit slightly higher saturation mobility. Linear mobility is comparable due to the excellent contact resistance achieved here. Both swing and threshold voltage are significantly better for the polymer devices due to a thinner gate dielectric and patterning of the semiconductor.

### 5.3.2.2 AC performance

Most applications require AC circuit operation. This means transistors have to switch at a high rate. Thus, it is important to measure the limitations of transistors at high frequencies. The transition frequency ( $f_T$ ), i.e. the frequency at which current gain becomes unity, was measured for these low-voltage transistors. Transistors were tested in an inverter configuration with an external load resistor (see Figure 5-29). The input current was calculated from the measured AC input voltage and overlap capacitances. The output current was calculated from the measured AC output voltage, the applied load resistance and the measured capacitance of the probe. Figure 5-30 shows typical curves for the input and the output current and the transition frequency corresponds to the point where the two curves intersect. This was also modelled using the transistor's small signal equivalent circuit including the overlap capacitances including channel overlap (see Figure 5-31). The model calculates a higher value for  $f_T$  of 99kHz (see Figure 5-32) than the experimental result for this device of 55kHz. The experimental output current is slightly lower than the theoretical value even at 100Hz and it drops slowly as the frequency is increased. This might be explained by a slight dispersion of the dielectric or effects in the semiconductor that cannot switch fast enough such as trapping events. The highest transition frequency that was achieved was 121kHz (see Figure 5-33). This is a very respectable result, particularly considering the low operating voltage achieved herein.

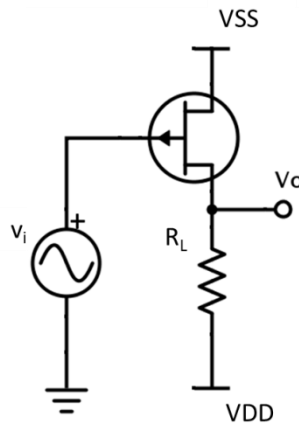


Figure 5-29. Circuit diagram of  $f_T$  measurement setup. A load resistor is applied to the transistor drain. A small signal AC signal  $v_i$  is applied to the gate and the out AC voltage  $v_o$  is measured.

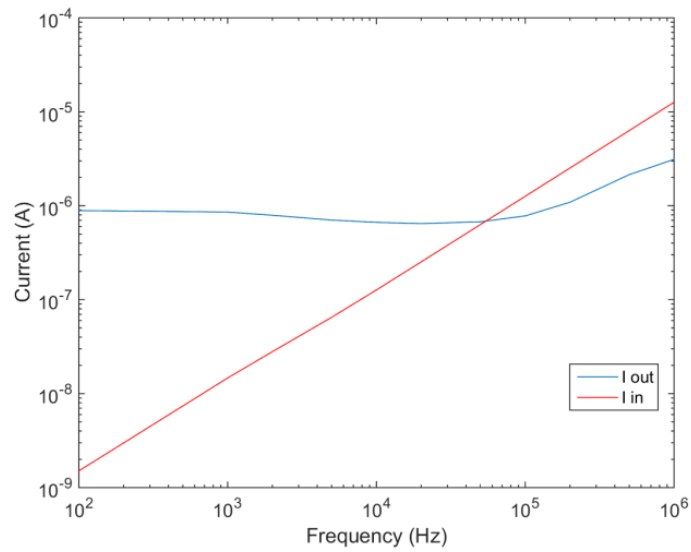


Figure 5-30. Experimental input and output currents giving a value of  $f_T$  of 55kHz.

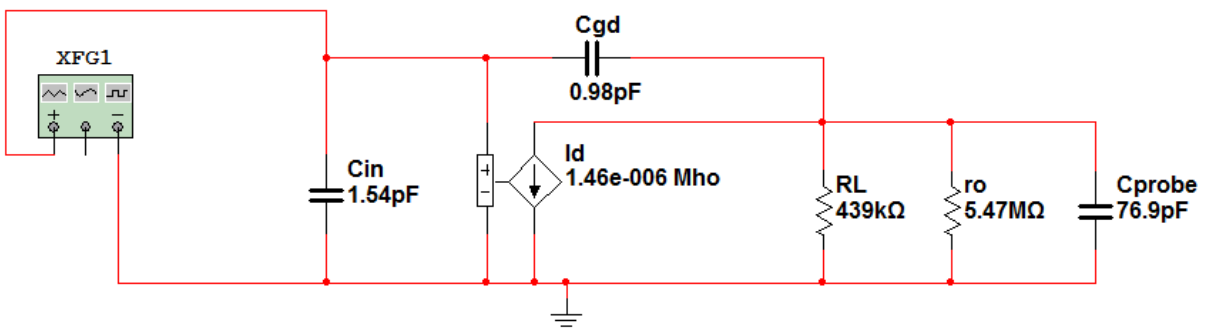


Figure 5-31. Small signal equivalent circuit including the transistor (current source and output resistance  $r_o$ ), the overlap capacitances including channel overlap as part of  $C_{in}$ , the load resistor  $R_L$  and the capacitance of the probe  $C_{probe}$ .

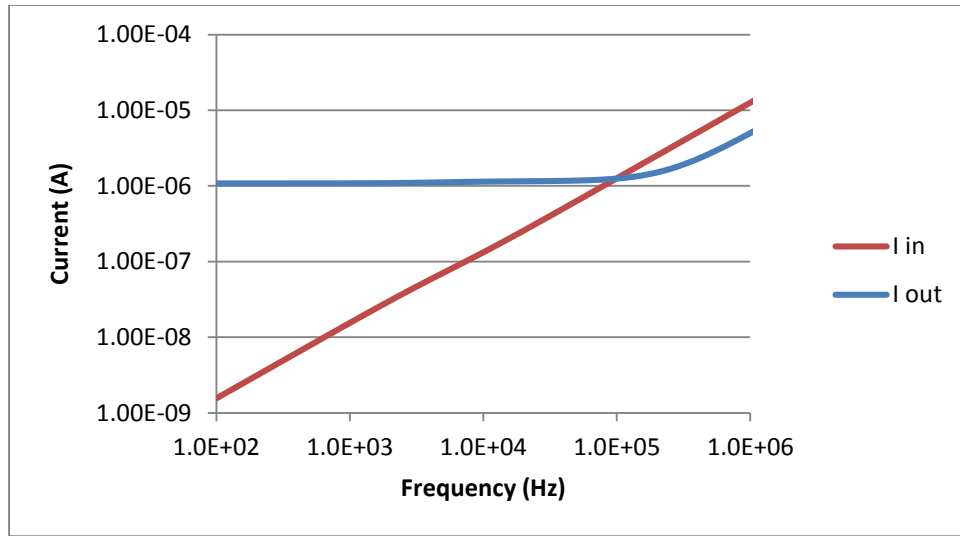


Figure 5-32. Modelling result for the same device as in Figure 5-30 using small signal equivalent circuit.

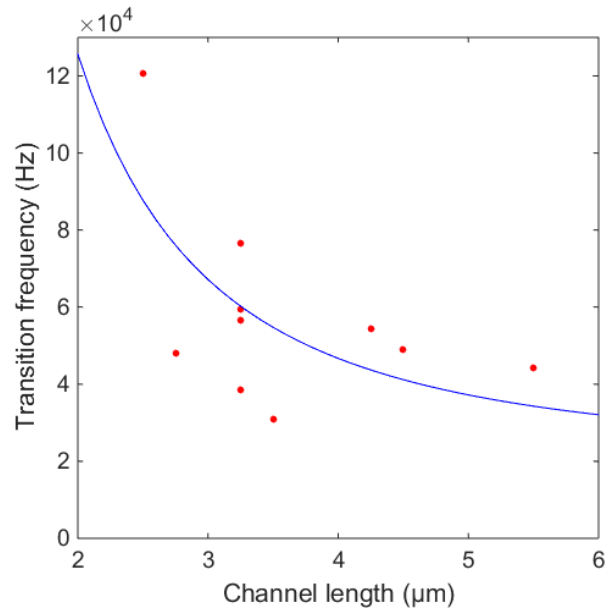


Figure 5-33. Experimental  $f_T$  for different channel lengths and fitted curve of  $1/L^2$  in blue.

### 5.3.2.3 Device stability

The bias stress stability of these devices was also examined. In any real application, devices need to operate consistently without shifts in their device parameters to ensure consistent circuit behavior. Devices were tested by applying a constant gate voltage equal to the supply voltage  $V_{DD}$  whilst keeping the drain and source at zero volts. Every five minutes an  $I_D$ - $V_G$  curve was measured with  $V_D=V_{DD}$ . Figure 5-34 shows these curves overlaid on each other for measurements conducted over 15 hours and Figure 5-35 shows the extracted device parameters. Initially, device parameters change quickly before levelling off. The threshold voltage shifts negatively whilst sub-threshold swing decreases. These changes are reversible if the gate voltage during the hold phase is cycled (see Figure 5-36). This suggests that the changes are due to the trapping of holes. As a negative gate voltage is applied, the Fermi level is moved closer to the HOMO level of the semiconductor filling traps with holes. This trapped positive charge results in the observed negative  $V_t$  shift. Swing becomes sharper since traps don't need to be filled anymore during turn-on. Mobility initially increases due to the larger number of filled deep trap states but then degrades slightly with time. This degradation is also seen during cycling. However, this degradation is very slow and of small magnitude. The maximum on-current changes by a larger fraction, mainly due to the shift in  $V_t$ . All of these shifts are relatively slow requiring several minutes. Thus, if these TFTs are switched at high AC frequencies, TFT performance will not shift during switching as long as the DC component of the applied voltages does not change.

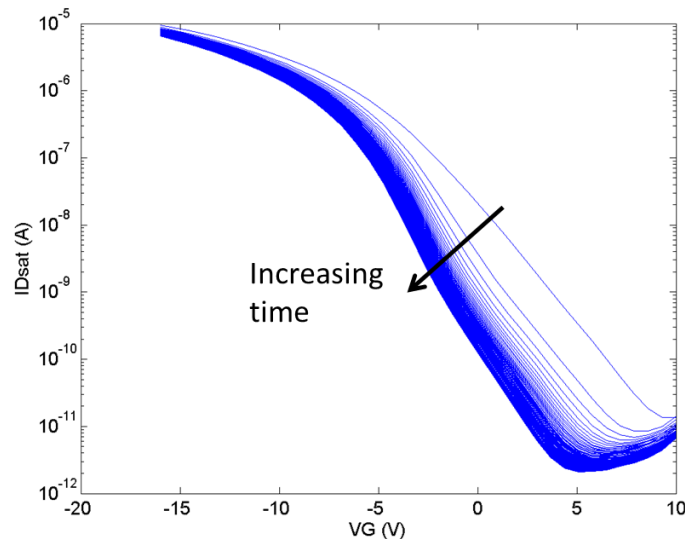


Figure 5-34. Overlaid transfer characteristics measured every 5 minutes over 15 hours.

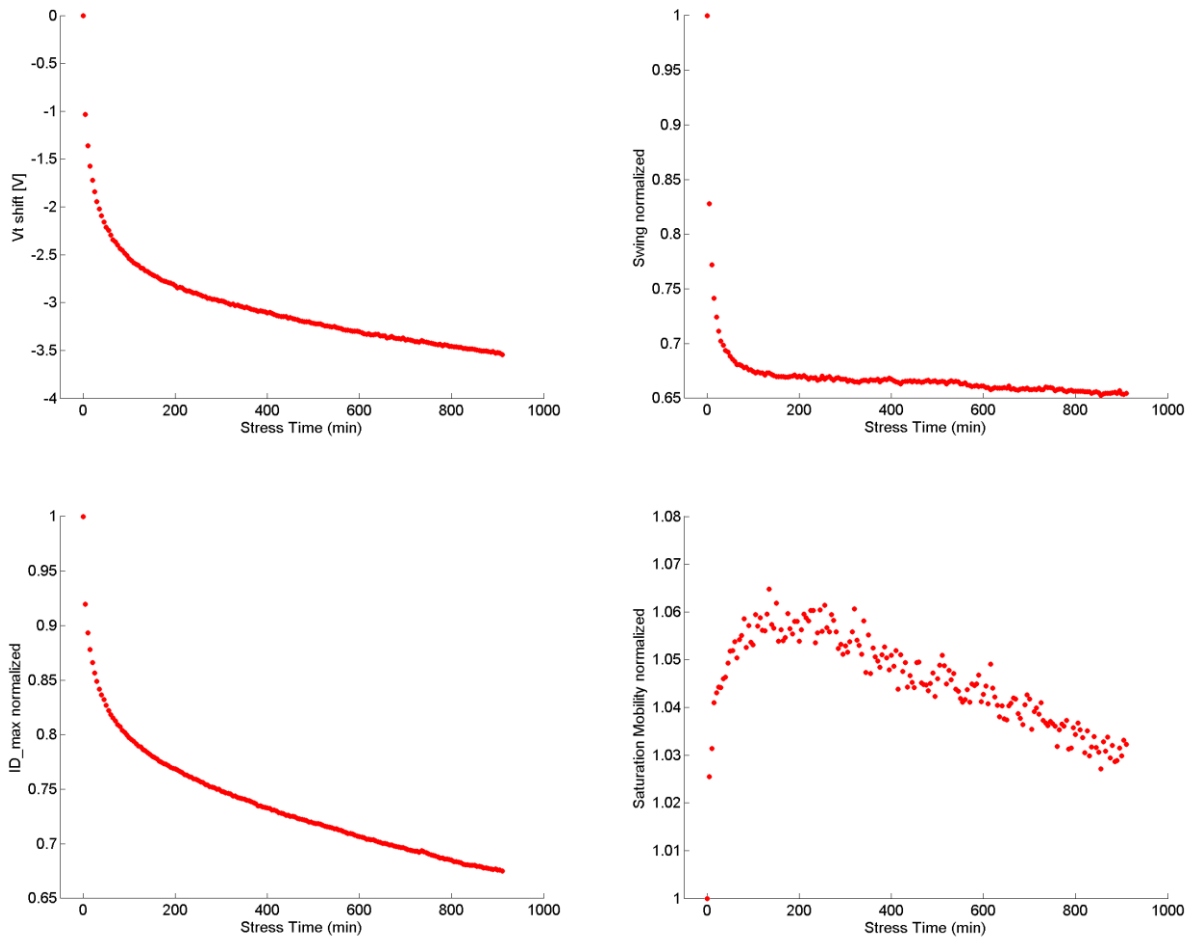


Figure 5-35. Transistor characteristics extracted from the transfer characteristics in Figure 5-34.

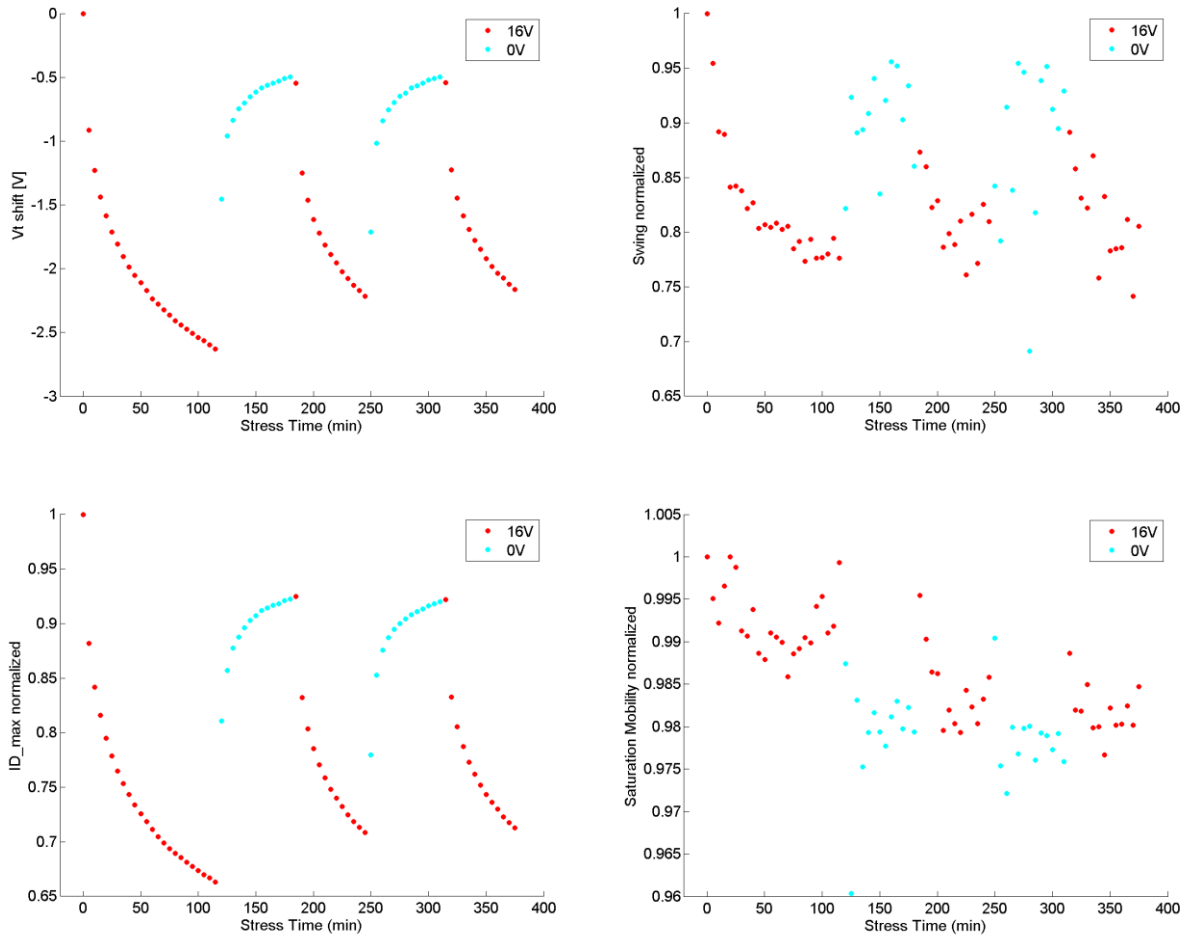


Figure 5-36. Cycling of hold voltage in between  $I_D$ - $V_G$  measurements showing reversibility of behavior with the exception of mobility.

## 5.4 Conclusions

In the first section of this chapter, a novel crystallization technique was demonstrated utilizing a scanned thermal gradient to anneal a solution processed, printable organic semiconductor. This leads to significantly improved electrical performance as well as significantly enlarged grains. Optimum crystallization and electrical performance can be obtained when scanning in parallel with the source and drain electrodes. The process is inherently compatible with roll-to-roll processing and flexible substrates, and results in significant performance improvements in printed organic transistors.

In the second section of this chapter, fully gravure printed organic thin-film transistors are demonstrated. Every transistor layer is high-speed printed at 1m/s. Highly-scaled source drain lines are printed with high yield down to 5 $\mu$ m linewidth and spacing. An amorphous polymer semiconductor is used for its good printability and uniformity. By patterning the semiconductor and scaling the dielectric, good off-state performance is achieved allowing operation below 5V. This is a significant step towards the realization of fully high-speed printed, low-cost, high-performance electronic systems.

## Chapter 6: Conclusions and future work

In this chapter, first the conclusions from this thesis are summarized. Then, suggestions are made for future work that could build specifically on the results of this thesis. Finally, broader suggestions are made to advance gravure printing as well as printed electronics in general.

### 6.1 Conclusions

In this thesis, gravure printing for printed electronics is advanced on multiple levels. The gravure process is advanced in terms of tooling and understanding of the printing physics of highly-scaled single layers as well as its application to substrate preparation and multi-layer device fabrication.

It is demonstrated how gravure printing can transform paper into a viable substrate for printed electronics. Printing of high-performance electronic devices onto paper has been limited by the large surface roughness and ink absorption of paper. Here, a local smoothing layer is printed using gravure to alleviate these problems. The ink viscosity when printing the smoothing layer is found to play a critical role in enabling smooth films without either ink absorption or printing artifacts. Organic thin-film transistors (OTFTs) are printed and optimized on top of the smoothed paper. Transistor performance is shown to be on-par with similar devices using the same materials and similar printing methods on plastic substrates demonstrating that smoothed paper is a viable substrate for printed electronics.

Next, the tooling of gravure cylinders was advanced by using a microfabrication based approach. Traditional roll making techniques are limited in terms of precision as feature sizes are scaled down. Both cell definition as well as surface roughness are limiting factors. This is overcome by fabricating a silicon printing plate using photolithography and standard etching techniques. A flexible metal printing plate that can be wrapped around a magnetic cylinder for high-throughput printing is fabricated from the silicon master employing a molding technique. The surface wetting properties of this metal printing plate can be modified by using a different surface layer and it is shown that this enables the printing of sub- $3\mu\text{m}$  features at  $1\text{m/s}$ .

The understanding of the printing physics of such highly-scaled features was advanced. It is demonstrated that more complex patterns experience proximity effects. The final printed patterns of lines printed in close proximity are studied and it is demonstrated how the proximity effect can be exploited to print otherwise unprintable patterns using assist features. By studying the ink levels inside gravure cells before and after ink transfer to the substrate, the mechanism for this effect is

studied and modelled. It is found that fluid flow in between cells that are connected by thin drag-out tails during transfer is responsible for the proximity effect and its dependence on printing conditions is understood.

Finally, advancements are made to printed organic thin-film transistors as an important technology driver and demonstrator for printed electronics. First, the crystallization of an organic semiconductor is significantly improved by employing a novel crystallization technique. By scanning a thermal gradient relative to the semiconductor on a plastic substrate, grain nucleation and growth are separated resulting in elongated and significantly enlarged grains. This improves electrical performance significantly. This technique is inherently suitable for roll-to-roll based manufacturing. The processing speed is significantly larger than previous directional crystallization techniques for organic semiconductors. Second, transistors are demonstrated where every layer is printed by gravure printing at 1m/s. Scaling of all layers both laterally and in terms of thickness and optimizing every layer results in good electrical performance, low-voltage operation and low variability. Transistors are characterized in terms of DC and AC performance as well as stability.

## **6.2 Future work**

There are a number of opportunities to build on the success of the gravure printed paper smoothing. There is a wide range of papers available and in use for a variety of applications. In order to use different papers, the process might need to be adapted for different papers. Since it was found that the polymer viscosity is a critical variable, further improvements can be expected from further tuning of the ink rheology. For example, different layers could be printed with different viscosity inks. The bottom layer(s) could be high viscosity to fill the paper pores whilst the top layer(s) could be lower viscosity to remove printing artefacts. Different smoothing materials could also be used to change the properties of the smoothed film such as temperature stability.

The novel roll fabrication method also offers opportunities for further work. The surface of the roll was modified using a boron-nitride hard layer. Further surface modifications can be considered. Different surface modifications can be developed for different applications with different inks and patterns. Selective surface modifications with hydrophobic land areas and hydrophilic cells could reduce the amount of ink residue on the land areas. This needs to be implemented without compromising the hardness and durability of the roll surface. Scale-up to larger roll dimensions and higher print speeds is another important area for further work.

The analysis of complex highly-scaled gravure patterns could be extended to a range of patterns. Closely spaced lines were chosen as a model system but real circuits contain a number of different patterns such as pads, lines, knees, tees, grids, via holes and others. Libraries and process models need to be developed to cover the full spectrum of patterns. The proximity effect was studied in the context of drag-out. It can also be studied in other contexts such as lubrication residue or ink squeezed out from cells during transfer when cells are closely spaced such as in 2D pads. It could also be induced on purpose for example by including very small cells that act as assist features. Further understanding could also be gained by conducting full 3D modelling.

The novel scanned annealing technique could also be improved further. It could be extended to other organic semiconductors. X-ray scattering and/or polarized spectroscopy measurements could be undertaken to further understand the origins of the significant performance improvements observed. Such measurements would have to account for the contacts, which clearly strongly affect crystallization. Currently, the technique relies on thermal energy being input from a heater bar in contact with the backside of the plastic substrate, which means heat needs to be conducted through the thickness of the substrate and a good thermal contact between the substrate and the bar is crucial. Using optical energy input could simplify this. Process throughput could also be improved by increasing the energy intensity and/or using multiple energy sources in parallel.

The main area offering opportunities for improvement of the fully gravure printed transistors demonstrated here is the gate dielectric. Especially the interplay with the printed gate and potentially the roughness of the underlying layers can be addressed to improve yield for thin dielectrics. A different approach would be to employ organic high-k materials to combine high gate capacitance with high yield due to a larger dielectric thickness. Organic semiconductors constantly improve due to new materials being synthesized and this will lead to further device performance improvements in the future. The next step will be to integrate these transistors with other high-speed printed devices such as sensors, passives, energy supplies or optical devices to create fully high-speed printed systems.

More generally, one of the next big topics that needs to be tackled to further advance high-resolution gravure printing is the doctor blade. Non-idealities due to the doctor blade were addressed in this thesis multiple times. Whilst non-idealities in traditional roll making were solved with a microfabrication based process, no significant effort has been undertaken to fabricate doctor blades that are optimized for high-resolution printing. These doctor blades need to be optimized in terms of dimensions, surface wetting properties and hardness. Commercial doctor blades could be a starting point for the application of coatings such as hard, hydrophobic ceramics such as ceria. New doctor blades would have to be evaluated not only in terms of printing performance but also

in terms of durability of both the blade and the roll. Further understanding is also required in terms of defect generation in the doctor blades that lead to variability and yield problems due to catastrophic streaking. Trade-offs between defect generation and lubrication film thickness need to be explored. Strategies such as a double blade setup could also be used to alleviate defect problems.

More generally, one of the biggest challenges for printed electronics at the moment is variability. There have been many reports pushing device performance, including this thesis, leading to fully printed devices with performance suitable for some applications. However, any realistic circuit application requires highly uniform devices fabricated with high yield. Some effort has been directed towards this direction, again including this thesis, however, further efforts are needed. Some improvements will come out of the more controlled tools and clean room environments available in industrial settings compared with research laboratories. However, basic research can add further insights into the fundamental mechanisms that lead to variability such as the above mentioned doctor blade defects or the effect of substrate contamination on the wetting behavior of scaled features. Another approach might be the development of fault tolerant circuits for printed electronics. If such efforts result in printed circuits that deliver consistent performance, printed electronics will be able to target a large number of interesting applications.

## Chapter 7: References

- [1] Subramanian, V., Chang, J. B., Vornbrock, A. de la F., Huang, D. C., Jagannathan, L., Liao, F., Mattis, B., Molesa, S., Redinger, D. R., et al., "Printed electronics for low-cost electronic systems: Technology status and application development," 2008, 17–24, IEEE.
- [2] Arias, A. C., MacKenzie, J. D., McCulloch, I., Rivnay, J., Salleo, A., "Materials and Applications for Large Area Electronics: Solution-Based Approaches," *Chem. Rev.* **110**(1), 3–24 (2010).
- [3] Moonen, P. F., Yakimets, I., Huskens, J., "Fabrication of Transistors on Flexible Substrates: from Mass-Printing to High-Resolution Alternative Lithography Strategies," *Adv. Mater.* **24**(41), 5526–5541 (2012).
- [4] Rustin, R., "Overview of plastic substrates for printed electronics."
- [5] Facchetti, A., "Semiconductors for organic transistors," *Mater. Today* **10**(3), 28–37 (2007).
- [6] Allard, S., Forster, M., Souharce, B., Thiem, H., Scherf, U., "Organic Semiconductors for Solution-Processable Field-Effect Transistors (OFETs)," *Angew. Chem. Int. Ed.* **47**(22), 4070–4098 (2008).
- [7] Sirringhaus, H., "Materials and Applications for Solution-Processed Organic Field-Effect Transistors," *Proc. IEEE* **97**(9), 1570–1579 (2009).
- [8] Sun, K., Zhang, S., Li, P., Xia, Y., Zhang, X., Du, D., Isikgor, F. H., Ouyang, J., "Review on application of PEDOTs and PEDOT:PSS in energy conversion and storage devices," *J. Mater. Sci. Mater. Electron.* **26**(7), 4438–4462 (2015).
- [9] Huang, D., Liao, F., Molesa, S., Redinger, D., Subramanian, V., "Plastic-Compatible Low Resistance Printable Gold Nanoparticle Conductors for Flexible Electronics," *J. Electrochem. Soc.* **150**(7), G412 (2003).
- [10] Perelaer, J., Smith, P. J., Mager, D., Soltman, D., Volkman, S. K., Subramanian, V., Korvink, J. G., Schubert, U. S., "Printed electronics: the challenges involved in printing devices, interconnects, and contacts based on inorganic materials," *J. Mater. Chem.* **20**(39), 8446 (2010).
- [11] Volkman, S. K., Yin, S., Bakhishev, T., Puntambekar, K., Subramanian, V., Toney, M. F., "Mechanistic Studies on Sintering of Silver Nanoparticles," *Chem. Mater.* **23**(20), 4634–4640 (2011).
- [12] Sirringhaus, H., "High-Resolution Inkjet Printing of All-Polymer Transistor Circuits," *Science* **290**(5499), 2123–2126 (2000).
- [13] Ling, M. M., Bao, Z., "Thin Film Deposition, Patterning, and Printing in Organic Thin Film Transistors," *Chem. Mater.* **16**(23), 4824–4840 (2004).
- [14] Molesa, S. E., de la Fuente Vornbrock, A., Chang, P. C., Subramanian, V., "Low-voltage inkjetted organic transistors for printed RFID and display applications," 109–112, IEEE.
- [15] Noh, Y.-Y., Zhao, N., Caironi, M., Sirringhaus, H., "Downscaling of self-aligned, all-printed polymer thin-film transistors," *Nat Nano* **2**(12), 784–789 (2007).
- [16] Sekitani, T., Noguchi, Y., Zschieschang, U., Klauk, H., Someya, T., "Organic transistors manufactured using inkjet technology with subfemtoliter accuracy," *Proc. Natl. Acad. Sci.* **105**(13), 4976–4980 (2008).
- [17] Tseng, H.-Y., Subramanian, V., "All inkjet-printed, fully self-aligned transistors for low-cost circuit applications," *Org. Electron.* **12**(2), 249–256 (2011).
- [18] Tseng, H.-Y., Purushothaman, B., Anthony, J., Subramanian, V., "High-speed organic transistors fabricated using a novel hybrid-printing technique," *Org. Electron.* **12**(7), 1120–1125 (2011).

- [19] Fukuda, K., Takeda, Y., Mizukami, M., Kumaki, D., Tokito, S., “Fully Solution-Processed Flexible Organic Thin Film Transistor Arrays with High Mobility and Exceptional Uniformity,” *Sci. Rep.* **4**, 3947 (2014).
- [20] Fukuda, K., Takeda, Y., Yoshimura, Y., Shiwaku, R., Tran, L. T., Sekine, T., Mizukami, M., Kumaki, D., Tokito, S., “Fully-printed high-performance organic thin-film transistors and circuitry on one-micron-thick polymer films,” *Nat. Commun.* **5** (2014).
- [21] Yoshimura, Y., Takeda, Y., Fukuda, K., Kumaki, D., Tokito, S., “High-speed operation in printed organic inverter circuits with short channel length,” *Org. Electron.* **15**(11), 2696–2701 (2014).
- [22] Grau, G., Kitsomboonloha, R., Swisher, S. L., Kang, H., Subramanian, V., “Printed Transistors on Paper: Towards Smart Consumer Product Packaging,” *Adv. Funct. Mater.* **24**(32), 5067–5074 (2014).
- [23] Kang, H., Kitsomboonloha, R., Ulmer, K., Stecker, L., Grau, G., Jang, J., Subramanian, V., “Megahertz-class printed high mobility organic thin-film transistors and inverters on plastic using attoliter-scale high-speed gravure-printed sub-5 $\mu$ m gate electrodes,” *Org. Electron.* **15**(12), 3639–3647 (2014).
- [24] Subramanian, V., Cen, J., de la Fuente Vornbrock, A., Grau, G., Kang, H., Kitsomboonloha, R., Soltman, D., Tseng, H.-Y., “High-Speed Printing of Transistors: From Inks to Devices,” *Proc. IEEE* **103**(4), 567–582 (2015).
- [25] Fukuda, K., Yoshimura, Y., Okamoto, T., Takeda, Y., Kumaki, D., Katayama, Y., Tokito, S., “Reverse-Offset Printing Optimized for Scalable Organic Thin-Film Transistors with Submicrometer Channel Lengths,” *Adv. Electron. Mater.* **1**(8), 1500145 (2015).
- [26] Grau, G., Kitsomboonloha, R., Kang, H., Subramanian, V., “High performance printed organic transistors using a novel scanned thermal annealing technology,” *Org. Electron.* **20**, 150–157 (2015).
- [27] Kitsomboonloha, R., Kang, H., Grau, G., Scheideler, W., Subramanian, V., “MHz-Range Fully Printed High-Performance Thin-Film Transistors by Using High-Resolution Gravure-Printed Lines,” *Adv. Electron. Mater.* **1**(12), 1500155 (2015).
- [28] Grau, G., Subramanian, V., “Fully High-Speed Gravure Printed, Low-Variability, High-Performance Organic Polymer Transistors with Sub-5V Operation,” *Adv. Electron. Mater.* **2**(4) (2016).
- [29] Chang, J. B., Liu, V., Subramanian, V., Sivula, K., Luscombe, C., Murphy, A., Liu, J., Fréchet, J. M. J., “Printable polythiophene gas sensor array for low-cost electronic noses,” *J. Appl. Phys.* **100**(1), 14506 (2006).
- [30] Someya, T., Kato, Y., Sekitani, T., Iba, S., Noguchi, Y., Murase, Y., Kawaguchi, H., Sakurai, T., “Conformable, flexible, large-area networks of pressure and thermal sensors with organic transistor active matrixes,” *Proc. Natl. Acad. Sci. U. S. A.* **102**(35), 12321–12325 (2005).
- [31] Park, E. S., Chen, Y., Liu, T.-J. K., Subramanian, V., “A New Switching Device for Printed Electronics: Inkjet-Printed Microelectromechanical Relay,” *Nano Lett.* **13**(11), 5355–5360 (2013).
- [32] Chung, S., Ul Karim, M. A., Kwon, H.-J., Subramanian, V., “High-Performance Inkjet-Printed Four-Terminal Microelectromechanical Relays and Inverters,” *Nano Lett.* **15**(5), 3261–3266 (2015).

- [33] Braam, K., Subramanian, V., “A Stencil Printed, High Energy Density Silver Oxide Battery Using a Novel Photopolymerizable Poly(acrylic acid) Separator,” *Adv. Mater.* **27**(4), 689–694 (2015).
- [34] Yang, J., Vak, D., Clark, N., Subbiah, J., Wong, W. W. H., Jones, D. J., Watkins, S. E., Wilson, G., “Organic photovoltaic modules fabricated by an industrial gravure printing proofer,” *Sol. Energy Mater. Sol. Cells* **109**, 47–55 (2013).
- [35] Tekoglu, S., Hernandez-Sosa, G., Kluge, E., Lemmer, U., Mechau, N., “Gravure printed flexible small-molecule organic light emitting diodes,” *Org. Electron.* **14**(12), 3493–3499 (2013).
- [36] Cook, B. S., Shamim, A., “Inkjet Printing of Novel Wideband and High Gain Antennas on Low-Cost Paper Substrate,” *IEEE Trans. Antennas Propag.* **60**(9), 4148–4156 (2012).
- [37] McKerricher, G., Gonzalez Perez, J., Shamim, A., “Fully Inkjet Printed RF Inductors and Capacitors Using Polymer Dielectric and Silver Conductive Ink With Through Vias,” *IEEE Trans. Electron Devices* **62**(3), 1002–1009 (2015).
- [38] Namsoo Lim., Jaeyoung Kim., Soojin Lee., Namyoung Kim., Gyoujin Cho., “Screen Printed Resonant Tags for Electronic Article Surveillance Tags,” *Adv. Packag. IEEE Trans. On* **32**(1), 72–76 (2009).
- [39] Sekitani, T., Nakajima, H., Maeda, H., Fukushima, T., Aida, T., Hata, K., Someya, T., “Stretchable active-matrix organic light-emitting diode display using printable elastic conductors,” *Nat Mater* **8**(6), 494–499 (2009).
- [40] Sekitani, T., Takamiya, M., Noguchi, Y., Nakano, S., Kato, Y., Sakurai, T., Someya, T., “A large-area wireless power-transmission sheet using printed organic transistors and plastic MEMS switches,” *Nat Mater* **6**(6), 413–417 (2007).
- [41] Krebs, F. C., “Fabrication and processing of polymer solar cells: A review of printing and coating techniques,” *Sol. Energy Mater. Sol. Cells* **93**(4), 394–412 (2009).
- [42] Hamsch, M., Reuter, K., Stanel, M., Schmidt, G., Kempa, H., Fügmann, U., Hahn, U., Hübler, A. C., “Uniformity of fully gravure printed organic field-effect transistors,” *Mater. Sci. Eng. B* **170**(1–3), 93–98 (2010).
- [43] Park, J.-U., Hardy, M., Kang, S. J., Barton, K., Adair, K., Mukhopadhyay, D. kishore., Lee, C. Y., Strano, M. S., Alleyne, A. G., et al., “High-resolution electrohydrodynamic jet printing,” *Nat. Mater.* **6**(10), 782–789 (2007).
- [44] Hannebauer, H., Dullweber, T., Falcon, T., Brendel, R., “Fineline Printing Options for High Efficiencies and Low Ag Paste Consumption,” *Energy Procedia* **38**, 725–731 (2013).
- [45] Erath, D., Filipović, A., Retzlaff, M., Goetz, A. K., Clement, F., Biro, D., Preu, R., “Advanced screen printing technique for high definition front side metallization of crystalline silicon solar cells,” *Sol. Energy Mater. Sol. Cells* **94**(1), 57–61 (2010).
- [46] “International Technology Roadmap for Photovoltaic (ITRPV), 2014 Results, Revision 1.”, (2015).
- [47] Joyce, M. J., Fleming III, P. D., Avuthu, S. G., Emamian, S., Eshkeiti, A., Atashbar, M., Donato, T., “Contribution of Flexo Process Variables to Fine Line Ag Electrode Performance,” *Int. J. Eng. Res. Technol.* **3**, ESRSA Publications (2014).
- [48] Sung, D., de la Fuente Vornbrock, A., Subramanian, V., “Scaling and Optimization of Gravure-Printed Silver Nanoparticle Lines for Printed Electronics,” *IEEE Trans. Compon. Packag. Technol.* **33**(1), 105–114 (2010).

- [49] Kitsomboonloha, R., Morris, S. J. S., Rong, X., Subramanian, V., “Femtoliter-Scale Patterning by High-Speed, Highly Scaled Inverse Gravure Printing,” *Langmuir* **28**(48), 16711–16723 (2012).
- [50] Nallan, H. C., Sadie, J. A., Kitsomboonloha, R., Volkman, S. K., Subramanian, V., “Systematic Design of Jettable Nanoparticle-Based Inkjet Inks: Rheology, Acoustics, and Jettability,” *Langmuir* **30**(44), 13470–13477 (2014).
- [51] Soltman, D., Smith, B., Kang, H., Morris, S. J. S., Subramanian, V., “Methodology for Inkjet Printing of Partially Wetting Films,” *Langmuir* **26**(19), 15686–15693 (2010).
- [52] Kang, H., Soltman, D., Subramanian, V., “Hydrostatic optimization of inkjet-printed films,” *Langmuir* **26**(13), 11568–11573 (2010).
- [53] Soltman, D., Smith, B., Morris, S. J. S., Subramanian, V., “Inkjet printing of precisely defined features using contact-angle hysteresis,” *J. Colloid Interface Sci.* **400**, 135–139 (2013).
- [54] de Gans, B.-J., Schubert, U. S., “Inkjet Printing of Well-Defined Polymer Dots and Arrays,” *Langmuir* **20**(18), 7789–7793 (2004).
- [55] Hu, H., Larson, R. G., “Marangoni Effect Reverses Coffee-Ring Depositions,” *J. Phys. Chem. B* **110**(14), 7090–7094 (2006).
- [56] Lim, J. A., Lee, W. H., Lee, H. S., Lee, J. H., Park, Y. D., Cho, K., “Self-Organization of Ink-jet-Printed Triisopropylsilylethynyl Pentacene via Evaporation-Induced Flows in a Drying Droplet,” *Adv. Funct. Mater.* **18**(2), 229–234 (2008).
- [57] Soltman, D., Subramanian, V., “Inkjet-Printed Line Morphologies and Temperature Control of the Coffee Ring Effect,” *Langmuir* **24**(5), 2224–2231 (2008).
- [58] Janssen, D., De Palma, R., Verlaak, S., Heremans, P., Dehaen, W., “Static solvent contact angle measurements, surface free energy and wettability determination of various self-assembled monolayers on silicon dioxide,” *Thin Solid Films* **515**(4), 1433–1438 (2006).
- [59] Cen, J., Kitsomboonloha, R., Subramanian, V., “Cell Filling in Gravure Printing for Printed Electronics,” *Langmuir* **30**(45), 13716–13726 (2014).
- [60] Bankoff, S. G., “Entrapment of gas in the spreading of a liquid over a rough surface,” *AIChE J.* **4**(1), 24–26 (1958).
- [61] Reddy, S., Schunk, P. R., Bonnecaze, R. T., “Dynamics of low capillary number interfaces moving through sharp features,” *Phys. Fluids* **17**(12), 122104 (2005).
- [62] Brethour, J. M., Benkeira, H., “Filling and Emptying of Gravure Cells – Experiment and CFD Comparison,” presented at ISCST, 2002, Minneapolis.
- [63] Noh, Y.-Y., Siringhaus, H., “Ultra-thin polymer gate dielectrics for top-gate polymer field-effect transistors,” *Org. Electron.* **10**(1), 174–180 (2009).
- [64] Jung, Y., Kline, R. J., Fischer, D. A., Lin, E. K., Heeney, M., McCulloch, I., DeLongchamp, D. M., “The Effect of Interfacial Roughness on the Thin Film Morphology and Charge Transport of High-Performance Polythiophenes,” *Adv. Funct. Mater.* **18**(5), 742–750 (2008).
- [65] Chabiny, M. L., Lujan, R., Endicott, F., Toney, M. F., McCulloch, I., Heeney, M., “Effects of the surface roughness of plastic-compatible inorganic dielectrics on polymeric thin film transistors,” *Appl. Phys. Lett.* **90**(23), 233508 (2007).
- [66] Kitsomboonloha, R., Subramanian, V., “Lubrication-Related Residue as a Fundamental Process Scaling Limit to Gravure Printed Electronics,” *Langmuir* **30**(12), 3612–3624 (2014).

- [67] Hariprasad, D., Grau, G., Schunk, R., Tjiptowidjojo, K., “A computational model for doctoring fluid films in gravure printing,” *J. Appl. Phys.* **119**, 135303 (2016).
- [68] Ceyhan, U., Morris, S. J. S., “On tail formation during gravure printing of sessile drops,” presented at 67th Annual Meeting of the APS Division of Fluid Dynamics, 2014, San Francisco.
- [69] Darhuber, A. A., Troian, S. M., Wagner, S., “Physical mechanisms governing pattern fidelity in microscale offset printing,” *J. Appl. Phys.* **90**(7), 3602 (2001).
- [70] Kapur, N., “A parametric study of direct gravure coating,” *Chem. Eng. Sci.* **58**(13), 2875–2882 (2003).
- [71] Yin, X., Kumar, S., “Flow visualization of the liquid emptying process in scaled-up gravure grooves and cells,” *Chem. Eng. Sci.* **61**(4), 1146–1156 (2006).
- [72] Cai, S., Bhushan, B., “Meniscus and viscous forces during normal separation of liquid-mediated contacts,” *Nanotechnology* **18**(46), 465704 (2007).
- [73] Huang, W.-X., Lee, S.-H., Sung, H. J., Lee, T.-M., Kim, D.-S., “Simulation of liquid transfer between separating walls for modeling micro-gravure-offset printing,” *Int. J. Heat Fluid Flow* **29**(5), 1436–1446 (2008).
- [74] Hoda, N., Kumar, S., “Boundary integral simulations of liquid emptying from a model gravure cell,” *Phys. Fluids* **20**(9), 92106 (2008).
- [75] Kang, H. W., Sung, H. J., Lee, T.-M., Kim, D.-S., Kim, C.-J., “Liquid transfer between two separating plates for micro-gravure-offset printing,” *J. Micromechanics Microengineering* **19**(1), 15025 (2009).
- [76] Dodds, S., Carvalho, M. da S., Kumar, S., “Stretching and slipping of liquid bridges near plates and cavities,” *Phys. Fluids* **21**(9), 92103 (2009).
- [77] Ghadiri, F., Ahmed, D. H., Sung, H. J., Shirani, E., “Non-Newtonian ink transfer in gravure–offset printing,” *Int. J. Heat Fluid Flow* **32**(1), 308–317 (2011).
- [78] Ahmed, D. H., Sung, H. J., Kim, D.-S., “Simulation of non-Newtonian ink transfer between two separating plates for gravure-offset printing,” *Int. J. Heat Fluid Flow* **32**(1), 298–307 (2011).
- [79] Sankaran, A. K., Rothstein, J. P., “Effect of viscoelasticity on liquid transfer during gravure printing,” *J. Non-Newton. Fluid Mech.* **175–176**, 64–75 (2012).
- [80] Nguyen, H. A. D., Lee, C., Shin, K.-H., Lee, D., “An Investigation of the Ink-Transfer Mechanism During the Printing Phase of High-Resolution Roll-to-Roll Gravure Printing,” *IEEE Trans. Compon. Packag. Manuf. Technol.* **5**(10), 1516–1524 (2015).
- [81] Kumar, S., “Liquid Transfer in Printing Processes: Liquid Bridges with Moving Contact Lines,” *Annu. Rev. Fluid Mech.* **47**(1), 67–94 (2015).
- [82] Grau, G., Cen, J., Kang, H., Kitsomboonloha, R., Scheideler, W. J., Subramanian, V., “Gravure-printed electronics: Recent progress in tooling development, understanding of printing physics, and realization of printed devices,” *Flex. Print. Electron.* (invited review under review).
- [83] Kang, H., Kitsomboonloha, R., Jang, J., Subramanian, V., “High-Performance Printed Transistors Realized Using Femtoliter Gravure-Printed Sub-10  $\mu\text{m}$  Metallic Nanoparticle Patterns and Highly Uniform Polymer Dielectric and Semiconductor Layers,” *Adv. Mater.* **24**(22), 3065–3069 (2012).
- [84] Minemawari, H., Yamada, T., Matsui, H., Tsutsumi, J. 'ya., Haas, S., Chiba, R., Kumai, R., Hasegawa, T., “Inkjet printing of single-crystal films,” *Nature* **475**(7356), 364–367 (2011).

- [85] Yuan, Y., Giri, G., Ayzner, A. L., Zoombelt, A. P., Mannsfeld, S. C. B., Chen, J., Nordlund, D., Toney, M. F., Huang, J., et al., “Ultra-high mobility transparent organic thin film transistors grown by an off-centre spin-coating method,” *Nat. Commun.* **5**, 3005 (2014).
- [86] de la Fuente Vornbrock, A., Sung, D., Kang, H., Kitsomboonloha, R., Subramanian, V., “Fully gravure and ink-jet printed high speed pBTTT organic thin film transistors,” *Org. Electron.* **11**(12), 2037–2044 (2010).
- [87] Sirringhaus, H., Kawase, T., Friend, R. H., Shimoda, T., Inbasekaran, M., Wu, W., Woo, E. P., “High-Resolution Inkjet Printing of All-Polymer Transistor Circuits,” *Science* **290**(5499), 2123–2126 (2000).
- [88] Noh, Y.-Y., Zhao, N., Caironi, M., Sirringhaus, H., “Downscaling of self-aligned, all-printed polymer thin-film transistors,” *Nat. Nanotechnol.* **2**(12), 784–789 (2007).
- [89] Sele, C. W., von Werne, T., Friend, R. H., Sirringhaus, H., “Lithography-Free, Self-Aligned Inkjet Printing with Sub-Hundred-Nanometer Resolution,” *Adv. Mater.* **17**(8), 997–1001 (2005).
- [90] Tobjörk, D., Österbacka, R., “Paper Electronics,” *Adv. Mater.* **23**, 1935–1961 (2011).
- [91] Kim, J.-Y., Park, S. H., Jeong, T., Bae, M. J., Song, S., Lee, J., Han, I. T., Jung, D., Yu, S., “Paper as a Substrate for Inorganic Powder Electroluminescence Devices,” *IEEE Trans. Electron Devices* **57**(6), 1470–1474 (2010).
- [92] Lim, W., Douglas, E. A., Norton, D. P., Pearton, S. J., Ren, F., Heo, Y.-W., Son, S. Y., Yuh, J. H., “Low-voltage indium gallium zinc oxide thin film transistors on paper substrates,” *Appl. Phys. Lett.* **96**(5), 53510 (2010).
- [93] Lamprecht, B., Thünauer, R., Ostermann, M., Jakopic, G., Leising, G., “Organic photodiodes on newspaper,” *Phys. Status Solidi A* **202**(5), R50–R52 (2005).
- [94] Yong-Hoon Kim., Dae-Gyu Moon., Jeong-In Han., “Organic TFT array on a paper substrate,” *Electron Device Lett. IEEE* **25**(10), 702–704 (2004).
- [95] Kim, Y. H., Moon, D. G., Kim, W. K., Han, J. I., “Organic thin-film devices on paper substrates,” *J. Soc. Inf. Disp.* **13**(10), 829–833 (2005).
- [96] Li, Y., Liu, C., Xu, Y., Minari, T., Darmawan, P., Tsukagoshi, K., “Solution-processed organic crystals for field-effect transistor arrays with smooth semiconductor/dielectric interface on paper substrates,” *Org. Electron.* **13**(5), 815–819 (2012).
- [97] Zhang, T., Wang, X., Li, T., Guo, Q., Yang, J., “Fabrication of flexible copper-based electronics with high-resolution and high-conductivity on paper via inkjet printing,” *J. Mater. Chem. C* **2**(2), 286 (2014).
- [98] Lim, W., Douglas, E. A., Kim, S.-H., Norton, D. P., Pearton, S. J., Ren, F., Shen, H., Chang, W. H., “High mobility InGaZnO<sub>4</sub> thin-film transistors on paper,” *Appl. Phys. Lett.* **94**(7), 72103 (2009).
- [99] Zschieschang, U., Yamamoto, T., Takimiya, K., Kuwabara, H., Ikeda, M., Sekitani, T., Someya, T., Klauk, H., “Organic Electronics on Banknotes,” *Adv. Mater.* **23**(5), 654–658 (2011).
- [100] Härtling, M., Zhang, J., Gamota, D. R., Britton, D. T., “Fully printed silicon field effect transistors,” *Appl. Phys. Lett.* **94**(19), 193509 (2009).
- [101] Yoon, B., Ham, D.-Y., Yarimaga, O., An, H., Lee, C. W., Kim, J.-M., “Inkjet Printing of Conjugated Polymer Precursors on Paper Substrates for Colorimetric Sensing and Flexible Electrothermochromic Display,” *Adv. Mater.* **23**(46), 5492–5497 (2011).
- [102] Lee, C.-G., Dodabalapur, A., “Solution-Processed High-k Dielectric, ZrO<sub>2</sub>, and Integration in Thin-Film Transistors,” *J. Electron. Mater.* **41**(5), 895–898 (2012).

- [103] Li, X., Ballerini, D. R., Shen, W., “A perspective on paper-based microfluidics: Current status and future trends,” *Biomicrofluidics* **6**(1), 11301-011301–011313 (2012).
- [104] Molesa, S. E., De La Fuente Vornbrock, A., Chang, P. C., Subramanian, V., “Low-voltage inkjetted organic transistors for printed RFID and display applications,” *Tech. Dig. - Int. Electron Devices Meet. IEDM* **2005**, 109–112, IEEE (2005).
- [105] Klauk, H., Halik, M., Zschieschang, U., Schmid, G., Radlik, W., Weber, W., “High-mobility polymer gate dielectric pentacene thin film transistors,” *J. Appl. Phys.* **92**(9), 5259 (2002).
- [106] Grau, G., Subramanian, V., “Effect of substrate roughness on the performance of printed OTFTs on paper substrates,” presented at MRS Fall Meeting, 3 December 2013, Boston.
- [107] McCulloch, I., Heeney, M., Bailey, C., Genevicius, K., MacDonald, I., Shkunov, M., Sparrowe, D., Tierney, S., Wagner, R., et al., “Liquid-crystalline semiconducting polymers with high charge-carrier mobility,” *Nat. Mater.* **5**(4), 328–333 (2006).
- [108] Xue, F., Liu, Z., Su, Y., Varahramyan, K., “Inkjet printed silver source/drain electrodes for low-cost polymer thin film transistors,” *Microelectron. Eng.* **83**(2), 298–302 (2006).
- [109] Kline, R. J., DeLongchamp, D. M., Fischer, D. A., Lin, E. K., Heeney, M., McCulloch, I., Toney, M. F., “Significant dependence of morphology and charge carrier mobility on substrate surface chemistry in high performance polythiophene semiconductor films,” *Appl. Phys. Lett.* **90**(6), 62117 (2007).
- [110] Hennig, G., Selbmann, K.-H., Brockelt, A., “Laser engraving in gravure industry,” *Proc SPIE* 6157, W. Gries and T. P. Pearsall, Eds., 61570C–61570C–14 (2005).
- [111] Clark, D. A., “Major Trends in Gravure Printed Electronics,” California Polytechnic State University (2010).
- [112] Gravure Association of America., Gravure Education Foundation, eds., *Gravure: process and technology*, Gravure Association of America, Rochester, NY (1991).
- [113] Grau, G., Scheideler, W. J., Subramanian, V., “High-resolution gravure printed lines: Proximity effects and design rules,” *Proc SPIE* 9569, 95690B–1, San Diego (2015).
- [114] Zhang, H., Ramm, A., Lim, S., Xie, W., Ahn, B. Y., Xu, W., Mahajan, A., Suszynski, W. J., Kim, C., et al., “Wettability Contrast Gravure Printing,” *Adv. Mater.* **27**(45), 7420–7425 (2015).
- [115] Grau, G., Kitsomboonloha, R., Subramanian, V., “Fabrication of a high-resolution roll for gravure printing of 2 $\mu$ m features,” *Proc SPIE* 9568, 95680M, San Diego (2015).
- [116] Arya, S. P. S., D’Amico, A., “Preparation, properties and applications of boron nitride thin films,” *Thin Solid Films* **157**(2), 267–282 (1988).
- [117] Ploof, L., “Electroless Nickel Composite Coatings,” *Adv. Mater. Process.* **166**(5), 36–38 (2008).
- [118] Buchheit, T. E., Goods, S. H., Kotula, P. G., Hlava, P. F., “Electrodeposited 80Ni–20Fe (Permalloy) as a structural material for high aspect ratio microfabrication,” *Mater. Sci. Eng. A* **432**(1–2), 149–157 (2006).
- [119] Choi, S.-J., Kim, H. N., Bae, W. G., Suh, K.-Y., “Modulus- and surface energy-tunable ultraviolet-curable polyurethane acrylate: properties and applications,” *J. Mater. Chem.* **21**(38), 14325 (2011).
- [120] Pforr, R., Ronse, K. G., Van den Hove, L., Yen, A., Palmer, S. R., Fuller, G. E., Otto, O. W., “Feature biasing versus feature-assisted lithography: a comparison of proximity correction methods for 0.5\*( $\lambda$ /NA) lithography,” *Proc SPIE* 2440 Opt. Microlithogr. VIII, T. A. Brunner, Ed., 150–170 (1995).

- [121] Garofalo, J., “Mask assisted off-axis illumination technique for random logic,” *J. Vac. Sci. Technol. B Microelectron. Nanometer Struct.* **11**(6), 2651 (1993).
- [122] Fung Chen, J., “Optical proximity correction for intermediate-pitch features using sub-resolution scattering bars,” *J. Vac. Sci. Technol. B Microelectron. Nanometer Struct.* **15**(6), 2426 (1997).
- [123] Chen, J. F., Laidig, T. L., Wampler, K. E., Caldwell, R. F., “Practical method for full-chip optical proximity correction,” *Proc SPIE 3051 Opt. Microlithogr. X*, G. E. Fuller, Ed., 790–803 (1997).
- [124] Bornemann, N., “Characterization and Investigation of Large-Area, Ultra-Thin Gravure Printed Layers,” PhD thesis, Technische Universität Darmstadt (2014).
- [125] Saffman, P. G., Taylor, G., “The Penetration of a Fluid into a Porous Medium or Hele-Shaw Cell Containing a More Viscous Liquid,” *Proc. R. Soc. Math. Phys. Eng. Sci.* **245**(1242), 312–329 (1958).
- [126] Tabeling, P., Zocchi, G., Libchaber, A., “An experimental study of the Saffman-Taylor instability,” *J. Fluid Mech.* **177**(1), 67 (1987).
- [127] Voß, C., “Analytische Modellierung, experimentelle Untersuchungen und dreidimensionale Gitter-Boltzmann Simulation der quasistatischen und instabilen Farbspaltung,” PhD thesis, Bergischen Universität Gesamthochschule Wuppertal (2002).
- [128] Reuter, K., Kempa, H., Brandt, N., Bartzsch, M., Huebler, A. C., “Influence of process parameters on the electrical properties of offset printed conductive polymer layers,” *Prog. Org. Coat.* **58**(4), 312–315 (2007).
- [129] Bornemann, N., Sauer, H. M., Dörsam, E., “Gravure Printed Ultrathin Layers of Small-Molecule Semiconductors on Glass,” *J. Imaging Sci. Technol.* **55**(4), 40201 (2011).
- [130] Hernandez-Sosa, G., Bornemann, N., Ringle, I., Agari, M., Dörsam, E., Mechau, N., Lemmer, U., “Rheological and Drying Considerations for Uniformly Gravure-Printed Layers: Towards Large-Area Flexible Organic Light-Emitting Diodes,” *Adv. Funct. Mater.* **23**(25), 3164–3171 (2013).
- [131] Anthony, J. E., Eaton, D. L., Parkin, S. R., “A Road Map to Stable, Soluble, Easily Crystallized Pentacene Derivatives,” *Org. Lett.* **4**(1), 15–18 (2002).
- [132] Hamilton, R., Smith, J., Ogier, S., Heeney, M., Anthony, J. E., McCulloch, I., Veres, J., Bradley, D. D. C., Anthopoulos, T. D., “High-Performance Polymer-Small Molecule Blend Organic Transistors,” *Adv. Mater.* **21**(10–11), 1166–1171 (2009).
- [133] Smith, J., Hamilton, R., McCulloch, I., Stingelin-Stutzmann, N., Heeney, M., Bradley, D. D. C., Anthopoulos, T. D., “Solution-processed organic transistors based on semiconducting blends,” *J. Mater. Chem.* **20**(13), 2562 (2010).
- [134] Hatano, M., Moon, S., Lee, M., Suzuki, K., Grigoropoulos, C. P., “Excimer laser-induced temperature field in melting and resolidification of silicon thin films,” *J. Appl. Phys.* **87**(1), 36 (2000).
- [135] Lee, M., Moon, S., Grigoropoulos, C. P., “In situ visualization of interface dynamics during the double laser recrystallization of amorphous silicon thin films,” *J. Cryst. Growth* **226**(1), 8–12 (2001).
- [136] Ryu, S.-G., Gruber, I., Grigoropoulos, C. P., Poulidakos, D., Moon, S.-J., “Large area crystallization of amorphous Si with overlapping high repetition rate laser pulses,” *Thin Solid Films* **520**(22), 6724–6729 (2012).

- [137] Lee, M., Moon, S., Hatano, M., Suzuki, K., Grigoropoulos, C. P., “Relationship between fluence gradient and lateral grain growth in spatially controlled excimer laser crystallization of amorphous silicon films,” *J. Appl. Phys.* **88**(9), 4994 (2000).
- [138] Sposili, R. S., Im, J. S., “Sequential lateral solidification of thin silicon films on SiO<sub>2</sub>,” *Appl. Phys. Lett.* **69**(19), 2864 (1996).
- [139] Liu, C.-Y., Bard, A. J., “In-Situ Regrowth and Purification by Zone Melting of Organic Single-Crystal Thin Films Yielding Significantly Enhanced Optoelectronic Properties,” *Chem. Mater.* **12**(8), 2353–2362 (2000).
- [140] Schweicher, G., Paquay, N., Amato, C., Resel, R., Koini, M., Talvy, S., Lemaire, V., Cornil, J., Geerts, Y., et al., “Toward Single Crystal Thin Films of Terthiophene by Directional Crystallization Using a Thermal Gradient,” *Cryst. Growth Des.* **11**(8), 3663–3672 (2011).
- [141] Natsume, Y., Minakata, T., Aoyagi, T., “Pentacene thin film transistors fabricated by solution process with directional crystal growth,” *Org. Electron.* **10**(1), 107–114 (2009).
- [142] Becerril, H. A., Roberts, M. E., Liu, Z., Locklin, J., Bao, Z., “High-Performance Organic Thin-Film Transistors through Solution-Sheared Deposition of Small-Molecule Organic Semiconductors,” *Adv. Mater.* **20**(13), 2588–2594 (2008).
- [143] Soeda, J., Uemura, T., Okamoto, T., Mitsui, C., Yamagishi, M., Takeya, J., “Inch-Size Solution-Processed Single-Crystalline Films of High-Mobility Organic Semiconductors,” *Appl. Phys. Express* **6**(7), 76503 (2013).
- [144] Tracz, A., Jeszka, J. K., Watson, M. D., Pisula, W., Müllen, K., Pakula, T., “Uniaxial Alignment of the Columnar Super-Structure of a Hexa (Alkyl) Hexa-peri-hexabenzocoronene on Untreated Glass by Simple Solution Processing,” *J. Am. Chem. Soc.* **125**(7), 1682–1683 (2003).
- [145] Pisula, W., Menon, A., Stepputat, M., Lieberwirth, I., Kolb, U., Tracz, A., Sirringhaus, H., Pakula, T., Müllen, K., “A Zone-Casting Technique for Device Fabrication of Field-Effect Transistors Based on Discotic Hexa-peri-hexabenzocoronene,” *Adv. Mater.* **17**(6), 684–689 (2005).
- [146] Miskiewicz, P., Mas-Torrent, M., Jung, J., Kotarba, S., Glowacki, I., Gomar-Nadal, E., Amabilino, D. B., Veciana, J., Krause, B., et al., “Efficient High Area OFETs by Solution Based Processing of a  $\pi$ -Electron Rich Donor,” *Chem. Mater.* **18**(20), 4724–4729 (2006).
- [147] Duffy, C. M., Andreasen, J. W., Breiby, D. W., Nielsen, M. M., Ando, M., Minakata, T., Sirringhaus, H., “High-Mobility Aligned Pentacene Films Grown by Zone-Casting,” *Chem. Mater.* **20**(23), 7252–7259 (2008).
- [148] Miskiewicz, P., Kotarba, S., Jung, J., Marszalek, T., Mas-Torrent, M., Gomar-Nadal, E., Amabilino, D. B., Rovira, C., Veciana, J., et al., “Influence of SiO<sub>2</sub> surface energy on the performance of organic field effect transistors based on highly oriented, zone-cast layers of a tetrathiafulvalene derivative,” *J. Appl. Phys.* **104**(5), 54509 (2008).
- [149] Tsydel, I., Kucinska, M., Marszalek, T., Rybakiewicz, R., Nosal, A., Jung, J., Gazicki-Lipman, M., Pitsalidis, C., Gravalidis, C., et al., “High-Mobility and Low Turn-On Voltage n-Channel OTFTs Based on a Solution-Processable Derivative of Naphthalene Bisimide,” *Adv. Funct. Mater.* **22**(18), 3840–3844 (2012).
- [150] Keum, C.-M., Kwon, J.-H., Lee, S.-D., Bae, J.-H., “Control of the molecular order and cracks of the 6,13-bis(triisopropylsilylethynyl)-pentacene on a polymeric insulator by anisotropic solvent drying,” *Solid-State Electron.* **89**, 189–193 (2013).

- [151] Yoon, M.-H., Yan, H., Facchetti, A., Marks, T. J., “Low-Voltage Organic Field-Effect Transistors and Inverters Enabled by Ultrathin Cross-Linked Polymers as Gate Dielectrics,” *J. Am. Chem. Soc.* **127**(29), 10388–10395 (2005).
- [152] Park, Y. D., Kim, D. H., Jang, Y., Hwang, M., Lim, J. A., Cho, K., “Low-voltage polymer thin-film transistors with a self-assembled monolayer as the gate dielectric,” *Appl. Phys. Lett.* **87**(24), 243509 (2005).
- [153] Lai, S., Cosseddu, P., Gazzadi, G. C., Barbaro, M., Bonfiglio, A., “Towards high frequency performances of ultra-low voltage OTFTs: Combining self-alignment and hybrid, nanosized dielectrics,” *Org. Electron.* **14**(3), 754–761 (2013).
- [154] Pierre, A., Sadeghi, M., Payne, M. M., Facchetti, A., Anthony, J. E., Arias, A. C., “All-Printed Flexible Organic Transistors Enabled by Surface Tension-Guided Blade Coating,” *Adv. Mater.* **26**(32), 5722–5727 (2014).
- [155] Park, S. K., Jackson, T. N., Anthony, J. E., Mourey, D. A., “High mobility solution processed 6,13-bis(triisopropyl-silylethynyl) pentacene organic thin film transistors,” *Appl. Phys. Lett.* **91**(6), 63514 (2007).
- [156] Hansen, C. M., “50 Years with solubility parameters—past and future,” *Prog. Org. Coat.* **51**(1), 77–84 (2004).
- [157] Hansen, C. M., “Aspects of solubility, surfaces and diffusion in polymers,” *Prog. Org. Coat.* **51**(1), 55–66 (2004).
- [158] Gaikwad, A. M., Khan, Y., Ostfeld, A. E., Pandya, S., Abraham, S., Arias, A. C., “Identifying orthogonal solvents for solution processed organic transistors,” *Org. Electron.* **30**, 18–29 (2016).
- [159] Hansen, C. M., *Hansen solubility parameters: a user’s handbook*, 2nd ed, CRC Press, Boca Raton (2007).

## Appendix A: Bending test strain calculation

The strain in the device layer and equivalent bending radius for bent paper without a PEN plastic carrier are calculated by treating the PEN-paper stack as a composite beam without any uniaxial tension or compression. The thicknesses of both the paper and the PEN were measured ( $t_{PAP}=70\mu\text{m}$ ,  $t_{PEN}=130\mu\text{m}$ ). The respective Young's moduli were measured through tensile tests ( $E_{PAP}=1.8\text{GPa}$ ,  $E_{PEN}=4.75\text{GPa}$ ). Composite beam theory then gives the following formulae for the distance of the neutral axis from the device layer on top of the composite beam  $y$ , the strain in the device layer  $\epsilon_{device}$  and the equivalent bending radius for bending of paper without a plastic carrier  $R_{equiv}$ :

$$y = t_{PEN} + t_{PAP} - \frac{\frac{t_{PEN}^2 E_{PEN}}{2} + (t_{PAP} + t_{PEN}) t_{PAP}}{\frac{E_{PEN}}{E_{PAP}} t_{PEN} + t_{PAP}} \quad \text{Eq. A-1}$$

$$\epsilon_{device} = \frac{y}{R_{dowel} + t_{adhesive} + t_{PEN} + t_{PAP} - y} \quad \text{Eq. A-2}$$

$$R_{equiv} = \frac{t_{PAP}}{2} \left( \frac{1}{\epsilon_{device}} - 1 \right) \quad \text{Eq. A-3}$$

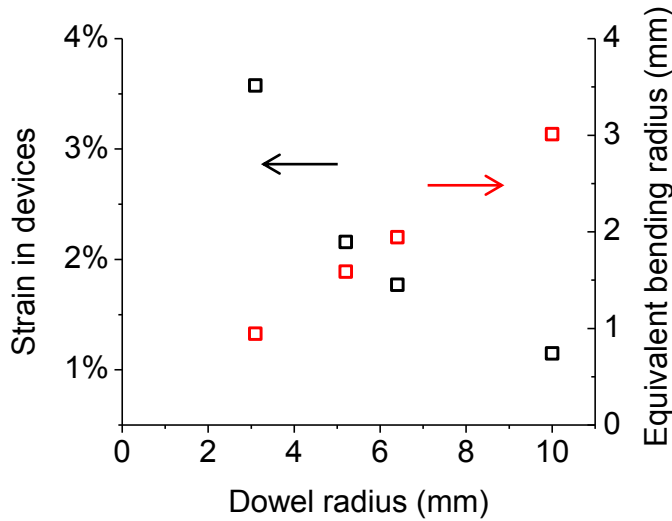


Figure A-1. Strain in device layer and equivalent bending radius for paper-only bending compared to paper-plastic sandwich.